PART I: VARIATION OF SEISMIC SOURCE PARAMETERS AND STRESS DROP WITHIN A DESCENDING SLAB AS REVEALED FROM BODY-WAVE PULSE-WIDTH AND AMPLITUDE ANALYSIS

PART II: A SEISMOLOGICAL INVESTIGATION OF THE SUBDUCTION MECHANISM OF ASEISMIC RIDGES

Thesis by

Wai-Ying Chung

In Partial Fulfillment of the Requirements
for the Degree of
Doctor of Philosophy

California Institute of Technology
Pasadena, California

1979

(Submitted December 28, 1978)

ACKNOWLEDGEMENTS

Throughout my stay at Caltech, I have benefitted greatly from the advice, encouragement, and support of professor Hiroo Kanamori. His excellent insight into geophysics and ready willingness to assist have been great resources for me.

I would also like to thank the many people at the Seismological Laboratory, both the past and present staff and students, who helped to shape the ideas presented in this thesis. In particular, I owe thanks to Yoshio Fukao for stimulating discussions on earthquake source and plate subduction, and Seiya Uyeda for helpful conversations about island arc tectonics. My colleagues Bob Geller, John Cipar and Seth Stein were particularly helpful during some portions of this work. I also benefitted from many interesting and constructive discussions with Bernard Minster and Don Helmberger. Tom Ahrens provided me with helpful advice on various aspects of my academic studies at Caltech.

Acknowledgement is made to the above persons and also to Don Anderson, Karen McNally, Mizuko Ishida, and Dave Cole who critically read all or part of this thesis.

The figures were skillfully drafted by Messrs. Lenches and Joseph Galvan. The manuscript was carefully typed by Mrs. Janet Boike.

Special acknowledgement is due my wife, Michelle. Her understanding and moral support added much to this endeavor.

This work was supported by the Division of Earth Sciences, National Science Foundation, NSF Grants EAR 76-14262, EAR 77-13641, and EAR 78-11973.

ABSTRACT

In Part I, a least squares searching technique has been developed to estimate the source dimensions of intermediate and deep focus earthquakes from the azimuthal variation of body-wave pulse-width. Modes of rupture propagation, seismic moment, stress drop and orientation of the slip plane can also be determined if both pulse-width and amplitude data are used. With this method, 17 intermediate and deep earthquakes in the Tonga-Kermadec arc system have been investigated in order to determine changes in the state of stress and source properties within a subducting slab. Three different modes of rupture, unilateral, bilateral, and circular faults, are compared and tested against observations. Results indicate that the unilateral fault is the best model for most of the earthquakes studied, the bilateral fault is the best model for some shocks, but the circular fault, in no cases, is better than the other two fault models. Stress drops of intermediate and deep focus earthquakes vary within a very large range, from 20 bars to 4617 bars, and change significantly with focal depth. Two high stress drop regions at depths about 360 km and 640 km seem to correlate with the depth ranges in which phase transitions occur. A relative minimum of stress drop is found at about 450 to 560 km where the annual number of earthquakes is particularly high. Earthquakes which occurred at the northern end of Tonga arc, where the Benioff zone is laterally bent, show systematically higher stress drops than other events at comparable depths but away from the bend. Also events in low seismicity regions appear to have higher stress drops than those

in high seismicity regions. Apparent stress is found to be smaller than half of the stress drop, and the upper bound of seismic efficiency appears to decrease as depth increases. A comparison of deep and shallow earthquake source parameters is also made.

In Chapter 1 of Part II, the subduction of the D'Entrecasteaux fracture zone-aseismic ridge system in the New Hebrides island arc is investigated on the basis of the focal process of the New Hebrides earthquake of January 19, 1969 (m_b = 6.4, h = 107 km), mechanisms of some related events, seismicity, and regional tectonics. A notable feature of this island arc is the discontinuity of the New Hebrides Trench in the central New Hebrides where the ridge-fracture zone is subducting and intersecting the arc. The 1969 New Hebrides earthquake occurred along the subducted portion of the fracture zone and is characterized by unusual wave forms with remarkably large excitation of long period waves. Body-wave and surface wave analyses reveal the earthquake was a complex event with a change of fault strike during the rupture process. The location and mechanism of this earthquake suggest that the D'Entrecasteaux fracture zone structurally extends to the east of the Trench. This structural boundary at depth seems to be reflected in the spatial distribution of two earthquake swarms which are bounded sharply at the latitude of 15.2°S. At the extension of the ridge-fracture zone, the activity of intermediate-depth earthquakes, which are characterized by a very consistent pattern of down-dip extensional mechanism, is much higher and their depths are systematically shallower than in the adjacent regions. These features can be interpreted as a consequence of

subduction of a buoyant ridge and the resultant increase in the extensional stress at the intermediate depths of the sinking slab. Fault-plane solutions of 22 earthquakes suggest that the subduction of aseismic ridges in the New Hebrides is characterized by high angle thrusts. The lithospheres on the two sides of the D'Entrecasteaux fracture zone under the arc subduct more or less independently and generate alternating left-lateral and right-lateral earthquakes along the subducted portion of the fracture zone.

In Chapter 2, tectonic features associated with a subducting fracture zone-aseismic ridge system in the New Hebrides island arc are investigated. Several notable features including a discontinuity of the trench, peculiar locations of two major islands (Santo and Malekula), regional uplift, and the formation of a basin are interpreted as a result of the subduction of a buoyant ridge system. The islands of Santo and Malekula are probably formed from uplifted mid-slope basement high while the interarc basin of this particular arc is probably a subsiding basin instead of a basin formed by backarc opening. The situation can be modeled by using a thin elastic half plate overlying a quarter fluid space with a vertical upward loading applied at the plate edge. This model is consistent with topographic and geophysical data. This study suggests that subduction of aseismic ridges can have significant effects on tectonic features at consuming plate boundaries.

In Chapter 3, seismicity near locations of aseismic ridge subduction has been investigated for five seismic regions: New Hebrides, Bonin-Mariana, Tonga-Kermadec, Peru and Northern Chile. The

maximum focal depth of intermediate-depth earthquakes beneath areas of aseismic ridge subduction is generally shallower than that on either side of the subducting ridge. This variation of focal depth in some cases forms a well-defined gap or quiet zone for intermediate-depth events. This phenomenon may be a consequence of differential subduction and difference in material properties between an aseismic ridge and the rest of the oceanic plate. Although at locations of aseismic ridge subduction large shallow earthquakes occur less frequently compared with the adjacent regions, small shallow earthquake activity is not always reduced. In addition, there is a high correlation between trench discontinuities and aseismic ridge subduction suggesting that a trench can be interrupted and divided into two sections by ridge subduction if the buoyant force associated with the ridge is strong enough.

TABLE OF CONTENTS

PART I

VARIATION OF SEISMIC SOURCE PARAMETERS AND STRESS DROP WITH A DESCENDING SLAB AS REVEALED FROM BODY-WAVE PULSE-WIDTH AND AMPLITUDE ANALYSIS

INTRODUCTION

Since the discovery of deep focus earthquakes (Wadati, 1928; Scrase, 1931; Stechschulte, 1932), evidence from deep earthquakes has furnished important clues about the earth's interior and has lent significant support to the new global tectonics. The deep sloping seismic zone found by Wadati (1935) and Benioff (1955) has been considered an expression of down-going lithospheric plate (Oliver and Isacks, 1967) and strongly supports an underthrusting of lithosphere beneath island arcs. Valuable information about the state of stress within a subducting slab and the driving mechanism of plate tectonics can also be obtained from studies of focal mechanisms of mantle earthquakes (Isacks and Molnar, 1971).

Even though a large amount of work has been done of deep earthquakes, the mechanism of deep-focus earthquakes remains a basic problem. Both shear dislocation and volumetric change due to phase transition (Knopoff and Randall, 1970) have been proposed as source mechanisms. However, no significant volume change at the source region has been observed (Randall and Knopoff, 1970; Aki, 1972; Okal and Geller, 1978); furthermore, first motions, amplitudes, and waveforms of P, S, Rayleigh and Love waves radiated from deep earthquakes can be explained quite well by using a shear dislocation source model (Isacks and Molnar, 1971; Fukao, 1970; Mikumo, 1971; Abe, 1972). This strongly suggests that shear faulting is a reasonable approximation to deep earthquake source. Therefore, in the present study, we assume that shear dislocation is the mechanism of deep-focus earthquake.

Determining the thermomechanical processes within subducting

lithospheric slabs has been a research area of great interest in recent years. A major difficulty with this kind of study comes from the fact that many physical parameters at great depths cannot be measured directly; as a consequence, few constraints can be placed on models of subduction. An important source of information about these processes comes from intermediate and deep focus earthquakes. The purpose of this study is to provide new seismological data which can be used as physical constraints to various thermomechanical models of plate subduction.

In recent years, several methods have been employed to study source parameters of intermediate and deep focus earthquakes, including analyses of body waves (Teng and Ben-Meanhem, 1965; Billinger, 1968; Berkhemer and Jacob, 1968; Khattri, 1969; Mikumo, 1969, 1971; Fukao, 1970, 1972; Wyss, 1970; Wyss and Molnar, 1972; Burdick and Helmberger, 1974; Sasatani, 1974; Chung and Kanamori, 1976; and Strelitz, 1977), surface waves (Wyss, 1970; Abe, 1972; Furumoto and Fukao, 1976; Chung and Kanamori, 1978; and Koyama, 1978), and free oscillations (Mendiguren, 1972; Dziewonski and Gilbert, 1974). For deep shocks, data from body waves are easier to obtain and usually provide a better resolution for the rupture process. For this reason, body wave data are used throughout this work. Earthquake source parameters can be estimated both in the frequency domain (Teng and Ben-Menahem, 1965; Khattri, 1969; Wyss, 1970; Wyss and Molnar, 1972) and the time domain (Bollinger, 1968, 1970; Berckhemer and Jacob, 1968; Mikumo, 1969, 1971; Fukao, 1970, 1972; Sasatani, 1974; Chung and Kanamori, 1976; Strelitz, 1977). In most of the frequency domain approaches, only the amplitude spectrum is explained. We prefer the

time domain approach because both phase and amplitude spectra can be interpreted simultaneously, and the theoretical prediction can be compared with observation in a more direct way.

In this study, we are going to determine the following source parameters: seismic moment M_o, source dimension L or a, fault area A, average dislocation $\bar{D}$, stress drop $\Delta\sigma$, apparent average stress $\eta\bar{\sigma}$, and the upper bound of seismic efficiency η_{max}, as well as mode of rupture: unilateral, bilateral, and circular faulting. Seventeen intermediate and deep focus earthquakes in the Tonga-Kermadec area have been investigated. We are particularly interested in learning how these parameters vary with local tectonic conditions and change as a function of depth. Source parameters of intermediate and deep focus earthquakes in Tonga-Kermadec area were studied by Wyss and Molnar (1972) using the corner frequency method developed by Brune (1970), Hanks and Wyss (1972) and Wyss and Hanks (1972). Kasahara (1957), Tsujiura (1972), Wyss (1970) and Wyss and Molnar (1972) investigated source parameters as a function of depth. Seismic moment is usually well determined; on the other hand, parameters such as source dimension, fault area, and stress drop are more model dependent. It is important to study these parameters by many different methods and to compare results from different models. In most previous source studies data were fit with an assumed mode of rupture and fault geometry without testing other possible models. In the present study, instead of assuming the same fault model for all events, several different models will be tested and compared; the best model is then used to compute the source parameters. This procedure

probably provides a better determination of source parameters.

As mentioned above, source dimensions and stress drops of deep earthquakes are model dependent; in particular estimated values for fault area and stress drop can vary substantially with different methods used. In order to investigate regional and depth variation of stress drop it is desirable to compare stress drops determined by the same method. If we can determine stress drops for a large number of events by employing a reasonably good technique we can, at least, have a good estimate of relative stress drops even though the absolute values are to some extent model dependent. In the early part of this study, we first develop a relatively new technique for determining the source dimension and stress drop of intermediate and deep focus earthquakes through an inversion of azimuthal change in pulse-width of body-waves. In the later part, the technique is applied to investigate the variation of stress drop at different parts of the Benioff zone in the Tonga-Kermadec arc.

A PROCEDURE FOR MODELING DEEP EARTHQUAKE SOURCE IN THE TIME DOMAIN

We can extract earthquake source parameters from time domain information in several different ways. P-wave first-motion data (Stauder, 1962) and S-wave polarization angles (Hirasawa, 1966) have been used to determine fault geometry. A rupture process of multiple shocks can be inferred by modeling the multiple arrivals of P-waves (Wyss and Brune, 1967; Trifunac and Brune, 1970; Fukao, 1972; Chung and Kanamori, 1976; Strelitz, 1977). Bollinger (1968)

used the spatial variation of body wave pulse width to study rupture mode, fault length, and rupture velocity. Synthetic seismograms have been used to determine focal depth (Helmberger, 1974; Chung and Kanamori, 1978; Stein, 1978) and other parameters (Fukao, 1970; Mikumo, 1969, 1971; Langston and Helmberger, 1975; Kanamori and Stewart, 1976, 1978).

In most of the earthquake source studies using synthetic seismograms, a trial and error method is employed to fit the wave-forms and usually is time consuming. In the present study, we introduce a searching procedure which can give an optimum estimate for several source parameters and a very good fit between theoretical and observed seismograms. The waveforms of most intermediate and deep focus earthquakes are very simple; the P-waves usually have a large first swing and a small second swing and then die away very quickly. The most important parameters characterizing the wave-form are the pulse-width and the amplitude of the first swing. The amplitude of the second swing can be, to some extent, handled by choosing a proper shape for the far field source time function. Therefore we can compute a good theoretical seismogram which fits the wave-forms of a simple deep earthquake if the width and the amplitude of the first swing are matched correctly. Seismic moment and source dimension can then be determined using source models. For shallow earthquakes, source dimension can be estimated from aftershock area, geodetic data, tsunami source area, surface wave directivity, as well as body wave analyses. For deep earthquakes, however, the first four of the above methods do not apply, hence body wave pulse-width becomes the fundamental

information for source size estimation. In this study, the duration of the far field source time function and its azimuthal variation are used to infer the source size. The determination of fault dimension involves assumptions regarding the fault geometry, mode of rupture, and dislocation rise time, and is often non-unique. In order to reduce the degree of non-uniqueness, we will model the observed duration of far field time function and its azimuthal variation with several simple source models; the one which best explains the observation is then used to calculate the fault dimension and other parameters.

Rupture Modes and Durations of Far Field Time Functions

The geometry of a real fault is usually irregular. However, several simple fault models have been used to make analytical formulation possible. Unilateral and bilateral faulting with a constant rupture velocity on a rectangular fault (Knopoff and Gilbert, 1959; Ben-Menahem, 1961, 1962; Haskell, 1969; Niazi, 1974) are frequently employed. Savage (1966) computed the pulse from a circular fault in which the rupture initiated at the center, and then propagated outward with a uniform velocity. Savage suggested that this fault rupture model might be more appropriate for deep earthquake sources. For the cases of unilateral and bilateral faulting it is usually assumed that the rupture occurs simultaneously over the entire width of the fault and that the fault length L is much larger than the fault width W. In this case the contribution from the fault width to the duration of the far field time function is assumed to be minor and can be neglected. If a rupture starts at point A and propagates unilaterally to point B

with a constant rupture velocity v_r (Figure 1a) the duration of the far field source time function T_s is given by

$$T_s = \frac{L}{v_r} - \frac{L}{v_c}\cos\theta + \tau_o \qquad (1)$$

where θ is the angle between the rupture direction and the ray taking off from point A to observation point P, τ_o is the rise time of dislocation, and v_c is the P or S wave velocity of the medium. If the rupture starts at A and propagates bilaterally to points B and C (Figure 1b), we have

$$T_s = \frac{L}{2v_r} + \frac{L}{2v_c}\left|\cos\theta\right| + \tau_o \qquad (2)$$

In Figure 1c, the rupture initiates at point O and propagates radially and symmetrically with a constant velocity on a circular fault with radius a. For this case we have

$$T_s = \frac{a}{v_r} + \frac{a}{v_c}\sin\xi + \tau_o \qquad (3)$$

where ξ is the angle between the normal to the fault plane and the ray taking off at O for the observation point P. Let us consider the unilateral case first. For each earthquake we can determine T_s at each individual station, and for given direction of fault propagation, we can calculate Θ for each station. With the value of T_s and θ at a number of stations we can determine the value of $(\frac{L}{v_r} + \tau_o)$ in equation (1) by using the method of least squares. Since there are several unknown parameters involved we would like to reduce the number of unknowns by constraining some of them within certain reasonable ranges. For a given value of v_r, if we let τ_o be zero and solve for L, from

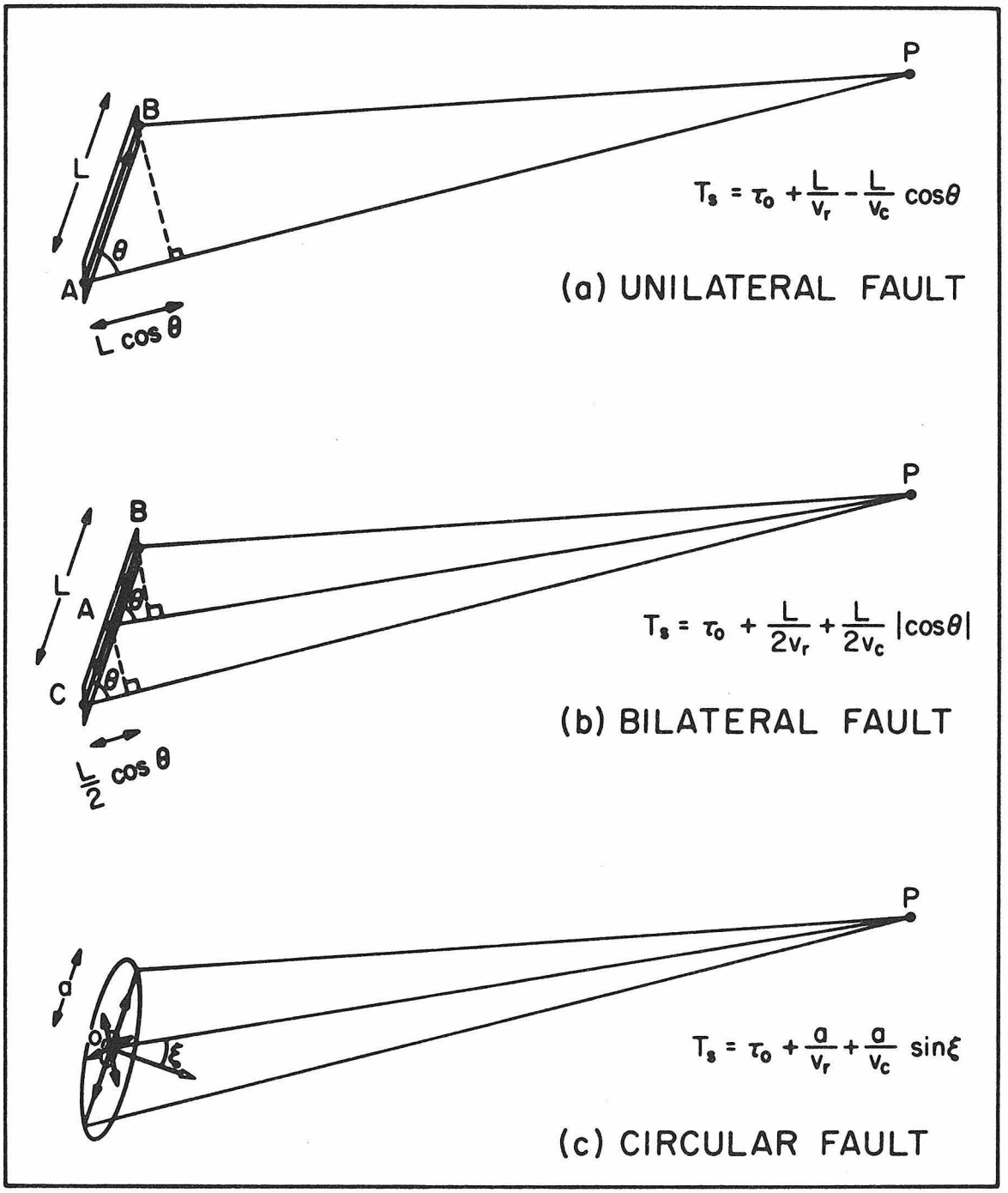

Figure 1. Three modes of rupture propagation.

$\frac{L}{v_r} + \tau_o$ = a known constant, we get a value of L which is larger than what it should be if $\tau_o \neq 0$. In other words we can get an upper bound of L by making $\tau_o = 0$ in (1). Then (1) can be written as

$$T_s = \frac{L}{v_c}\left(\frac{v_c}{v_r} - \cos\theta\right)$$

or
$$T_s = b\,X \tag{4}$$

if we let $b = \frac{L}{v_c}$ and $X = \left(\frac{v_c}{v_r} - \cos\theta\right)$. It is easy to see that all equations (1), (2), and (3) can be written as equation (4) if we let

$$b = \begin{cases} \frac{L}{v_c} & \text{for unilateral fault} \\ \frac{L}{2v_c} & \text{for bilateral fault} \\ \frac{a}{v_c} & \text{for circular fault} \end{cases} \tag{5}$$

and

$$X = \begin{cases} \frac{v_c}{v_r} - \cos\theta & \text{for unilateral fault} \\ \frac{v_c}{v_r} + |\cos\theta| & \text{for bilateral fault} \\ \frac{v_c}{v_r} + \sin\xi & \text{for circular fault} \end{cases} \tag{6}$$

Synthetic Body-Wave Seismogram and Determination of the Duration of Far Field Source Time Function

Fukao (1970) determined the durations of boxcar far field time functions by matching synthetic seismograms to observation. Another

way to determine the duration without doing synthetic seismograms for each individual event was employed by Bollinger (1968, 1970) who calculated theoretical relationship between the duration of far field time function T_s and the pulse-width on a long period record T_r and then determined T_s directly from a theoretical curve. We use Bollinger's approach with some modification. In constructing the theoretical relationship between T_s and T_r we use proper far field source time functions and take attenuation into account.

For a given far field source time function S(t) with a certain duration and shape, far field synthetic seismograms $u_c(t)$ can be generated by using standard techniques, for example, similar to that described in Chung and Kanamori (1976). The expression for $u_c(t)$ is

$$u_c(t) = \frac{M_o}{4\pi\rho_h v_{c,h}^3} \frac{g(\Delta,h)}{a} R_{\theta\phi}^c \cdot S\left(t-T_o^c\right) * Q\left(t,\frac{T_o^c}{Q_{av}^c}\right)$$

$$* C(t) * I(t) \qquad (7)$$

where M_o is the seismic moment, ρ_h the density at the source, $v_{c,h}$ the wave velocity at the source, and c stands for P or S depending upon the kind of wave considered. $g(\Delta,h)$is the geometrical spreading factor, a the earth's radius, $R_{\theta\phi}^c$ the radiation pattern, T_o^c the travel time, $Q\left(t,\frac{T_o^c}{Q_{av}^c}\right)$ the attenuation filter of the earth (Carpenter, 1966, 1967), Q_{av}^c the average value of Q over the ray path, C(T) the crust-filter, and I(t) the impulse response of the recording instrument. The area under the far field time function S(t) has been normalized to one representing unit seismic moment (10^{25} dyne-cm). The geometrical spreading factor, $g(\Delta,h)$, which is a function of epicentral distance Δ,

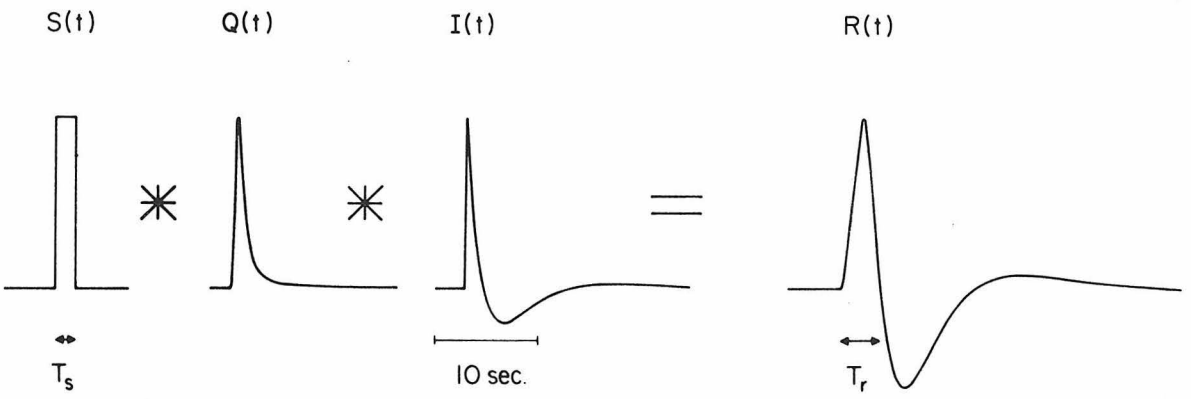

Figure 2. Calculation of theoretical pulse-width T_r on a seismic record R(t) by convolving a boxcar far field time function S(t) having a duration T_s with a Q-filter Q(t) and an instrument impulse response I(t). * stands for convolution operation. The far field source time function S(t) can be different from a boxcar, which is just an example used in this figure.

focal depth h, and earth structure, is given by (Honda, 1962; Bullen, 1963):

$$g(\Delta,h) = \left(\frac{\rho_h v_{c,h}}{\rho_o v_{c,o}} \frac{\sin i_h}{\sin \Delta} \frac{1}{\cos i_o} \left|\frac{di_h}{d\Delta}\right|\right)^{1/2} \qquad (8)$$

where ρ_o, $v_{c,o}$ and i_o are the density, the wave velocity, and the angle of incidence at the surface respectively, and i_h is the incidence angle or take-off angle at the source depth h. For P waves from shallow teleseismic events, $T_o^P/Q^P_{av} \sim$ 1s (Carpenter and Flinn, 1965; Kanamori, 1967). For intermediate and deep focus earthquakes we use T_o^P/Q^P_{av} = 0.75s. If we just consider the effect of the free-surface under the station C(t) reduces to a constant C_o given by

$$C_o = 2 \qquad \text{for SH waves}$$

and

$$C_o = \frac{6 \cos i \csc^2 i \,(1+3\cot^2 i)}{4 \cot i \cot g + (1+3\cot^2 i)^2} \qquad \text{for P waves}$$

(Bullen, 1965) where i is the incident angle of P waves and g the reflection angle of the SV waves which are generated by the reflection at the free surface. Hence we have

$$u_c(t) = \frac{M_o}{4\pi\rho_h v^3_{c,h}} \frac{g(\Delta,h)}{a} R^c_{\theta,\phi} C_o \cdot S(t-T_o^c) * Q\left(t, \frac{T_o^c}{Q_{av}^c}\right) * I(t) \qquad (9)$$

As far as computing the theoretical pulse-width of the first swing on the long-period record is concerned we just need to convolve the far field source time function with the Q filter and the impulse response of the instrument (Figure 2). The T_s versus T_r relationship is a function of the far field time history S(t). In this study T_s versus T_r relationships are calculated for boxcar and triangle far field time functions (Figures 3 and 4); and then we use the average

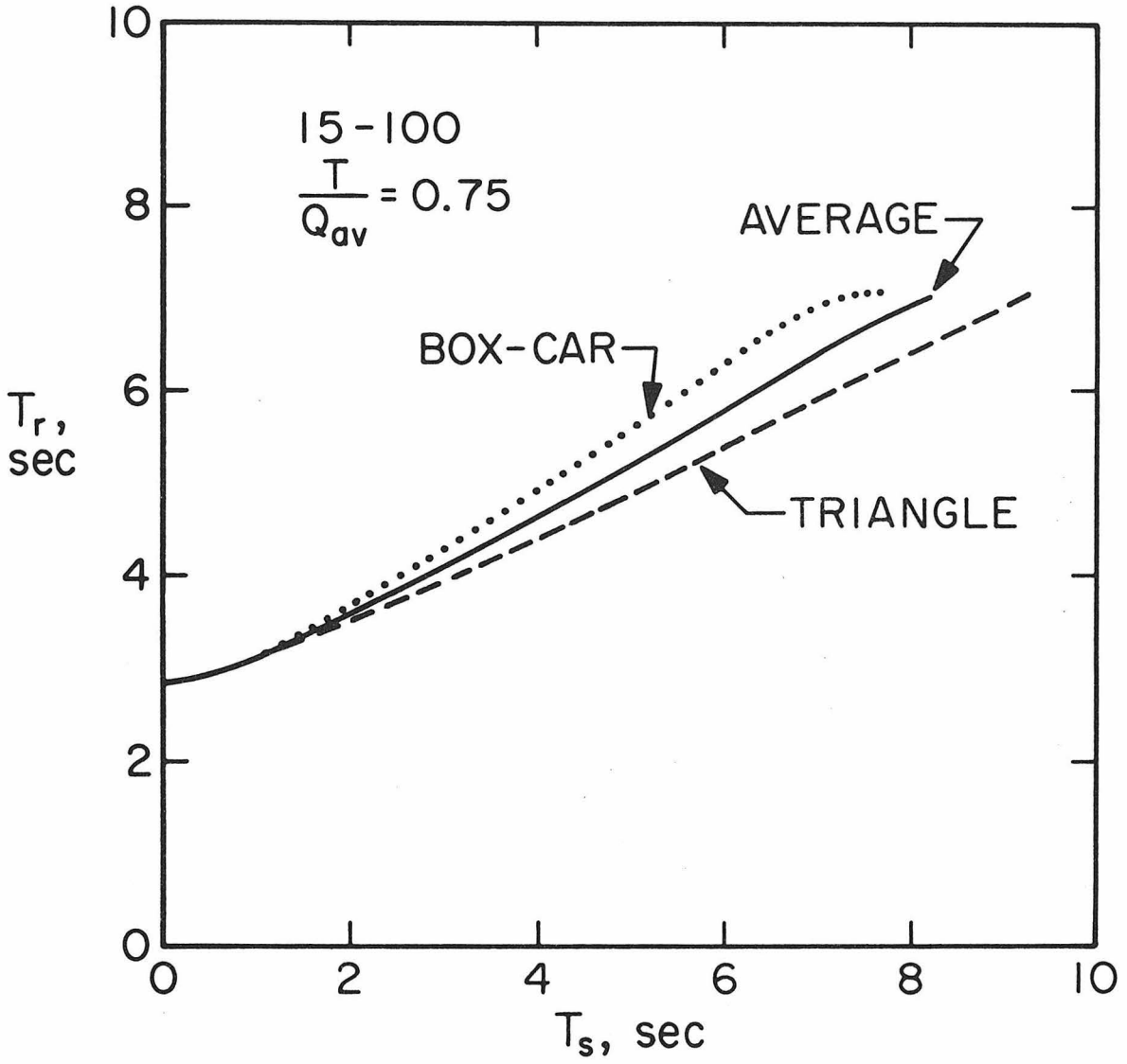

Figure 3. Relationship between the observed pulse-width T_r on a seismic record and the duration T_s of far field source time function. The dashed and dotted curves are for triangular and boxcar far field time functions respectively, while the solid curve is the average. The recording instrument used is WWSSN long period seismograph (15-100), and $\left(\frac{T_o}{Q_{av}}\right)^P = 0.75$

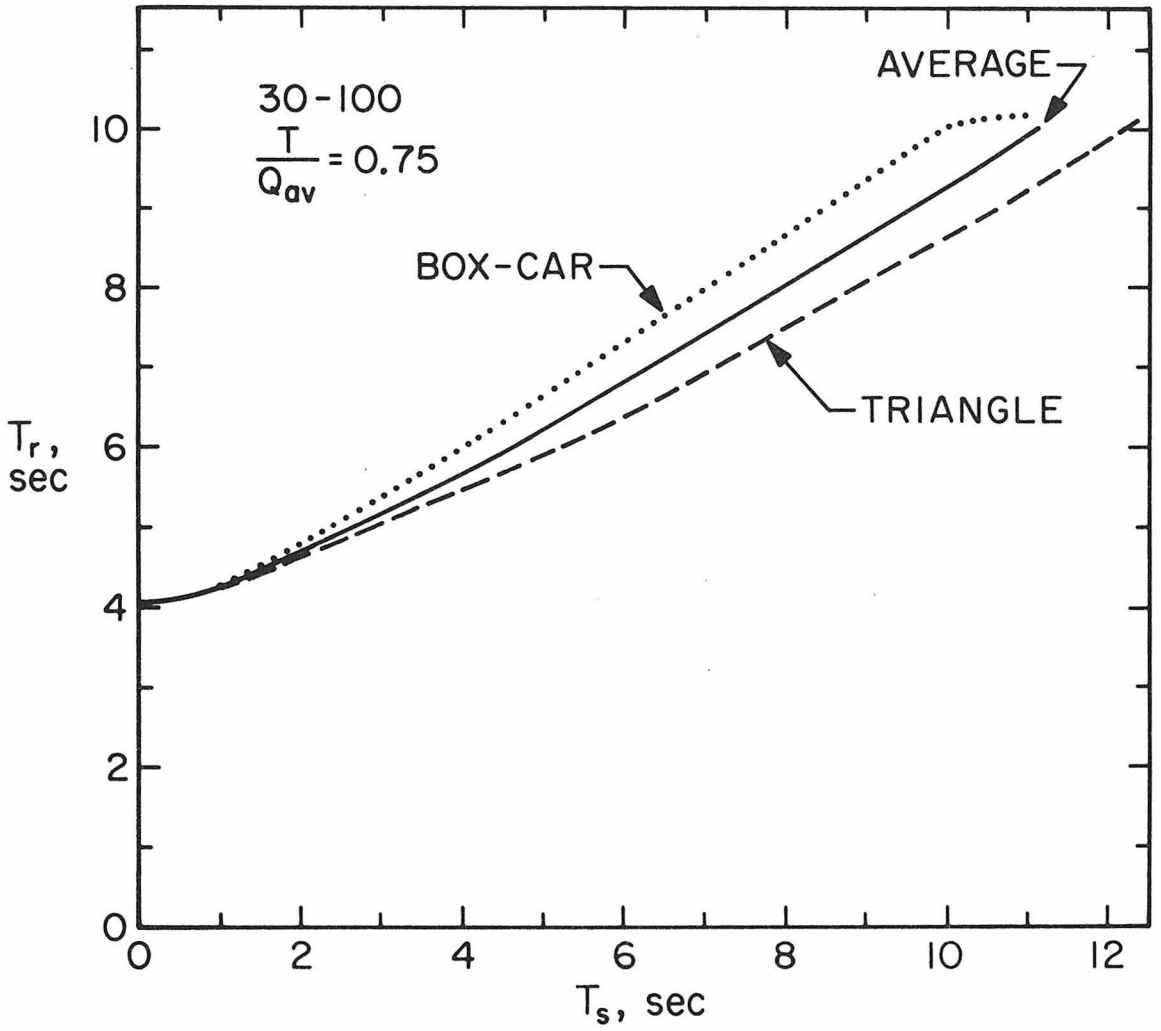

Figure 4. T_r versus T_s relationships for long period (30-100) WWSSN instrument and $\left(\frac{T_o}{Q_{av}}\right)^P = 0.75$. See the caption of Figure 3 for the other representations.

in the following analysis to estimate the duration of far field time function from the observed pulse-width on seismic records. Without going through a detailed wave-form analysis, we do not know the shape of the far field source time function accurately. By using the above average T_s versus T_r relationship we imply that the far field time function is assumed to be in between a triangle and a boxcar. As will be shown in a later section, this simple method gives a very satisfactory result.

Slip Plane Orientation, Mode of Rupture, and Source Dimension Inferred from Least Squares Searching Technique

Usually we have ambiguity in determining which nodal plane is the fault even though the focal mechanism is known. A way to remove this ambiguity is to study the azimuthal change in body-wave pulse-width. The durations of far field source time functions, T_s's, can be determined from the pulse-widths at a number of stations by the method described in the previous section. For a given nodal plane and a given rupture direction we can calculate θ's or ξ's for the stations. Least squares technique can then be applied to equations (1), (2), (3) or (4) with the known values of T_s's and θ's or ξ's. The rupture direction is also an unknown, and we can try many rupture directions on each nodal plane and do a least squares fit for each case. The rupture direction and the nodal plane which best fit the data are then determined to be the rupture direction and the slip plane.

We also compare results for each of the three modes of rupture propagation discussed above. The one that explains the data best is

used to calculate source parameters. In addition to the determinations of fault plane, rupture direction, and mode of rupture, we can determine the value b (in equation (5)) from which source dimension can be obtained if a reasonable value of v_c is used. The width of a rectangular fault is usually very difficult to estimate accurately from far field seismic data. Geometric similarity $\frac{W}{L}$ = constant has been used and observed by Abe (1975) and Geller (1976). For large shallow earthquakes, $\frac{W}{L} \approx 0.5$ was reported by Abe (1975) and Geller (1976). For smaller shallow events, $\frac{W}{L} \approx 0.4$ has also been observed (Ellsworth, 1975). We assume that the fault width W equals to 0.4 of the fault length for the earthquakes in this study. The consequent stress drops will be slightly different if a different width to length ratio is assumed. Nevertheless, the relative stress drops do not change in any significant way with a change in $\frac{W}{L}$.

Determinations of Seismic Moment and Stress Drop

Seismic moments are determined by comparing the theoretical and observed amplitudes. The theoretical amplitudes are computed using the method described in an earlier section with a trapezoid far field source time function S(t) (Figure 16).

For a circular fault with radius a (Eshelby, 1957; Keilis Borok, 1959), the stress drop is given by

$$\Delta\sigma = \frac{7\pi}{16} \mu \frac{\overline{D}}{a}$$

or

$$\Delta\sigma = \frac{7}{16} \frac{M_o}{a^3} \qquad (10)$$

where μ, $\overline{D}$, and M_o are rigidity, average dislocation, and seismic

moment respectively. For a rectangular fault with length L and width W, we calculate the radius of its equivalent circular fault with area A = LW and use equation (10) to obtain stress drop.

DATA ANALYSIS AND RESULTS

The Tonga-Kermadec area is one of the most active regions in the world for both shallow and deep seismicity. Near the northern end of the area, the Tonga trench and associated Benioff zone curve abruptly to the west while the rest of the Tonga-Kermadec arc is remarkably linear. Because of its high activity, the Tonga-Kermadec area presents a unique opportunity for a detailed study of mantle earthquakes. The most ideal way to investigate the variation of stress drop and other source parameters within a descending slab is to do a detailed study of a very large number of earthquakes and to sample different parts of the slab evenly. However, estimation of stress drop is usually quite involved and time consuming. At present, it is impractical to determine the stress drops of a very large number of events. Instead, we are limited to analyzing a relatively small number of events. Seventeen earthquakes (Table 1 and Figure 5) in the Tonga-Kermadec area with depths ranging from about 100 to 650 km and long-period body-wave magnitude m_B from 5.7 to 6.6 are investigated. We would like to investigate earthquakes with known fault plane solutions, and also want to have about the same number of samples for each depth range. As a result, the number of samples for different dpeth ranges are not proportional to the seismicity because the seismicity of Tonga-Kermadec varies with depth (Figure 23). The

TABLE 1

Event	Date			Time			Lat.	Long.	Depth	Magnitude
	m	d	y	h	m	s	Degrees		km	m_b
1	3	11	68	8	26	32.8	16.2S	173.9W	112	6.2
2	8	12	67	9	39	44.3	24.7S	177.5W	134	6.5
3	12	8	65	18	5	25.2	37.1S	177.5E	156	6.0
4	5	1	69	19	5	24.5	16.7S	174.6W	205	6.1
5	3	18	65	6	22	12	19.9S	175.9W	219	6.0
6	9	4	67	3	51	58.9	31.4S	179.4W	231	6.2
7	9	26	68	14	37	46.2	20.9S	176.7W	251	6.0
8	6	4	74	4	14	13.8	15.895	175.04W	256	6.3
9	2	22	75	22	4	33.5	24.98S	178.88W	333	6.6
10	1	20	68	21	21	31.6	29.9S	179.5W	349	6.0
11	7	21	73	4	19	13.7	24.83S	179.19W	373	6.1
12	11	18	65	20	0	19.5	12.8S	177.8W	424	6.2
13	2	3	76	12	27	30.1	25.14S	179.7E	477	6.0
14	1	28	66	4	36	45.3	17.64S	177.01E	545	5.8
15	7	21	66	18	30	15.3	17.8S	178.6W	590	5.8
16	3	17	66	15	50	33.1	21.1S	179.2W	630	6.2
17	12	9	65	13	12	55.3	18.12S	178.12W	649	5.7

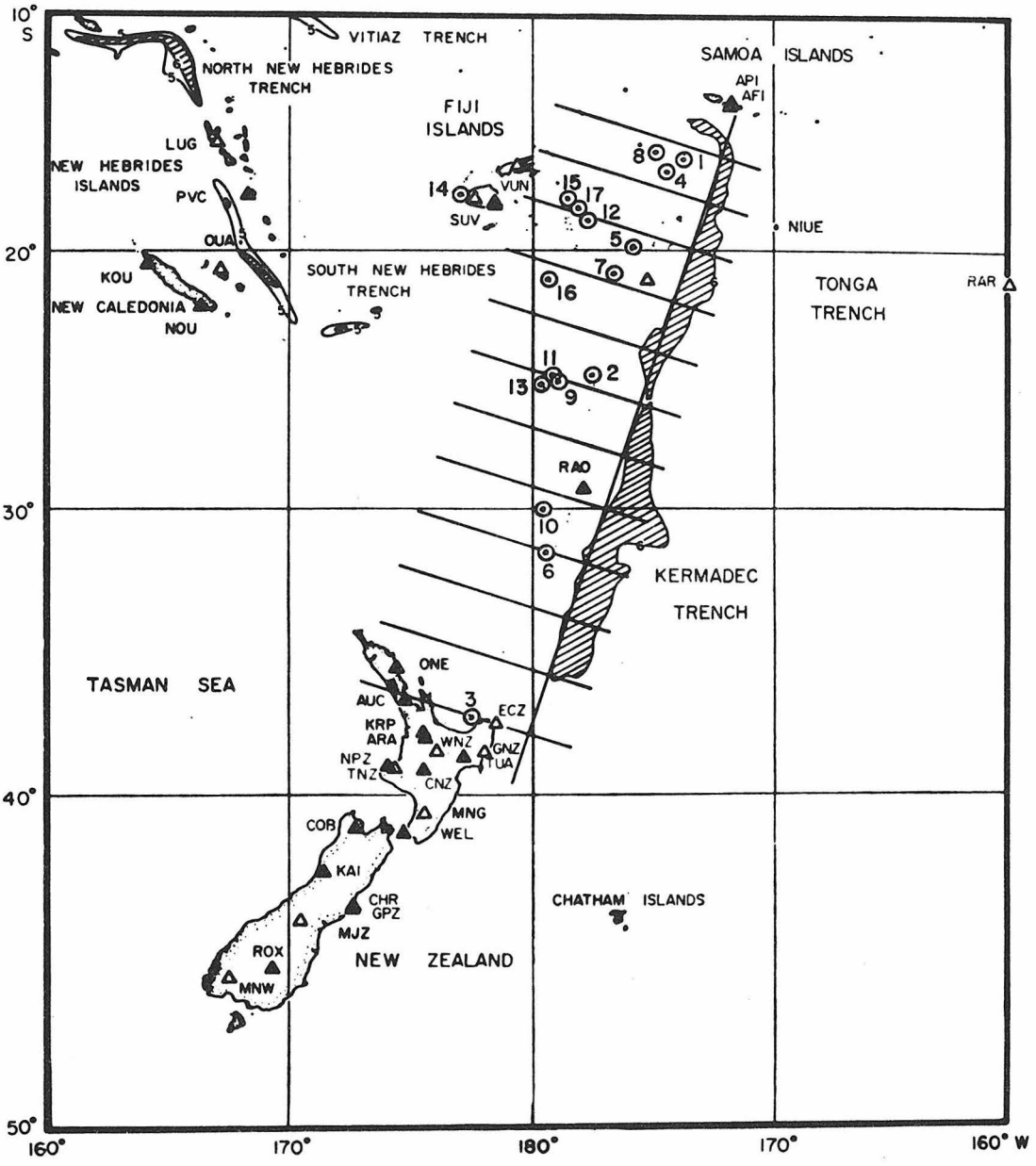

Figure 5. Locations of the 17 earthquakes in the Tonga-Kermadec arc. Open circles with dots and associated numbers are earthquake epicenters and event numbers in Table 1 respectively, while triangles stand for local seismic stations. The line segments indicate the locations of the vertical sections used in Figures 23 and 24. (Modified from Sykes, 1966).

number of earthquakes studied here is only a small percentage of the total number of events of the same magnitude range in the Tonga-Kermadec area. The percentages are roughly 23%, 32%, and 7% for depth-ranges from 100 to 250 km, 251 to 480 km, and greater than 480 km, respectively. In Table 1, events are numbered in an order of increasing focal depth. Focal mechanisms of earthquakes 5, 12, 14, 15, 16, and 17 were studied by Isacks et al. (1969) while the mechanisms of events 1, 2, 3, 6, and 10, and 4 and 7, were determined by Isacks and Molnar (1971) and Wyss and Molnar (1972), respectively. (Figure 6a, b, and c). Fault plane solutions of shocks 8, 9, 11, and 13 are determined in this study (Figure 6d). Most of the first-motion data are read from the WWSSN long-period records. In some cases the data reported by ISC and the WWSSN short-period records are used to supplement the long period data. We try to avoid multiple events and study earthquakes with very simple wave-forms (Figure 19 and 20). Duration of the first half swing of each event is measured from the long period WWSSN records at many stations. The number of stations used for the duration measurement for each event ranges from 6 to 17, and for most events the number is larger than 11. The durations of the recorded half swings are then converted to the source duration by using the solid curves in Figures 3 and 4. Having the values of T_s (equation 4) at a number of stations, the searching process described above is carried out through a series of least squares analyses. We do a least squares fit for each possible combination of the source parameters and for each fault plane orientation and mode of rupture. For example, there are two possible fault planes, three possible

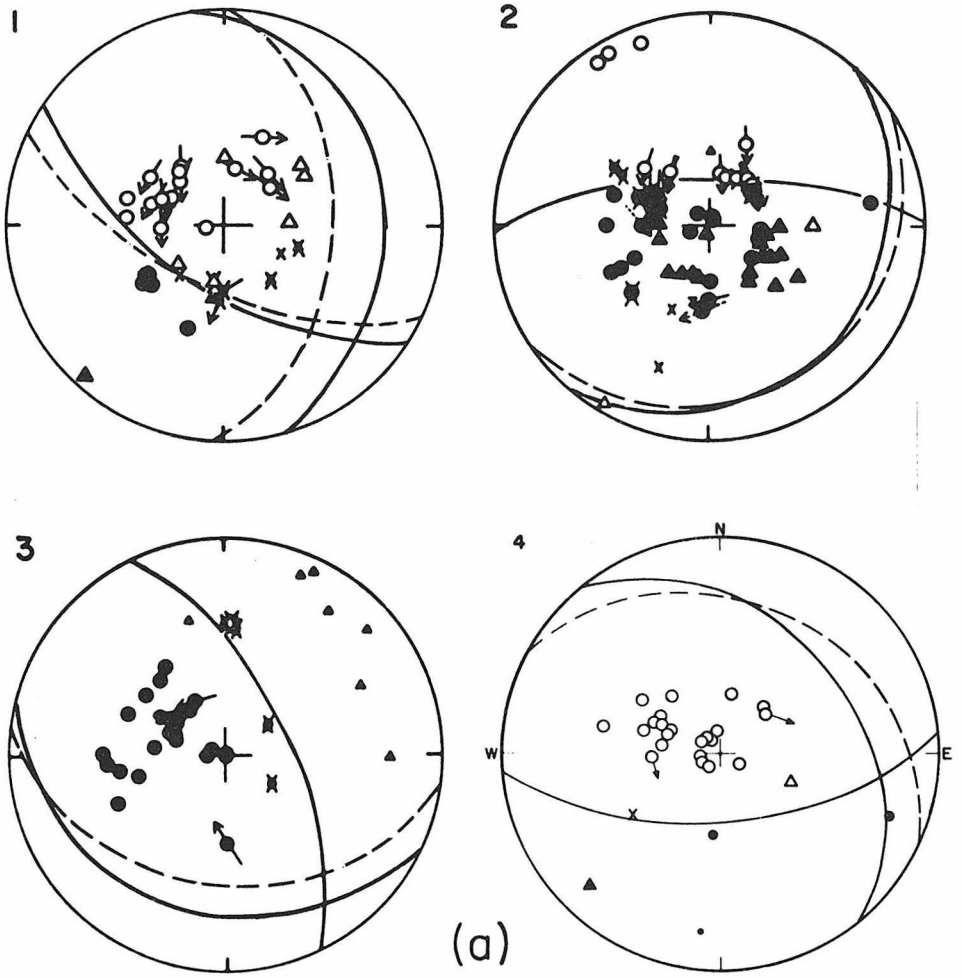

Figure 6. Fault plane solutions of the 17 earthquakes studied. Solutions in (a), (b) and (c) are taken and modified from Isacks et al. (1969), Isacks and Molnar (1971) and Wyss and Molnar (1972). The solid curves are the improved focal mechanisms from this study or the well constrained mechanisms of the above investigators; the dashed curves are the solutions reported by the previous authors. (d) fault plane solutions and equal area projections of P-wave first motions on the lower hemisphere from this study. Closed and open circles represent compressions and dilatations respectively. Large circles are more reliable data. Event number is given at the upper left of each solution.

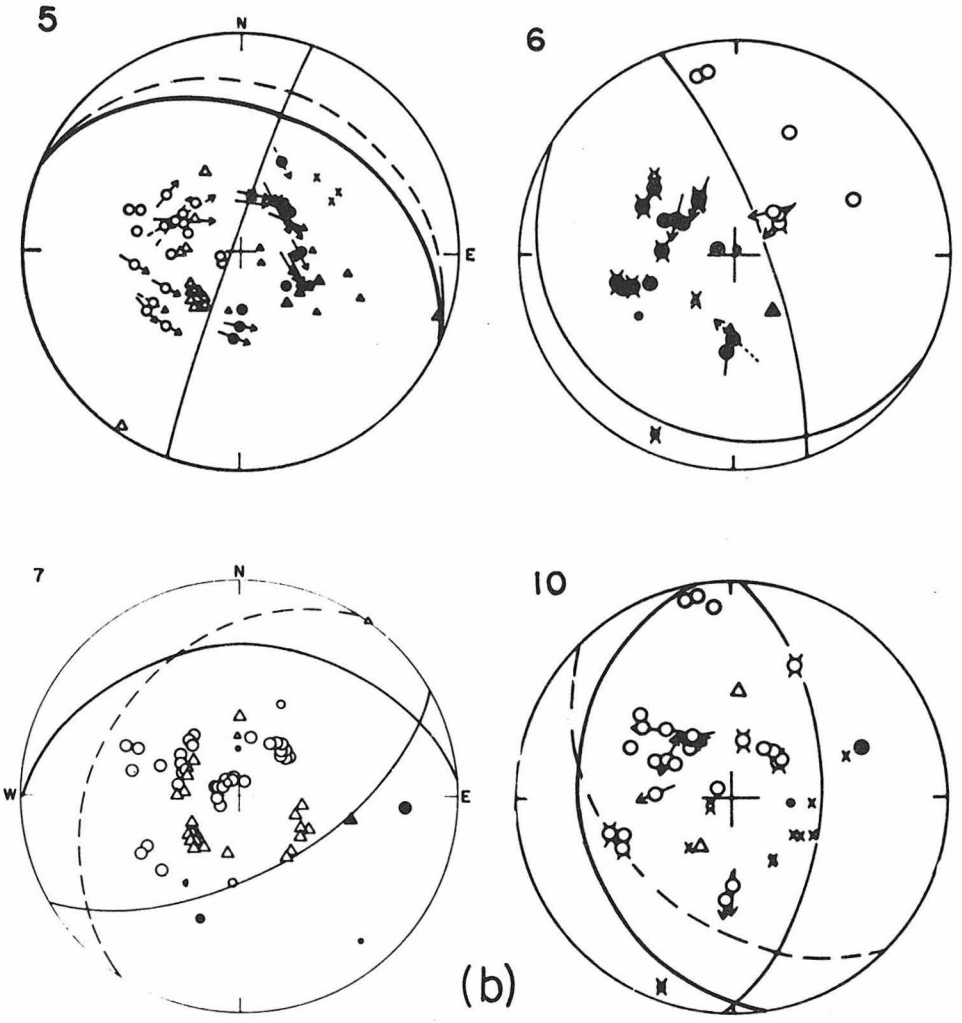

Figure 6.

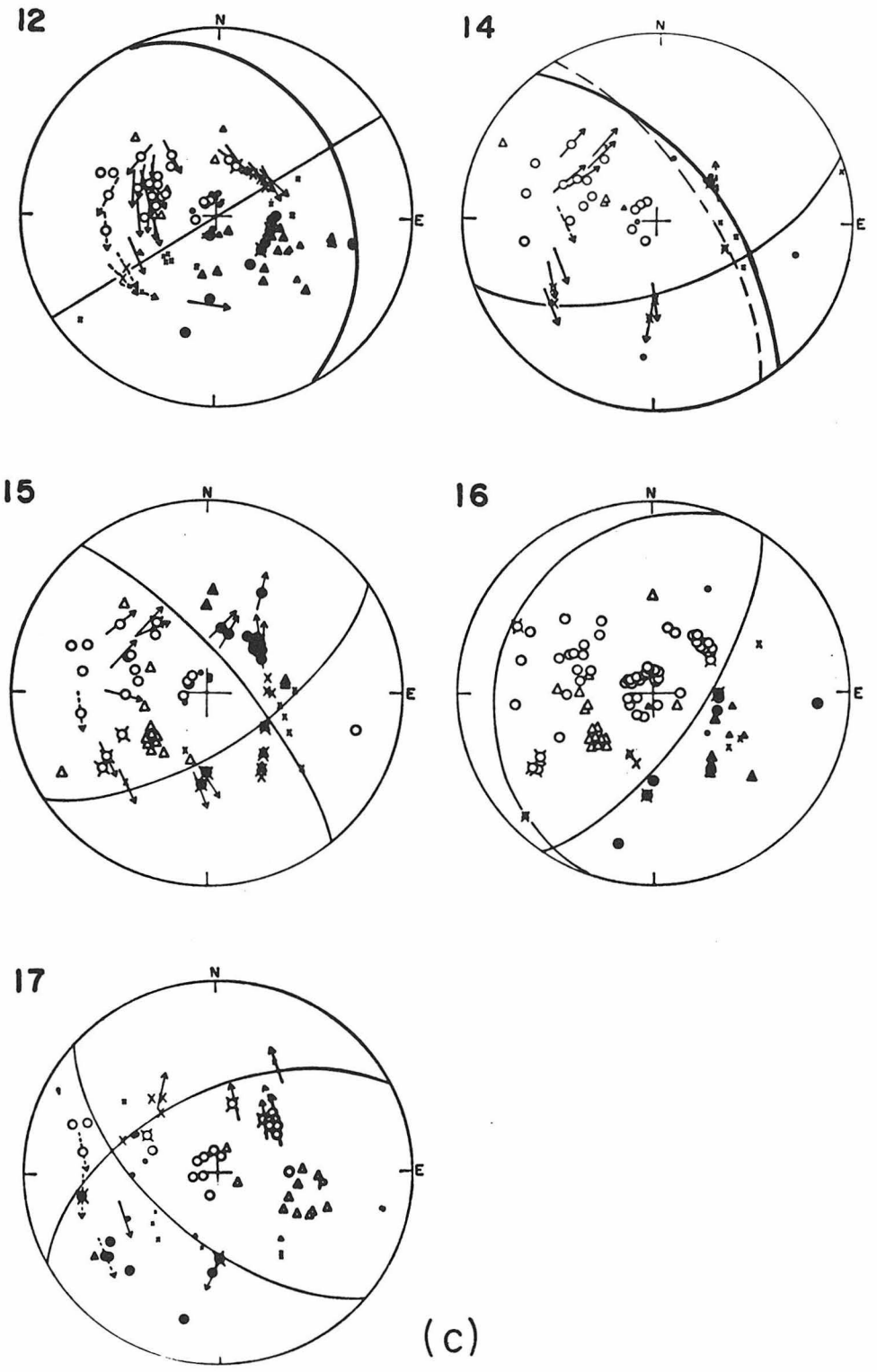

Figure 6.

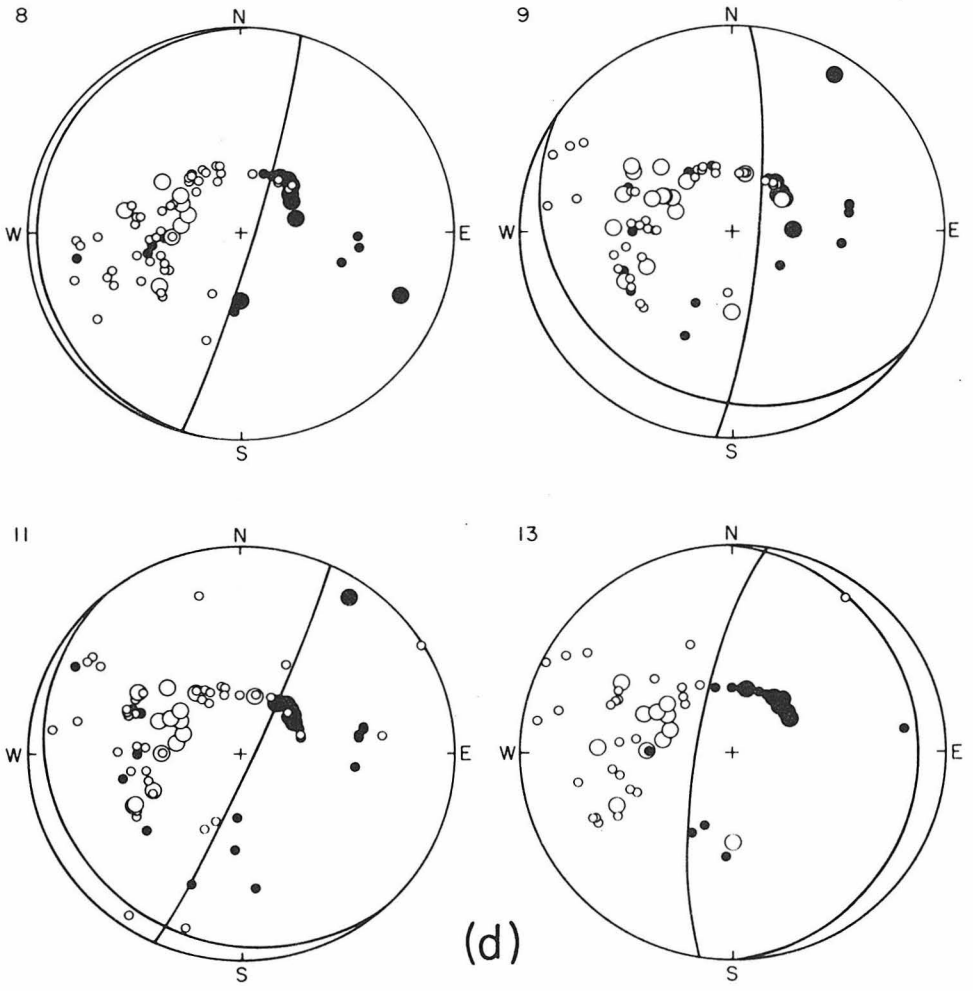

Figure 6.

rupture modes for each fault plane and the rupture direction can vary from 0 to 360° on each fault plane for the unilateral case. The rupture direction is defined as positive if it is measured counterclockwise from the horizontal on the fault plane. Constraining the rupture direction on the fault plane we vary the rupture direction and do a least squares fit for every ten degrees. The rupture velocity is constrained within 0.4 to 0.9 shear wave velocity (v_s) and a fit is done for each increase of 0.1 v_s. Root-mean-square errors of estimate or standard errors of estimate (SEE) of all the least squares fits are then compared. The mode of rupture, the direction and velocity of rupture propagation, and the fault plane orientation which give a minimum SEE are adopted to be the solution. Using reasonable values for wave velocity v_c at the source depths we can calculate the fault dimensions for the earthquakes.

In the above discussion, we assumed that the fault plane solution were well determined. In many cases, as we can see in Figure 6, one of the nodal planes is not well constrained by P-wave first motions even though the other plane is constrained quite well. Uncertainty in the orientation of one of the nodal planes can introduce error into the estimation of source parameters. In view of this, P-wave amplitude data are used to further constrain the focal mechanism. Preliminary values for source dimension, rupture direction, and rupture velocity obtained from the searching process are used to calculate theoretical P-wave amplitudes with trapezoid far field time functions. S(t) (Figure 16) whose rise times t_1s are about 0.2 times of the total duration T_s's of the time functions. The reason for using trapezoid time function is that this simple time function produces synthetics

which fit the observed wave-forms quite well. Theoretical amplitudes at about 10 stations are calculated for a number of fault plane solutions which are within the uncertainty range of P-wave mechanisms. The focal mechanism which best explains the observed amplitude pattern is determined to be the solution. With this improved fault plane solution we go back to redo the least squares searching process and determine the source parameters. This additional constraint from amplitude data reduces the scatter of seismic moments and improves the least squares fits. The improved focal mechanisms (Table 2) are shown as solid curves in Figure 6 while the mechanisms without amplitude constraint are given as dashed curves.

To illustrate the procedures in obtaining involved source parameters we discuss two examples. For the case of earthquake number 13, the nodal plane, which has a strike of N 9° E and a dip angle of 76° to the west has root-mean-squares errors of estimate of 0.835 sec, 0.655 sec and 0.704 sec for the best fits of the circular, the unilateral, and the bilateral faults respectively. For the other nodal plane, which has strike N 1.5° W and dip angle 14° to the east, the best fits for the circular, the unilateral, and the bilateral rupture modes have root-mean-squares errors of estimate of 0.786 sec, 0.639 sec, and 0.675 sec, respectively. The second nodal plane, which has smaller standard errors of estimates, is therefore inferred to be the slip plane. The best least squares fits for the three rupture modes for the second nodal plane are given in Figures 7, 8 and 9. As we can see from the figures, the scatter for the circular rupture is larger than those for the unilateral and bilateral cases. If we examine the

TABLE 2

Event	Strike (°)	Dip Angle (°)	Slip Angle (°)	Standard Error of Estimate		
				Circular (sec)	Unilateral (sec)	Bilateral (sec)
1	125	67	251	0.988	0.848	0.850
	346.4	29.5	-52.5	0.882	0.847	0.878
2	37.5	26.7	43.7	1.036	0.970	0.905
	267	72	110	1.039	0.919	1.002
3	117.5	29.7	56.2	0.795	0.635	0.729
	335	66	108	0.817	0.660	0.660
4	85	64	240	1.065	0.955	1.019
	317.8	38.9	315.7	1.148	1.029	1.029
5	199	87	126	1.420	1.210	1.303
	292.7	36.1	4.8	1.436	1.289	1.289
6	119	16	50	1.402	1.201	1.241
	340	78	100.4	1.334	1.235	1.272
7	61	60	-104	0.952	0.911	0.935
	267.5	32.8	- 62.3	0.950	0.916	0.886
8	16	85	- 90	1.697	1.525	1.528
	196	5	- 90	1.581	1.332	1.642
9	4.8	80	- 72	1.700	1.617	1.617
	124	20.5	-149.3	1.486	1.409	1.508
10	3.	57	277	0.809	0.691	0.735
	170.3	33.7	259.4	0.816	0.698	0.778
11	24.4	85.3	- 80	0.990	0.896	0.897
	139	11.2	-155	0.910	0.827	0.923
12	237	90	120	1.035	0.967	1.003
	327	30	0	0.978	0.921	0.971
13	189	76	92.5	0.835	0.655	0.704
	358.5	14	79.8	0.786	0.639	0.675
14	69	60	215	0.454	0.435	0.440
	319.7	60.2	324.8	0.505	0.482	0.482
15	56	66	195.2	0.583	0.533	0.533
	320	76	325.5	0.557	0.530	0.530

TABLE 2 - continued

Event	Strike (°)	Dip Angle (°)	Slip Angle (°)	Standard Error of Estimate		
				Circular (Sec)	Unilateral (sec)	Bilateral (sec)
16	34	70	274.8	1.058	0.838	0.882
	200	20	230	0.885	0.860	0.717
17	132	62	-39.3	1.084	1.064	1.006
	243	56	214.5	1.112	1.067	1.023

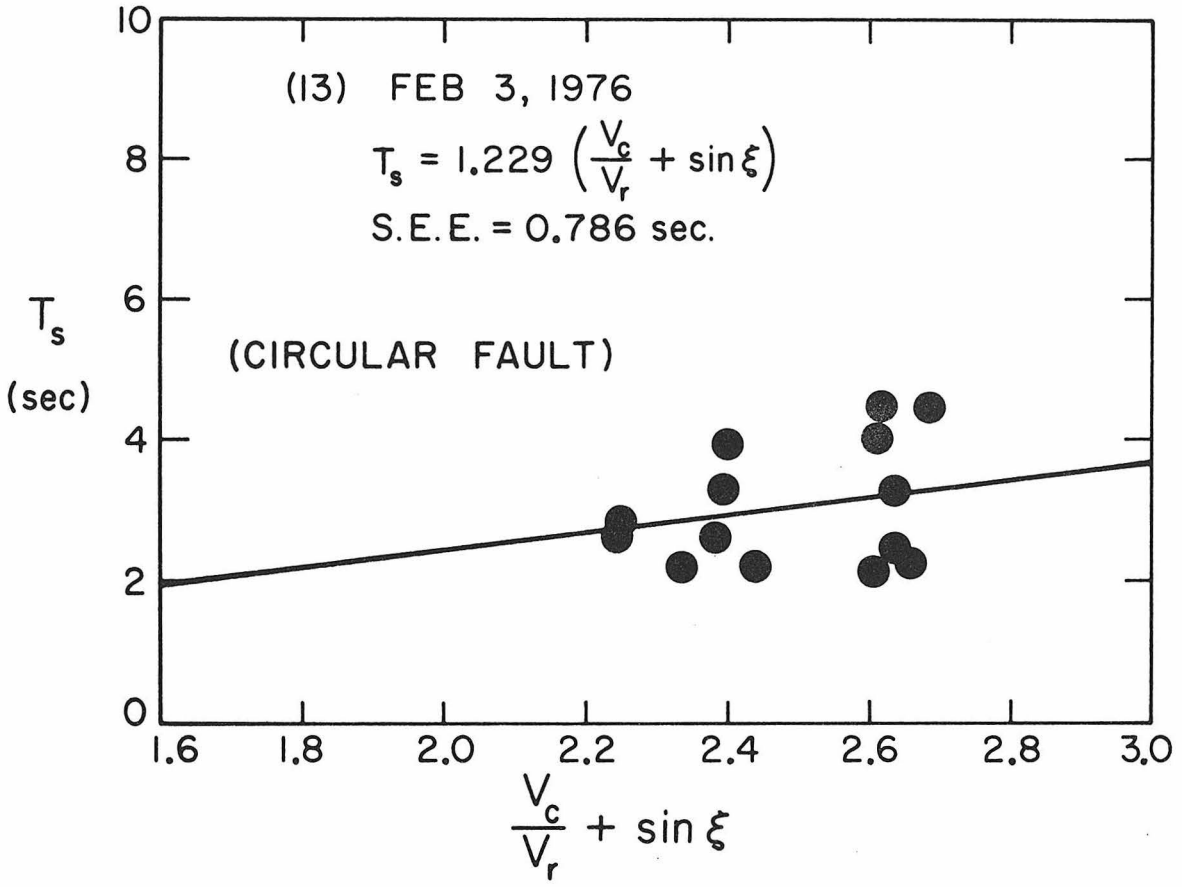

Figure 7. The best least squares fit for earthquake number 13 with a circular fault model. SEE stands for standard error of estimate.

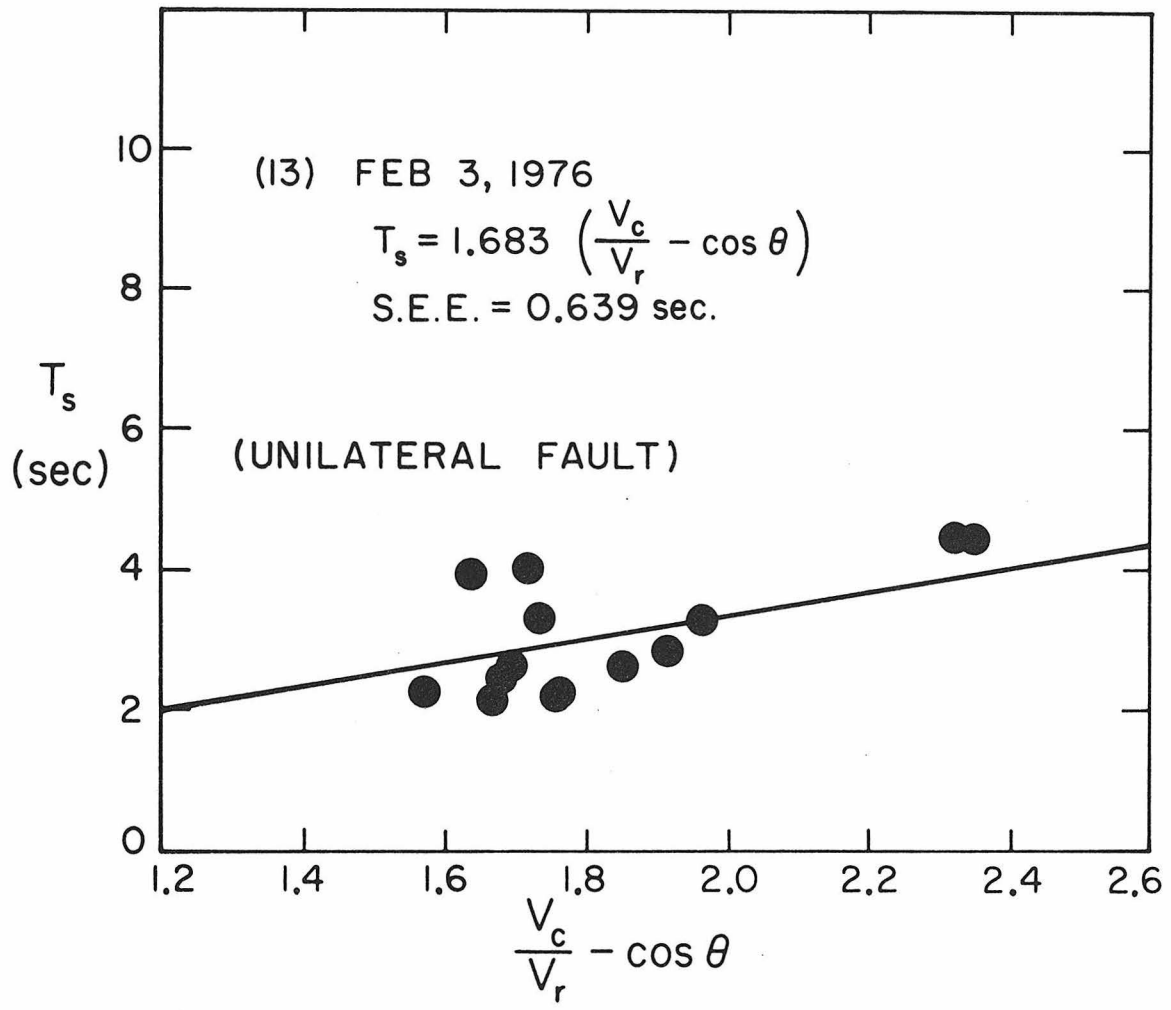

Figure 8. The best least squares fit for earthquake 13 with a unilateral fault.

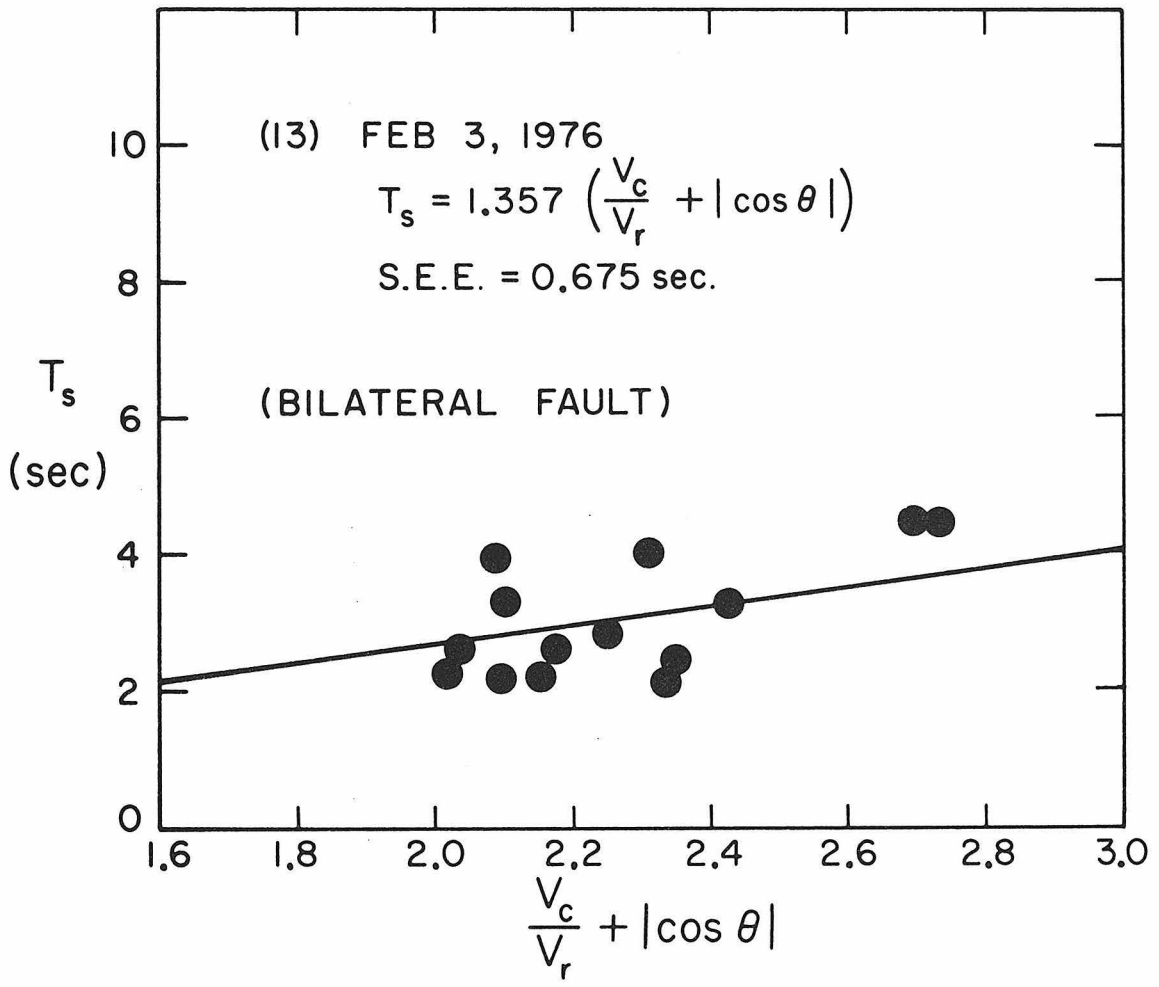

Figure 9. The best least squares fit for earthquake 13 with a bilateral fault.

TABLE 3

STATION DATA AND PULSE WIDTHS

No.	Date m	d	y	Station	Distance (°)	Azimuth (°)	Take-off angle (°)	Pulse-width (sec)
1	3	11	68	ADE	46.2	237	35.5	4.22
				ANP	75.1	302	25.3	5.28
				BAG	72.2	294	26.3	4.72
				COL	83.2	11	22.3	4.41
				COR	76	35	25.0	4.95
				DAV	64.1	286	29.2	4.39
				GUA	50.2	304	34	4.58
				HKC	80.1	297	23.5	4.85
				LON	78.2	34	24.2	5.21
				MAT	69.2	320	27.5	5.55
				MUN	64.7	242	29	4.67
				RAB	35.5	286	39.4	5.26
				SEO	77.1	315.6	24.6	4.29
				TAU	42.4	223	37.0	5.07
				TUC	77.3	51	24.4	5.61
				WEL	26.9	199	41.8	6.35
2	8	12	67	ALQ	89.6	51	20.6	3.75
				ANP	77.2	306	24.8	3.87
				BKS	81.0	41	23.3	5.04
				CHG	92.2	290	20.4	3.45
				COL	92.3	12	20.4	4.93
				GUA	53	312	33.2	4.04
				KIP	49.6	24	34.5	4.81
				LEM	73.5	270.0	26.0	3.44
				LON	87.1	35	21.1	4.85
				MUN	58.1	247	31.4	4.36
				PEL	89.6	127	20.6	3.78
				RAB	35.7	300	39.7	5.27
				SBA	53.7	184	33.0	4.44
				SEO	81.1	318	23.3	4.44
				SHK	75.7	319	25.3	4.89
				SPA	65.4	180	29.0	4.29
				UNM	87.8	68	20.9	4.67
3	12	8	65	ADE	31.3	262	41.5	4.91
				BAG	75.5	303.8	25.6	5.06
				CHG	92.4	291.7	20.5	5.29
				CTA	32.0	293	41.33	5.11
				DAV	65.4	301	29.6	4.42
				HNR	31.8	326	41.4	4.37
				MAN	73.9	303	26.1	4.71
				MUN	50	257	34.7	4.56

TABLE 3 - continued

No.	Date m	d	y	Station	Distance (°)	Azimuth (°)	Take-off angle (°)	Pulse-width (sec)
				NHA	80.6	293.0	23.7	4.57
				PMG	38.9	307	38.9	4.96
				RAB	40.1	318	38.4	4.18
				RIV	21.7	271	47.7	4.52
				SNG	83.9	283.6	22.3	4.28
				SPA	53.1	180	33.5	3.59
				TAU	23.8	246	45	4.73
4	5	1	69	ANP	74.8	302.6	26.4	3.30
				BAG	71.8	294	27.4	3.32
				CHG	92.0	288.9	21.1	4.40
				CTA	37.2	259	40.5	4.81
				GSC	75.3	45.7	26.2	4.13
				HNR	25.8	283.1	44.0	4.51
				LUB	85.5	53	22.2	3.17
				PMG	37.9	276	40.2	3.69
				SHK	71.4	316	27.6	3.88
5	3	18	65	ADE	42.6	239.7	39	6.02
				ALQ	85.5	51	22.5	3.82
				ANP	75.5	304	26.5	4.94
				BAG	72.1	295.5	27.7	5.16
				CTA	35.5	263	41.8	5.32
				DAV	63.5	289.0	31.0	4.51
				GSC	78.4	45.8	25.3	4.92
				GUA	50.9	308	35.6	4.03
				HNR	25.5	291	44.8	5.85
				LEM	75.0	268.1	26.6	4.42
				MAN	70.9	294.1	28.1	4.75
				MUN	61.4	243.8	31.8	5.25
				PEL	91.4	126	21.4	5.07
				PMG	37.1	281	41.2	5.50
				RAB	34.8	292	42.0	6.11
				RIV	32.3	237.8	43.6	5.27
6	9	4	67	AFI	18.7	24	52.6	3.31
				BKS	87.1	42	23.1	3.71
				CHG	92.8	290	22.7	3.72
				GSC	88.6	47	23.1	4.44
				SBA	47.0	184	39.6	2.69
				SEO	85.0	320	24.0	2.71
				SPA	58.8	180	34.6	2.64

TABLE 3 - continued

No.	Date m	d	y	Station	Distance (°)	Azimuth (°)	Take-off angle (°)	Pulse-width (sec)
7	9	26	68	ALQ	86.7	50.8	22.5	4.38
				BAG	71.8	296.1	28.2	3.8
				BKS	77.8	41	26.1	3.61
				COL	88.4	12	22.1	2.74
				COR	81.1	35.2	24.6	3.89
				DAV	63.1	289.8	31.5	3.17
				DUG	85	43.7	23.0	4.33
				HKC	79.8	299	25.1	3.97
				HNR	25.0	294	45.7	3.87
				LEM	74.1	269	27.3	3.02
				LON	83.6	35	23.5	3.68
				PMG	36.4	283	42.0	3.61
				RAB	34.3	295	42.8	3.91
				RIV	31.1	239	44.0	3.33
				SEO	78.7	317.6	25.6	3.00
				TUC	82.3	51.3	24.1	3.73
8	6	4	70	ADE	45.4	236.4	38.3	6.17
				ANP	74.1	302.6	27.3	5.84
				BKS	72.9	41.3	27.8	4.06
				COL	83.2	11.3	23.7	6.03
				COR	76.4	35.3	26.5	3.10
				GSC	75.1	46.0	27.0	4.90
				HKC	79.0	297.0	25.4	5.06
				LEM	76.0	266.8	26.6	4.81
				LPS	90.0	75.2	21.8	4.69
				MUN	63.9	241.9	31.2	5.97
				SPA	74.7	180.0	27.1	4.30
9	2	22	75	ALQ	90.8	51.6	23.2	6.25
				BKS	82.1	41.9	25.7	4.25
				CHG	91.0	290.2	23.2	5.56
				COL	92.8	12.7	23.1	4.78
				COR	85.8	36.2	24.1	3.11
				DAV	62,7	293.0	33.7	5.78
				GIE	89.0	88.7	23.4	3.59
				GUA	52.1	313.3	38.0	5.88
				HKC	80.2	300.1	26.6	5.49
				MAN	70.5	297.2	30.5	4.52
				MUN	56.7	247.0	36.0	5.42
				PMG	35.8	289.6	45.3	4.26
				RAB	34.7	301.9	45.9	5.77
				RIV	27.5	244.3	48.6	5.05
				TUC	86.4	51.9	24.0	3.94

TABLE 3 - continued

No.	Date m	d	y	Station	Distance (°)	Azimuth (°)	Take-off angle (°)	Pulse-width (sec)
10	1	20	68	ADE	35.4	251	45.5	2.54
				ANP	78.7	307.7	27.1	3.30
				BKS	86.2	42.0	24.0	3.02
				DAV	64.3	296	33.1	3.28
				GSC	87.7	46.7	23.6	3.26
				GUA	55.3	316.4	36.6	3.31
				HKC	82.2	301.1	25.6	3.33
				HNR	28.1	313	48.4	3.11
				LEM	71.8	273	30.0	3.07
				MAT	77.2	326	27.7	4.04
				PMG	37.3	296	44.7	3.83
				RAB	37.1	308	44.7	3.51
				SBA	48.3	184	39.6	2.62
				TUC	89.9	52	23.2	3.68
11	7	21	73	ADE	37.6	244.4	46.3	4.20
				ALQ	90.9	51.7	24.0	3.11
				ANP	75.9	306.6	29.3	4.14
				BAG	71.6	298.6	31.1	4.87
				CHG	90.6	290.3	24.0	4.24
				GUA	51.8	313.5	39.6	3.38
				HKC	79.9	300.3	27.6	4.43
				LEM	71.9	270.8	30.9	3.72
				MAT	73.1	325.3	30.5	4.34
				MUN	56.5	247.0	37.4	3.65
				RAB	34.3	302.1	47.9	3.90
				RIV	27.3	243.9	50.8	4.51
				SNG	84.2	280.6	25.6	4.53
				TUC	86.5	52.1	24.8	3.40
12	11	18	65	ANP	73.5	304.5	30.9	2.99
				BAG	70.0	296	32.4	3.65
				CTA	33.9	262	49.1	2.67
				DAV	61.5	289	36.1	3.20
				GUA	48.8	308	41.7	3.47
				HKC	78.1	299	28.9	3.33
				HNR	23.5	290	53.2	4.28
				LEM	73.3	268	31.0	2.04
				MAN	68.8	294.6	33.0	3.79
				MAT	69.0	323	32.9	4.11
				NHA	78.3	287	28.8	3.55
				PEL	93.4	127	24.4	3.58
				PMG	35.2	281	48.5	4.02
				RAB	32.8	293	49.2	3.65
				RAR	17.0	261	60.1	3.87

TABLE 3 - continued

No.	Date m	d	y	Station	Distance (°)	Azimuth (°)	Take-off angle (°)	Pulse-width (sec)
				SBA	59.6	184	36.9	2.37
				SNG	84.4	279.5	25.9	3.35
13	2	3	76	ADE	37.1	244.7	49.6	4.88
				ANP	75.7	306.9	31.0	3.89
				BAG	71.3	299.0	33.4	4.26
				BKS	82.7	42.3	27.6	3.81
				CHG	90.3	290.5	25.4	3.9
				COR	86.4	36.6	26.2	3.65
				CTA	31.8	272.1	52.4	4.24
				DAV	62.1	293.5	37.3	3.68
				DUG	89.9	44.8	25.5	4.63
				HKC	79.6	300.6	29.2	3.67
				RAB	34.1	303.0	51.2	3.71
				RIV	26.7	244.3	54.8	4.87
				SEO	80.0	319.7	29.0	4.58
				SNG	83.8	280.9	27.1	4.01
14	1	28	66	BAG	65.1	298.1	38.1	3.50
				CTA	29.2	260.3	57.7	3.64
				DAV	56.4	291.3	42.1	3.30
				GUA	44.3	312	48.7	3.04
				LEM	68.4	269.5	36.4	3.12
				MAN	63.8	296.7	38.7	3.54
				NHA	73.2	289.0	34.0	3.33
				PMG	30.1	282	57.2	3.78
				RAB	27.8	296	58.5	3.44
				SNG	79.3	281.1	30.9	3.69
15	7	21	66	BAG	69.0	296	37.4	3.61
				BKS	76.6	43	33.4	3.32
				COR	80.0	37	31.7	3.0
				CTA	33.3	260	57.9	3.44
				DAV	60.5	289	41.8	3.58
				DUG	84.0	45	29.5	3.84
				HKC	77.0	299	33.2	3.963
				MAN	67.7	295	38.1	3.57
				NHA	77.3	287	33.1	3.56
				PMG	34.3	280	57.3	3.24
				RAB	31.7	292	59.0	3.12
				SHK	69.7	319	36.9	3.82
				SNG	83.5	280	29.7	3.55

TABLE 3 - concluded

No.	Date m	d	y	Station	Distance (°)	Azimuth (°)	Take-off angle (°)	Pulse-width (sec)
16	3	17	66	ADE	39.4	240	56.3	5.18
				ALQ	88.6	52	29.3	4.75
				BOZ	90.2	40	29.0	4.52
				COL	89.0	13	29.2	4.34
				COR	82.9	37	31.4	3.60
				GUA	49.3	311	49.7	4.43
				LEM	71.9	269.6	36.5	4.06
				PMG	34.4	285	59.9	5.24
				RAB	32.5	297	61.4	5.42
				RIV	29.1	238	64.1	4.51
				SEO	77.3	319	34.3	4.93
				SNG	83.5	280.2	30.3	4.35
				SPA	69.0	180	38.0	5.33
17	12	9	65	ADE	41.8	237.5	54.7	2.77
				BKS	76.5	42	34.7	2.9
				PMG	34.8	280	59.7	3.84
				RIV	31.6	234.3	62.1	2.98
				SBA	60.2	184	43.6	3.70
				TUC	81.6	52	31.8	3.92

standard errors of estimate, we find that the unilateral rupture has the minimum error and gives the best fit. The data used for the analysis are given in Table 3, which includes the stations used, their epicentral distances, azimuths from the source, take-off angles at the source, and pulse-width of the first swings on long period seismograms. From the best fits of the unilateral fault we get rupture propagation direction = 0°, rupture velocity $v_r = 0.9\ v_s$, $\frac{L}{v_p} = 1.683$ seconds. If we take $v_p = 9.45$ km/sec for focal depth h = 477 km, we have L = 15.9 km. Another example of our analysis is given to earthquake number 1 which has a strike of N 125° E and a dip angle 67° to the southwest for one of the nodal planes and a strike of N 19.6° W and a dip angle 29.5° to the east for the other nodal plane. For the first nodal plane, the standard errors of estimates for the best fits of the circular fault the unilateral and the bilateral faults are 0.988 sec, 0.848 sec, and 0.850 sec, respectively while the corresponding errors for the three rupture modes for the second nodal plane are 0.882 sec, 0.847 sec and 0.878 sec, respectively. The minimum standard errors for planes one and two are 0.848 sec and 0.847 sec, respectively, and, so are very close (Figures 10, 11, 12, 13, 14 and 15). In this case, we have two sets of solutions for the source parameters; their average values are given in Table 4. As one can see, the standard errors of estimate for the unilateral and the bilateral cases for nodal plane one are 0.848 sec and 0.850 sec. Since these values are nearly equal, we use both unilateral and bilateral cases for the calculation of the stress drop. For most earthquakes studied, however, one rupture mode is usually better than the others and this ambiguity does not exist.

TABLE 4

SOURCE PARAMETERS

No.	h km	m_b	M_o dyne-cm 10^{25}	L km	A km^2	$\bar{D}$ cm	$\Delta\sigma$ bars	rupture mode	Rupture Direction Degree	v_r/v_s	Range of $\Delta\sigma$ bars	$\eta\bar{\sigma}$ bars	η_{max} %
1	112	6.2	7.25	16	102	105.7	180.5	u	40,160	0.65	20∿ 230	5.7	8.7∿ 4.9
2	134	6.5	12.27	23.8	227	77.8	87.4	b	20	0.9	89∿ 100	14.2	32.7∿28.5
3	156	6.0	2.57	12.8	65.3	55.8	118.5	u	0	0.9	22∿ 119	3.5	31.7∿ 5.9
4	205	6.1	2.56	16	102	33.9	60.5	u	70	0.9	53∿ 61	6.8	25.5∿ 22.1
5	219	6.0	3.59	15.5	95.5	49.6	93.7	u	130	0.9	75∿ 94	4.2	11.1∿ 8.9
6	231	6.2	6.58	5.2	10.6	812.1	4617	u	270	0.9	553∿4617	6.5	2.4∿ 0.3
7	251	6.0	1.91	14.9	89.1	27.7	55.3	b	140	0.9	55∿ 192	6.4	23.9∿ 6.7
8	256	6.3	24.89	18.9	143.5	223.8	352.7	u	110	0.9	76∿ 353	2.7	7.2∿ 1.6
9	333	6.6	33.01	17.6	123.6	320.6	585.1	u	20	0.9	96∿ 585	13.0	27.1∿ 4.4
10	349	6.0	3.58	6.0	14.2	294.9	1630.6	u	170	0.9	482∿1631	3.4	1.4∿ 0.4
11	373	6.1	6.18	11.2	50.5	139.5	419.8	u	50	0.9	69∿ 420	4.6	13.4∿ 2.2
12	424	6.2	4.40	8.7	30.3	149.6	641.8	u	140	0.9	257∿ 642	11.8	9.2∿ 3.7
13	477	6.0	6.10	15.9	101.2	58.0	146.2	u	0	0.9	35∿ 146	2.4	13.8∿ 3.3
14	545	5.8	1.77	9.8	38.0	38.5	184.3	u	50	0.9	49∿ 184	3.8	15.5∿ 4.1

TABLE 4 - concluded

No.	h km	m_b	M_o dyne-cm 10^{25}	L km	A km^2	$\bar{D}$ cm	$\Delta\sigma$ bars	rupture mode	Rupture direction degree	v_r/v_s	Range of $\Delta\sigma$ bars	$\eta\bar{\sigma}$ bars	η_{max} %
15	590	5.8	5.78	9.9	43.1	84.1	586.0	u,b	270,90	0.9	130∿1042	2.0	3.1∿0.4
16	630	6.2	29.27	37.4	560.4	38.0	53.8	b	50	0.9	54∿ 964	2.4	8.8∿0.5
17	649	5.7	5.31	12.8	65.8	57.1	242.2	b	20	0.9	242∿2444	0.8	0.7∿0.1

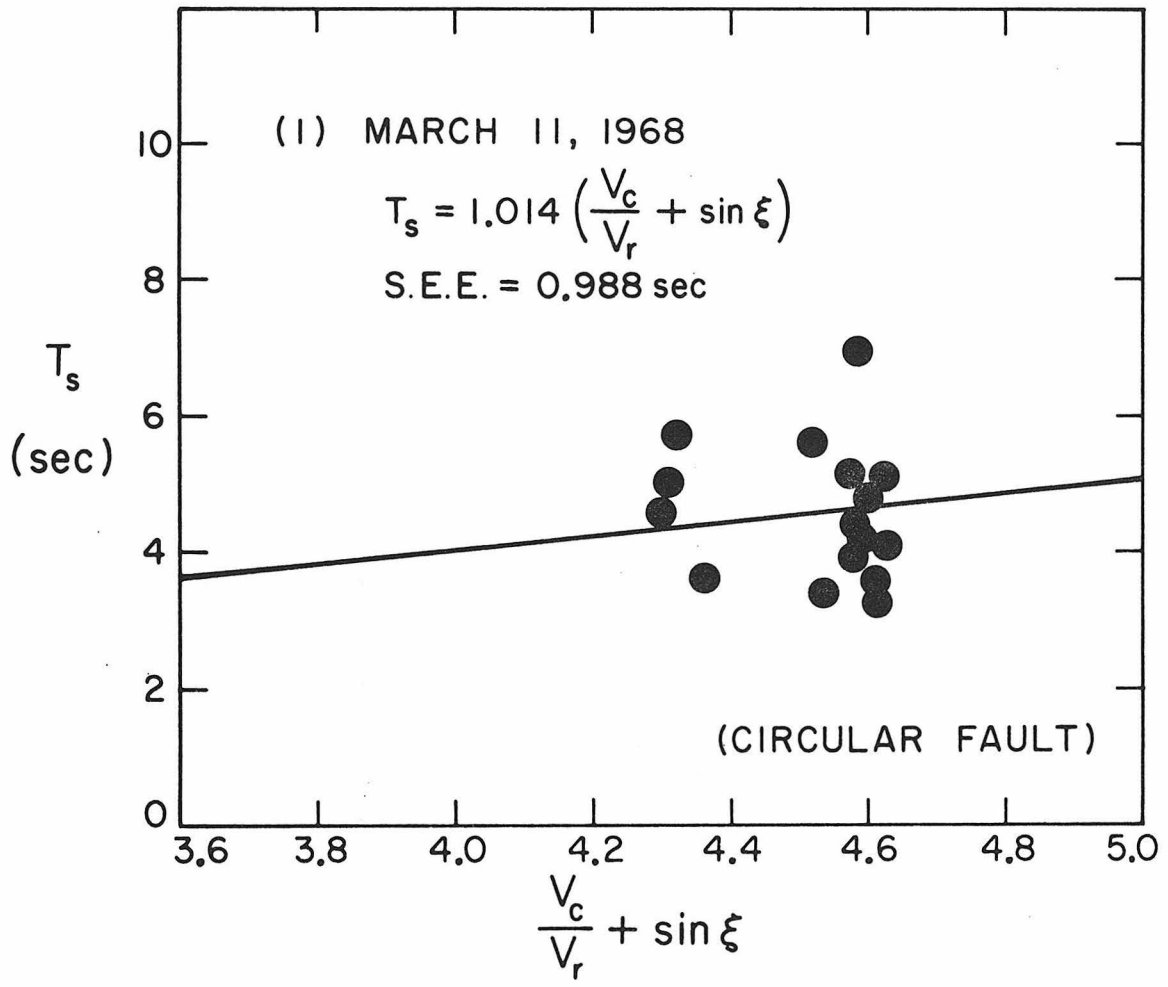

Figure 10. Least squares fit for event 1 with a circular fault on the first nodal plane.

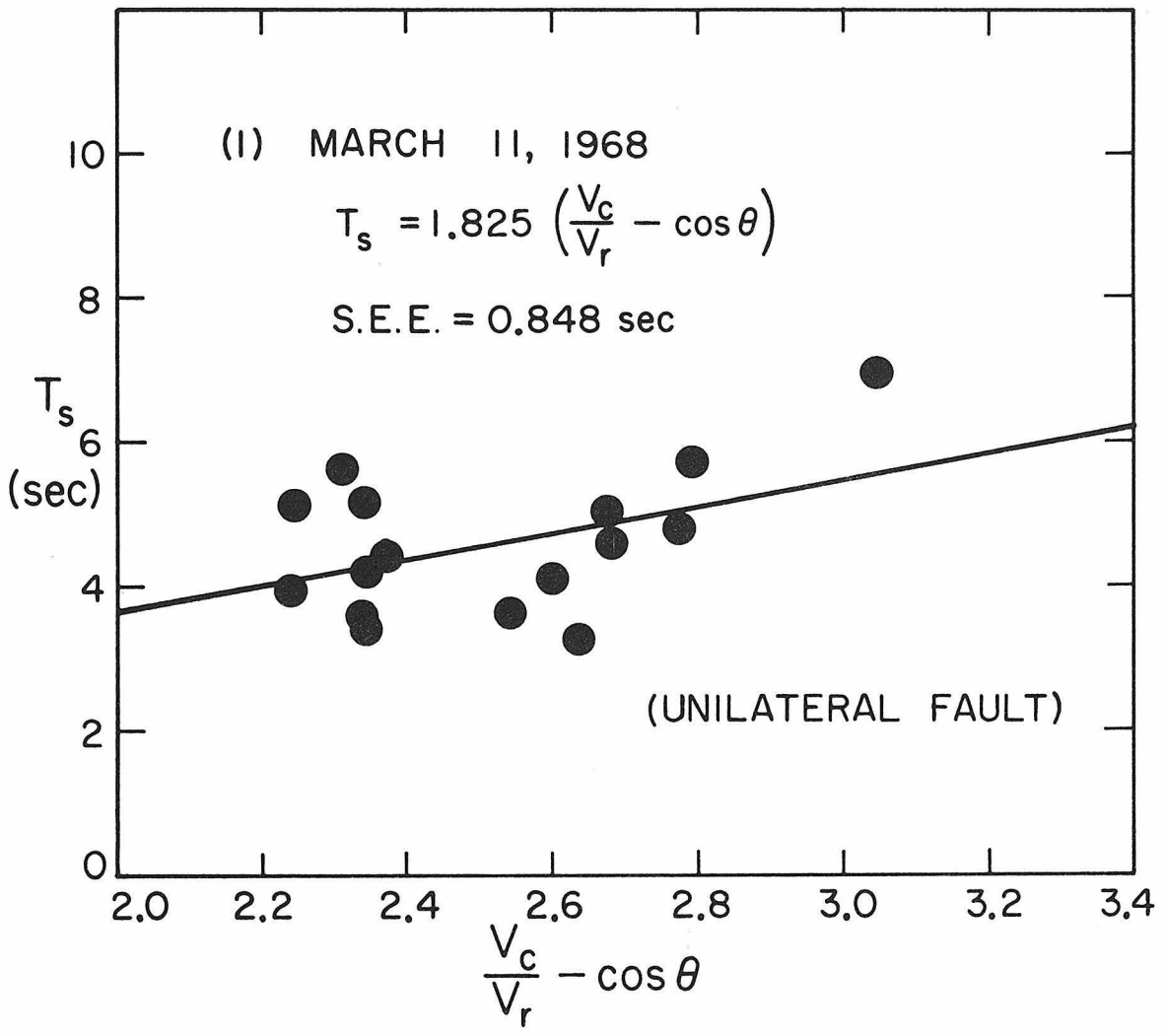

Figure 11. Least squares fit for event 1 with a unilateral fault on the first nodal plane.

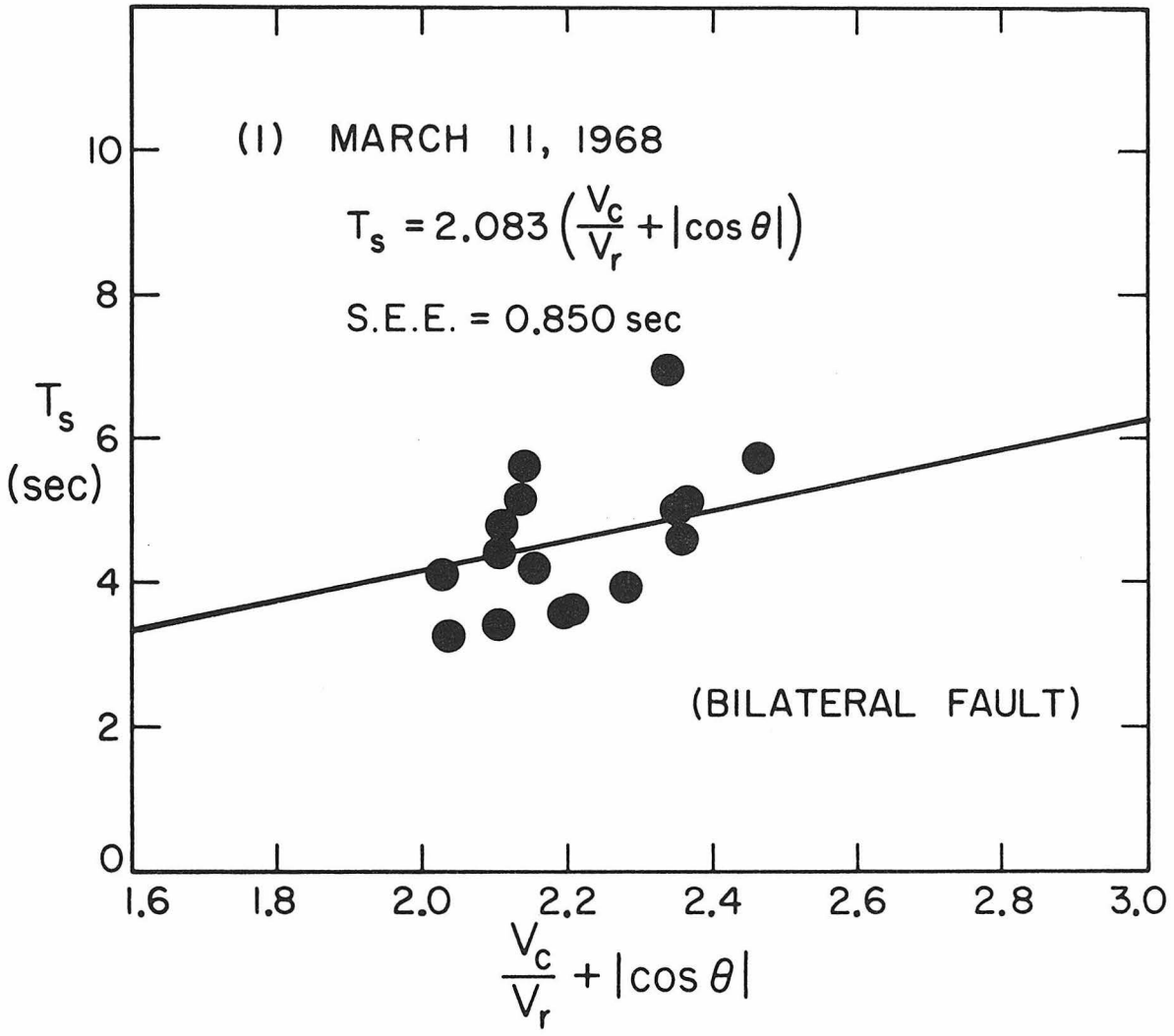

Figure 12. Least squares fit for event 1 with a bilateral fault on the first nodal plane.

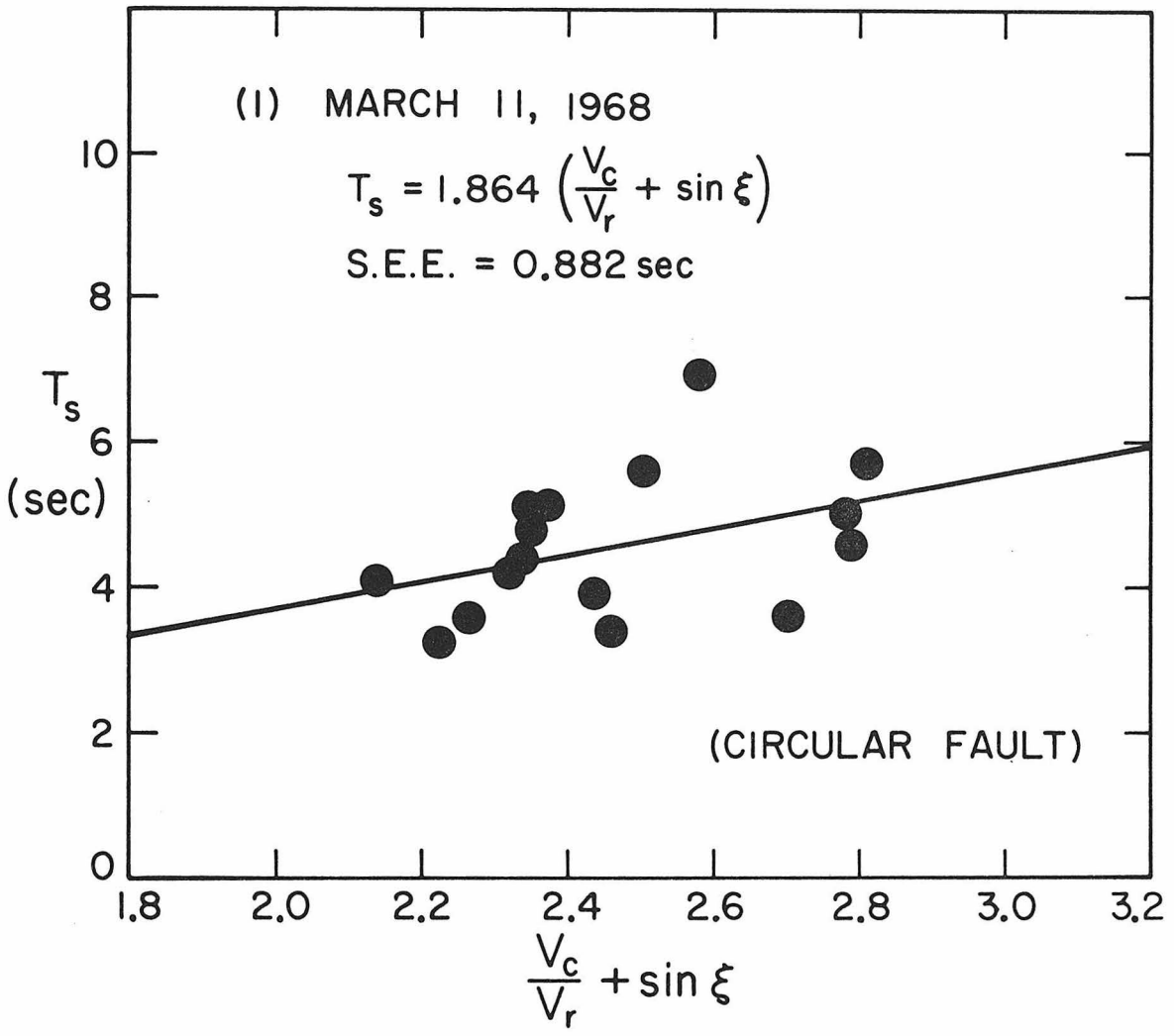

Figure 13. Least squares fit for event 1 with a circular fault on the second nodal plane.

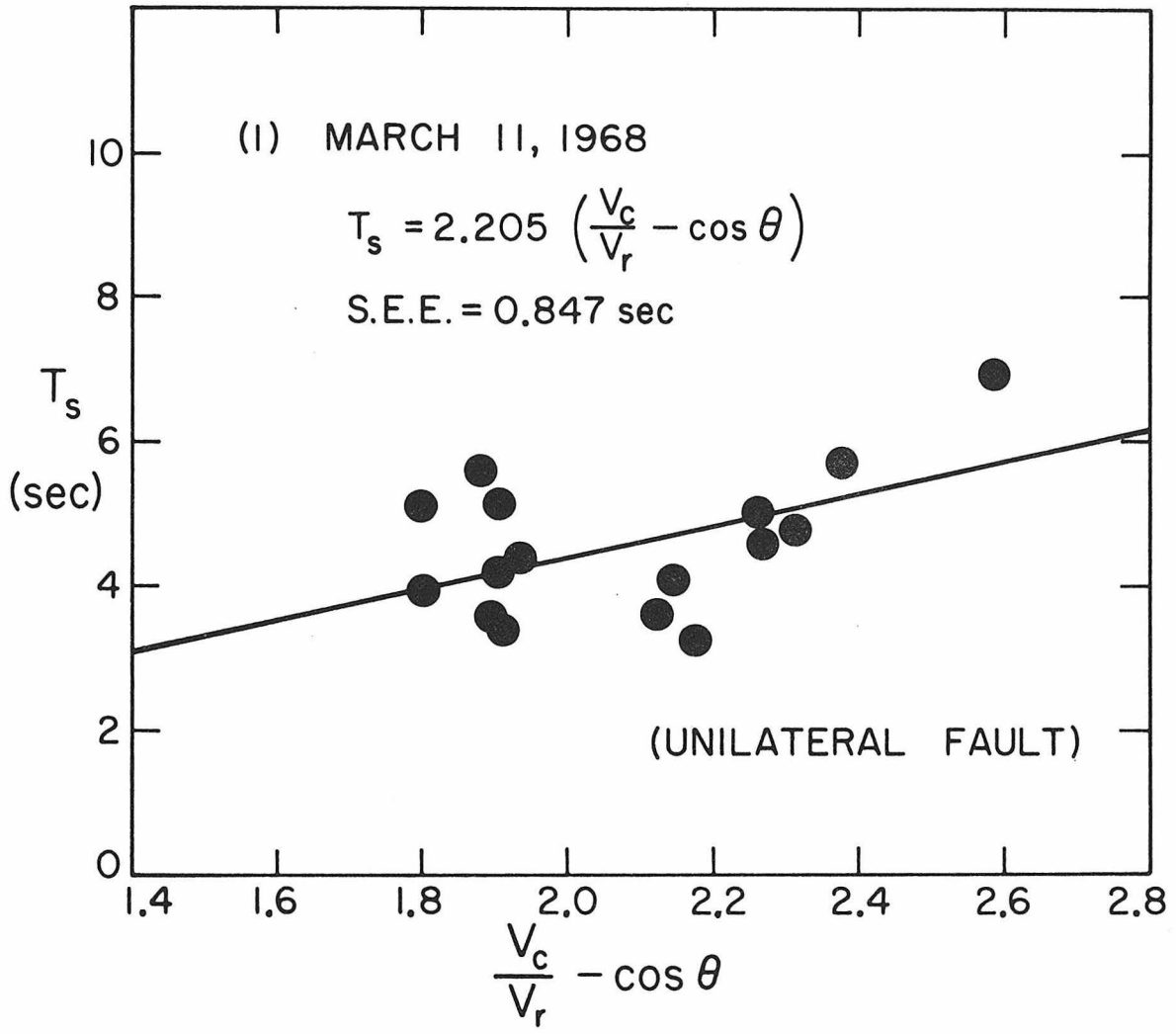

Figure 14. Least squares fit for event 1 with a unilateral fault on the second nodal plane.

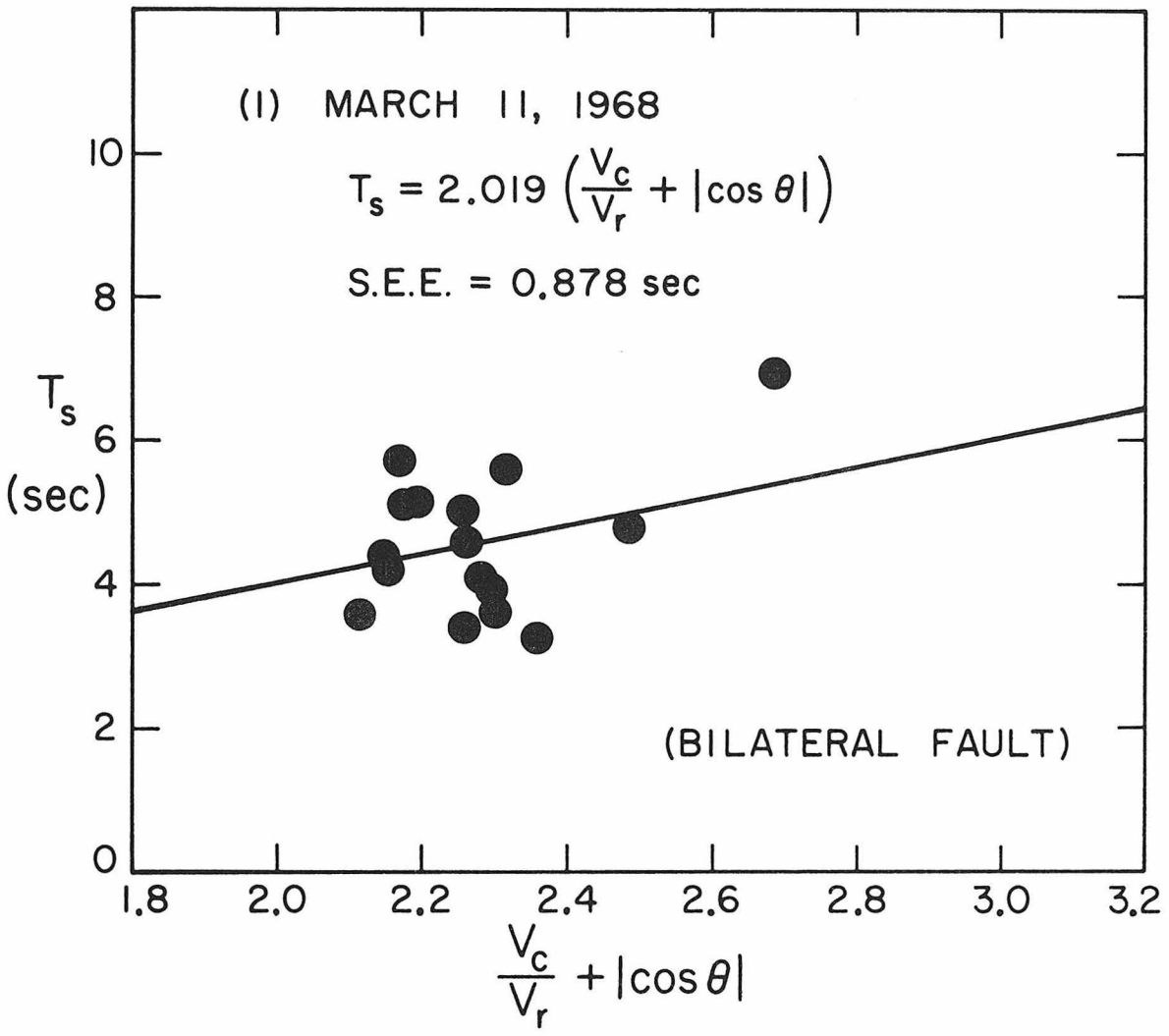

Figure 15. Least squares fit for event 1 with a bilateral fault on the second nodal plane.

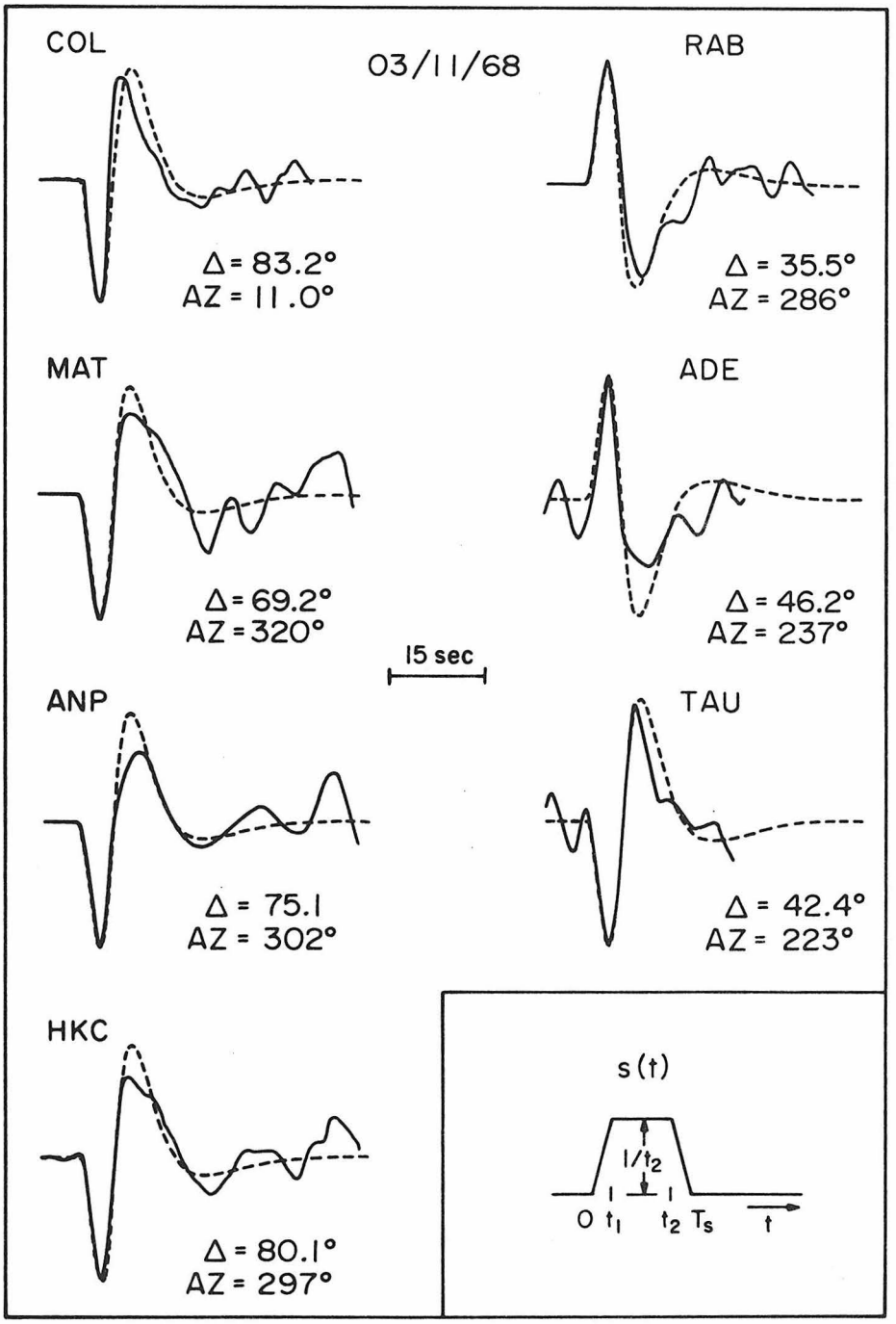

Figure 16. A comparison between the synthetic (dashed curves) and observed (solid curves) seismograms of earthquake number 1 at seven stations. Trapezoid time functions with unit area, rise time t_1, and duration T_s, as shown in the lower right of the figure, are used to compute the synthetics.

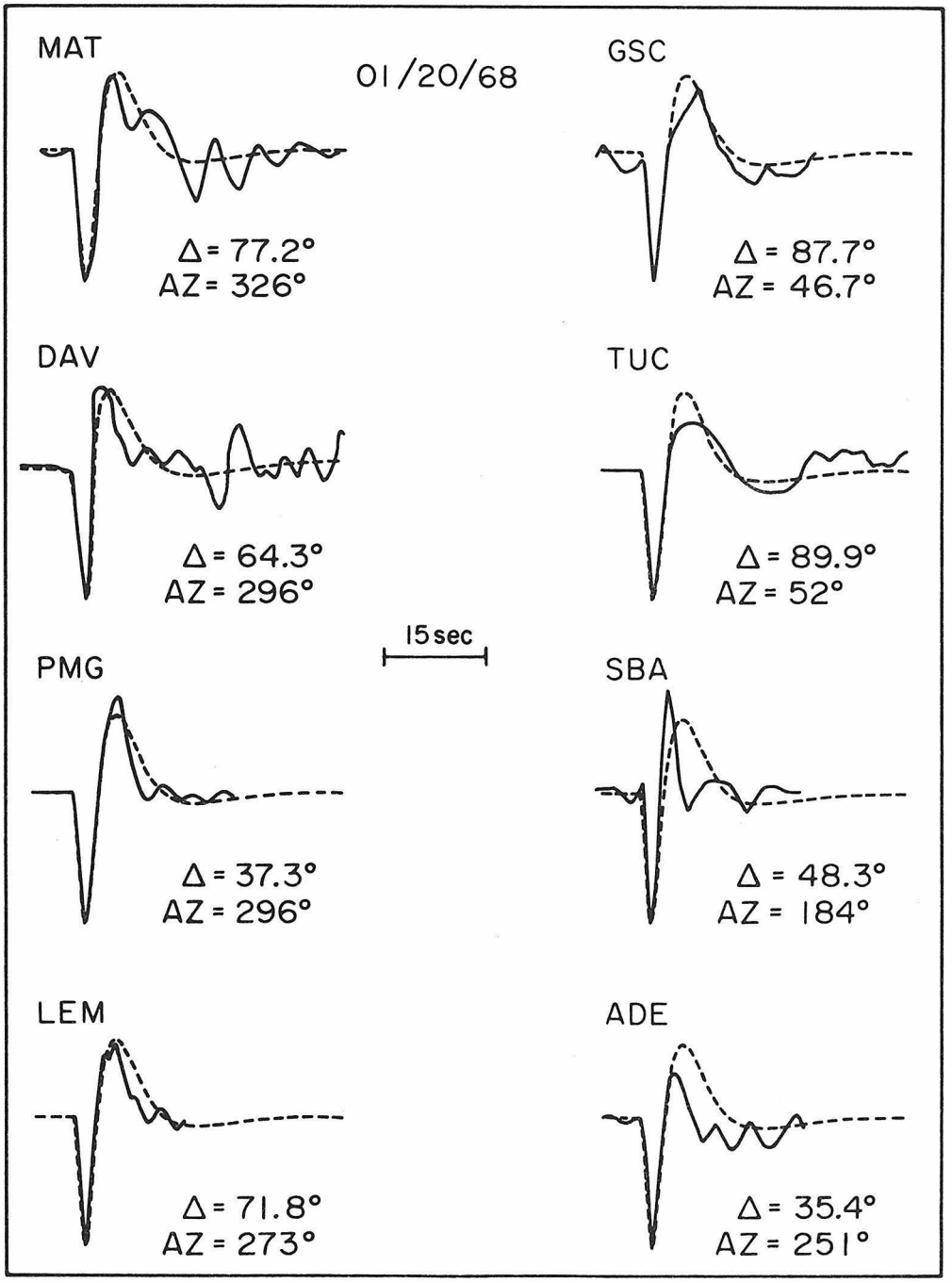

Figure 17. A comparison between the synthetic (dashed curves) and observed (solid curves) seismograms of earthquake number 10 at eight stations.

However, since the difference between the unilateral and the bilateral case is not always very large, we obtain the solutions and present the source parameters for both models to show the possible range of the uncertainty, i.e., a range of values instead of a single value from the optimum solution. Source parameters for all the earthquakes determined in this way are summarized in Tables 2, 3 and 4.

In order to test the quality of the present results synthetic seismograms from the estimated source parameters are computed and then compared with observations. Figure 16 shows an example of comparison for event number 1 at seven stations with good azimuthal coverage. Usually the seismic moment can be determined quite well; so we want to check the other parameters which may be slightly more uncertain. In comparing the synthetics with observations, we compare only the wave-forms but not the absolute amplitude. Theoretical seismograms are computed from a source with unit seismic moment (10^{25} dyne-cm), the mode of rupture determined above, and the trapezoid far field time function described in the previous section; the amplitudes of both the synthetics and the observations are then normalized to a common value (Figure 16). As we can see in the figure, the synthetics match the observed wave-forms very well. Another comparison is done for event number 10 for eight stations (Figure 17). Again, a good fit is obtained suggesting that the results from the pulse-width and least squares searching method are correct. Seismic moment of each earthquake is estimated by comparing the theoretical and observed amplitudes at a number of stations. The seismic moments of the 17 events are given in Table 4. The number of stations used

for moment determination varies from six to ten; for most events ten stations are used. Assuming that fault widths equal 0.4 times fault lengths for rectangular faults, we can calculate fault areas, average dislocations, and stress drops. Results are given in Table 4.

DISCUSSION

Modes of Rupture Propagation for Intermediate and Deep Focus Earthquakes

Unilateral and bilateral fault propagation has been observed and studied for several earthquakes. Other modes of rupture such as circular and elliptical faults have also been suggested and used (Savage, 1966). Savage pointed out that shallow earthquake faults are limited in upward extent by the free surface and perhaps also in downward extent by the effects of friction. Thus large shallow earthquake faults may tend to be quite elongated horizontally. On the other hand, deep-focus earthquakes are not subject to these effects and Savage suggested that circular faults were more appropriate for deep earthquakes. In this study, we compared three simple modes of rupture propagation, unilateral, bilateral, and circular faulting, trying to find the one which best explained the observations. These three models, of course, are simplified ones. For real earthquakes, fault geometries are often irregular and ruptures can be very unsmooth and non-uniform (Haskell, 1964, 1966; Boore and Joyner, 1978). For example a series of ruptures occurring on a fan shaped fault plane was reported by Fukao (1972); that fault strikes could change directions during complex ruptures was reported by Chung and Kanamori

(1978) and Kanamori and Stewart (1978). In view of this, we tried to avoid complicated events and tested which of the above three simple models is the best approximation for relatively simple intermediate and deep earthquakes. Results (Tables 2 and 4) show that for the 17 events studied, unilateral rupture fits the observations best for 12 events, bilateral rupture gives best fits for four shocks, both unilateral and bilateral faulting fit the data about equally well for one case, and in no cases does circular faulting give the best fit. The inadequacy of the circular rupture mode is quite significant in that the occurrence of a symmetrically circular fault requires that the material properties and the stress field at the earthquake source region be perfectly homogeneous and isotropic. A slight deviation from this ideal case can cause very different modes of rupture. Earthquake epicenters are not uniformly distributed on the earth's surface and even within a seismic belt the spatial pattern of seismicity is often non-uniform suggesting that spatial variation in stress field and material properties plays an important role at earthquake sources. For shallow earthquakes, the epicenter of a main shock is, in many cases, located near one end of the after-shock zone instead of at the center. This again suggests that ruptures usually do not develop symmetrically, which is consistent with our results. Interestingly, our results indicate that the higher the degree of symmetry of the rupture mode the worse it fits the observed data.

Source Dimensions and Fault Areas

As shown in Table 4, the source dimensions or fault lengths

of the 17 earthquakes, which have magnitude m_B ranging from 5.7 to 6.6, vary from about 5 to 37 km with an average of about 15 km. Assuming W = 0.4L, we have fault areas ranging from about 10 to 560 km^2 with an average of about 110 km^2. The fault lengths obtained in this study are in agreement with Mikumo's (1972) results for earthquakes with comparable magnitudes; the fault areas, however, are slightly smaller than those of Mikumo (1972). The fault lengths and areas determined here are smaller than the diameters and areas estimated by Wyss and Molnar (1972). As pointed out by Wyss and Molnar (1972), their source dimensions are larger than estimates based on most other models. Wyss and Molnar's results for deep earthquakes are based on the Brune spectral theory (Brune, 1970) with an empirical constant which was calibrated by using four shallow earthquakes (Hanks and Wyss, 1972; Wyss and Hanks, 1972). Wyss and Shamey (1975) recalibrated the constant for deep earthquakes by comparing the fault areas determined from the corner frequency method and those from aftershock data for two deep events with only three to four reasonably located aftershocks. Because of the paucity of data used and the large uncertainty in determining fault area from a small number of aftershocks, the calibration of the empirical constant for deep events is questionable. Besides, aftershock areas may not be representative of the faulting area for common deep earthquakes, which usually do not have aftershocks. Hence, fault areas of deep events obtained from the above corner frequency method may be subject to large uncertainty.

The method used in the present study is free from the above

problem and probably gives more reliable results. In addition, circular faults were assumed in Brune's spectral theory without testing whether a circular fault model was really better than other fault models. As discussed in a previous section, we compared several common fault models and then used the best one to estimate the fault area. This procedure probably provides a more valid estimate of the fault area.

Seismic Moments and Average Dislocations

The seismic moments determined from the time domain analysis here are consistent with Wyss and Molnar's (1972) results within a factor of two even though a larger number of stations are used in this study. The average dislocations from this study vary within about 0.3 to 8 meters.

Stress Drops

Stress drops of intermediate and deep focus earthquakes reported by previous investigators (Berkhemer and Jacob, 1968; Fukao, 1970, 1971; Mikumo, 1971, 1972; Abe, 1972; Wyss and Molnar, 1972) vary over a large range. For some cases, different authors gave different stress drop values for the same event (Aki, 1972). The uncertainty of stress drops of intermediate and deep events is quite large, and the uncertainty arises mainly from the uncertainty in the fault area. In this paper, we try to reduce the uncertainty by first comparing several fault models with observations and then compute the fault area with the best model. Our stress drops vary from about 20 to 4617 bars with a mean value of about 476 bars. Except for several

events with high stress drops, the stress drops obtained here are well within the range of Mikumo's (1971, 1972) results. On the other hand, the present results are much higher than Wyss and Molnar's (1972) stress drops which range from about 4 to 70 bars with an average of about 13 bars. Wyss and Molnar's results are very much lower than those determined by most other investigators. Even though the upper bounds of the stress drops determined in this study are significantly higher than previous results from other investigators, they still fall within the range of the fracture strength or frictional strength of rocks observed in laboratory tests (Byerlee, 1977).

We now investigate the uncertainty of our stress drop determinations. To get some idea about the sensitivity of synthetic wave-forms to changes in fault length, we compare the long period P-wave seismogram of event number 1 recorded at Hong Kong (HKC) with synthetics calculated for one half, once and twice the estimated fault length of 14.5 km found in this study (Figure 18). Obviously, the synthetics from twice and one-half of the estimated fault length, or 29 km and 7.25 km, do not fit the observation. Judging from this comparison, the fault length can be resolved to better than a factor of two for using the pulse-width technique. We probably can resolve the fault length within a factor of 1.5 which corresponds to a factor of 3 for stress drop from our method. The resolutions of stress drops for other events here are probably similar.

Since pulse-width is used to determine fault length, errors in pulse-width measurements can introduce uncertainties into the estimates of fault length and stress drop. The pulse-width or T_r usually

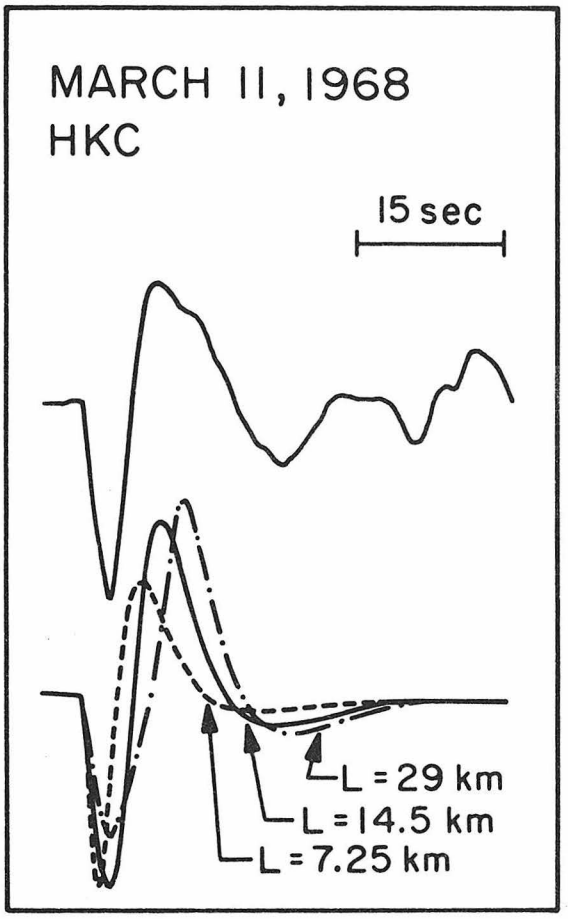

Figure 18. A comparison of the observed seismogram of event 1 at Hong Kong, China (Δ = 80.1°, AZ = 297°) with three synthetics generated from three different fault lengths.

can be measured to within 0.1 second. As one can see from Figures 3 and 4, the slopes of the T_r versus T_s curves are relatively smaller when T_r is small. As a result, for a given uncertainty in T_r, the uncertainty in T_s increases as the pulse-width decreases. The error in fault length due to error in pulse-width measurement can vary from a few percent to about 35 percent while the stress drop can change by a factor of about 1.5 to 2.5 for some of the earthquakes studied here. The high stress drop values are subjected to larger uncertainty. The uncertainty in stress drop due to error in pulse-width measurement is probably less than a factor of three.

The range of variation in stress drop is so large that we can even visually see the differences in wave-forms between events with different stress drop. Figure 19 presents long and short period seismograms of three earthquakes, events 10, 12, and 1, recorded at Hong Kong, China. We try to compare seismograms of different events recorded at a same station; therefore, differences in wave-forms can not be attributed to structural effect under the station. The amplitudes of these three events on the long-period records are nearly identical but short period amplitudes are quite different. Event 10 has the highest stress drop, roughly one order of magnitude higher than event 1. The short period amplitude of event 10 is significantly higher than that of event 1. With a stress drop between that of events 10 and 1, event 12 has a short period amplitude between events 10 and 1. The short period amplitudes of events 10 and 12 are not as different as events 10 and 1; similarly, stress drops for events 10 and 12 only differ by about a factor of two.

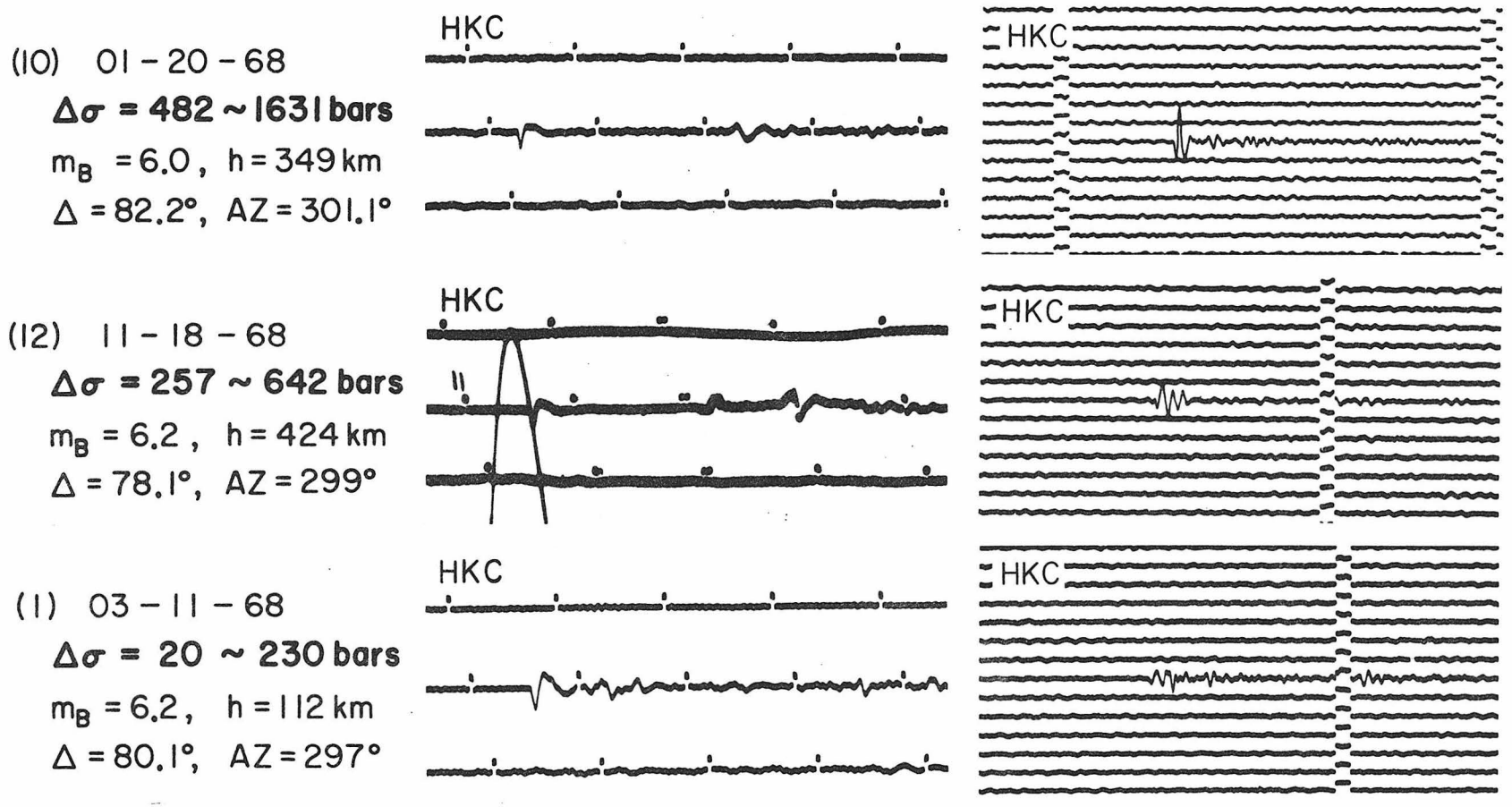

Figure 19. WWSSN long and short period seismograms of events 10, 12, and 1 recorded at HKC.

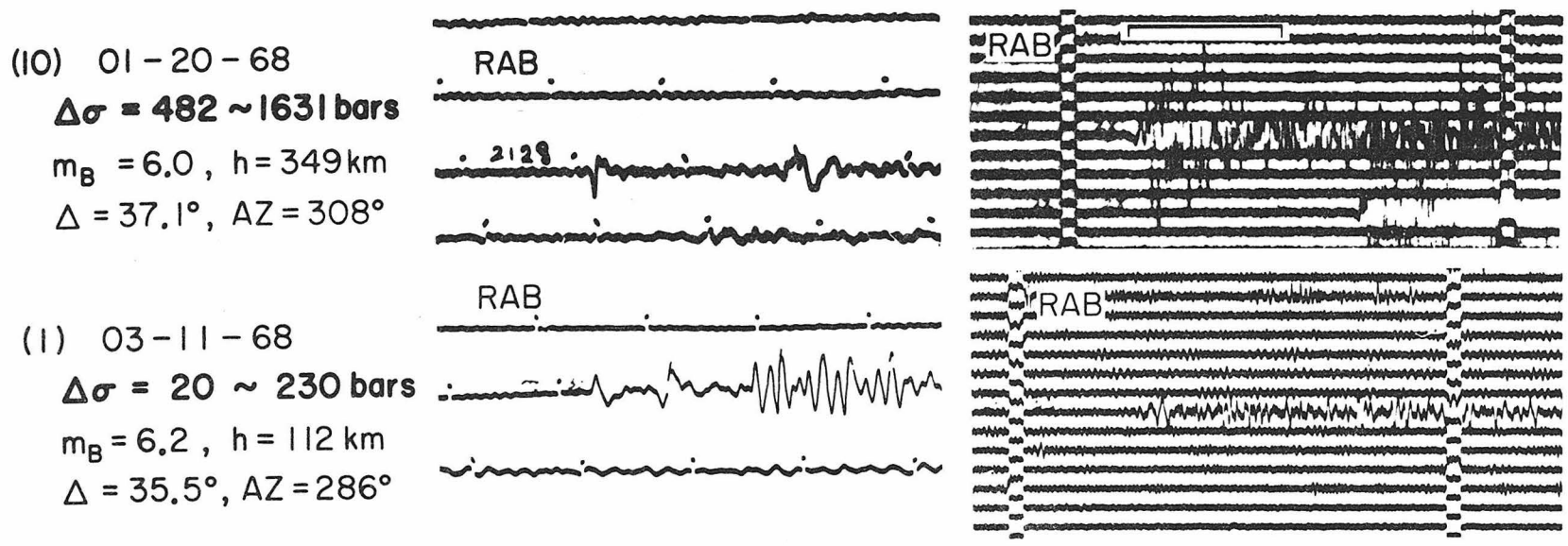

Figure 20. WWSSN long and short period seismograms of events 10 and 1 recorded at RAB.

Figure 20 shows the long and short period seismograms of events 10 and 1 recorded at RAB. The long period amplitudes of these two shocks are about the same; however the high stress drop event number 10 has a much smaller pulse-width. The short period amplitude of event 10 is also significantly higher than that of event 1. These observations are qualitatively consistent with the relative stress drops determined in the previous sections.

At this point, one might ask whether the differences in pulse-width and short-period amplitude are due to difference in attenuation at different depths instead of difference in stress drop. However, the differential attenuation is not a dominant effect in our observations. First of all, since the earthquakes studied are all in the Tonga-Kermadec area, all the ray paths from the source to station are almost identical. Path difference is mainly from a small section near the source because the ray path for a relatively shallow event is slightly longer, by a length roughly equal to the difference in the source depth, than that of a deeper event. Direct P-phases from events deeper than the bottom of the low velocity zone (LVZ) do not travel through the LVZ above it near the source. On the other hand, direct P-phases from relatively shallow shocks must travel through the LVZ before they penetrate to great depth. The question then is whether the differential attenuation due to this path difference is strong enough to significantly affect the observed seismic signals. As mentioned above, for P-waves from shallow events at teleseismic distances the travel time over average $Q_p\left(\frac{T_o}{Q_{av}}\right)^P$, is approximately 1 sec. For different depths, $\left(\frac{T_o}{Q_{av}}\right)^P$ changes and can

be calculated from existing models for Q and velocity. Based on the velocity and Q structures of Anderson and Hart (1976, 1978), the difference in $\left(\frac{T_o}{Q_{av}}\right)^P$ for a change from 112 to 349 km in depth is about 0.1 sec. The effect from this change in $\left(\frac{T_o}{Q_{av}}\right)^P$ on wave-forms is negligible. Hence the observed differences in wave-form in Figures 19 and 20 cannot be explained in terms of differential attenuation in normal mantle. In addition, below the depth of minimum Q in the low velocity zone, Q increases almost monotonically with depth. This simple change in Q with depth cannot explain the relatively complex variation in stress drop observed in this study as will be shown in the next section. Zones of extremely low Q have been observed above inclined seismic zones of intermediate and deep earthquakes (Utsu, 1971; Barazangi and Isacks, 1971). This low Q zone extends from the surface to about 300 km in depth. However, the following observations suggest that the existence of this low Q zone cannot explain our observations of pulse-width or our stress drop pattern. Because the low Q zone is limited to the region above the inclined seismic zone, rays traveling in the direction opposite to the dip direction should not be affected by the anomalously high attenuation. Only rays traveling in the dip direction of and above the seismic zone are subjected to high attenuation. If the observed change in pulse-width is due to the existence of the anomalously low Q zone, the pulse-widths recorded at stations in the dip direction of the Benioff zone should be longer than those recorded at stations in the opposite direction of the seismic zone. No systematic patterns like this have been observed, suggesting that the pulse-width is not affected by the above situation. The dip

angles of the Benioff zone are about 42° in many parts of the Tonga-Kermadec area. On the other hand most of the stations used in this study are at teleseismic distances. The take-off angles at the earthquake source for those stations are roughly from 22 to 30° and are significantly smaller than the dip angle of the Benioff zone. Hence most of the observed seismic waves did not go through the extremely low Q region and are free from the above differential attenuation problem. As will be shown in the next section, stress drop varies significantly with depth below 300 km which is roughly the bottom of the extremely low Q zone; this again cannot be explained by the low Q zone discussed above. Therefore the observed change in pulse-width or stress drop must, to first order, be due to the earthquake source.

Depth and Lateral Variations of Stress Drops

Variation of apparent average stress as a fucntion of depth was studied by Wyss (1970). He found that for shallow earthquakes a mean value for the apparent average stress is 18 bars. The mean value for depths between 45 and 150 km is 270 bars. Around 600 km depth the mean value is very similar to that at the surface, 21 bars. Wyss explained the differences in apparent average stress in terms of differences in strength of the material in the source region. Wyss and Molnar (1972) studied the variation of source parameters with depth in the Tonga arc and found that the stress drops were between 4 and 70 bars. Their stress drops did not change much with depth, but were slightly larger at intermediate depths than at great depths. The apparent stresses were also found larger at intermediate depths.

The stress drops determined from the present study are plotted as a function of depth in Figure 21. The upper and lower bounds of stress drop for each event are calculated for unilateral and bilateral faults respectively while the circles give the stress drops calculated from the best solutions of the least squares searching process. Another way to show the variation of stress drop with depth is to plot the average value of the stress drop range for each event versus depth as presented in Figure 22. The most obvious feature of these two figures is that the stress drop varies over a very large range and changes considerably with depth. For depth between 100 and 220 km, the level of stress drop is low and varies from 20 to 230 bars. From about 230 to 430 km the stress drops are significantly higher and range from 55 to 4617 bars. A decrease to a relative minimum of stress drop occurs from about 450 to 560 km. The stress drop again increases from 570 to 650 km.

Stress drop is controlled by the ambient stress level, material strength, and other properties at the source region. Because the physical and chemical processes and material properties within a descending plate and the driving mechanism of plate tectonics are not fully understood, the reason for the observed stress drop pattern is not completely clear. However, we would like to point out some interesting correlations between the stress drop pattern and some other geophysical observations and to provide some preliminary interpretations of the observed patterns. The depth range of the low stress drop region, from 100 to 220 km, is roughly coincident with the low velocity zone in the upper mantle even though it is not clear why this

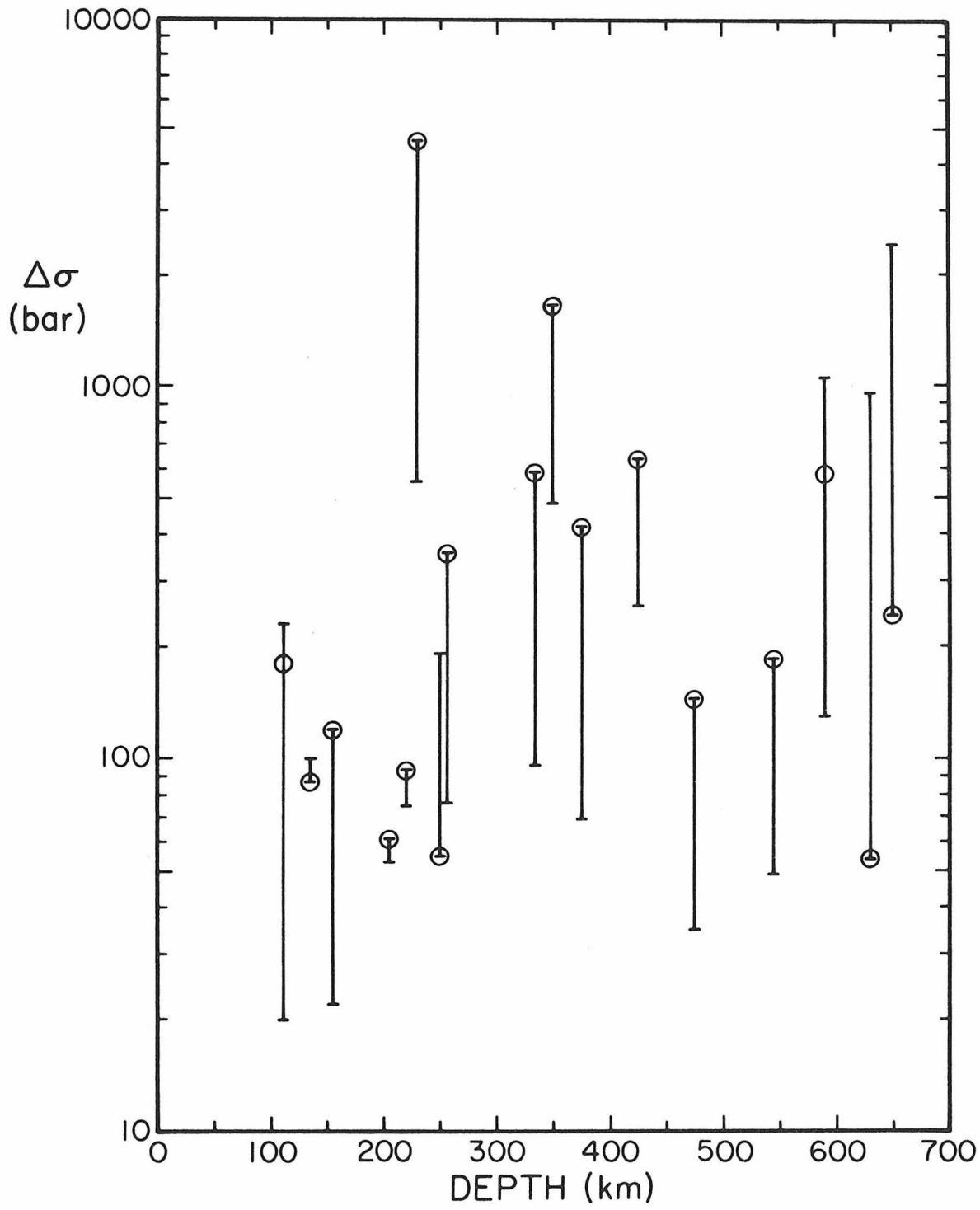

Figure 21. Variation of stress drop as a function of depth.

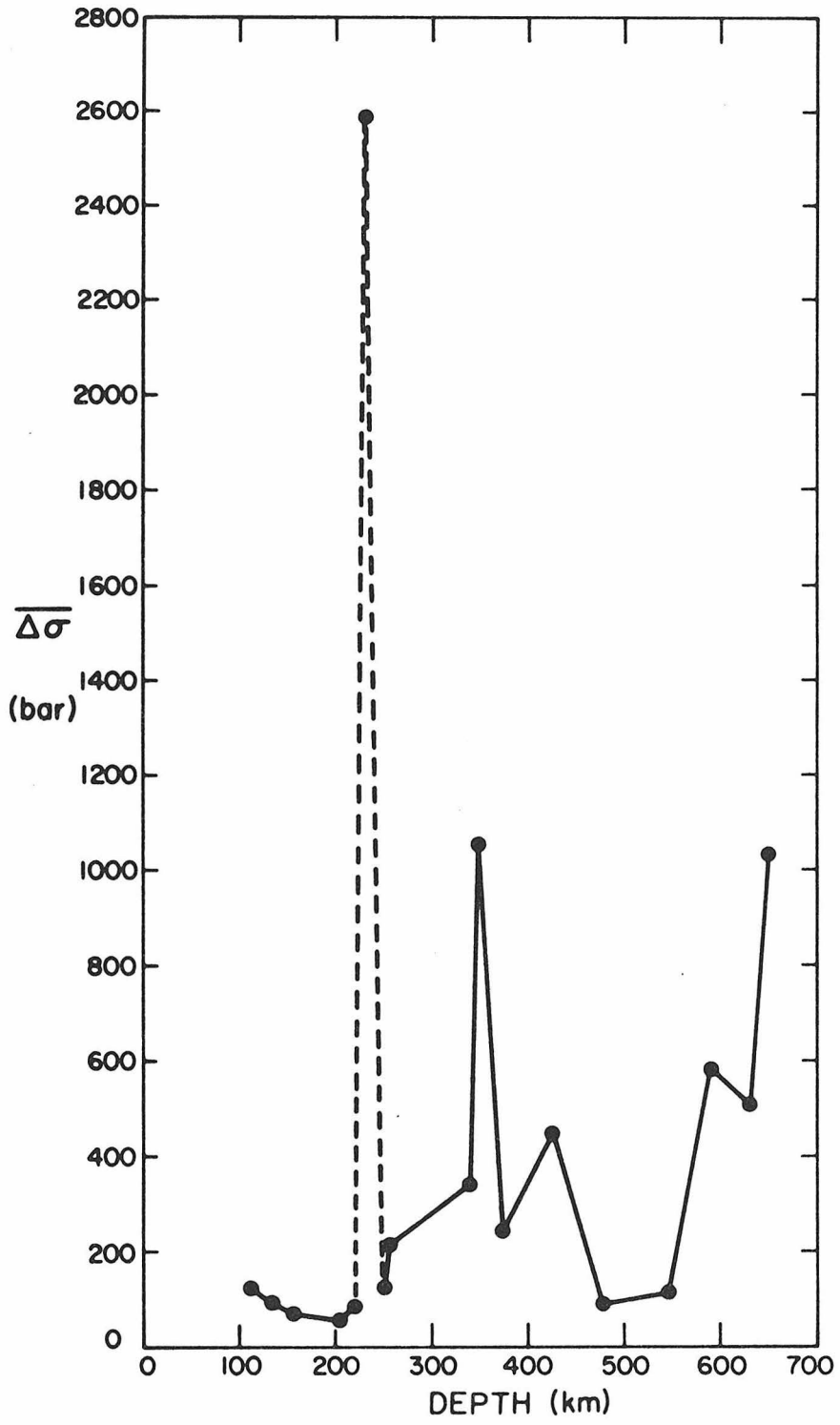

Figure 22. Variation of stress drop as a function of depth. Only the averaged values of the stress drop ranges are shown in this plot on a linear scale.

should happen. Event 6 (Figure 22) has a very high stress drop compared to the other shocks at about the sample depth. As will be discussed in a later section, the high stress drop of this event can be explained by some reasons besides the depth effect. When we discuss the change of stress drop as a function of depth event 6, therefore, is not considered. We have a peak of stress drop at a depth of about 350 to 390 km or slightly shallower than 400 km. The rapid increase in seismic wave velocities at the depth of about 400 km has been related to the olivine-spinel transition in the mantle (Anderson, 1967). As the Clapeyron slope $\frac{dP}{dT}$ (where P and T stand for pressure and temperature respectively) of the transition is positive the phase boundary of the olivine-spinel transition within the descending lithosphere should be elevated from the normal depth in the mantle because of the lower temperature within the slab (Turcotte and Schubert, 1971; Ringwood, 1972). The depth of the observed peak of stress drop seems to be coincident with the depth range of the olivine-spinel transition in the subducting slab and may be associated with the phase transition. From about 450 to 560 km we have a region of low stress drop. Tsujiura (1972) studied the spectra of S waves from intermediate and deep earthquakes in and near the Japanese arc and found that high frequency components, observed for events shallower than 400 km, are lost for earthquakes deeper than about 400 km. He suggested that his observation was probably due to a difference in source spectrum for events above or below a boundary at around 400 km. Tsujiura's boundary is very close to our boundary of decreasing stress drop at about 450 km (Figures 21 and 22). This boundary is also coincident with the depth of increasing

seismicity in the Tonga-Kermadec area (Figure 23). A simple way to explain the above observations is the following. If the material strength is lower below 450 km we should observe relatively low stress drop events. If, in addition, the rates of stress accumulation at different depths are roughly the same we need a larger number of lower stress drop events to release the stress. This explains the increase of annual number of earthquakes in the range below the boundary. For depths from 570 to 650 km, our data (Figure 22) show a rapid increase of stress drop; this depth range is very close to the range of rapid increase in wave velocities between 600 and 700 km. This high velocity gradient region has been related to the spinel-oxide transformation in the mantle (Anderson, 1976). As the slope of the Clapeyron curve for the phase change is not well known the elevation of the phase boundary within the slab is uncertain. However, the coincidence between the depth ranges of the observed high stress drop and the phase transition again suggest the phase change may have something to do with the stress drop. Interestingly enough, as one can see in Figure 23, this depth range of increasing stress drop corresponds to a decrease in deep seismicity.

When an oceanic lithosphere is descending beneath an island arc, different parts of the lithosphere usually are subjected to different degrees of contortion. As a consequence, different portions of the plate may be under different stress. The contours of hypocentral depth of the Tonga-Kermadec area (Figures 24a and b) show that at the northern end of the Tonga arc the subducting plate is abruptly bent laterally and at depth from about 400 to 500 km the plate is locally

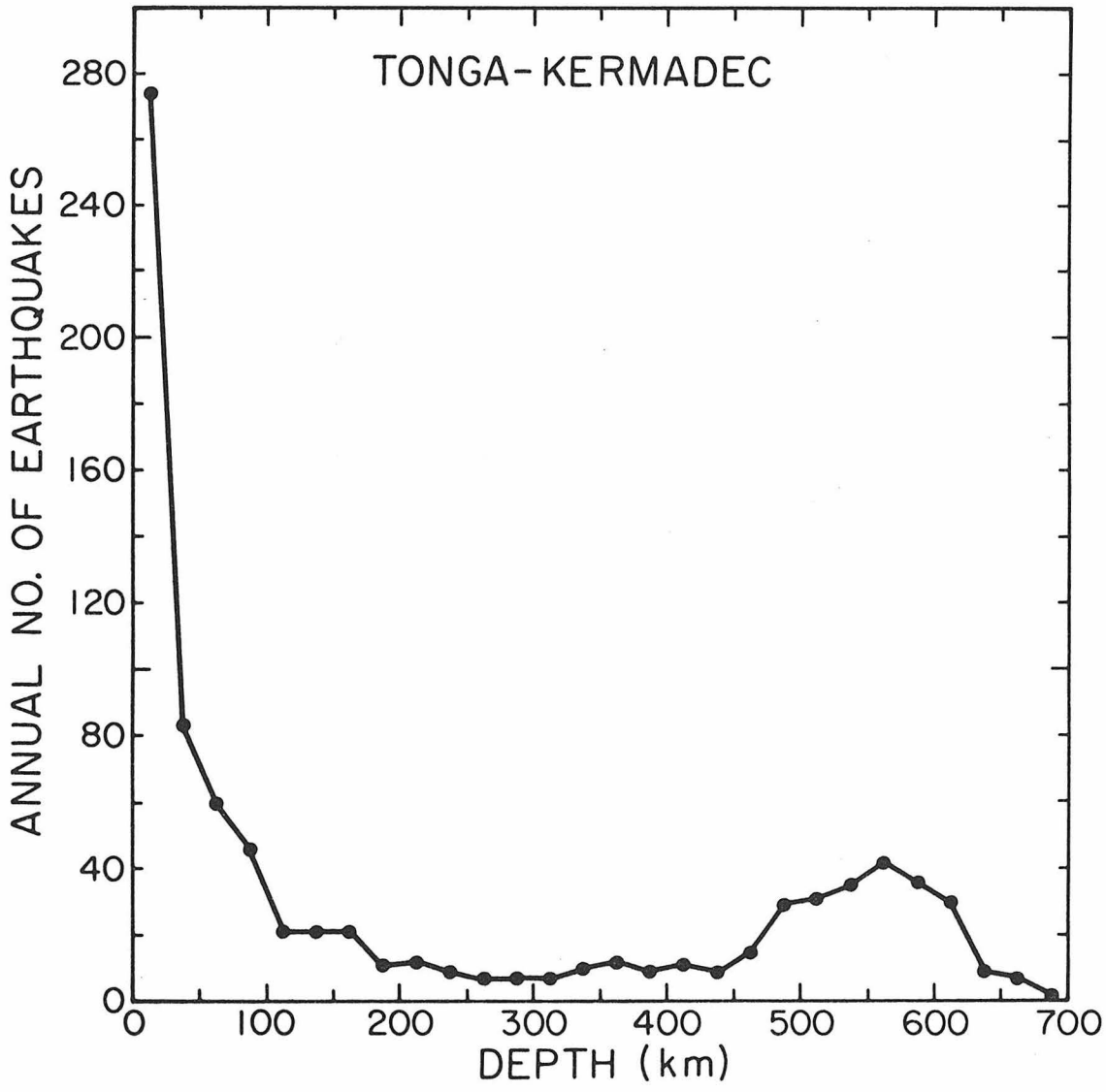

Figure 23. Number of earthquakes per year versus depth in the Tonga-Kermadec area (redrawn from Sykes, 1966).

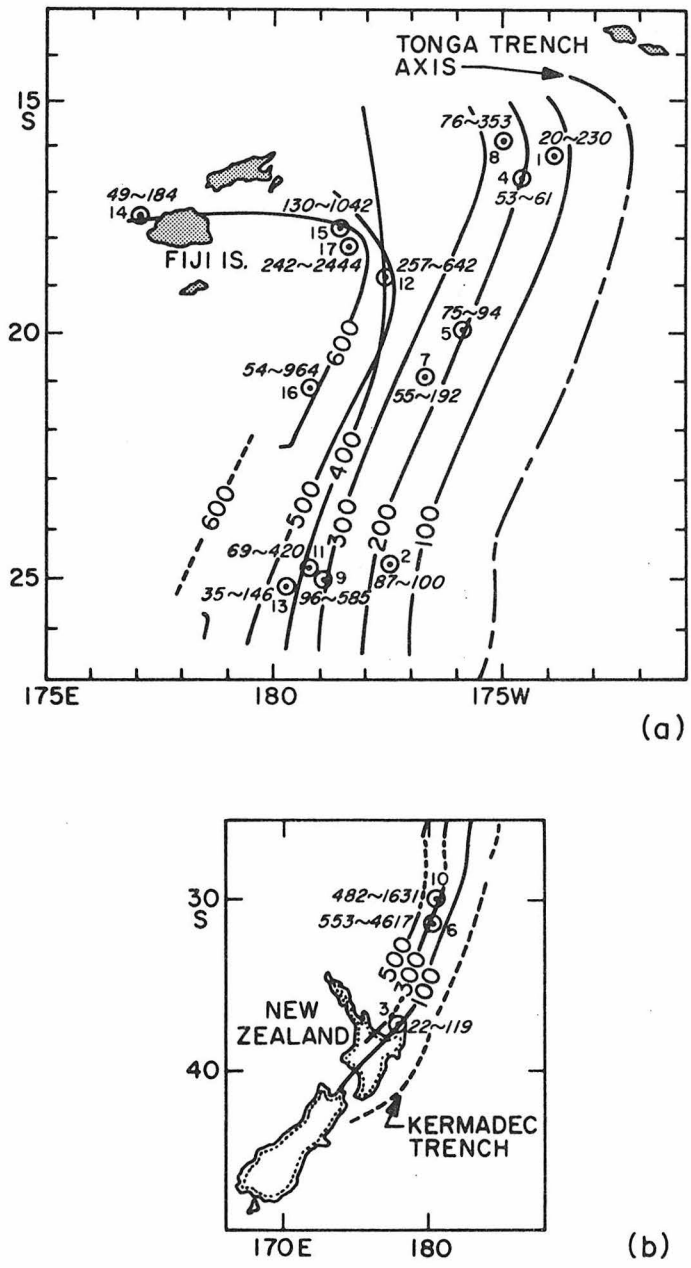

Figure 24 (a) and (b). Ranges of stress drop and epicentral location of the 17 earthquakes in the Tonga-Kermadec area. Open circle with dot in it represents earthquake epicenter; event numbers and ranges of stress drops are given by the sides of the epicenters. The curves are contours of hypocentral depth which are adopted from Isacks et al. (1969) and Isacks and Molnar (1971).

contorted as shown by the overlapping of 400 and 500 km contours. We would like to investigate whether these plate contortions can have any effect on stress drops and also to see whether there are any correlations of the stress drop pattern with other tectonic or geophysical features in the area. Figures 24a and b present the earthquake epicenters and the range of stress drops for the 17 events. Earthquakes 14, 15, 16 and 17 all have similar focal depths which range from about 545 to 650 km. Events 15 and 17 are located at the big bend; on the other hand, events 14 and 16 are away from the bend. Interestingly, events 15 and 17 have higher stress drops than events 14 and 16. The stress drops of events 15 and 17 are 130 to 1042 bars and 242 to 2444 bars respectively, whereas events 14 and 16 have stress drops of 49 to 184 bars and 54 to 964 bars respectively. Earthquakes 12 and 13 are of comparable depths. Event 12, which is located at a place of severe plate distortion, has a stress drop of 257 to 642 bars while event 13 has a relatively small stress drop of 35 to 146 bars. One more example comes from events 4, 5, 7 and 8 which, again, have similar depths. Event 8, which is located near the lateral bending at the north end of the arc, has a higher stress drop of 76 to 353 bars; whereas events 4, 5 and 7, which are further away from the bend, just have stress drops of 53 to 61 bars, 75 to 94 bars, and 55 to 192 bars respectively. The above observations are consistent with what we expect for the stress distribution at and near a local bend of an elastic plate.

As can be seen in Figure 24b, earthquake 6, which is not located near any bend of the plate, has a very high stress drop, 553 to 4617

bars. This high stress drop cannot be explained in terms of plate bending. Therefore, we must look for other explanations. Figure 25 is a projection of the 17 earthquakes of this study and Sykes' (1966) relocated hypocenters, which occurred between 1959 and February 1962, onto a vertical plane parallel to the trend of the arc. It should be pointed out here that because the 17 events were selected in a particular way their hypocenter distribution is not a good representation of the general seismicity. The general seismicity pattern is represented by the distribution of the open circles in Figures 25 and 26. Event 6 is located at the center of a relatively quiet area of seismicity (Figure 25) and has a stress drop higher than those of events 5, 7 and 8 which are located in areas of relatively high seismicity. Figures 26a to 261 are projections of hypocenters of different sections of the Tonga-Kermadec arc and the 17 shocks onto vertical planes perpendicular to the arc (Figure 5). Again we can see event 6 is within an area of relatively low seismicity (Figure 26d). Figure 26g shows the locations and stress drops for events 2, 9, 11 and 13. Events 9 and 11, which are located within a region of relatively low activity, have higher stress drops than those of events 2 and 13 which are located in higher activity regions. With another examination of Figures 21 and 24 we can see that the high stress drop region between depths 220 to 450 km is also roughly the region of low seismicity of the arc. This again shows the correlation between high stress drop and low seismicity. There are at least two ways to explain the existence of a low seismicity, or quiet, region in the subducting plates. One is that the relatively quiet region represents a "weak"

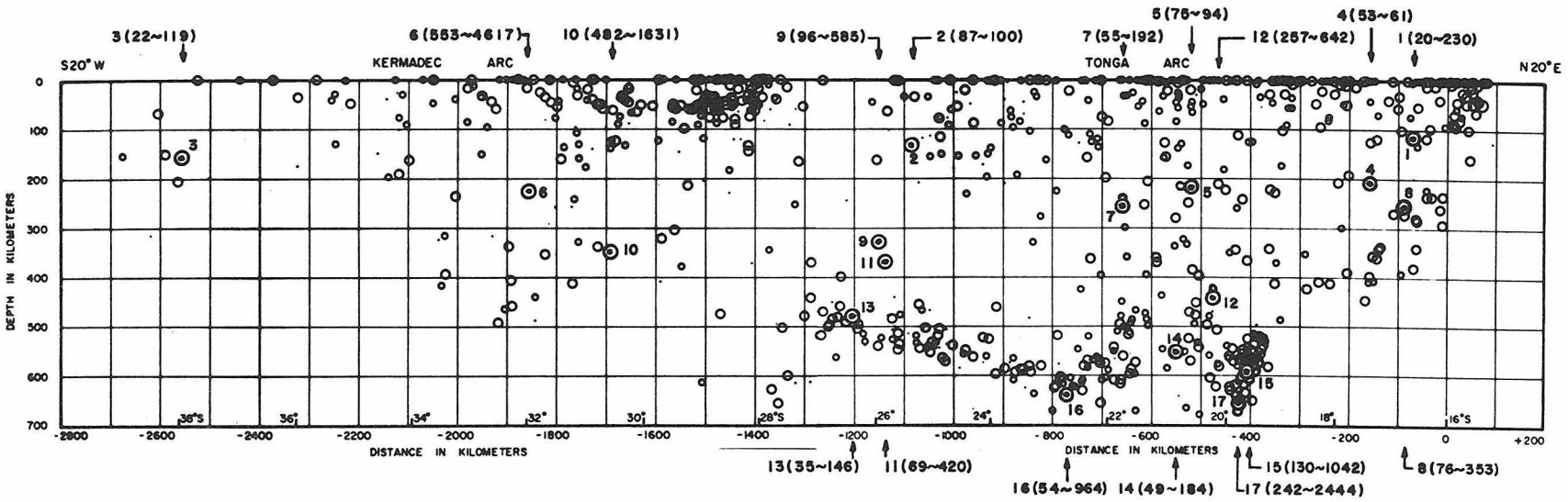

Figure 25. Ranges of stress drop and locations of the 17 earthquakes in the Benioff zone. The hypocenters of the 17 events and Sykes' (1966) relocated earthquake foci have been projected onto a vertical plane, shown in Figure 5, running parallel to the trend of the arc. The values within the parentheses are ranges of stress drop while the numbers to the left of the parentheses are event numbers.

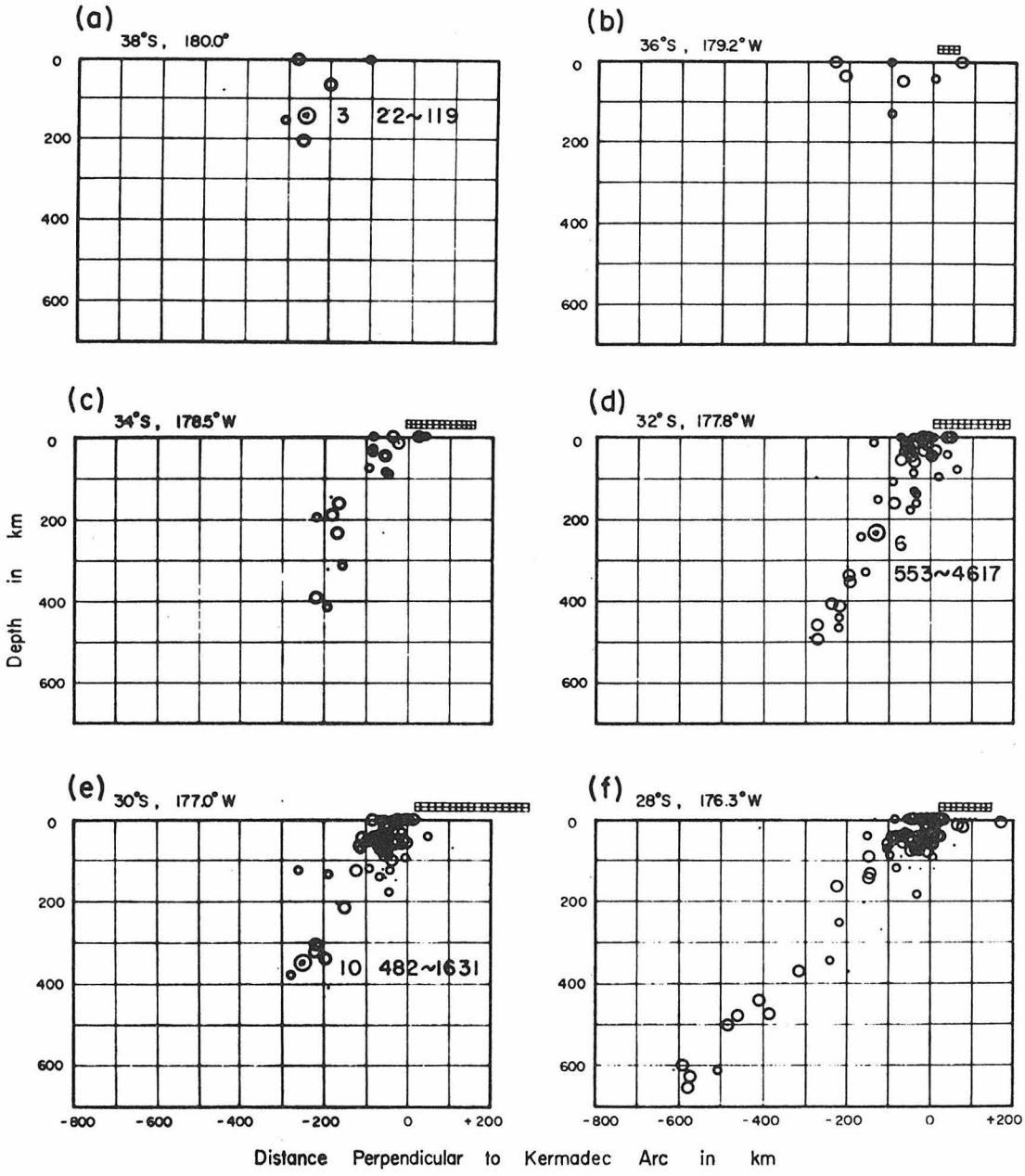

Figure 26. Projections of the 17 earthquakes and the hypocenters of different sections of the Tonga-Kermaded arc onto vertical planes shown in Figure 5, perpendicular to the arc. Each of the earthquakes studied in this work is represented by an open circle with a dot in it. Event number and range of stress drop are given by the side of the related hypocenter.

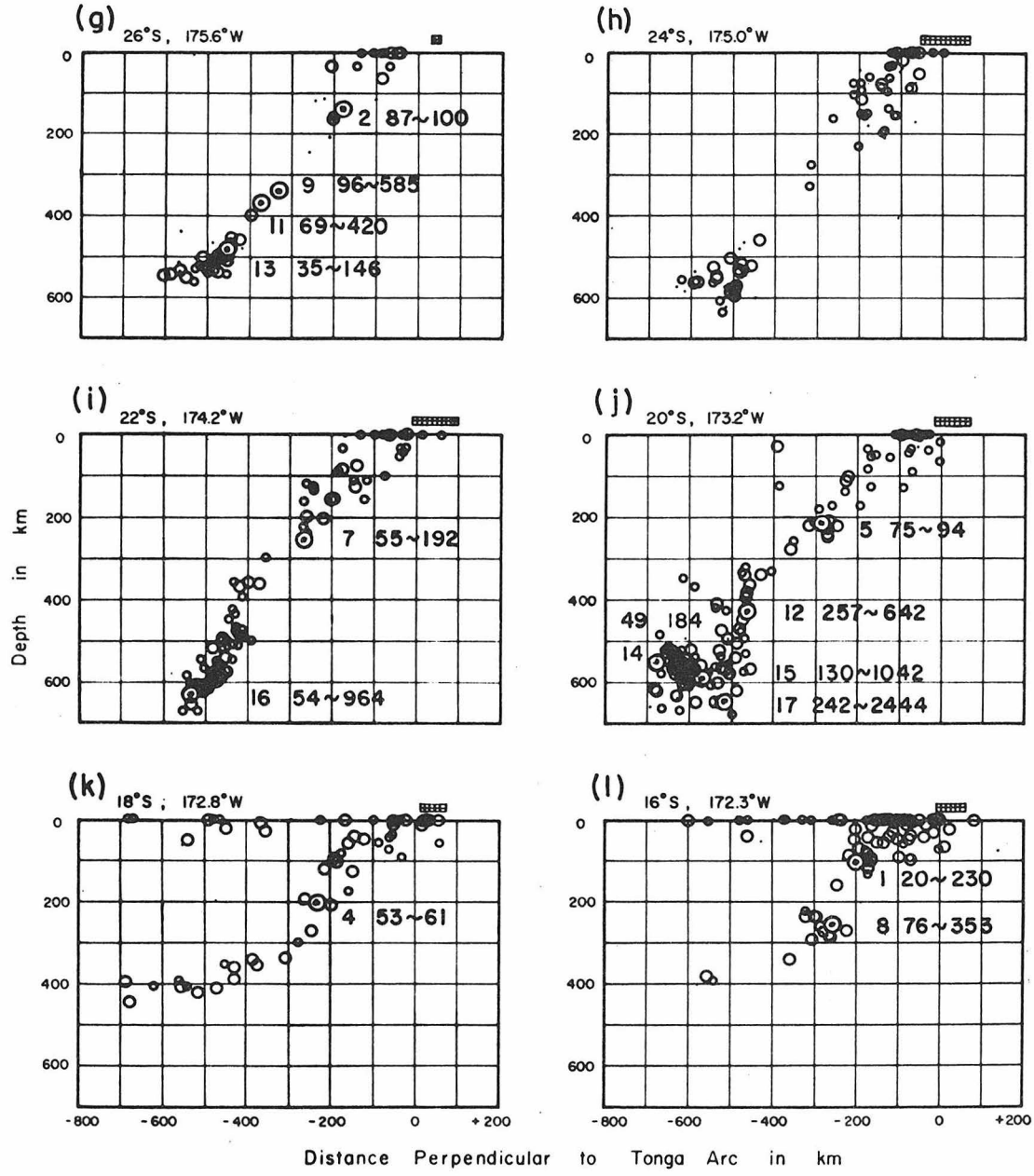
(g) 26°S, 175.6°W
2 87~100
9 96~585
11 69~420
13 35~146
(h) 24°S, 175.0°W
(i) 22°S, 174.2°W
7 55~192
16 54~964
(j) 20°S, 173.2°W
5 75~94
8
49 184
12 257~642
14
15 130~1042
17 242~2444
(k) 18°S, 172.8°W
4 53~61
(l) 16°S, 172.3°W
1 20~230
8 76~353
0
200
400
600
Depth in km
-800 -600 -400 -200 0 +200
Distance Perpendicular to Tonga Arc in km

Figure 26.

portion of the lithosphere where the stresses are released in the form of creep instead of brittle fracture. Another explanation is that the region represents a "hard" portion of the lithosphere where the material is strong enough to sustain high stresses. The observed high stress drops associated with the low seismicity area seems to favor the latter explanation.

Magnitude, Apparent Stress, and Stress Drop

Besides stress drop, another stress estimate which can be calculated from the observed variable is the apparent stress. Apparent stress is defined as the product of seismic efficiency, η, and the average stress, $\bar{\sigma}$, between the initial, σ_1, and the final, σ_2, shear stresses across the fault surface (Wyss and Brune, 1968)

$$\bar{\sigma} = \frac{1}{2} (\sigma_1 + \sigma_2)$$

Seismic efficiency is defined as the ratio of seismic wave energy E, to the total strain energy, W, released:

$$\eta = \frac{E}{W}$$

and

$$W = \bar{\sigma}\, \bar{D}\, A$$

where $\bar{D}$ is the average dislocation and A is the fault area. Apparent stress can be expressed as

$$\eta\bar{\sigma} = \frac{E}{\bar{\sigma}DA} \cdot \bar{\sigma} = \frac{E}{DA} = \frac{\mu E}{\mu DA}$$

or

$$\eta\bar{\sigma} = \mu \frac{E}{M_o}$$

Usually the energy-magnitude relation

$$\log E = 5.8 + 2.4\ m_B$$

developed by Gutenberg and Richter (1956) is employed to determine the seismic energy E from the body wave magnitude m_B. The magnitudes used to derive this formula were determined from the instruments available around 1945, which were mostly broad band mechanical types; the period range of P waves was mainly from 4 to about 10 sec (Gutenberg, 1945; Geller, 1976). However, since the introduction of m_B the definition of body-wave magnitude has been changed by various investigators, seismological stations and agencies (Abe and Kanamori, 1978). For example, since 1963 the Earthquake Data Reports (EDR) and the Bulletin of International Seismological Center (ISC) have published body-wave magnitudes m_B determined from short-period body waves of usually about one second period. This short-period m_b differs markedly from the intermediate to long period m_B used by Gutenberg and Richter. Thus the use of short-period m_b to obtain seismic energy E is not appropriate. A problem with the conventional magnitude scales is that they suffer saturation when the rupture dimension of the earthquake exceeds the wavelengths of the seismic waves recorded and used in magnitude determinations (Kanamori, 1977; Geller, 1976; Abe and Kanamori, 1978). This saturation leads to an inaccurate estimate of energy released in large earthquakes. The short period m_b saturates at a much shorter fault length or lower magnitude than the long period m_B. The source dimensions of intermediate and deep focus earthquakes, however, are considerably smaller than those for great shallow earthquakes and long-

period m_B probably represents the overall size of the earthquake reasonably well. In view of this, we determine m_B from the long-period records of WWSSN and use it to calculate E and then $\eta\bar{\sigma}$. The apparent stress determined in this study is given in Table 4.

Another advantage of using m_B is that one obtains a better correlation between log M_o and body-wave magnitude of intermediate and deep focus earthquakes. Figures 27 and 28 present log M_o versus m_b and log M_o versus m_B respectively. The values of m_b are taken from U.S.G.S. reports while m_B values are determined in this study. The log M_o versus m_b data for intermediate and deep focus earthquakes have large scatter as shown in Figure 27. The scatter is significantly reduced if we use m_B instead of m_b as demonstrated in Figure 28. This probably means that m_B is a better measure of earthquake size for the magnitude range in the present study, and short period waves are more sensitive to heterogeneities along the path and structural effects near the source and receiver.

Direct measurement of the absolute stress near an earthquake is not feasible from analyses of seismic radiation. However, two stress estimates, the apparent stress and the stress drop, can be made from observed variables. Savage and Wood (1971) studied the relation between apparent stress and stress drop. Assuming constant initial, final, and frictional stresses over an elliptical fault, they found

$$\eta\bar{\sigma} = \frac{1}{2}(\sigma_1 - \sigma_2) - (\sigma_f - \sigma_2)$$

where σ_f is the dynamic frictional stress. Since $\eta\bar{\sigma}$ and $\Delta\sigma$ can be determined we can obtain an estimate of the difference between the

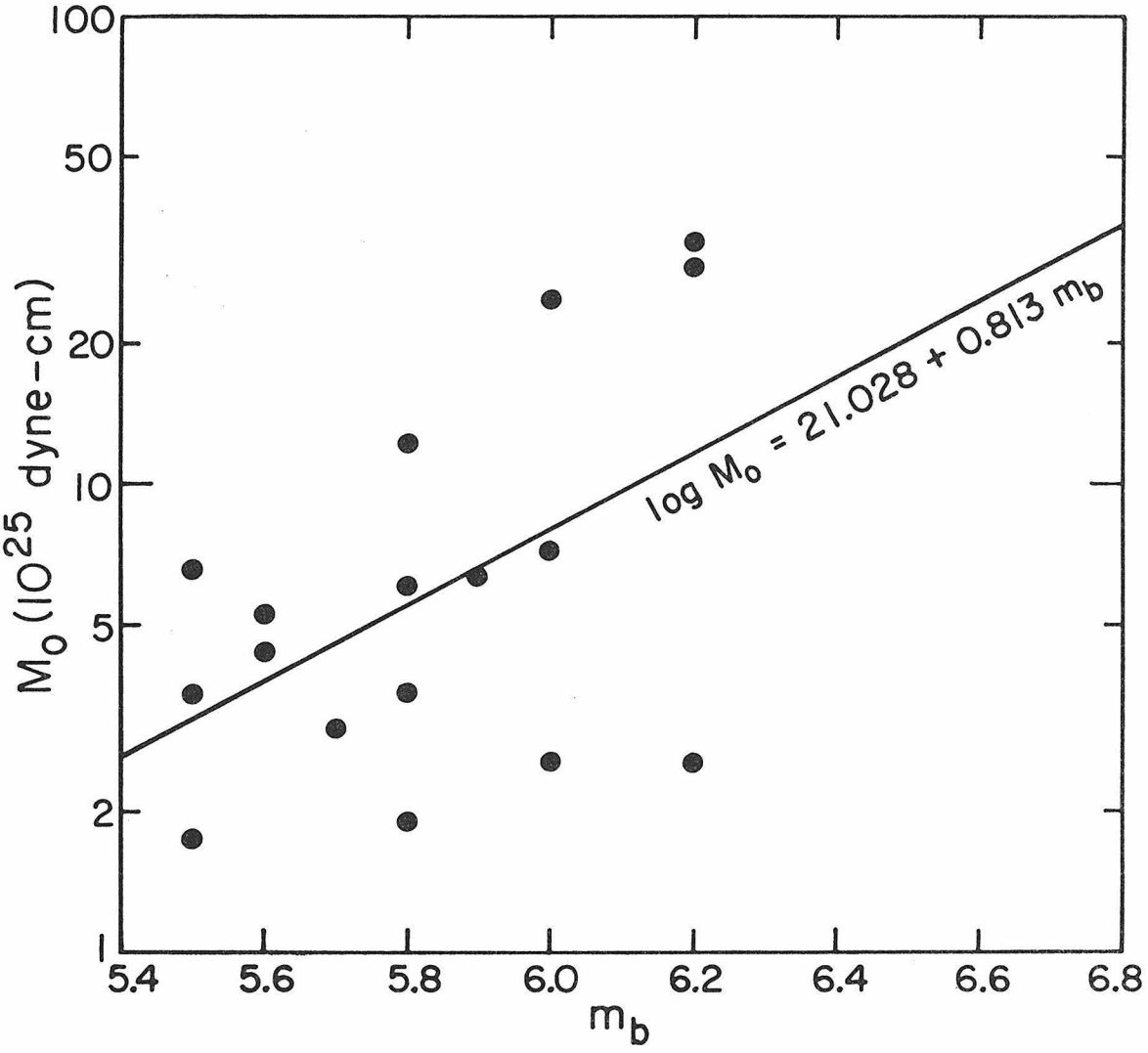

Figure 27. Relation between seismic moment M_o and short period body wave magnitude m_b.

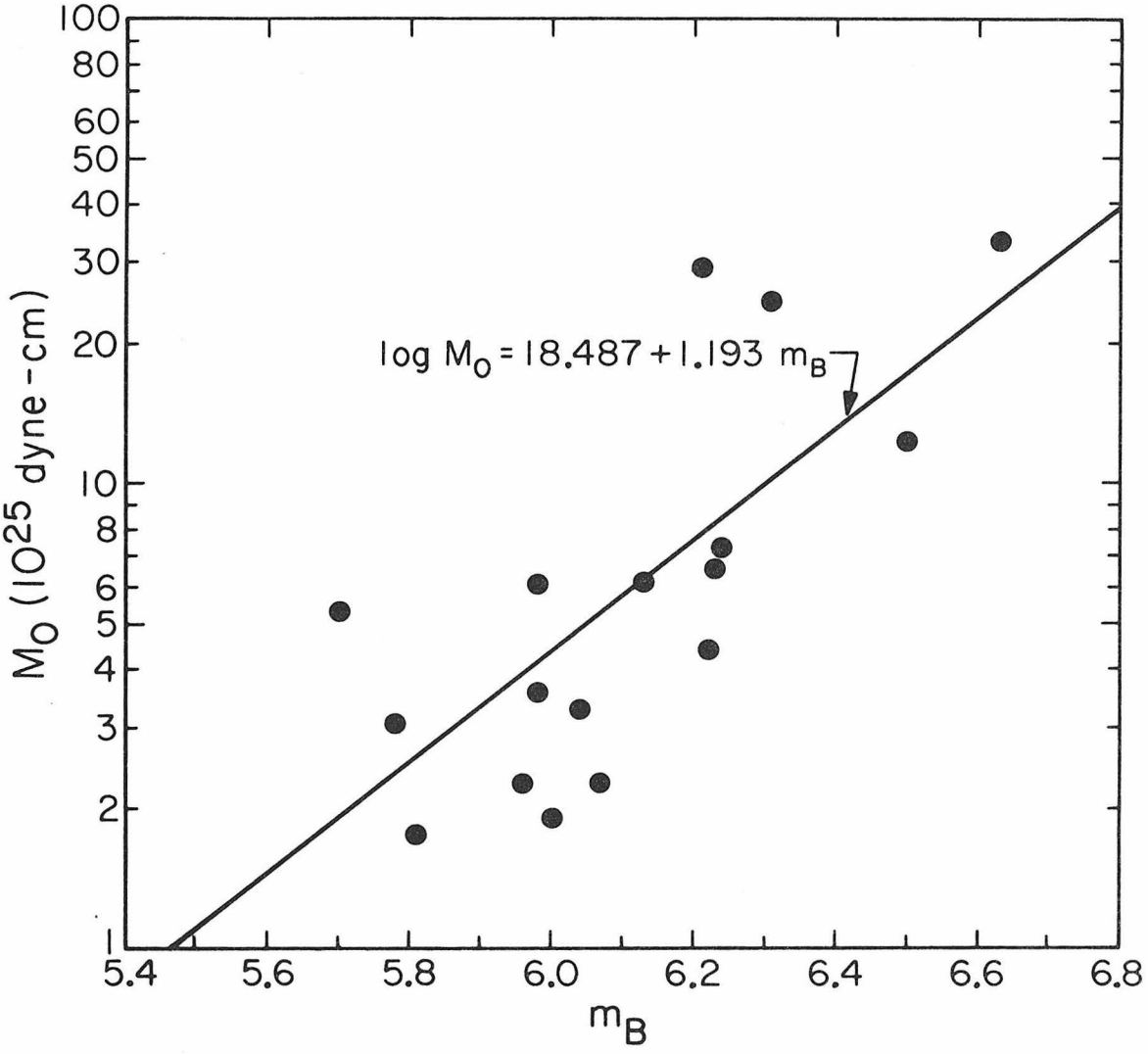

Figure 28. Relation between M_o and long period body wave magnitude m_B.

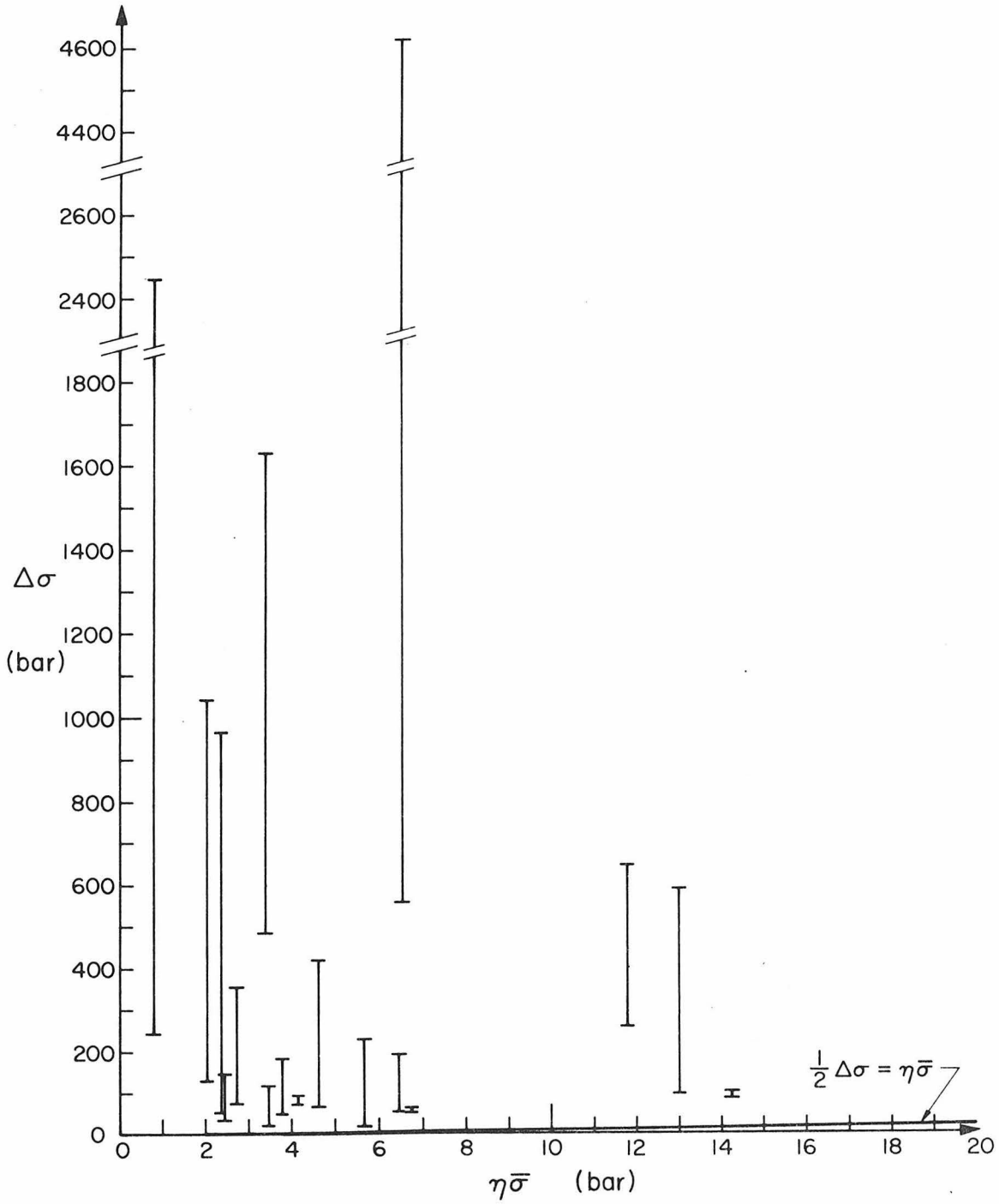

Figure 29. Relation between stress drop and apparent stress of intermediate and deep focus earthquakes.

frictional stress and the final stress. If $\sigma_f = \sigma_2$ we have $\eta\bar{\sigma} = 1/2\Delta\sigma$; and $\eta\bar{\sigma} < 1/2\Delta\sigma$ when $\sigma_f > \sigma_2$. Figure 29 is a plot of $\Delta\sigma$ versus $\eta\bar{\sigma}$ for the 17 intermediate and deep focus earthquakes in the present study. Our data indicate $1/2\Delta\sigma > \eta\bar{\sigma}$ suggesting $\sigma_f > \sigma_2$ at the earthquake source.

Seismic Efficiency of Intermediate and Deep Focus Earthquakes

If both apparent stress and stress drop are known we can estimate the upper bound of seismic efficiency. Since

$$\eta\bar{\sigma} = \mu \frac{E}{M_o}$$

we have

$$\eta = \frac{\mu E}{1/2(\sigma_1+\sigma_2)M_o}$$

If $\sigma_2 = 0$ we have $\sigma_1 = \Delta\sigma$; and $\sigma_1 > \Delta\sigma$ when $\sigma_2 > 0$. Hence $\sigma_1 \geq \Delta\sigma$ if $\sigma_2 \geq 0$.

$$\eta \leq \frac{2\mu E}{M_o \Delta\sigma}$$

$$\eta_{max} = \frac{2\eta\bar{\sigma}}{\Delta\sigma}$$

If the stress is completely released during faulting or $\sigma_2 = 0$, $2\eta\bar{\sigma}/\Delta\sigma$ gives the actual efficiency. The upper bounds of the seismic efficiency of the 17 earthquakes are listed in Table 4. Figure 30 presents η_{max} as a function of depth. η_{max} varies from about 0.1% to 33%, and with some scatter, the upper bound of η_{max} decreases with depth. Since the seismic energy equals the difference between the total strain energy and the work done against friction W_f, we have

$$E = W - W_f$$

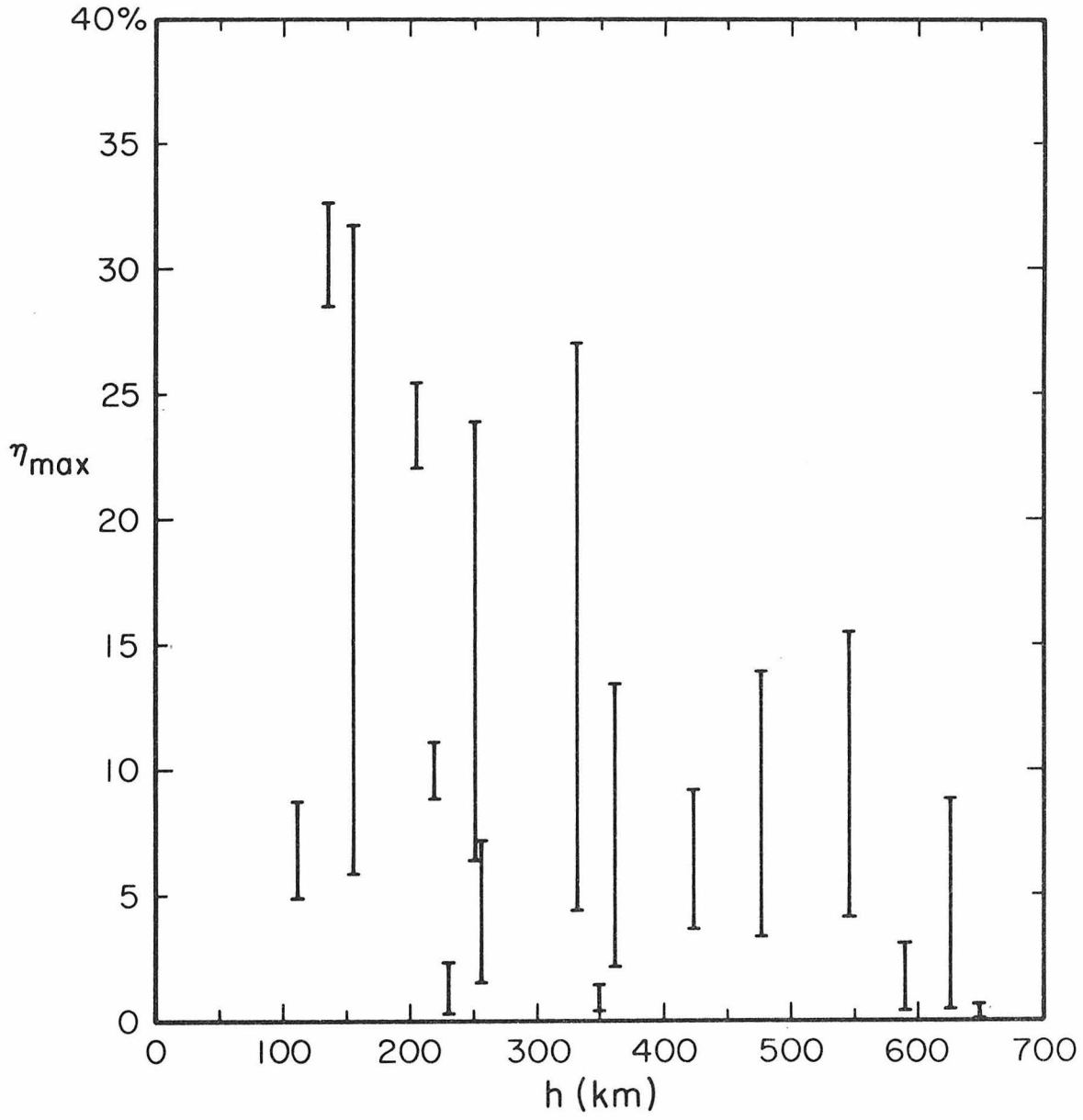

Figure 30. Relation between the upper bound of seismic efficiency, η_{max}, and focal depth, h.

and $$\eta = \frac{W - W_f}{W}$$

where $$W_f = \sigma_f \overline{D} A \ .$$

Frictional stress appears to be an important parameter controlling seismic efficiency. At present it is not completely known how the frictional stress varies with depth and what kind of friction law it should follow. If, somehow, the frictional force increases as a function of depth, then we should have a decrease of seismic efficiency with depth because more energy is spent in moving the fault against friction. The η_{max} versus depth data in this study suggests an increase of frictional stress with depth.

A Comparison of Deep and Shallow Earthquake Source Parameters

Empirical relations among source parameters of shallow focus earthquakes have been studied by many investigators. Based on an extensive set of data for shallow earthquakes with $M_s \geq 6$ Kanamori and Anderson (1975) found that the stress drops of large inter-plate earthquakes are remarkably constant falling between 10 and 100 bars with an average of 30 bars. Intra-plate earthquakes show systematically larger stress drops, about 100 bars. The present results indicate that the situation for intermediate and deep earthquakes is quite different: the stress drops vary over a large range, from several tens of bars to several kilobars, and are significantly higher than those for shallow earthquakes. Since the focal depths for the events studied here range from about 100 to 650 km, the observed large variation of stress drop probably reflects a large variation of material strength and stress

level within this wide range of depth within the earth. The log A (fault area) versus log M_o plot of intermediate and deep earthquakes has a very large scatter instead of falling on a narrow linear trend as the case for large shallow shocks. Kanamori and Anderson (1975) also found that $\eta\bar{\sigma} \approx 1/2\Delta\sigma$ suggesting that the final stress is approximately equal to the frictional stress σ_f, i.e., $\sigma_f \simeq \sigma_2$. The situation for intermediate and deep focus earthquakes is again different; our results indicate $1/2\Delta\sigma > \eta\bar{\sigma}$ suggesting that the frictional stress is larger than the final stress, i.e., $\sigma_f > \sigma_2$.

CONCLUSIONS

The pulse-width and least squares searching method developed in this study has proved to be a powerful and fast technique to extract source parameters from isolated seismic signals. Trial and error approach to fitting observed data with synthetics is then avoided. With this method, one can analyze a large number of intermediate and deep focus earthquakes within a relatively short time and obtain source parameters with a homogeneous method. This is very important for studying relative stress drop between events or variations of stress drop with a region or depth.

For most of the 17 earthquakes studied, a unilateral fault model best explained the azimuthal variation of P-wave pulse-width. A bilateral fault model gave the best fit for some events, but in no cases did the circular fault model explain the data better than either the unilateral and bilateral faults. This may suggest that stresses and material properties at the earthquake sources are not perfectly

homogeneous and isotopic; the highly symmetric mode of rupture (represented by the circular fault model) is, therefore, unlikely.

The 17 earthquakes with magnitude m_B ranging from 5.1 to 6.6 and with focal depths from about 100 to 650 km yield seismic moments, fault length, and average dislocations which vary from about 1.8×10^{25} to 3.3×10^{26} dyne cm, 5 to 37 km, and 0.3 to 8 m, respectively, and corresponding mean values of 9.08×10^{25} dyne-cm, 14.84 km, and 1.5 m respectively. Stress drop varies over a very large range from 20 to 4617 bars with an average of 476 bars.

Stress drop shows significant variations with depth and lateral position along the arc. For depth between 100 and about 220 km, the stress drop level is low with a mean of 86 bars. From about 230 to 430 km the average stress drop is several times higher with a peak at a depth of about 360 km. A low stress drop region is located at about 450 to 560 km, coincident with a zone of high seismic activity. For depths between 580 to about 650 km, the stress drops are again quite high. The two high stress drop regions at about 360 and 640 km may be associated with the olivine-spinel and spinel-oxide phase transitions within the subducting lithosphere. In addition, earthquakes at and near some local bends of the subducting plate have significantly higher stress drops than earthquakes at comparable depths but away from bends. There is also some correlation between low seismicity and high stress drop suggesting that the relatively aseismic areas of subducting slabs in the deep mantle have high breaking strength.

The apparent stress is smaller than half of the stress drop, i.e., $\eta\bar{\sigma} < \frac{1}{2} \Delta\sigma$ for intermediate and deep focus earthquakes suggesting that

the frictional stress is substantially higher than the final stress at the earthquake source.

The upper bound of the seismic efficiency varies from about 0.1% to 33% for the earthquakes studied and decreases as focal depth increases. This change with depth may imply that the frictional stress increases with depth.

The source properties of intermediate and deep focus earthquakes are different from those of large shallow earthquakes in many aspects. For instance, range of stress drop, moment-magnitude relation, relation between apparent stress and stress drop are significantly different. These differences probably reflect differences in material properties and state of stress between the surface and the deep interior of the earth.

REFERENCES

Abe, K. (1972). Focal process of the South Sandwich Islands earthquake of May 26, 1964, Phys. Earth Planet. Int., 5, 110-122.

Abe, K. (1975). Reliable estimation of the seismic moment of large earthquakes, J. Phys. Earth, 23, 381-390.

Abe, K. and H. Kanamori (1978). Temporal variation of the activity of intermediate and deep focus earthquakes,

Aki, K. (1966). Generation and propagation of G waves from the Niigata earthquake of June 16, 1964, Bull. Earthquake Res. Inst. Tokyo Univ., 44, 23-88.

Aki, K. (1972). Earthquake mechanism, in A. R. Ritsema (ed.), The Upper Mantle, Tectonophysics, 13, 423-446.

Anderson, D. L. (1967). Phase changes in the upper mantle, Science, 157, 1165-1175.

Anderson, D. L. (1976). The 650 km mantle discontinuity, Geophys. Res. Lett., 3, 347-349.

Anderson, D. L. and R. S. Hart (1976). An earth model based on free oscillations and body waves, J. Geophys. Res., 81, 1461-1475.

Anderson, D. L. and R. S. Hart (1978). Attenuation models of the earth, Phys. Earth Planet. Int., 16, 289-306.

Barazangi, M. and B. Isacks (1971). Lateral variations of seismic wave attenuation in the upper mantle above the inclined earthquake zone of Tonga island arc: Deep anomaly in the upper mantle, J. Geophys. Res., 76, 8493-8516.

Benioff, H. (1955). Seismic evidence for crustal structure and tectonic activity, in. A. Poldervaart (ed.), Crust of the Earth (a Symposium) Geol. Soc. Am., Spec. Papers, 62, 67-74.

Ben-Menahem, A. (1961). Radiation of seismic surface-waves from finite moving-source, Bull. Seism. Soc. Am., 51, 401-435.

Ben-Menahem, A. (1962). Radiation of seismic body waves from a finite moving source in the earth, J. Geophys. Res., 67, 345-350.

Berckhemer, H. and K. Jacob (1968). Investigation of the dynamical process in earthquake foci by analyzing the pulse shape of body waves, Final Scientific Report of AF-61 (052)-801, National Technical Information Service, Washington, D.C.

Bollinger, G. A. (1968). Determination of earthquake fault parameters from long-period P waves, J. Geophys. Res., 73, 785-807.

Bollinger, G. A. (1970). Fault length and fracture velocity for the Kyushu, Japan, earthquake of October 3, 1963, J. Geophys. Res., 75, 955-964.

Boore, D. M. and W. B. Joyner (1978). The influence of rupture incoherence on seismic directivity, Bull. Seism. Soc. Am., 68, 283-300.

Brune, J. N. (1970). Tectonic stress and spectra of seismic shear waves from earthquakes, J. Geophys. Res., 75, 4997-5009.

Bullen, K. E. (1963). An Introduction to the Theory of Seismology, Third ed., Cambridge Univ. Press, Cambridge, 381 pp.

Burdick, L. and D. V. Helmberger (1974). Time functions appropriate for deep focus earthquakes, Bull. Seism. Soc. Am., 64, 1419-1428.

Byerlee, J. (1977). Friction of rocks, Proceedings of Conference II: Experimental studies of rock friction with application to earthquake prediction, ed. J. F. Evernen, U. S. Geol. Survey, Menlo Park, 55-77.

Carpenter, E. W. (1966). Absorption of elastic waves -- an operator for a constant Q mechanism, Atomic Weapons Research Establishment Report O-43/66, London, Her Majesty's Stationary Office.

Carpenter, E. W. (1967). Teleseismic signals calculated for underground, underwater, and atmospheric explosions, Geophysics XXXII, No. 1, 17-32.

Carpenter, E. W. and E. A. Flinn(1965). Attenuation of teleseismic body waves, Nature, 207, 745-746.

Chung, W.-Y. and H. Kanamori (1976). Source process and tectonic implications of the Spanish deep-focus earthquake of March 29, 1954, Phys. Earth Planet. Int., 13, 85-96.

Chung, W.-Y. and H. Kanamori (1978). Subduction process of a fracture zone and aseismic ridges -- the focal mechanism and source characteristics of the New Hebrides earthquake of 1969 January 19 and some related events, Geophys. J. R. astr. Soc., 54, 221-240.

Dziewonski, A. M. and F. Gilbert (1974). Temporal variations of seismic moment tensor and the evidence of precursive compression for deep earthquakes, Nature, 247, 185-188.

Ellsworth, W. L. (1975). Bear Valley, California, earthquake sequence of February-March, 1972, Bull. Seism. Soc. Am., 65, 483-506.

Eshelby, J. D. (1957). The determination of the elastic field of an ellipsoidal inclusion and related problem, Proc. Roy. Soc. London, Series A, 241, 376-396.

Fukao, Y. (1970). Focal process of a deep-focus earthquake as deduced from long-period P and S waves, Bull. Earthquake Res. Inst., 48, 707-727.

Fukao, Y. (1972). Source process of a large deep-focus earthquake and its tectonic implications -- the Western Brazil earthquake of 1963, Phys. Earth Planet. Int., 5, 61-76.

Furumoto, M. and Y. Fukao (1976). Seismic moment of great deep shocks, Phys. Earth Planet. Int., 11,352-357.

Geller, R. J. (1976). Scaling relations for earthquake source parameters and magnitudes, Bull. Seism. Soc. Am., 66, 1501-1523.

Gutenberg, B. (1945). Amplitudes of P, PP, and S and magnitude of shallow earthquakes, Bull. Seism. Soc. Am., 35, 57-69.

Gutenberg, B. and C. F. Richter (1956). Magnitude and energy of earthquakes, Ann. Geofis., 9, 1-15.

Hanks, T. and M. Wyss (1972). The use of body-wave spectra in the determination of seismic-source parameters, Bull. Seism. Soc. Am., 62, 561-589.

Haskell, N. R. (1964). Total energy and energy spectral density of elastic wave radiation from propagating faults, Bull. Seism. Soc. Am., 54, 1811-1841.

Haskell, N. R. (1966). Total energy and energy spectral density of elastic wave radiation from propagating faults, Part II, A statistical source model, Bull. Seism. Soc. Am., 56, 125-140.

Haskell, N. R. (1969). Elastic displacements in the near-field of a propagating fault, Bull. Seism. Soc. Am., 59, 865-908.

Helmberger, D. V. (1974). Generalized ray theory for shear dislocation Bull. Seism. Soc. Am., 64, 45-64.

Hirasawa, T. (1966). A least squares method for the focal mechanism determination from S wave data: Part I, Bull. Earthquake Res. Inst. Tokyo Univ., 44, 901-918.

Honda, H. (1962). Earthquake mechanism and seismic waves, Geophysical Notes, Fac. Sci., Tokyo Univ., 15, 1-97.

Isacks, B. and P. Molnar (1971). Distribution of Stresses in the descending lithosphere from a global survey of focal-mechanism solutions of mantle earthquakes, Rev. Geophys. Space Phys., 9 103-174.

Isacks, B., L. R. Sykes and J. Oliver (1969). Focal mechanisms of deep and shallow earthquakes in the Tonga-Kermadec region and the tectonics of island arc, Geol. Soc. of Am. Bull., 80, 1443-1470.

Kanamori, H. (1967). Attenuation of P waves in the upper and lower mantle, Bull. Earthquake Res. Inst. Tokyo Univ., 45, 299-312.

Kanamori, H. (1970). Velocity and Q of mantle waves, Phys. Earth Planet. Int., 2, 259-275.

Kanamori, H. (1977). The energy release in great earthquakes, J. Geophys. Res., 82, 2981-2987.

Kanamori, H. and D. L. Anderson (1975). Theoretical basis of some empirical relations in seismology, Bull. Seism. Soc. Am., 65, 1073-1095.

Kanamori, H. and G. S. Stewart (1976). Mode of the strain release along the Gibbs fracture zone, Mid-Atlantic ridge, Phys. Earth Planet. Int., 11, 312-332.

Kanamori, H. and G. S. Stewart (1978). Seismological aspects of the Guatemala earthquake of February 4, 1976, J. Geophys. Res.

Kasahara, K. (1957). The nature of seismic origins as inferred from seismological and geodetic observations, Bull. Earthquake Res. Inst. Tokyo Univ., 35, 473-532.

Keilis Borok, V. (1959). On estimation of the displacement in an earthquake source and of source dimensions, Ann. Geofis (Rome), 12, 205-214.

Khattri, K. N. (1969). Determination of earthquake fault plane, fault area, and rupture velocity from the spectra of long period P waves and the amplitude of SH waves, Bull. Seism. Soc. Am., 59, 615-630.

Knopoff, L. and F. Gilbert (1959). Radiation from a strike-slip fault, Bull. Seism. Soc. Am., 49, 163-178.

Knopoff, L. and M. J. Randall (1970). The compensated linear-vector dipole: A possible mechanism for deep earthquakes, J. Geophys. Res., 75, 4957-4963.

Koyama, J. (1978). Seismic moment of the Vladivostok deep-focus earthquake of September 29, 1973, deduced from P waves and mantle Rayleigh waves, Phys. Earth Planet. Int., 16, 307-317.

Langston, C. A. and D. V. Helmberger (1975). A procedure for modeling shallow dislocation sources, Geophys. J., 42, 117-130.

Mendiguren, J. (1972). Source mechanisms of a deep earthquake from analysis of world-wide observations of free oscillations, Ph.D. Thesis, Massachusetts Institute of Technology, Cambridge, Massachusetts.

Mikumo, T. (1969). Long-period P waveforms and the source mechanism of intermediate earthquakes, J. Phys. Earth, 17, 169-192.

Mikumo, T. (1971). Source process of intermediate-depth earthquakes as inferred from long-period P and S wave forms, 1. Intermediate-depth earthquakes in the Southwest Pacific region, J. Phys. Earth, 19, 1-19.

Mikumo, T. (1972). Focal process of deep and intermediate earthquakes around Japan as inferred from long-period P and S waveforms, Phys. Earth Planet. Int., 6, 293-299.

Niazi, M. (1974). Earthquake source dynamics from far field amplitude and phase spectra of body waves, Geophys. J. R. astr. Soc., 37, 31-44.

Okal, E. and R. Geller (1978). On the observability of isotropic seismic sources; the July 31, 1970 Chilean earthquake, Phys. Earth Planet. Int., (in press).

Oliver, J. and Isacks, B. (1967). Deep earthquake zones, anomalous structures in the upper mantle and the lithosphere, J. Geophys. Res., 72, 4259-4275.

Randall, M. J. and L. Knopoff (1970). The mechanism at the focus of deep earthquakes, J. Geophys. Res., 75, 4965-4976.

Ringwood, A. E. (1972). Phase transformations and mantle dynamics, Earth Planet. Sci. Lett., 14, 233-241.

Sasatani, T. (1974). Source process of a deep-focus earthquake in the Sea of Okhtosk as deduced from long-period P and SH waves, J. Phys. Earth, 22, 279-297.

Savage, J. C. (1966). Radiation from a realistic model of faulting, Bull. Seism. Soc. Am., 56, 577-592.

Savage, J. C. and M. D. Wood (1971). The relation between apparent stress and stress drop, Bull. Seism. Soc. Am., 61, 1381-1388.

Scrase, F. (1931). The reflected waves from deep focus earthquakes, Proc. Royal Soc. (London), 132, 213-235.

Stauder, W. S. J. (1962). The focal mechanism of earthquakes, in Advances in Geophysics, 9, 1-76.

Stechschulte, V. (1932). The Japan earthquake of March 29, 1928 and the problem of depth of focus, Bull. Seism. Soc. Am., 22, 81-137.

Stein, S. (1978). An earthquake swarm on the Chagos-Laccadive Ridge and its tectonic implications, Geophys. J. R. astr. Soc., 55, 577-588.

Strelitz, R. A. (1977). Source Processes of Three Complex Deep Focus Earthquakes, Ph.D. Thesis, Princeton University.

Sykes, L. R. (1966). The seismicity and deep structure of island arcs, J. Geophys. Res., 71, 2981-3006.

Teng, T. L. and A. Ben-Menahem (1965). Mechanism of deep earthquakes from spectrums of isolated body-wave signals, 1. Banda Sea earthquake of March 21, 1964, J. Geophys. Res., 70, 5157-5170.

Trifunac, M. D. and J. N. Brune (1970). Complexity of energy release during the Imperial Valley, California earthquake of 1940, Bull. Seism. Soc. Am., 60, 137-160.

Tsujiura, M. (1972). Spectra of body waves and their dependence on source depth, I. Japanese arc, J. Phys. Earth., 20, 251-266.

Turcotte, D. L. and G. Schubert,(1971). Structure of the olivine-spinel phase boundary in the descending lithosphere, J. Geophys. Res., 76, 7980-7987.

Utsu, T. (1971). Seismological evidence for anomalous structure of island arcs with special reference to the Japanese region, Rev. Geophys. Space Phys., 9, 839- 890.

Wadati, K. (1928). Shallow and deep earthquakes, Geophys. Mag. (Tokyo), 1, 162-202.

Wadati, K. (1935). On the activity of deep-focus earthquakes in the Japan-Island and neighborhood, Geophys. Mag., 8, 305-326.

Wyss, M. (1970). Stress estimates for South American shallow and deep earthquakes, J. Geophys. Res., 75, 1529-1544.

Wyss, M. and J. Brune (1967). The Alaska earthquake of 28 March 1964: A complex multiple rupture, Bull. Seism. Soc. Am., 57, 1017-1023.

Wyss, M. and J. Brune (1968). Seismic moment, stress, and source dimensions for earthquakes in the California-Nevada region, J. Geophys. Res., 73, 4681-4694.

Wyss, M. and T. Hanks,(1972). The source parameters of the San Fernando earthquake inferred from teleseismic body waves, Bull. Seism. Soc. Am., 62, 591-602.

Wyss, M. and P. Molnar (1972). Source parameters of intermediate and deep focus earthquakes in the Tonga arc, Phys. Earth Planet. Int., 6, 279-292.

Wyss, M. and L. J. Shamey (1975). Source dimensions of two deep earthquakes estimated from aftershocks and spectra, Bull. Seism. Soc. Am., 65, 403-409.

PART II

A SEISMOLOGICAL INVESTIGATION OF THE SUBDUCTION MECHANISM OF ASEISMIC RIDGES

INTRODUCTION

Over the past fifteen years, numerous papers on various aspects of plate subduction and the nature of convergent plate boundaries have been published. Convergent plate boundaries can be classified into two types: oceanic and continental subduction. Significant differences in mode of subduction and subsequent geological and geophysical phenomena exist between these two types of subduction even though there are many similarities. For example, deep depressions and arc-like structures are common features; other similarities can also be observed in the gravity field, heat flow anomalies, earthquake source mechanism, and geological data. On the other hand, the differences are the existence or absence of deep focus earthquakes, "narrow" versus "extremely broad" zones of shallow seismicity, occurrence of high plateau with abnormally thick crust, and mode of crustal shortening.

Most previous works are concerned with subduction of oceanic plates although several works have been done on continental subduction as well. In the present study a different type of subduction, subduction of oceanic aseismic ridge and fracture zone, is investigated. The differences between subductions of oceanic and continental plates mentioned above are usually considered to be due to differences in density and resistance against subduction associated with the two types of plates. Aseismic ridges usually have density in between pure ocean and pure continent and tend to resist subduction. Besides aseismic ridges, fracture zones are also large and common structures on the ocean floor. In this paper we will investigate the subduction of

fracture zones and aseismic ridges, especially their interaction with the overriding plate and the differences between this type of subduction and that associated with pure oceanic and continental crusts.

In the first chapter, seismological methods are employed to investigate the earthquakes associated with the subduction of a fracture zone-aseismic ridge system in the New Hebrides island arc. Attention is especially focused on (1) the nature of plate movement near the subduction boundary, (2) how the seismicity is affected by this type of subduction, and (3) the source characteristics and the rupture process of an earthquake which occurred on the subducted portion of the fracture zone. Several significant differences between this type of subduction involving aseismic ridges and the more typical oceanic subduction are found and discussed in this chapter.

In the second chapter, tectonic anomalies associated with this type of subduction boundary in the New Hebrides arc are investigated. Several complex tectonic features are interpreted by using a simple mechanical model and the effect of buoyant forces associated with low density ridges. It is concluded that subduction of aseismic ridge can have significant effects on tectonic features at converging plate edges.

In the third chapter, seismicity at five regions of aseismic ridge subduction around the world are studied. A coherent change in seismicity pattern is found near the ridge-arc intersections. This observation is discussed as a consequence of aseismic ridge subduction.

Chapter 1

THE FOCAL MECHANISM AND SOURCE CHARACTERISTICS OF THE NEW HEBRIDES EARTHQUAKE OF JANUARY 19, 1969 AND SOME RELATED EVENTS -- SUBDUCTION PROCESS OF A FRACTURE ZONE AND ASEISMIC RIDGES

INTRODUCTION

Within the framework of plate tectonics, earthquake activity near converging plate boundaries has been explained as a consequence of interaction between plates. Investigation of earthquake focal mechanisms and seismicity patterns provides valuable information about the nature of plate interaction, deformation, and consequent strain release at plate boundaries. In most models of plate interaction used previously, oceanic plates are considered to be homogeneous and isotropic. However, oceanic plates are far from uniform; features such as fracture zones, sea mounts, and aseismic ridges are frequently seen on the oceanic lithosphere. Because of this heterogeneity, different parts of the oceanic plate may behave differently in subduction and plate interaction processes. For instance, an aseismic ridge usually has a lower density compared to other portions of the oceanic plates. Structural roots have been found under uplifted features on the oceanic floor indicating that such regions have densities intermediate between oceans and continents (Den et al., 1971; Ludwig et al., 1973; Kelleher and McCann, 1976). Because of their lower density compared to normal oceanic lithosphere, aseismic ridges may tend to resist subduction or subduct in a different way. Previous workers have suggested that the subduction process seems to be modified and the geometry of plate boundary can be affected by subduction of aseismic ridges because of the associated buoyant force. Vogt (1973) and Vogt et al. (1976) studied the effect of ridge subduction on the shape of the overriding island arc and the associated seismicity. They found that aseismic ridges often trend into cusps

or irregular indentations in the trace of the subduction zone. They also found that a region of reduced seismicity seems to be associated with many consumed ridges. Kelleher and McCann (1976) found that at locations where bathymetric highs, or aseismic ridges intersect with active trenches, large shallow earthquakes occur less frequently and have generally smaller rupture lengths than events along adjacent segments of the plate boundary. In this paper, the interaction between a trench and a subducting ridge-fracture zone system and its consequent tectonic movements and earthquake source characteristics are investigated through a detailed study of the New Hebrides earthquake of January 19, 1969 (origin time: $18^h50^m52.4 \pm 0.37^s$ GCT; latitude 14.89 ± 0.021°S, and longitude 167.22 ± 0.018°E), earthquake focal mechanisms, seismicity as well as tectonic features in the New Hebrides island arc. The New Hebrides earthquake of January 19, 1969 (hereafter called the New Hebrides earthquake) appears to be an abnormal event because of its unusual wave-forms with prominent excitation of long period waves. Seismological data and tectonic setting suggest that the earthquake occurred on the subducted portion of the D'Entrecasteaux fracture zone, which has a topographic ridge (or aseismic ridge) on each side of it. Detailed analysis of this event will therefore not only improve our understanding of the source of this unusual earthquake but also provide important clues to the subduction process of fracture zones and aseismic ridges.

REGIONAL SETTING OF THE NEW HEBRIDES ISLAND ARC

The New Hebrides island arc is a member of the western Pacific

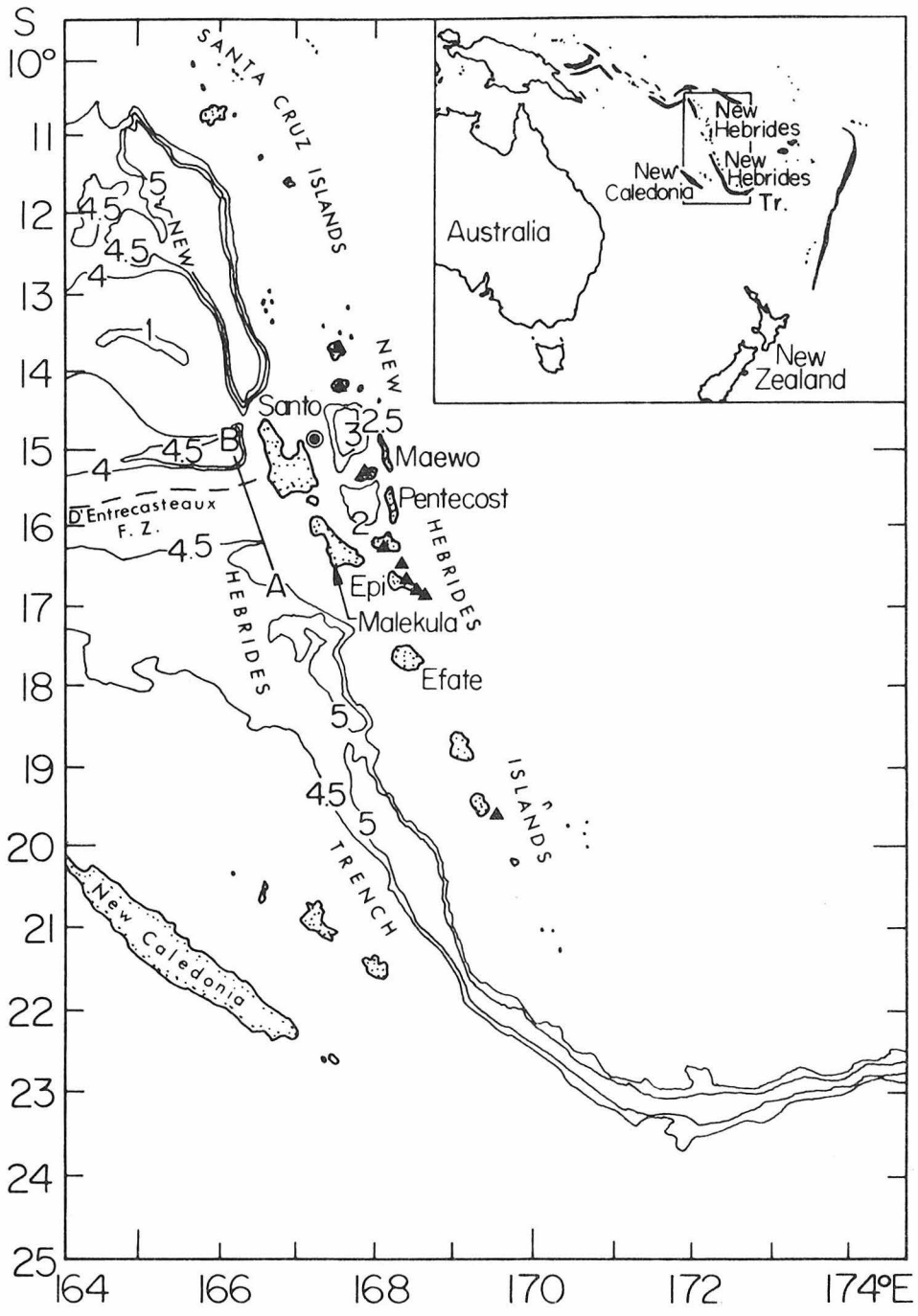

Figure 1.1. The New Hebrides Island arc system and related features. ⊙ is the epicenter of the January 19, 1969 earthquakes; ▲ represents historically active volcano. Submarine contours are in kilometers. The dashed line shows approximately the trace of the fracture zone.

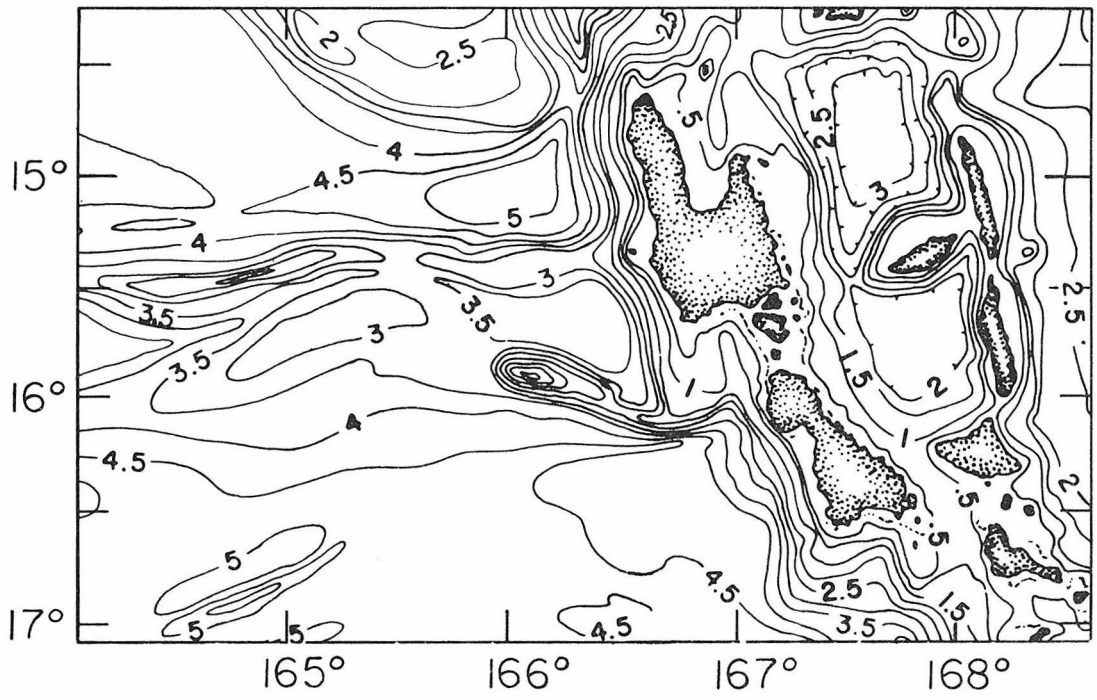

Figure 1.2. Bathymetry of the New Hebrides island arc and its vicinity. Contour interval is 0.5 km (after Chase, 1971).

island arc system characterized by high seismicity and intense volcanic activity. With its center at about 16°S and 168°E (Figure 1.1), the New Hebrides arc extends south from the Santa Cruz Islands at 11°S to the islets Methew and Hunter at 22°S. The dip of the subducted plate steepens very rapidly under the New Hebrides arc compared with many other island arcs; the Benioff zone dips toward ENE with a dip angle of about 70° (Santo, 1970; Dubois, 1971), in contrast with those of most of the western Pacific island arcs which dip toward the west. Earthquake swarms are very common; shallow shocks often occur closely both in time and space (Santo, 1970). The most remarkable feature of this island arc is perhaps the discontinuity of the New Hebrides Trench in the central New Hebrides (Figures 1.1 and 1.2) where a transverse feature called D'Entrecasteaux fracture zone (Mallick, 1973; Luyendyk et al., 1974) with a topographic ridge on each side of it intersects the island arc. Despite the interruption of the trench, earthquakes occur to depths of at least 250 km under the entire length of the arc system suggesting that the two trench sections belong to a single subduction zone or a single island arc system. The ridges associated with the D'Entrecasteaux fracture zone are aseismic ridges and are distinct from seismically active mid-oceanic ridges. There are several kinds of aseismic ridges on the sea floor, for example hot-spot traces (Wilson, 1965; Morgan, 1971, 1972, 1973), fracture ridges (Menard and Chase, 1970), or remnant arcs (Karig, 1972). The ridges discussed in this paper are the kind associated with a fracture zone or fracture ridges. Figure 3 shows the bathymetry and gravity along line AB on Figure 1.1, perpendicular to the D'Entrecasteaux

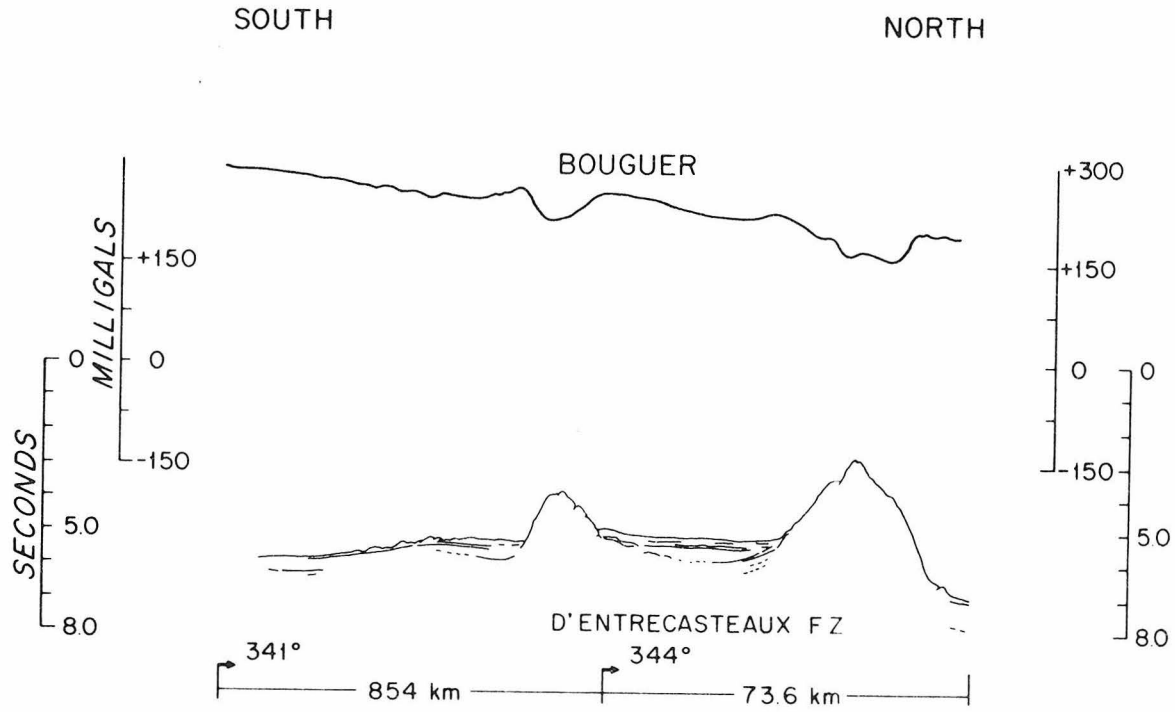

Figure 1.3. Bougar anomaly and two-way travel time from surface to ocean bottom of seismic wave across line AB of Figure 1. (after Luyendyk et al., 1974).

fracture zone. Bouguer gravity anomalies show relative minima of about 30 to 40 milligals over the crests of the ridges suggesting low-density structural roots under the ridges. More details about the geological setting and tectonic evolution of the New Hebrides island arc are given by Mitchell and Warden (1971), Karig and Mammerickx (1972), Mallick (1973), and Luyendyk *et al.* (1974).

SPECIAL CHARACTERISTICS OF THE BODY AND SURFACE WAVES

The New Hebrides earthquake had a focal depth of 107 km and m_b = 6.4 according to our redeterminations (m_b = 6.2 according to I.S.C. Bulletin). This earthquake is remarkable for its unusual wave-forms with prominent long period body waves and surface waves which are rare for intermediate earthquakes of comparable depth and m_b. The difference is apparent in Figure 1.4. In this figure seismograms of the New Hebrides earthquake recorded at Pasadena, California by three types of seismographs having different pass bands are compared with those of intermediate-depth earthquakes from other regions. The seismographs used are the Benioff short period (1-0.2), the long-period Benioff (1-90) and the Press-Ewing seismograph (30-90) which sample seismic wave energies at high, intermediate and low frequency bands respectively. In order to demonstrate the difference in the excitation at different periods between different events, the maximum amplitude of direct P of the Benioff 1-90 records for all the events is normalized to a common value while the amplitude ratio between different kinds of seismograms for each event is preserved. The ratio of the maximum amplitudes of long period record to short period record for the New

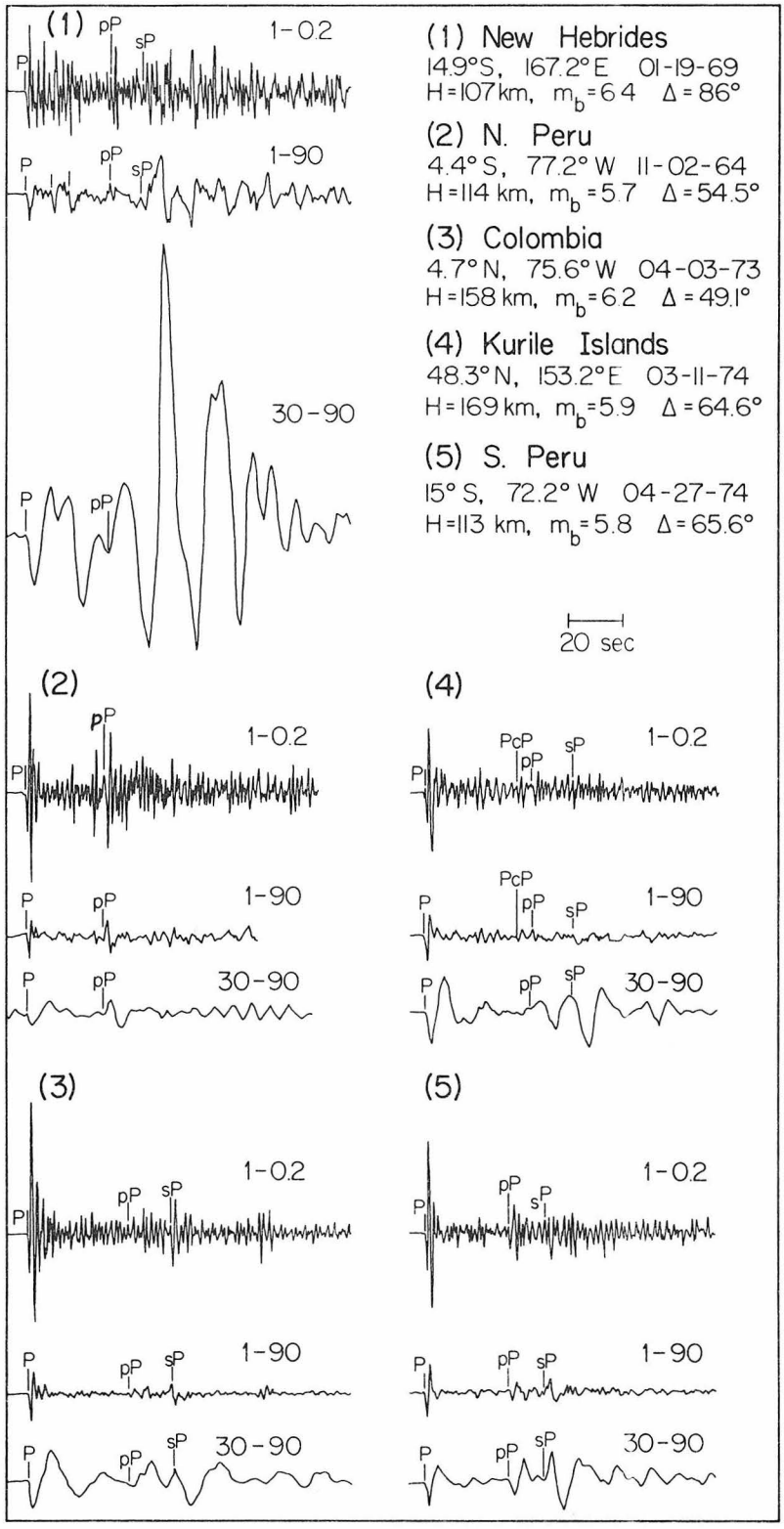

Figure 1.4. A comparison of the New Hebrides intermediate-depth earthquake with other intermediate events occurring in other seismic zones. All the seismograms are normalized vertical components recorded at Pasadena, California.

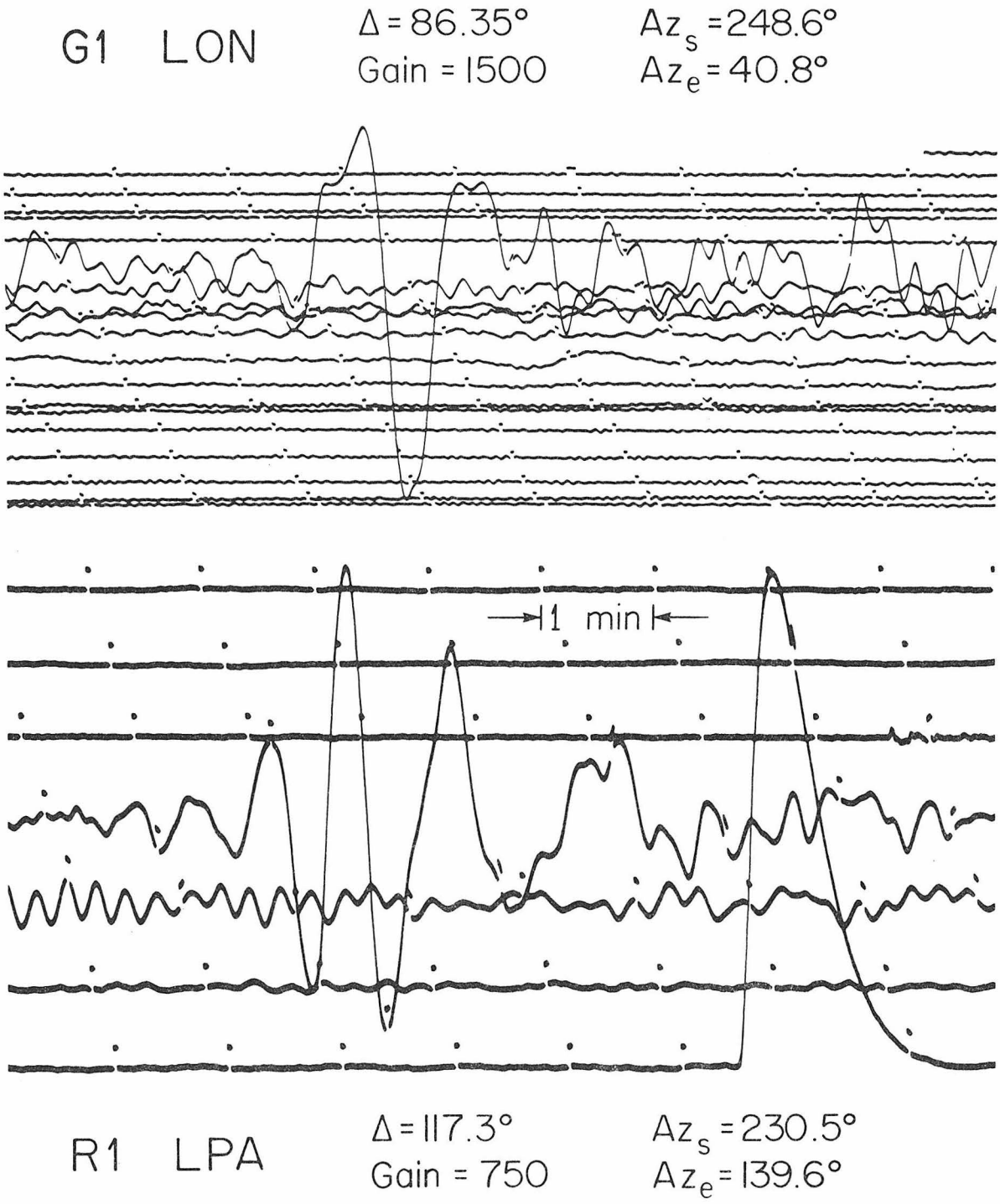

Figure 1.5. Love waves, G1 and Rayleigh waves, R1 recorded by the long-period seismographs at LON and LPA respectively.

Hebrides earthquake is about 30 times greater than that of the November 2, 1964 event which occurred in North Peru and is, on the average, more than one order of magnitude larger than the other four events. The long duration of the seismogram of the New Hebrides event is also notable. This long duration of the seismogram indicates that the earthquake is a very complicated multiple event. The unusual wave-form cannot be attributed to the crustal effect under the recording station because the wave-form for other earthquakes is relatively simple. The New Hebrides earthquake also generated long period surface waves of about 80 to 100 sec which were recorded by all the WWSSN stations; most intermediate shocks with comparable m_b usually excite small or undetectable surface waves. Figure 1.5 displays two sample records of G1 and R1 from the earthquake.

FAULT PLANE SOLUTIONS AND ALIGNMENT OF EARTHQUAKE HYPOCENTERS

The fault plane solution of the New Hebrides earthquake is constrained very well, as shown in Figure 1.6. Twenty-seven P-wave first motions from the long period WWSSN records and one first motion from the Press-Ewing seismogram at Pasadena are used. Fifteen P-wave first motions reported in the I.S.C. Bulletin are also used. The focal depth reported by I.S.C. is 114 ± 3.6 km. Comparison of the observed records with the synthetic seismograms of P and pP suggests a depth of about 100 km. In view of the uncertainty of the velocity structure in the vicinity of the source region we use the average focal depth, 107 km. If only P-wave first motions are used, the strike of the steeply dipping nodal plane can be moved by several degrees.

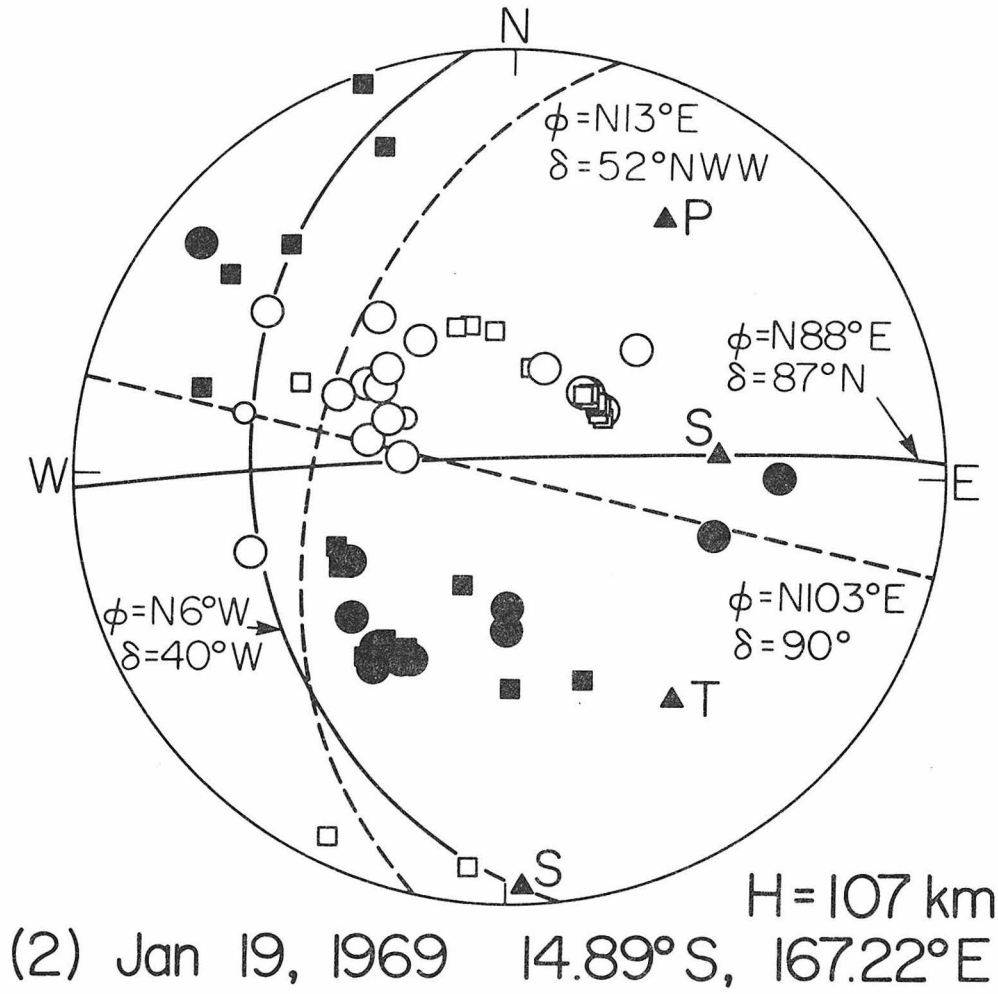

Figure 1.6. Equal area projection of P-wave first motions on the lower hemisphere. Open circles and squares represent dilations recorded by WWSSN stations and non-WWSSN stations respectively. Closed circles and squares represent compressions read from WWSSN and non-WWSSN stations respectively. Large symbols are more reliable data. Compressional and tensile axes, and slip vectors are represented by solid triangles with labels P, T, and S respectively. ϕ and δ stand for strike and dip angle respectively. The number at the lower left corner is the earthquake number used in Table 1.1. The solid curves represent the P-wave mechanism, while the dashed curves show the mechanism obtained from surface-wave data.

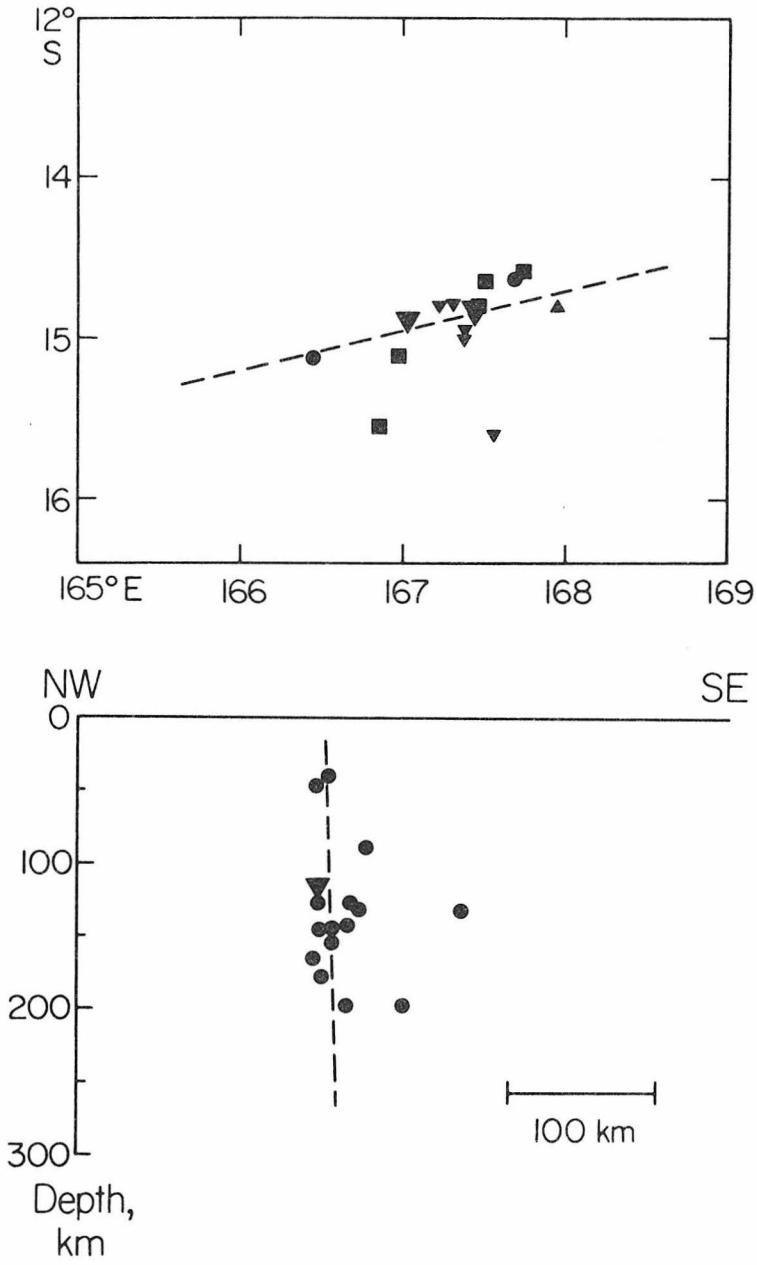

Figure 1.7. (a) Different symbols represent events of different depth (h) ranges: ●: 0 ≤ h < 50 km; ▲: 50 ≤ h < 100; ▼: 100 ≤ h < 150; ■: 150 < h < 200; ◆: 200 < h < 250. The large ▼ is the January 19, 1969 event. The dashed line shows the trend of the trend of the epicenter distribution. (b) Projection of all of hypocenters in (a) on a vertical plane perpendicular to the dashed line in (a).

However, this plane is further constrained by P-wave synthetic seismograms, as will be discussed later. The strike and dip of this plane are determined to be N88°E and 87°N respectively while the other nodal plane strikes N6°W and dips 40° to the west. Figure 1.7a shows the distribution of epicenters of earthquakes which occurred during the seven-month period after the New Hebrides event. The data are taken from the U.S.G.S. and I.S.C. catalogues. Their magnitudes range from 4.3 to 5.4. The overall distribution of the epicenters is along a trend with a strike of about N76°E which agrees well with that of the nearly vertical nodal plane of the New Hebrides earthquake (Figure 1.6). Figure 1.7b shows the projection of the same set of earthquake hypocenters onto a vertical plane perpendicular to the trend of the epicenters. The vertical alignment of the hypocenters suggests that the vertical EW striking nodal plane represents the fault plane of the New Hebrides earthquake.

INTERPRETATION OF FAR FIELD BODY WAVE SEISMOGRAMS

In order to investigate the details of the multiple shock sequence of the New Hebrides earthquake long period P wave seismograms recorded by the WWSSN are interpreted by using synthetic seismograms. Far field seismograms which include P, pP, and sP from a double couple or shear dislocation point source in a homogeneous half space are synthesized by using the method described in Langston and Helmberger (1975) and Helmberger (1974). The upper part of Figure 1.8 shows a sample of the long period WWSSN records. The lower part of the figure is a synthetic seismogram from a point source having a ramp dislocation with a rise

time of 3 sec and a depth of 100 km. For the velocity in the half space, we used the velocity obtained from the Jeffreys structure by averaging the velocity over the depth range from 0 to 100 km. The approximate agreement of the pP and sP wave-forms suggest that the depth of 100 km is reasonable. When the fault plane is nearly vertical, as in the case of the New Hebrides earthquake, sP is the predominant phase on the far field record. From Figure 1.8 it is obvious that a single source cannot explain the observed seismogram. The total duration of the synthetic P, pP and sP is only about 50 sec, while the duration of the observed seismogram is as long as 80 sec suggesting a rupture duration as long as 30 sec. We try to fit the first 14 sec of the vertical long period records, which are free from the contamination of pP and sP of the first event, by using two point sources with ramp dislocations placed at the same location. The method of matching the wave-form with the synthetics is similar to that described by Chung and Kanamori (1976). The fault plane solution of the first event is further constrained by simultaneously fitting the wave-forms at nine stations (ANP, BKS, CHG, COR, GUA, MUN, RAR, SHK and TAU [Figure 1.9 and Table 1.1]). The azimuthal coverage of the station is reasonably good. The pulse that follows the first one with the same polarity is interpreted as the second event. In fitting the wave-form of the second event, we first used the same focal mechanism as the first event and then slightly adjusted it to obtain a better fit. Figure 1.9 compares the observed record with the synthetics computed for the first two events. The source parameters of the first and second events are determined as

TABLE 1.1

Station	Δ	AZ_{es}	AZ_{se}	First motion	Waves Used		
AAE	129.30	269.55	101.80			G	R
ADE	32.47	226.86		C	P		
AFI	20.38	89.89		C	P		
AKU	129.10	2.83	353.40			G	R
ANP	59.74	311.36	126.80	D	P	G	R
ANT	111.87	123.50	241.60			G	R
BAG	55.55	302.23		D	P		
BHP	114.60	86.85	257.70			G	R
BKS	84.35	48.58	246.40	D	P		R
BMO	90.42	43.53		D	P		
BRW	89.41	10.94		D	P		
BUL	126.40	230.60	127.40			G	R
BUT	93.95	43.51		D	P		
CHG	75.04	294.41	111.70	D	P	G	R
COL	86.53	17.59	223.24	D	P	G	R
COR	86.38	42.12	245.15	D	P	G	R
CTA	20.63	252.52		D	P		
DAV	46.69	295.04		D	P		
CUR	89.50	48.91		D	P		
FGU	94.74	49.06		D	P		
GCA	91.98	52.37		D	P		
GDH	120.00	15.58	313.25			G	R
GRM	119.10	217.43	135.43			G	R
GUA	35.84	320.95	141.23	D	P		
HHM	93.71	40.98		D	P		
HKC	63.76	304.42	120.55	D	P	G	R
HNR	8.93	306.67		C	P		
KIP	49.67	44.20		D	P		
KOD	92.33	270.90	104.62	D	P		R
KON	132.40	344.80	29.96			G	R
KOU	6.28	205.87		D	P		
KRK	119.11	344.25	48.83			G	R
KTG	124.21	3.73	349.25			G	R
LMP	1.62	159.21		C	P		
LON	88.20	40.60	246.14	D	P	G	R
LPA	114.52	140.20	228.90			G	R
LPB	117.11	117.63	243.25			G	R
LOR	144.90	340.17	28.80			G	R
MAL	157.00	342.53	21.17				R
MMA	90.69	55.54		D	P		
MUN	49.32	240.55	82.15	C	P	G	R
NAT	149.70	130.32	227.80			G	R
NAI	128.39	256.21	110.09			G	R
NOU	7.40	185.39		D	P		

TABLE 1.1 - continued

Station	Δ	AZ_{es}	AZ_{se}	First motion	Waves Used		
PAS	86.00	53.29		D	P		
PEL	107.00	132.01	238.90			G	
PRE	123.20	225.04	130.66			G	R
PVC	3.02	159.44		C	P		
QUI	113.37	96.79	253.75			G	R
RAB	18.23	304.22		D	P		
RAR	31.98	106.21		C	P		
RIV	23.79	214.77		C	P		
SAV	31.84	209.05		C	P		
SBA	62.97	180.10	0.43	C	P	G	R
SHA	110.00	62.43	264.15			G	R
SHK	59.10	326.96	140.30	D	P	G	R
SHL	83.59	298.45		D	P		
SLD	84.78	49.64		D	P		
SNG	69.54	283.63		D	P		
SPA	75.69	180.00	12.80	D	P	G	R
STU	141.66	336.36	35.86			G	R
TAU	32.72	207.53	37.46	C	P		R
TOO	29.67	216.42		C	P		
TUC	91.27	57.02	253.20	D	P	G	R
UNM	98.13	72.19	257.09				R
VAL	143.00	357.40	4.10			G	R
WIN	132.63	218.77	139.10			G	R

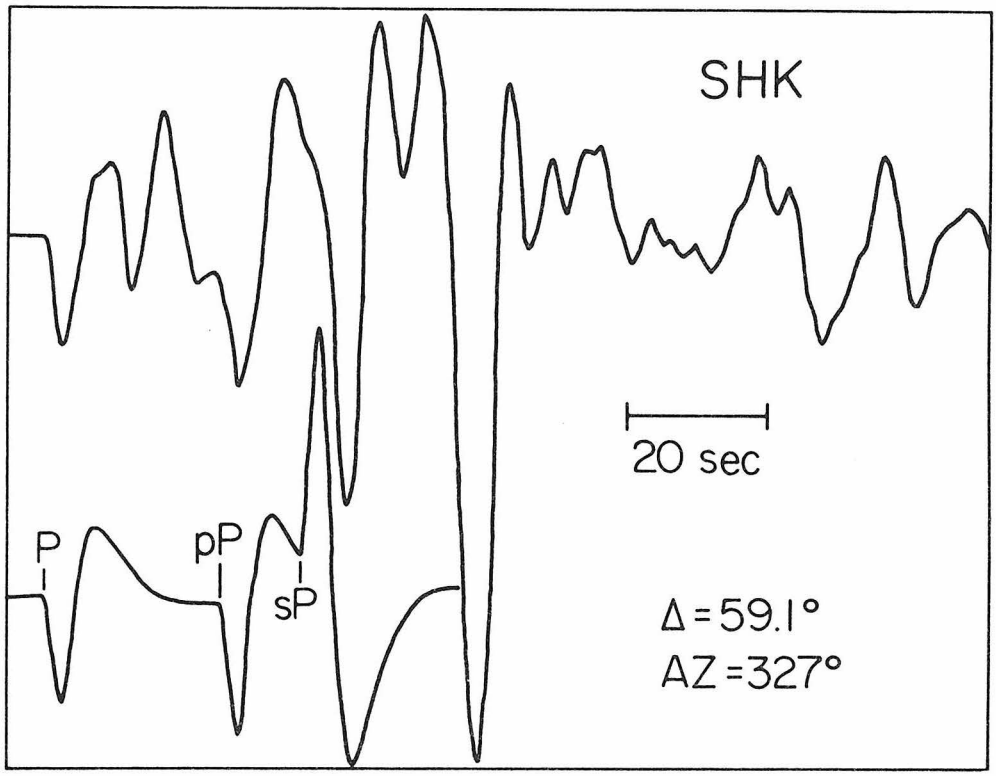

Figure 1.8. A comparison of the observational record of the New Hebrides event recorded at SHK with a synthetic seismogram. The New Hebrides earthquake appears to be a very complicated multiple shock.

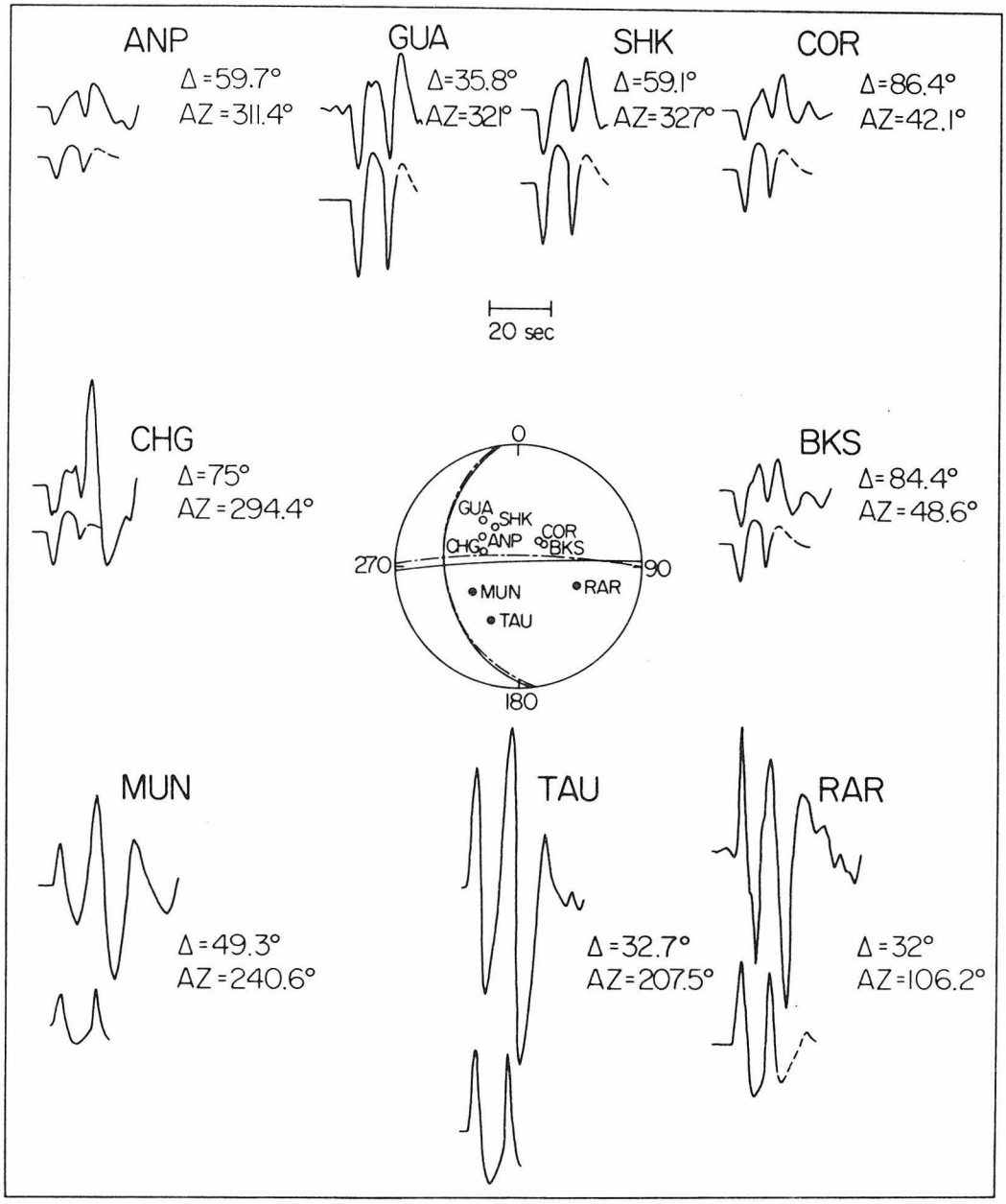

Figure 1.9. Observed P-wave forms (upper traces) and matched synthetics (lower traces). Only the first 14 sec (before the first pP arrival) are matched. The fault plane solutions of the first and the second shocks are presented by solid and dashed curves, at the center, respectively. Close and open circles give the locations and first motions of the nine stations used.

follows: strike ϕ_1 = N88°E, ϕ_2 = N91°E; dip angle δ_1 = 87°N, δ_2 = 83°N; slip angle λ_1 = 50°, λ_2 = 50°; seismic moment m_{01} = 1.8 x 10^{26} dyne-cm, m_{02} = 2.3 x 10^{26} dyne-cm; rise-time τ_1 = 3 sec, τ_2 = 2 sec. The difference in the origin time between the first and the second shock is about 10.5 sec. Since the accuracy of the determination of rise time is about one second, the difference between τ_1 and τ_2 is of marginal significance. The above result suggests that after the first break a larger fracture took place with a slight change in the strike direction. It was further followed by more energetic ruptures which appear as the large swings in the later part of the records (Figure 1.4 and Figure 1.8). The seismic moments of the later events seem to be even larger than those of the first two. This is similar to the case of the Spanish deep focus earthquake of 1954 (Chung and Kanamori, 1976).

SOURCE PARAMETERS AND RUPTURE PROCESS FROM SURFACE WAVES

An important set of data of the earthquake comes from long period surface waves, G1 and R1, which are recorded at many WWSSN stations with a good azimuthal coverage. Long period surface waves provide reliable information about the overall characteristics of the source. In this paper the gross source parameters and faulting process of the New Hebrides event are extracted from surface waves by using the method described in Kanamori (1970a) (see also Kanamori and Cipar, 1974; Kanamori and Stewart, 1976; Saito, 1967). The vertical components of Rayleigh waves are windowed between group velocities of 3.23 and 4.35 km/sec while the two horizontal components of Love waves are

windowed from 3.71 to 4.76 km/sec, and are combined to obtain the transverse component. After low pass filtering is applied to remove the components with periods shorter than 40 sec the seismograms are equalized to a distance of 90° and to a magnification of 1500. The earth model 5.08 M (Kanamori, 1970b) and Q values in Figure 14 of Kanamori and Stewart (1976) (which is based on the data of Smith, 1972 and Tsai and Aki, 1969) were used in the above equalization and the later synthesis of surface waves. For intermediate-depth events, the waveform of Love waves is sometimes complicated by higher modes, especially for a pure dip-slip source. However, for a source with large strike slip component at a depth of about 100 km, as in the case of the New Hebrides earthquake, the excitation of all the higher mode Love waves is much smaller than those of the fundamental mode (Fukao and Abe, 1971). Thus the higher-mode contribution is neglected in our analysis. In fact, as will be shown later, the actual waveforms can be closely approximated by synthetic seismograms consisting of only fundamental modes. Figures 1.10 and 1.11 show the equalized R1 and G1 respectively. The radiation patterns of the maximum peak to peak trace amplitude are shown by the circular plots at the center. The radiation pattern is two-lobed for Rayleigh waves and four-lobed for Love waves. The maximum amplitude of Love waves is slightly larger than that of Rayleigh waves. The difference in the group arrival times and the waveform from one station to another reflects the regional variation of velocity and Q structure. In order to interpret these data, synthetic seismograms are computed for a point source at a depth of 107 km with a step dislocation and the

focal mechanism determined from the P-wave data. As shown in Figure 1.12, neither the lobe-direction nor amplitude ratio of G1 to R1 can be explained by this source model. Starting from this model, a better model was sought by changing the strike azimuth, slip vector and dip angle slightly. We found that a mechanism with fault strike = N103°E, dip angle = 90° and slip angle = 38° can explain the data reasonably well (Figures 1.13 and 1.14). A seismic moment of 5×10^{26} dyne-cm is obtained. This moment is relatively large for earthquakes of comparable magnitude. As shown in Figure 1.6, this mechanism is considerably different from the P-wave mechanism. Since P-waves and surface waves carry information at different periods, the surface-wave mechanism should not necessarily be identical to the P-wave mechanism. In particular, for a complex event such as the New Hebrides earthquake in which the first event is relatively small, it is not surprising that the overall mechanism represented by surface waves is considerably different from that of the very beginning of the rupture.

The seismic moment determined from surface waves is only slightly larger than the sum of the moments of the first two events. Since the body waves from later events are very large (Figures 1.4 and 1.8), one would expect a much larger surface-wave moment than the sum of the first two events. However, this discrepancy is not surprising in view of the uncertainty in the determination of body-wave moment; a factor of 2 to 4 scatter is not uncommon.

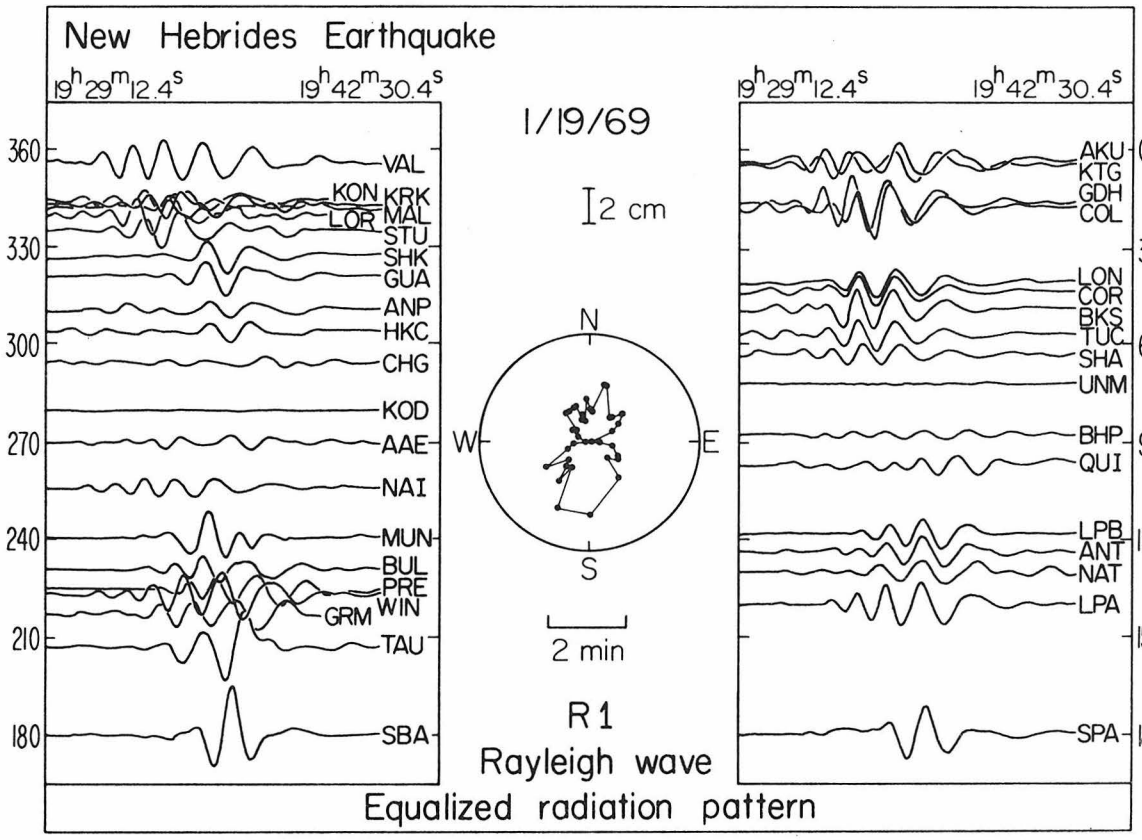

Figure 1.10. Rayleigh waves (R1) equalized to a propagation distance of 90°. The vertical scale gives the amplitude on the standard 15-100 seismogram with a magnification of 1500. Upward motion is taken positive.

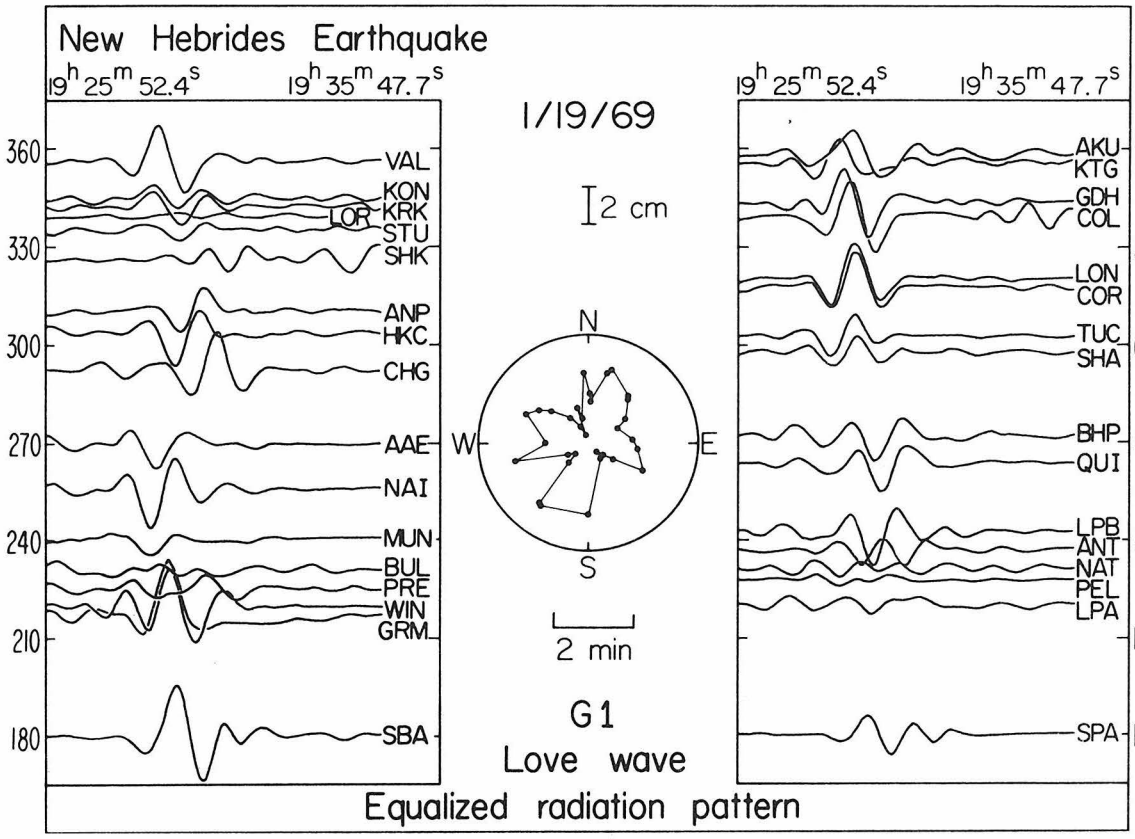

Figure 1.11. Love waves (G1) equalized to a propagation distance of 90°. The vertical scale gives the amplitude on the standard 15-100 seismogram with a magnification of 1500. Clockwise motion around the source is taken positive.

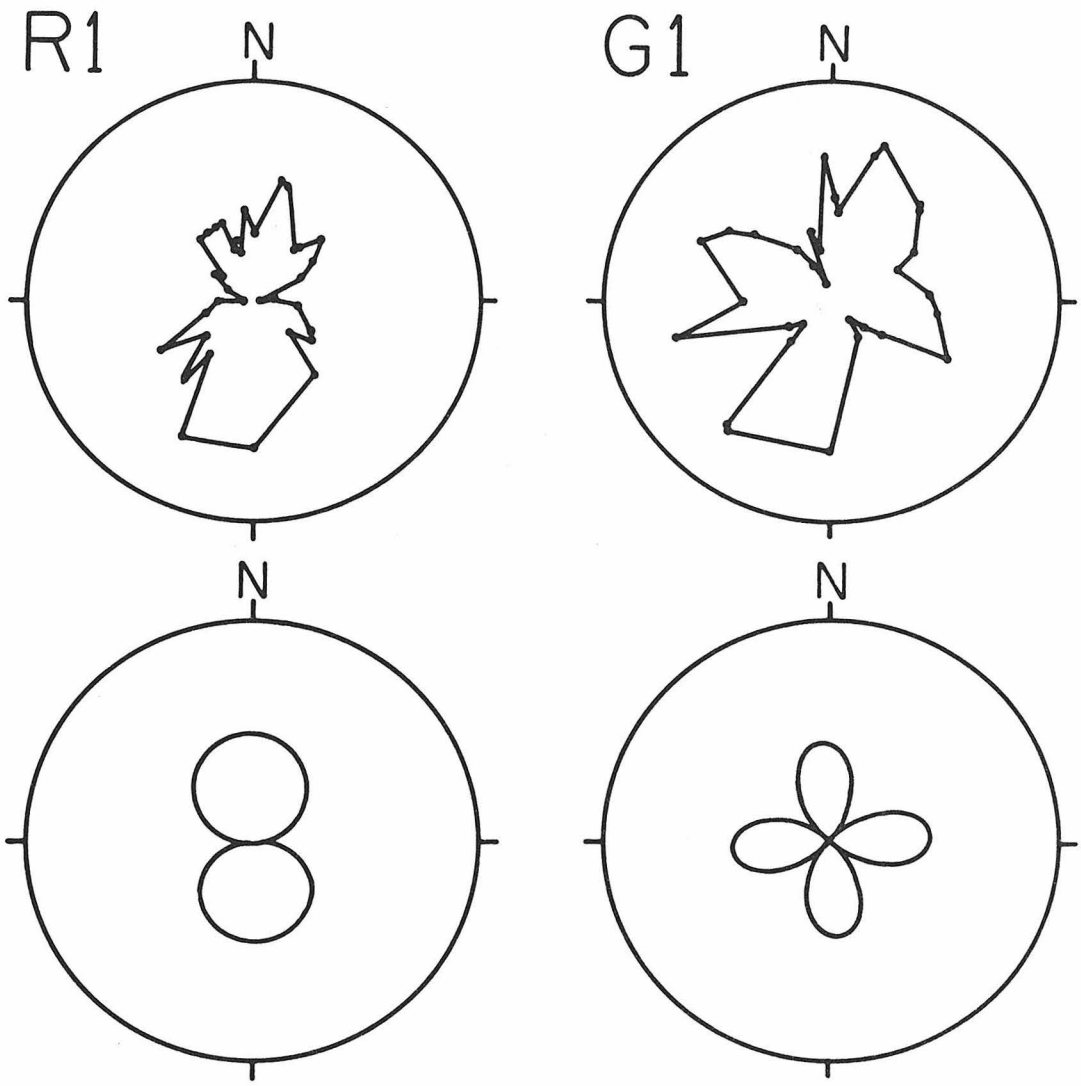

Fiugre 1.12. A comparison of the observed radiation patterns of R1 and G1 (top) with the synthetic patterns (bottom) generated from a point source with a step dislocation and the focal mechanism determined from P-wave data.

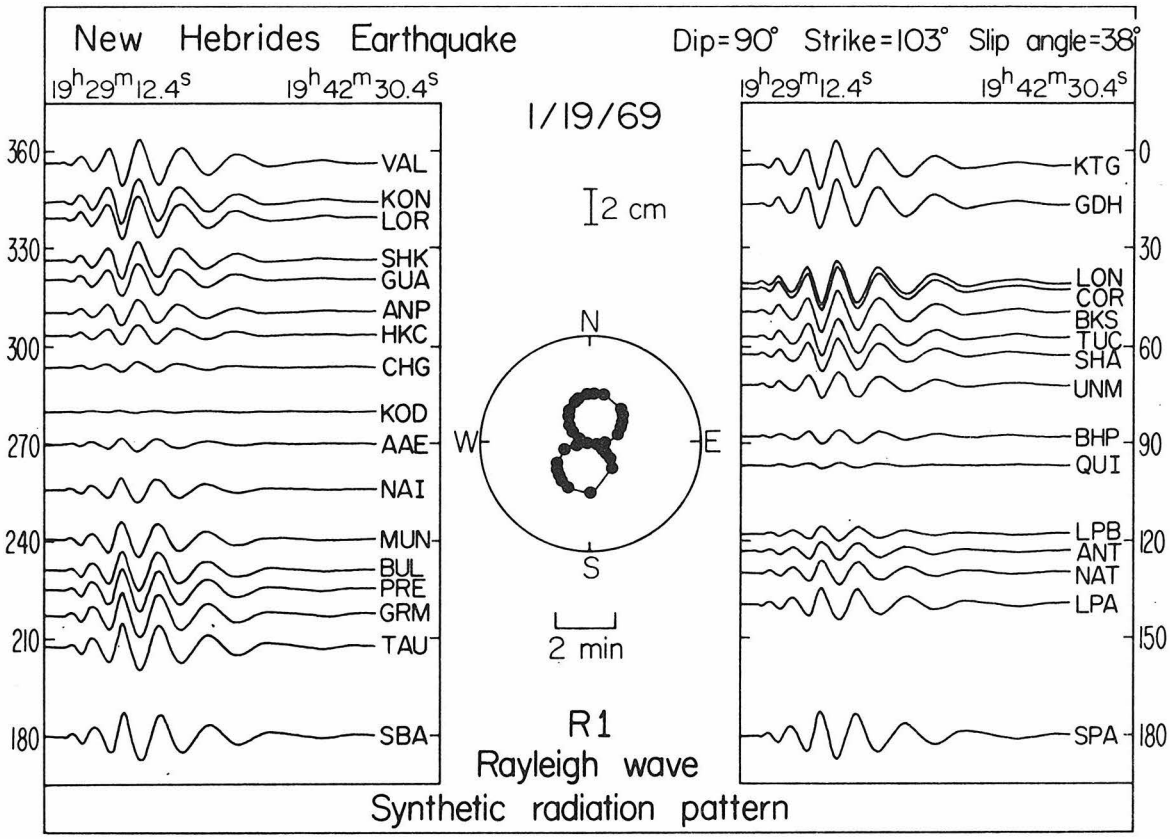

Figure 1.13. Synthetic Rayleigh waves (R1) at a propagation distance of 90°. The vertical scale is the same as that in Figure 10.

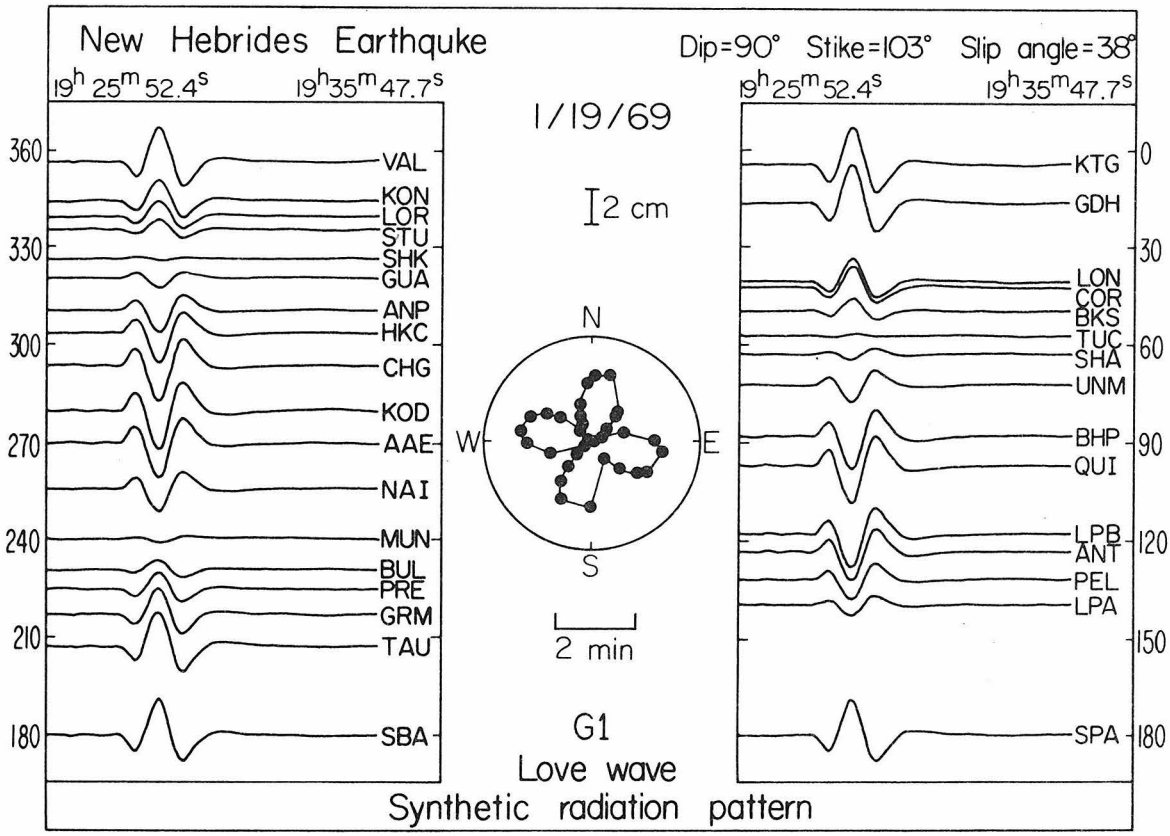

Figure 1.14. Synthetic Love waves (G1) at a propagation distance of 90°. The vertical scale is the same as that in Figure 11.

SPATIAL DISTRIBUTION OF TWO EARTHQUAKE SWARMS

As shown in the previous sections, the New Hebrides earthquake occurred on the extension of the subducting D'Entrecasteaux fracture zone and its fault motion has a large strike-slip component, in the down-dip direction of the Benioff zone, on a vertical fault plane parallel to the fracture zone. This mechanism suggests that the D'Entrecasteaux fracture zone structurally extends to the east of the trench, the earthquake representing displacement along the subducted portion of the fracture zone. Vertical fault-like features within the subducted plate in this area has been pointed out by Isacks and Barazangi (1977), Chung and Kanamori (1977), and Isacks et al. (1977). It is interesting to note that two earthquake swarm activities one from July 23 to October 4, 1965 and the other from December 28, 1973 to February 14, 1974 are spatially bounded by a parallel at 15.2°S, the extension of the D'Entrecasteaux fracture zone (Figure 1.15). It is possible that this sharp boundary is a surface manifestation of the structural boundary in the subducted fracture zone at depths.

SEISMICITY PATTERN ASSOCIATED WITH RIDGE SUBDUCTION

Kelleher and McCann (1976) studied the distribution of great shallow earthquakes along subduction zones and their relations with aseismic ridges and bathymetric highs. They pointed out that the zones where aseismic ridges intersect with active trenches are characterized, in many instances, by gaps of intermediate depth hypocenters. Vogt et al. (1976) studied the effect of subduction of aseismic ridges on seismicity and found that a region of reduced

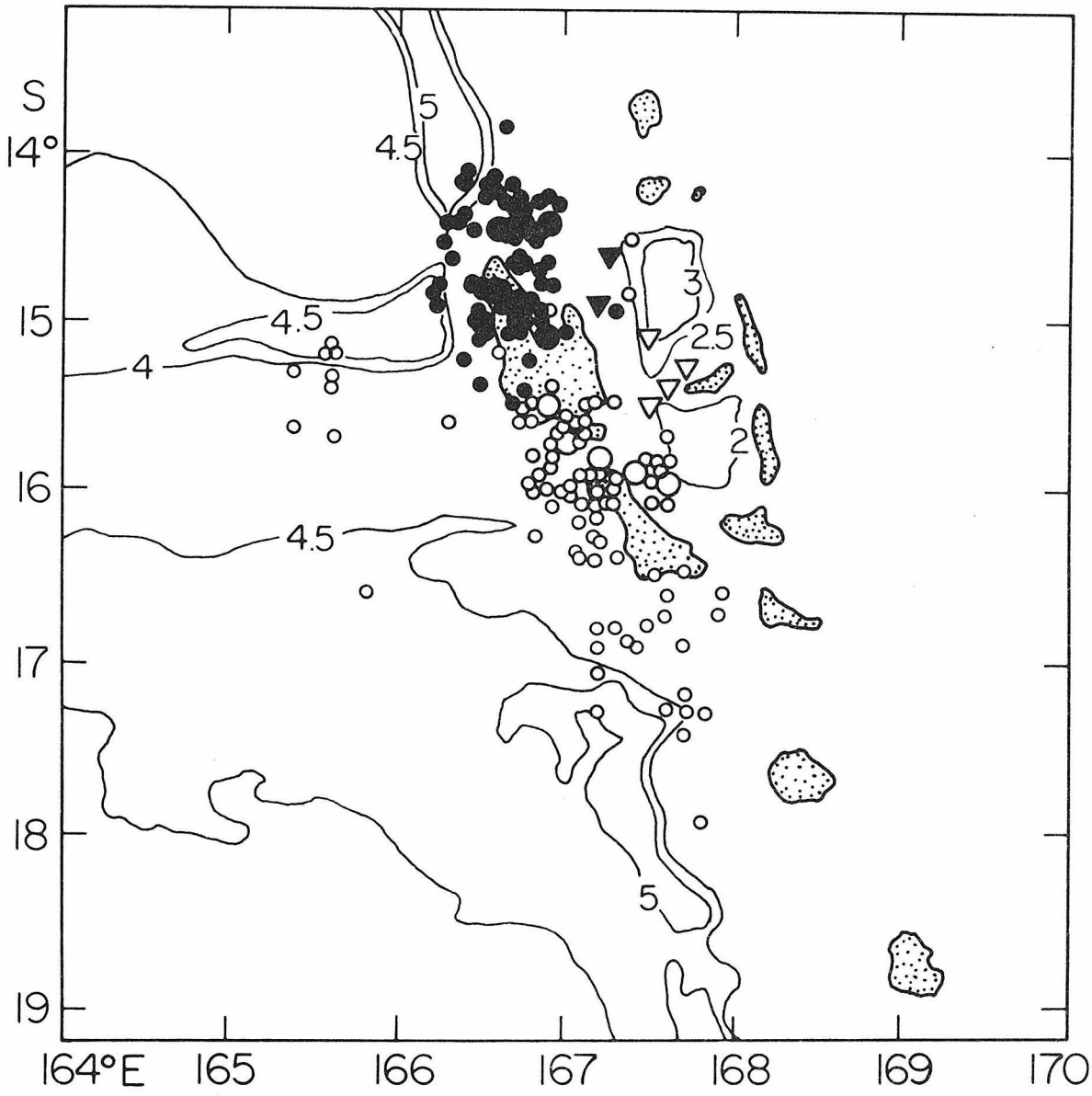

Figure 1.15. Closed and open symbols represent events of the swarms of 1973 and 1965 respectively, while circles and triangles stand for shallow and intermediate shocks, respectively.

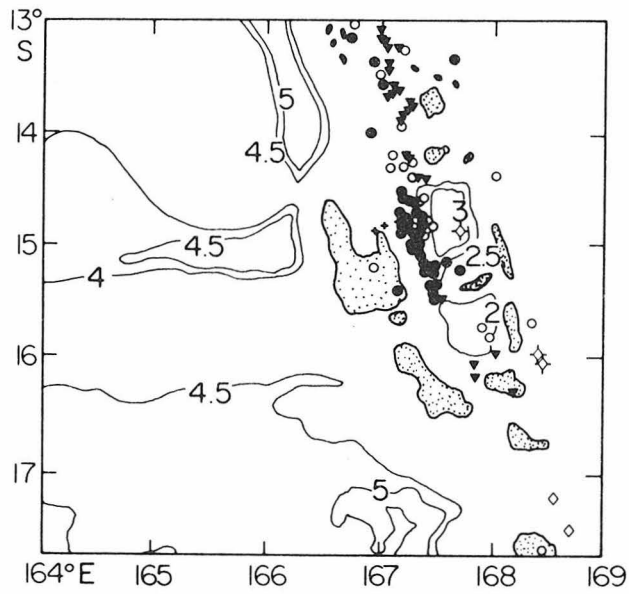

Figure 1.16. Different symbols represent events of different depth (h) ranges: +: 95 ≤ h < 110 km; ●: 110 ≤ h < 150; 0: 150 ≤ h < 180; ▼: 180 ≤ h < 220; ◆: 220 ≤ h < 230; ✧: 230 ≤ h < 270. Submarine contours are in kilometers.

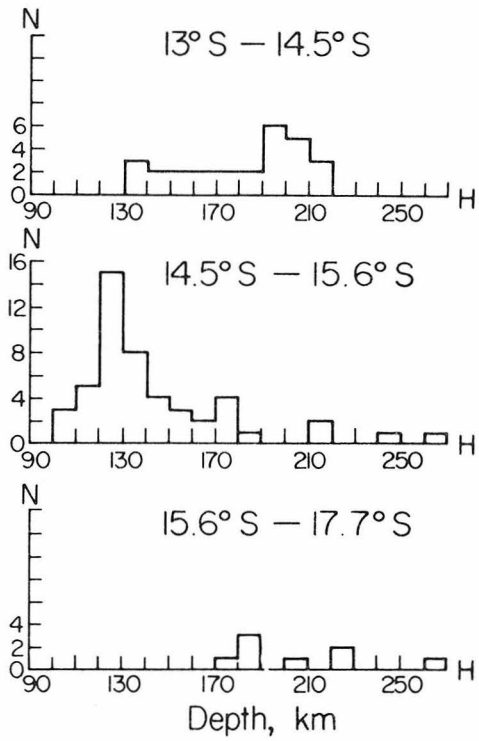

Figure 1.17. N and H represent number of earthquakes and focal depth respectively.

seismicity seems to be associated with many consumed ridges. Since the foregoing analyses suggest that the D'Entrecasteaux fracture zone is subducting beneath the New Hebrides arc, detailed analysis of seismicity in this region would provide further information regarding the nature of ridge subduction. Figure 1.16 shows the distribution of all the epicenters of intermediate events (focal depth between 90 to 270 km) which occurred in the period from December 1, 1970 to December 31, 1974 in the area. The data are taken from the U.S.G.S. and I.S.C. catalogues. We divide the region into three zones. Zone 1 is from 13 to 14.5°S, an area to the north of the ridge fracture zone system; zone 2 is 14.5 to 15.6°S, the extension of the ridge; and zone 3 is 15.6 to 17.7°S, an area to the south of the ridge. It is clear that the earthquakes on the extension of the ridges (zone 2) are shallower than those occurring to the north and to the south. Figure 1.17 presents histograms of the focal depth distribution in the three zones. The difference in the focal depth distributions between the zone along the ridge extension and those on the two sides of it is clear. The peak of the distribution is at 120 to 130 km in zone 2 while it is at a much larger depth in zones 1 and 3. It is also remarkable that the activity at the intermediate depth is very high in zone 2. The seismicity in this region has been also studied by Santo (1970). The seismicity pattern discussed above is clearly seen in Santo's (1970) Figure 6. Santo also noted that the dip angle of the Benioff zone is about 65° in the region where the trench is missing while it is 70° along most parts of the New Hebrides arc. We interpret that the lower dip angle of the Benioff zone suggests that the Benioff

zone is locally deformed or uplifted due to the upward pulling of the buoyant force while the relatively shallow depth of the seismic activity may be interpreted by a similar mechanism and/or by differential subduction near the location of ridge subduction with the lithospheres on the two sides of the D'Entrecasteaux fracture zone subducting faster than the portion with the ridges. An increase in resistance against subduction due to the buoyancy probably enhances the down-dip extensional stress in the slab causing higher seismic activity at the intermediate depth.

FOCAL MECHANISMS BETWEEN 14 and 16°S, THE NEW HEBRIDES ISLANDS, AND MODE OF STRAIN RELEASE ALONG A SUBDUCTING RIDGE-FRACTURE ZONE

Focal mechanisms of intermediate and deep earthquakes of the New Hebrides region that occurred between 1962 and 1968 have been studied by Isacks and Molnar (1971). Shallow earthquakes for the period from 1963 through part of 1969 have been investigated by Johnson and Molnar (1972). In this paper we made focal mechanism determinations for ten additional earthquakes that occurred in the central New Hebrides region, especially along the extension of the D'Entrecasteaux fracture zone. Figure 1.18 presents 22 fault-plane solutions (Tables 1.2 and 1.3); numbers 1 to 10 are new solutions of the present study while numbers 11 to 18 are taken from Johnson and Molnar (1972) and numbers 19 to 22 from Isacks and Molnar (1971). The first motion data of direct P used in our study are shown in Figure 1.19. Most of the first-motion data are read from the WWSSN long-period records. In some cases the data reported by I.S.C. and the WWSSN short-period

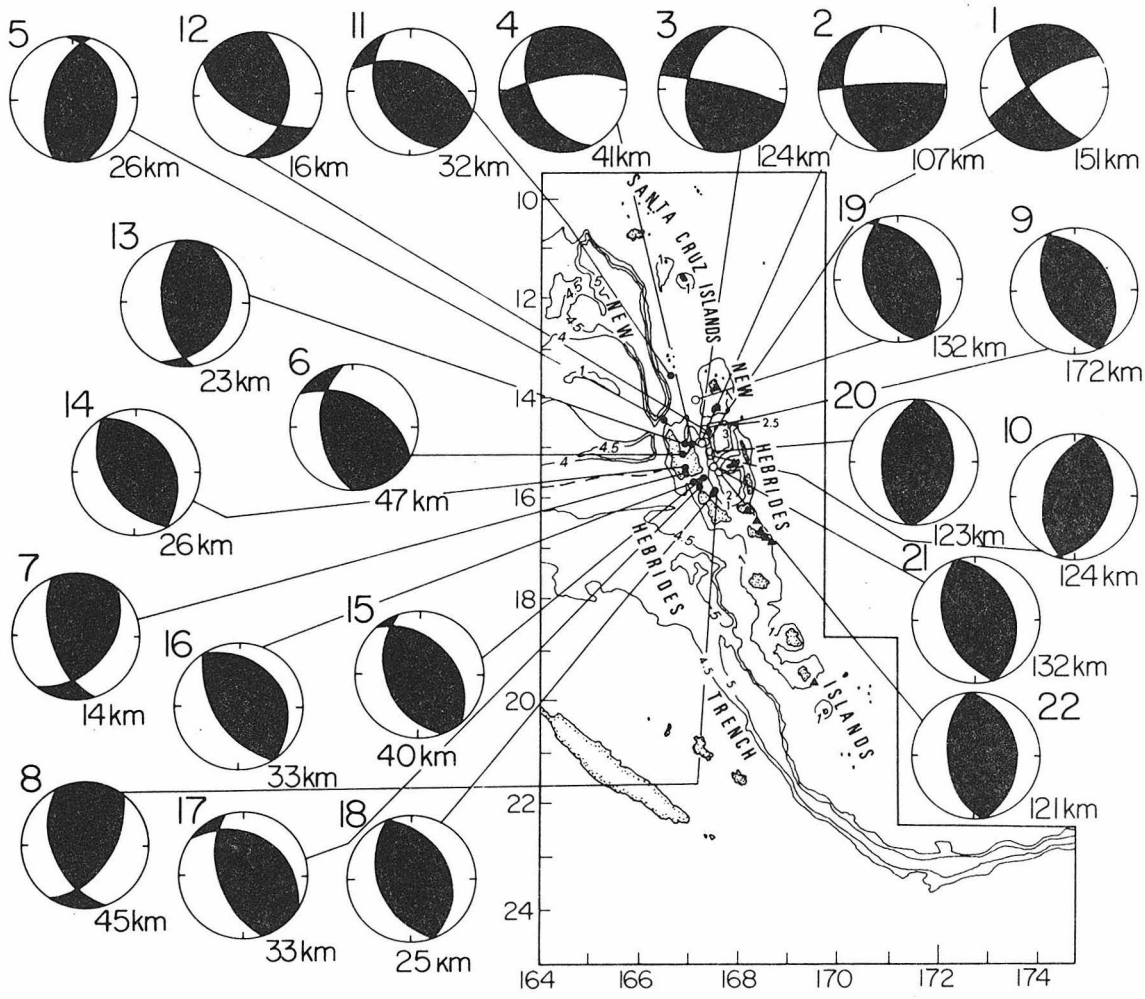

Figure 1.18. The dark quadrants are the P-wave compression first-motion quadrants on the lower hemisphere. Filled and unfilled circles represent shallow and intermediate events respectively. The numbers to the upper left and lower right of each fault plane solution are event number and focal depth of the corresponding earthquake respectively. See the caption of Figure 1.1 for the rest of the symbols and representation.

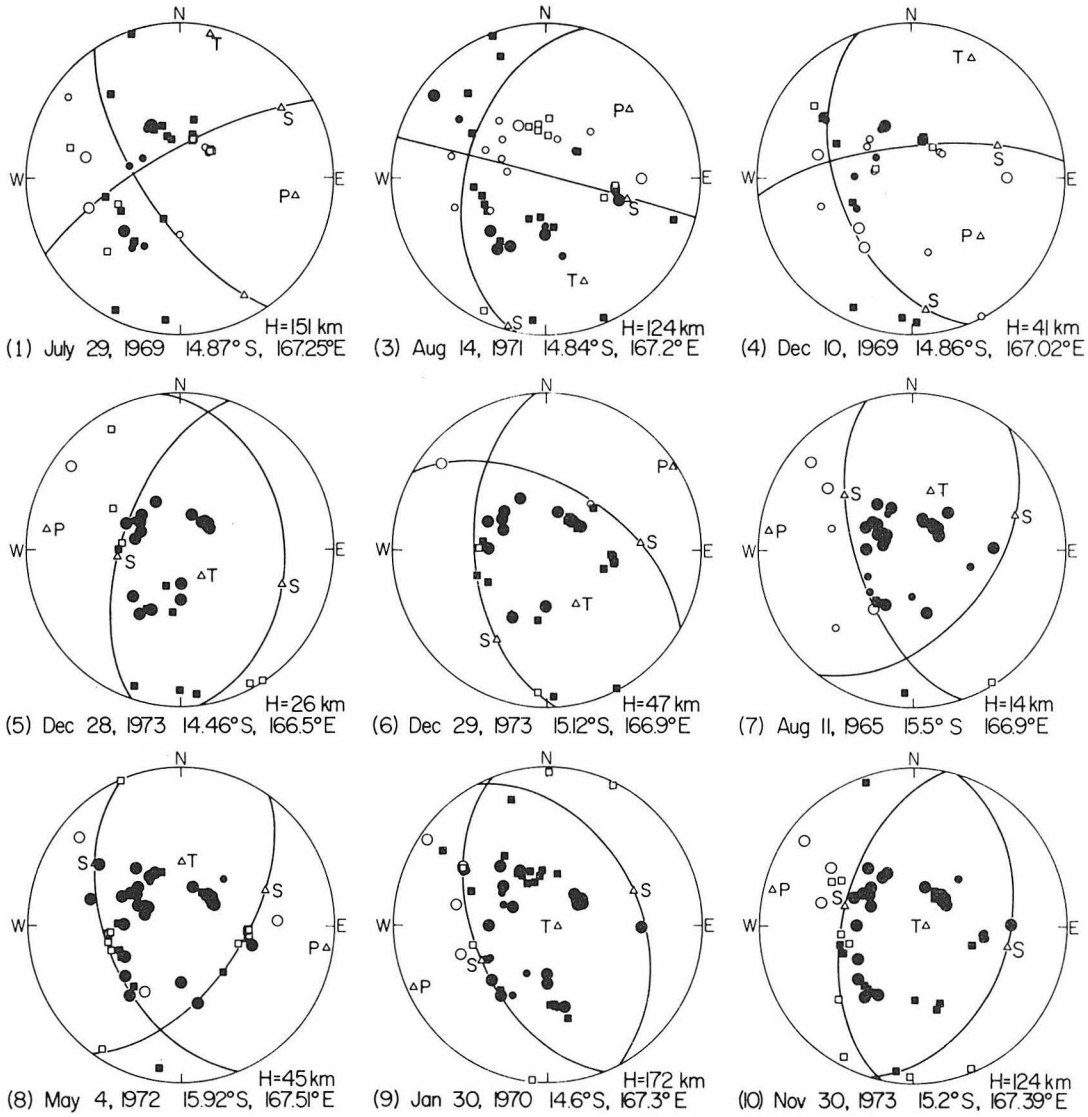

Figure 1.19. First motion data of P waves on the lower hemisphere for the focal mechanism solutions determined in this study. Symbols in this figure have the same meanings as those used in Figure 1.6.

TABLE 1.2

Event	Date	Location (°)	Depth (km)	Strike (°)	Dip (°)	m_b
1	July 29, 1969	14.87S 167.25E	151	240.7	76	5.3
				146.4	70	
2	January 19, 1969	14.89S 167.22E	107	268.0	87	6.4
				174.0	40	
3	August 14, 1971	14.84S 167.20E	124	284.5	89	5.5
				193.3	46	
4	December 10, 1969	14.86S 167.02E	41	263.8	73.5	5.5
				154.8	50	
5	December 28, 1973	14.46S 166.50E	26	354.0	33.4	6.4
			1	198.4	59.0	
6	December 29, 1973	15.12S 166.90E	47	175.9	51.1	6.2
				299.9	55.3	
7†	August 11, 1965	15.50S 166.90E	14	38.5	47.5	6.3
				161.5	59.3	
8	May 4, 1972	15.92S 167.51E	45	35.5	47.7	6.1
				158	49.7	
9	January 30, 1970	14.6 S 167.30E	172	158.4	50.0	5.7
				333.0	40.1	
10	November 30, 1973	15.2 S 167.39E	124	16.4	38.7	6.0
				192.2	51.4	

†Event 7 (this study) and event 14 (Johnson and Molnar, 1972) -- see Table 1.3 -- represent the same earthquake.

TABLE 1.3

Event	Date	Location	Depth (km)	Pole to Nodal Plane Azimuth	Plunge	
11	January 10, 1965	13.5S 166.6E	32	65	56	*
				199	36	*
12	May 20, 1965	14.7S 167.4E	16	34	28	*
				278	40	*
13	August 24, 1967	14.9S 166.9E	23	83	28	*
				290	60	*
14†	August 11, 1965	15.4S 166.9E	26	60	40	*
				240	50	*
15	November 12, 1966	15.6S 167.3E	40	70	42	*
				232	46	*
16	August 11, 1965	15.7S 167.1E	33	58	30	*
				238	60	*
17	August 11, 1965	15.8S 167.2E	33	73	30	*
				215	54	*
18	August 12, 1965	15.9S 167.5E	25	70	40	*
				250	50	*
19	December 1, 1966	14 S 167.1E	132	245	48	**
				72	42	**
20	November 4, 1963	15.1S 167.4E	123	275	50	**
				95	40	**
21	March 31, 1967	15.4S 167.5E	132	253	50	**
				73	40	**
22	July 9, 1964	15.5S 167.6E	121	263	54	**
				83	36	**

*Taken from Johnson and Molnar (1972).

**Taken from Isacks and Molnar (1971).

†See footnote to Table 1.2.

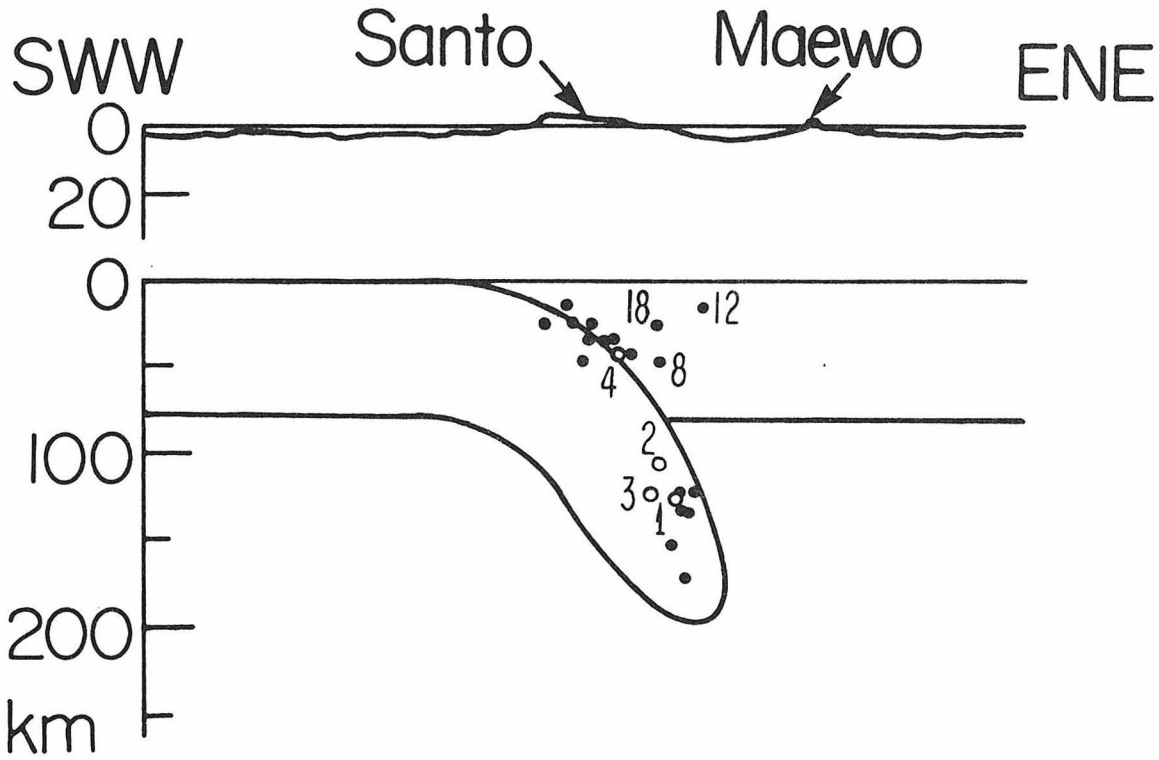

Figure 1.20. Closed and open circles stand for earthquakes with thrust faulting and strike slip faulting respectively. Event numbers are given for some earthquakes.

records are used to supplement the first-motion data. There are two classes of fault-plane solutions in Figure 1.18: thrust faults along the trend of the island arc and oblique strike slip faults along the extension of the fracture zone. The distribution of the seismic stations is inadequate to constrain the E or ENE dipping planes of some of the thrust events. Nevertheless their mechanisms are obviously high angle thrust fault and show a very consistent pattern; their dip angles and the slip vector orientation on the E or ENE dipping planes are about the same. The average dip angle is 43 ± 10° and the average azimuth and plunge of the slip vector are N71 ± 17°E and 36 ± 8 respectively. Usually low angle thrust faults are observed in island arcs such as Alaska and the Aleutian Islands (Plafker, 1972; Stauder, 1968; Kanamori, 1970c), Kurile Islands (Stauder, 1976; Kanamori, 1970a), Japan (Kanamori, 1971, 1972; Shimazaki, 1974), and Chile (Plafker, 1972; Kanamori and Cipar, 1974); the dip angle of these thrust events is usually 10 to 30°. But no mechanism of low angle thrust faulting is found in the central New Hebrides, where the trench does not exist. Figure 1.20 shows the topography of the central New Hebrides and the projections of the 22 earthquake foci on Figure 1.18 on a vertical plane perpendicular to the island arc. All shallow events except events 12 and 18, and probably event 8, fall on an ENE dipping plate boundary (dip angle ≈ 34° for depth of about 20 to 50 km). In view of this and their very consistent slip vector directions, these earthquakes are considered to be inter-plate earthquakes. Their slip vectors, then, represent the motions of the Australian plate relative to the overriding plate. Averaging

the dip angles obtained from foci distribution and fault plane solutions of these interplate events, the dip angle of the plate interface is determined to be about 38° at the depth of about 20 to 50 km. Focal mechanism of earthquakes which occurred to the north of 14°S and to the south of 16°S are characterized by high angle thrust faulting as well as faulting with irregular orientation; typical low angle thrusts are rare and are found only near the northern and southern ends of the arc (Chung, unpublished data). The high angle thrusts predominate particularly at the section where aseismic ridges are subducting. The dip angles of the thrust fault planes and the plunges of the slip vectors are larger in this arc than in many other subduction boundaries. Probably, this is a consequence of the abnormally rapid steepening of the subducted slab under this arc. On the other hand, events 12 and 18, and probably event 8, represent intraplate earthquakes occurring in the overriding plate indicating that the compressional stress axes are about horizontal and trending from EW to ENE-SWW. All the intermediate depth earthquakes, except events 1 and 4, show very consistent down-dip extensional mechanisms. This is probably a feature associated with ridge subduction. Usually down dip extension is considered to be due to the downward pull of the sinking oceanic plate due to its relatively high density compared with the surrounding mantle. In this region the low density ridge at the upper part of the sinking slab resists subduction thereby enhancing the extensional stress in the down-going lithosphere.

The mechanism of the events with a large strike slip component is constrained very well. Along the extension of the D'Entrecasteaux

fracture zone there is an intermediate shock, event 3 (m_b = 5.5, h = 124 km) which has about the same mechanism as that of the January 19, 1969 earthquake, event 2 (Figures 1.18, 1.19 and 1.6, and Table 1.2). There are two shocks, one shallow (event 4: h = 41 km, m_b = 5.5) and one intermediate-depth (event 1: h = 151 km, m_b = 5.3) whose mechanism is completely opposite to that of the two events mentioned above. The hypocenters of these four events have been relocated by using the master event method. Since event 2 is the largest shock it is used as a calibration earthquake and the hypocenters of events 1, 3 and 4 are calculated with respect to it. The result indicates that the four earthquakes are on the extension of the D'Entrecasteaux fracture zone. The ENE striking nodal plane of event 1 is closer to the strike of the D'Entrecasteaux fracture zone than the other nodal plane. Also the EW striking plane of event 4 is subparallel to the strike of the fracture zone. If we take these nodal planes as the fault plane these events represent right lateral slip along the fracture zone which is opposite to that represented by events 2 and 3. This result may seem somewhat unusual, but it may be explained in terms of differential subduction. Because of the buoyance, the ridge-fracture zone system encounters resistance upon subduction (Figure 1.21). A slight difference in the resistance against the oceanic lithosphere to the north and to the south of the ridge-fracture zone system may result in differential motion between these two lithospheres. When the oceanic lithosphere to the south of the ridge advances or subducts with respect to that to the north of it, a left-lateral faulting such as events 2 and 3 occurs along the subducted fracture zone. On the other hand, when

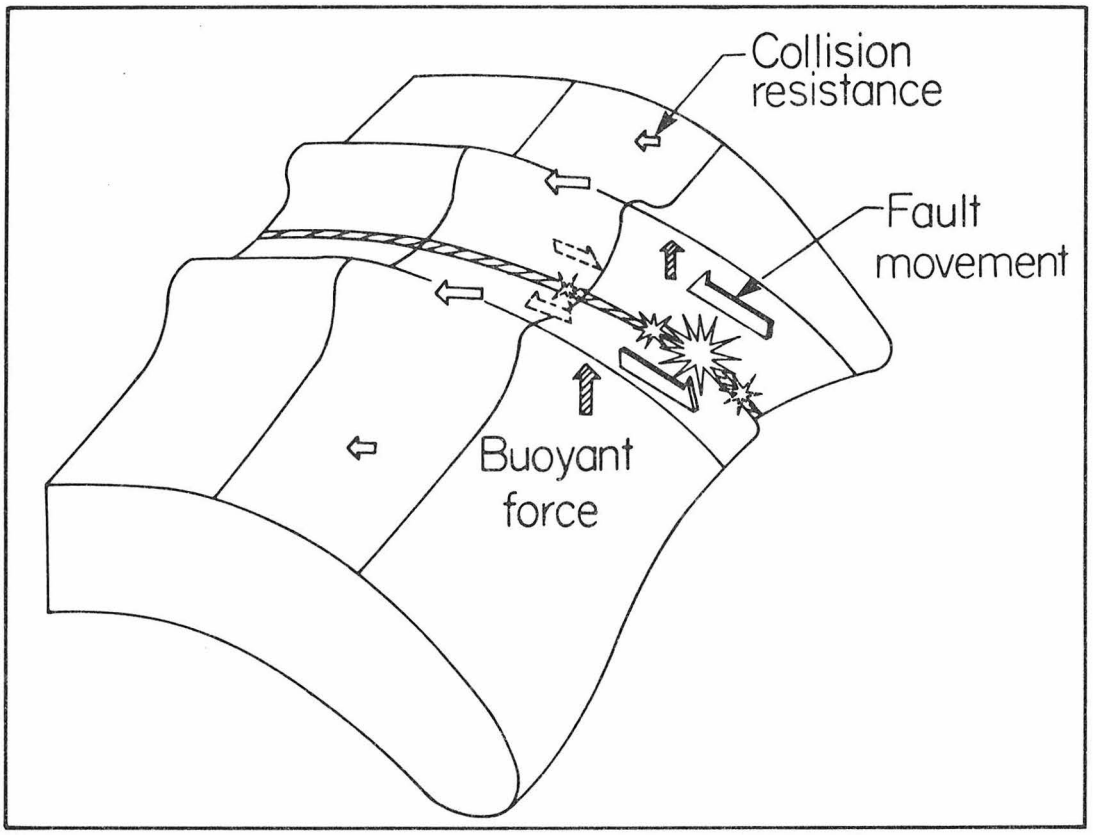

Figure 1.21. Schematic three-dimensional model for the subduction of a ridge-fracture zone system and the associated tectonic movements. Large star stands for large earthquake; the longer the arrow the larger the quantity involved.

the lithosphere to the north of the fracture zone advances, a right-lateral faulting such as events 1 and 4 occurs. This alternating motion along the subducted portions of the D'Entrecasteaux fracture zone may be the cause of the existence of the two mechanisms having an opposite sense of motion. This situation is illustrated schematically in Figure 1.21 in which open arrows represent collision resistance of the overriding plate against the subducting lithosphere, hatched arrows buoyant forces associated with the ridges, half arrows fault movements, and stars earthquakes along the fracture zone. The larger the symbols, the larger the quantity involved. The stars outlined by solid lines and half arrows represent earthquakes 2 and 3 and the left lateral displacement during the earthquakes whereas the dashed stars and dashed half arrows stand for events 1 and 4 and the associated right lateral movement at different stages of plate subduction. The alternating left-lateral and right-lateral motions may be one of the characteristic tectonic movements associated with subduction of buoyant ridge-fracture zone system.

CONCLUSIONS

The New Hebrides earthquake of January 19, 1969, which occurred near the intersection of the aseismic ridge-fracture zone system, the D'Entrecasteaux fracture zone, and the New Hebrides trench provided a unique opportunity for studying the subduction process of fracture zones and aseismic ridges. The earthquake is a complex multiple shock having a relative excitation of long period body waves more than one order of magnitude larger than other common shocks of comparable

m_b and depth. The earthquake was initiated by a left-lateral motion on a vertical E-W striking fault plane with a slip vector subparallel to the down dip direction of the Benioff zone. The strike direction, then, changed clockwise by 15° during the rupture. The location, mechanism and complexity of this earthquake suggest that the earthquake represents faulting along the subducted portion of the D'Entrecasteaux fracture zone. The complexity may reflect a highly heterogeneous stress distribution along the fracture zone. The focal depths of intermediate-depth events are shallower and the dip angle of Benioff zone is smaller near the location of ridge-fracture zone subduction than in the adjacent regions. These features can be interpreted as a consequence of differential subduction and local uplift of the Benioff zone caused by the Buoyant force associated with the subduction of the low density ridge. These intermediate-depth events have a very consistent pattern of down-dip extension mechanisms indicating that the extensional stress in the slab is enhanced by the resistance of the aseismic ridge against subduction. The lithospheres on either side of the fracture zone subduct more or less independently and generate alternate left lateral and right lateral earthquakes along the subducted portion of the fracture zone. This type of subduction has not been found prior to this study and may represent a process characteristic of subduction of fracture zones and aseismic ridges.

REFERENCES

Chase, C. G. (1971). Tectonic history of the Fiji plateau, Geol. Soc. Am. Bull., 82, 3087-3110.

Chung, W. Y. and Kanamori, H. (1976). Source process and tectonic implications of the Spanish deep-focus earthquake of March 29, 1954, Phys. Earth Planet. Int., 13, 85-96.

Chung, W. Y. and Kanamori, H. (1977). Focal mechanism of the New Hebrides earthquake of January 19, 1969 and ridge subduction under the New Hebrides arc, Abstract, Abstracts with Programs, 9, no. 4, February, 1977, Cordilleran Section, 73rd annual meeting, The Geological Society of America.

Den, N., W. J. Ludwig, S. Murauchi, M. Ewing, H. Hotta, T. Asanuma, T. Yoshii, A. Kabotera and K. Hagiwara (1971). Sediments and structure of the Earuipik-New Guinea rise, J. G. R., 76, 4711-4723.

Dubois, J. (1971). Propagation of P waves and Rayleigh waves in Melanesia: structural implications, J. G. R., 76, 7217-7240.

Fukao, Y. and K. Abe (1971). Multi-mode Love waves excited by shallow and deep earthquakes, Bull. Earthquake Res. Inst., 49, 1-12.

Helmberger, D. V. (1974). Generalized ray theory for shear dislocations, Bull. Seism. Soc. Am., 64, 45-64.

Isacks, B. L. and P. Molnar (1971). Distribution of stresses in the descending lithosphere from a global survey of focal-mechanism solutions of mantle earthquakes, Rev. Geophys. Space Phys., 9, 103-174.

Isacks, B. L. and Barazangi, M. (1977). Geometry of Benioff zones: Lateral segmentation and downwards bending of the subducted lithosphere, in Talwani, M. and Pitman, W. C. III, eds., Island Arcs Deep Sea Trenches and Back-Arc Basins, A. G. U. Maurice Ewing Series 1.

Isacks, B., M. Barazangi, C. Stephens, J. York, R. Louat, G. Pascal, B. Pontoise and J. Dubois (1977). Geometry of the lithosphere subducted beneath the central New Hebrides island arc, Abstract, EOS Trans., 58, June 1977.

Johnson, T. and P. Molnar (1972). Focal mechanisms and plate tectonics of the Southwest Pacific, J. G. R., 77, 5000-5031.

Kanamori, H. (1970a). Synthesis of long period surface waves and its application to earthquake source studies -- Kurile Islands earthquake of October 13, 1963, J. G. R., 75, 5011-5027.

Kanamori, H. (1970b). Velocity and Q of mantle waves, Phys. Earth Planet. Int., 2, 259-275.

Kanamori, H. (1970c). The Alaska earthquake of 1964: radiations of long-period surface waves and source mechanisms, J. G. R., 75, 5029-5040.

Kanamori, H. (1971). Focal mechanism of the Tokashi-Oki earthquake of May 16, 1968: contortion of the lithosphere at a junction of two trenches, Tectonophysics, 12, 1-13.

Kanamori, H. (1972). Tectonic implications of the 1944 Tonankai and the 1946 Nankaido earthquakes, Phys. Earth Planet. Int., 5, 129-139.

Kanamori, H. and J. J. Cipar (1974). Focal process of the great Chilean earthquake of May 22, 1960, Phys. Earth Planet. Int., 9, 128-136.

Kanamori, H. and G. Stewart (1976). Mode of the strain release along the Gibbs fracture zone, Mid-Atlantic ridge, Phys. Earth Planet. Int., 11, 312-332.

Karig, D. E. (1972). Remnant arcs, Geol. Soc. Am. Bull., 83, 1057-1068.

Karig, D. E. and J. Mammerickx (1972). Tectonic framework of the New Hebrides island arc, Marine Geol., 12, 187-205.

Kelleher, J. and W. McCann (1976). Buoyant zones, great earthquakes and unstable boundaries of subduction, J. G. R., 81, 4885-4896.

Langston, C. A. and D. V. Helmberger (1975). A procedure for modeling shallow dislocation sources, Geophys. J. R. astr. Soc., 42, 117-130.

Ludwig, W. J., S. Murauchi, N. Den, P. Buhl, H. Aotta, M. Ewing, T. Asamuma, T. Yoskii, and N. Sakajiri (1973). Structure of East China Sea-West Philippine Sea margin off southern Kyushu, Japan, J. G. R., 78, 2526, 2536.

Luyendyk, B. P., W. B. Bryan and P. A. Jezek (1974). Shallow structure of the New Hebrides Island Arc, Bull. Geol. Soc. Am., 85, 1287-1300.

Mallick, D. I. J. (1973). Some petrological and structural variations in the New Hebrides, in The Western Pacific: Island Arcs, Marginal Seas, Geochemistry, P. J. Coleman (ed.), Nedlands, Univ. of Western Australia Press, 193-211.

Menard, H. W. and T. E. Chase (1970). Fracture zones, in The Sea, V. 4, A. E. Maxwell (ed.), New York, Interscience Pubs., Inc., 421-443.

Mitchell, A. H. G. and A. J. Warden (1971). Geological evolution of the New Hebrides island arc, Geol. Soc. London J., 127, 501-529.

Morgan, W. J. (1971). Convection plumes in the lower mantle, Nature 280, 42-43.

Morgan, W. J. (1972). Deep mantle convection plumes and plate motions, Am. Assoc. Petroleum Geologists Bull., 56, 203-213.

Morgan, W. J. (1973). Plate motions and deep mantle convection, in Studies in Earth and Space Sciences (Hess Volume), R. Shagam et al. (eds.), Geol. Soc. Am. Mem. 132, 7-22.

Plafker, G. (1972). Alaskan earthquake of 1964 and Chilean earthquake of 1960, implications for arc tectonics, J. G. R., 77, 901-925.

Saito, M. (1967). Excitation of free oscillations and surface wave by a point source in a vertically heterogeneous earth, J. G. R., 72, 3689-3699.

Santo, T. (1970). Regional study on the characteristic seismicity of the world: Part III New Hebrides Islands region, Bull. Earthquake Res. Inst., 48, 1-18.

Shimazaki, K. (1974). Nemuro-Oki earthquake of June 17, 1973: a lithospheric rebound at the upper half of the interface, Phys. Earth Planet. Int., 9, 314-327.

Smith, S. W. (1972). The anelasticity of the mantle, Tectonophysics, 13, 601-622.

Stauder, W. (1968). Tensional character of earthquake foci beneath the Aleutian Trench with relation to sea-floor spreading, J. G. R., 73, 7693-7701.

Stauder, W. (1976). Fault motion in the larger earthquakes of the Kurile-Kamchatka arc and of the Kurile-Hokkaido corner, J. G. R., 81, 297-308.

Tsai, Y. B. and K. Aki,(1969). Simultaneous determination of the seismic moment and the attenuation of seismic waves, Bull. Seism. Soc. Am., 59, 275-287.

Vogt, P. R. (1973). Subduction and aseismic ridges, Nature, 241, 189-191.

Vogt, P. R., A. Lowrie, D. Bracey and R. Hey (1976). Subduction of aseismic oceanic ridges: effects on shape, seismicity and other characteristics of consuming plate boundaries, Geol. Soc. Am. Spec. Paper 172, 59 pp.

Wilson, J. T. (1965). Evidence from ocean islands suggesting movement in the earth, Royal Soc. London Philos. Trans., Ser. A., 258, 145-165.

Chapter 2

A MECHANICAL MODEL FOR PLATE DEFORMATION ASSOCIATED WITH ASEISMIC RIDGE SUBDUCTION IN THE NEW HEBRIDES ARC

INTRODUCTION

Previous workers (Vogt, 1973; Vogt et al., 1976; Kelleher and McCann, 1976; Chung and Kanamori, 1977, 1978) have suggested that the process of plate subduction and the geometry of plate boundaries can be affected by subduction of aseismic ridges because of the associated buoyant force. Vogt (1973) and Vogt et al. (1976) found that aseismic ridges on oceanic plates often trend into cusps or irregular indentations in the trace of the subduction zone, and a region of reduced seismicity seems to be associated with many consumed ridges. Kelleher and McCann (1976) studied the distribution of great earthquakes in the Circum-Pacific belt and found that where aseismic ridges or bathymetric highs interact with active trenches, large shallow earthquakes occur less frequently and have generally smaller rupture lengths than large events along adjacent segments of the plate boundary. Chung and Kanamori (1977, 1978) found that the subduction process, earthquake mechanisms, and seismicity patterns are significantly different in a region where an aseismic ridge-fracture zone meets the New Hebrides trench. At the extension of the aseismic ridges of the D'Entrecasteaux (ridge-fracture) zone, intermediate depth earthquakes have shallower focal depths than those occurring on either side. There is also some suggestion that the dip angle of the Benioff zone of the section where the aseismic ridge is subducting is smaller than in the adjacent sections. These can be explained in terms of local uplift of the Benioff zone due to the buoyant force associated with a low density ridge. In this paper we investigate the nature of plate interaction and deformation at the boundary of aseismic ridge subduction

in the New Hebrides island arc by using a simple thin elastic plate model. We first summarize various tectonic features of the New Hebrides arc.

REGIONAL SETTING AND TECTONIC ANOMALIES OF THE NEW HEBRIDES ISLAND ARC

The most remarkable feature of this island arc is perhaps the discontinuity of the New Hebrides Trench between 14.5°S and 16.5°S (Figures 2.1 and 2.2) where a transverse feature called D'Entrecasteaux fracture zone (Mallick, 1973; Luyendyk et al., 1974), with a topographic ridge on each side of it, abuts the island arc. Earthquake hypocenters extend to depths of at least 250 km below the entire length of the arc and there is no diminution of seismicity beneath the trench gap suggesting that the two trench sections belong to a single subduction zone or a single arc system. Extensive uplift is observed at the section including the Santo, Malekula, Maewo and Pentecost islands. Some areas have undergone Quaternary uplift of at least a few hundred meters (Mitchell, 1968; Coleman, 1970; Mitchell and Warden, 1971). During the earthquake swarm of August, 1965, the largest shocks of which were of magnitude 7 or larger, an uplift of 50 to 80 cm in the northern part of the island of Malekula occurred along about 100 km of coastline (Beniot and Dubois, 1971). Near the trench gap there is an abrupt change in the spatial distribution of islands and in the structure of the arc. The two largest islands, Santo and Malekula, deviate from the general trend of the arc and are located at a position which should be a part of the trench if the trench were continuous

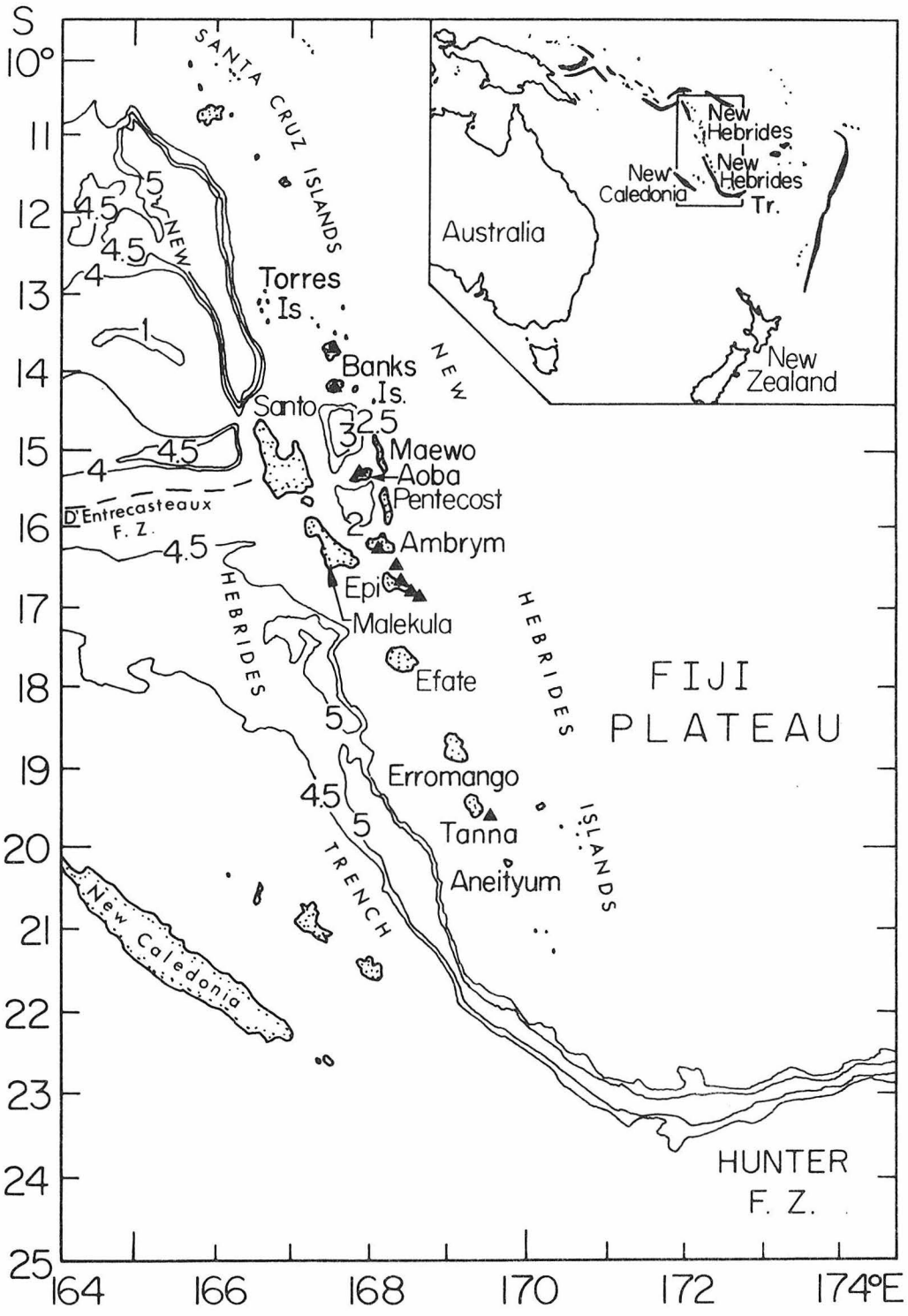

Figure 2.1. The New Hebrides island arc and some related features. Submarine contours are in kilometers. ▲ represents historically active volcano.

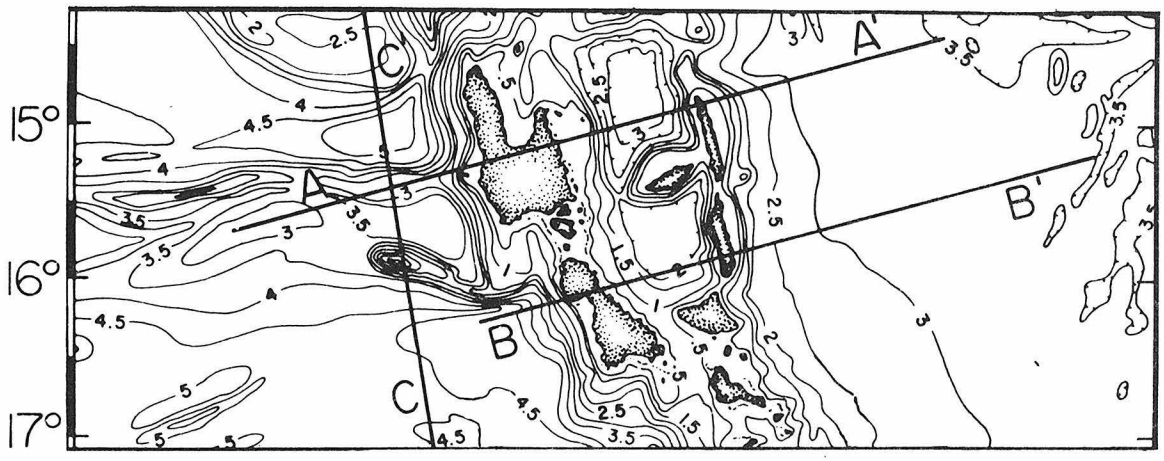

Figure 2.2. Bathymetry of the New Hebrides island arc and its vicinity. Contour interval is 0.5 km (after Chase, 1971).

(Figures 2.1 and 2.2). To the north and south of the trench gap the island arc appears to be a single arc but within the area it becomes a multiple arc. East of Santo and Malekula, there is a basin which is well developed compared with other depressions of this arc; no comparable basins occur elsewhere in the New Hebrides island arc.

The geology of the New Hebrides islands is relatively well known. Details about the geology as well as tectonics of the island arc have been studied and summarized by Mitchell (1970), Mitchell and Warden (1971), Karig and Mammerickx (1972), Mallick (1973), Luyendyk et al. (1974), Colley and Warden (1974) and Dugas et al. (1977). The islands of the New Hebrides can be divided roughly into three belts: a western belt consisting of the Torres Islands, Santo and Malekula; an eastern belt comprising the Maewo and Pentecost islands; and a central chain including the Banks Islands, Aoba, Ambrym, Epi, Efate, Erromango, Tanna and Aneityum. The central chain includes all the active and most of the recently extinct volcanoes. The islands of the New Hebrides consist primarily of volcanic, volcanoclastic and recent sedimentary rocks. The volcanism in the western belt is mainly pre-middle Miocene; the eastern belt is mainly Late Miocene to Early Pliocene; the central belt is mainly Pliocene to Recent. The periods of volcanism among the belts overlap slightly.

The concept of an extensional origin of inter-arc basin or back arc opening was developed by Karig (1970, 1971a, 1971b) based on studies of the Tonga-Kermadec and the Mariana arc systems. Based on the similarity in tectonic positions, Karig and Mammerickx (1972) proposed that the basin in the New Hebrides is of extensional origin.

According to Luyendyk et al. (1974), however, no well-developed interarc basins comparable to the Lau Basin of the Tonga arc system are present in the New Hebrides. Marine geophysical data indicate that more than 1 km of undisturbed sediment is present; no axial high is found and the central basin lacks steep walls. Regional dips of sediment layers in the basin are toward the basin center rather than subhorizontal or outward dipping as would be expected if rifting is occurring (or has occurred). Thus an alternate mechanism for the origin of the interarc basin seems unnecessary. In this paper, we suggest that this well developed basin is related to subduction of the D'Entrecasteaux ridge rather than by back-arc extension.

A MECHANICAL MODEL OF ASEISMIC RIDGE SUBDUCTION

Chung and Kanamori (1977 and 1978) suggested, on the basis of various seismological data, that the buoyant D'Entrecasteaux ridge-fracture zone is underthrusting beneath the New Hebrides arc. The plate interaction near the subduction boundary is schematically shown in Figure 2.3. When a ridge is subducted the upward loading on the upper plate is larger than usual because of the buoyant force. The ridge resists subduction and interacts strongly with the overriding plate. As a consequence, the large upward loading lifts up the trench floor and the edge of the overriding plate. The islands of Santo and Malekula were probably formed by an uplifted portion of the outer arc or the trench slope break (Dickinson, 1973; Karig, 1974), which is located between the trench and the volcanic arc. This explains the interruption of the New Hebrides trench, the

observed uplift in the area, and the location of the two large islands which are off the general trend of the New Hebrides arc. As illustrated by Figure 2.3, the upward force applied on the overriding plate by the ridge also causes subsidence some distance from the boundary of the overriding plate. Similar subsidence associated with uplift is observed in other situations. For instance during thrust earthquakes along subducting plate boundaries, such as the great Chilean earthquake of 1960, the Alaskan earthquake of 1964 (Plafker, 1972), and the Nankaido earthquake of 1946 (Fitch and Scholz, 1971), uplifts were observed on the seaward side while subsidence occurred in a broad zone on the landward side. A similar situation is the subsidence and uplift associated with glacial loading, at the site of the downward loading subsidence occurs but some distance away uplift occurs (Haskell, 1935; Walcott, 1970; Sweeney, 1977). Another example is the deflection of the oceanic plate near the trench. At the trench downward deflection occurs while at a distance of the order of 100 km seaward an outer rise can be observed (Hanks, 1971; Watts and Talwani, 1974; Caldwell et al., 1976). This kind of trench-outer rise profile has been interpreted as the deflection of a semi-infinite plate, overlying a fluid quarter space, on which vertical and horizontal loads are applied at the edge. Parameters such as effective (elastic) plate thickness, flexural rigidity and the magnitude of vertical and horizontal loading can be estimated by modeling these processes. In the following we model the overriding lithosphere by a semi-infinite elastic thin plate and the underlying asthenosphere (and the lower lithosphere) by a fluid quarter space.

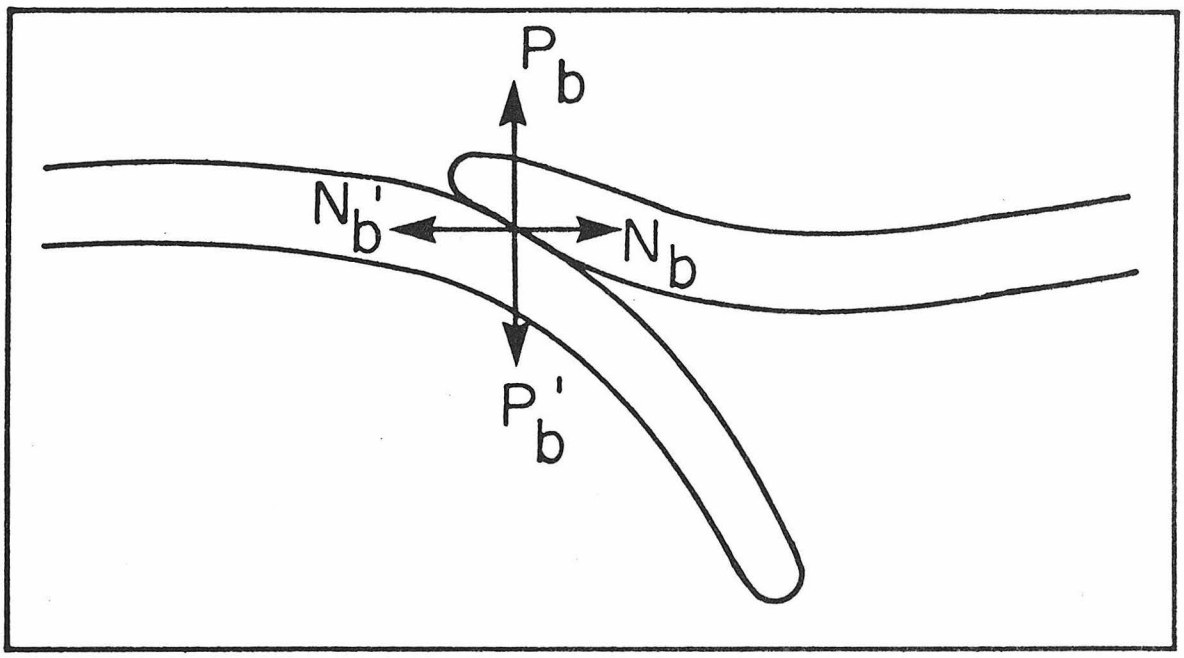

Figure 2.3. A schematic representation of the interaction between a subducting aseismic ridge and the overriding plate. N_b is the horizontal force applied to the overriding plate by the ridge; N_b' is the reaction applying to the ridge by the overriding plate; P_b' is the vertical loading applied to the ridge by the upper plate while P_b is the reaction applying to the upper plate by the ridge.

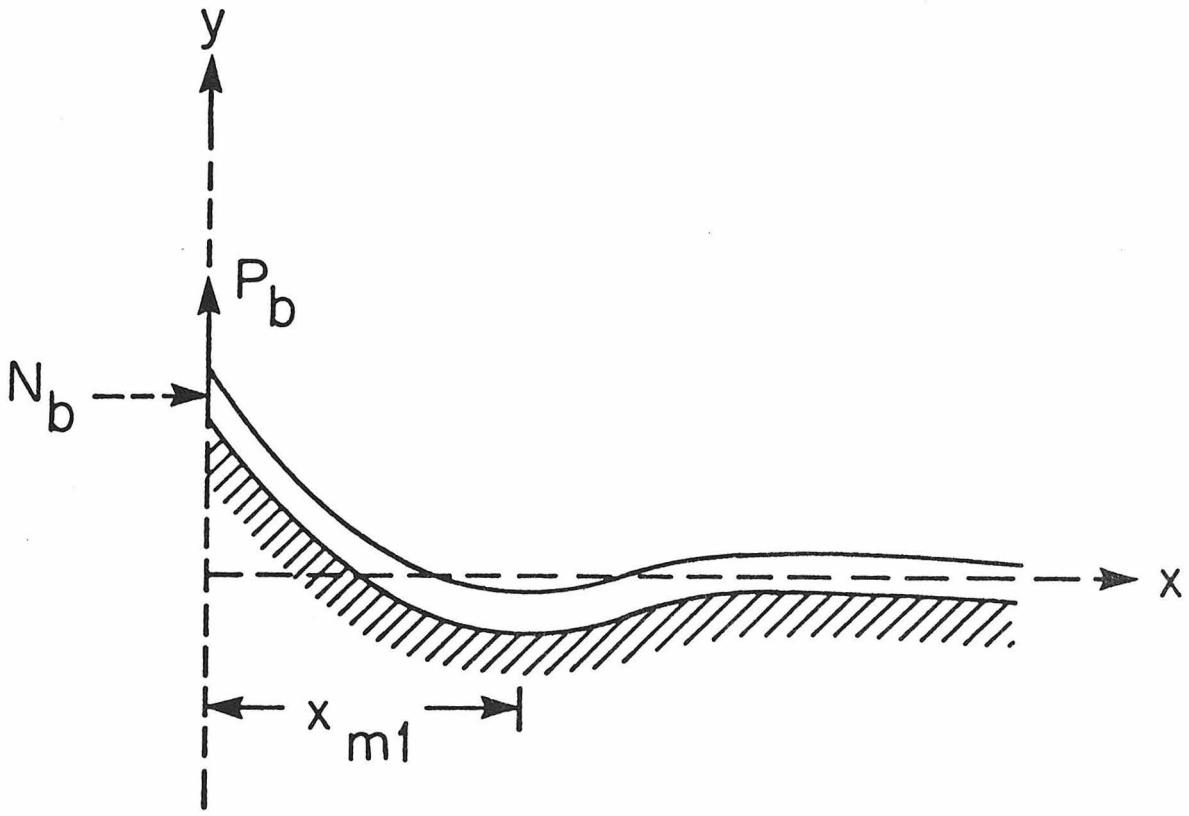

Figure 2.4. Deflection of a thin elastic half plate over a fluid quarter space under horizontal and vertical loadings (N_b and P_b) at the plate edge. X_{m_1} is the location of the first relative minimum on the deflected surface.

The geometry of the present problem is illustrated schematically in Figure 2.4. The edge of the semi-infinite plate is locally subject to vertical upward loading due to the buoyant force associated with the low density ridge. This model is adequate if the time of loading is much longer than the relaxation time of the asthenosphere and much shorter than that of the lithosphere. We simplify the three dimensional problem to a two dimensional problem, and the upward loading to an upward line force at the plate edge (x = 0, Figure 2.4). The notation employed in this paper is similar to that used by Hanks (1971) and is given in Table 2.1). For the bending of a thin elastic half plate over a fluid quarter space, in a constant gravity field, the deflection y satisfies (Hetenyi, 1946)

$$D \frac{d^4y}{dx^4} - N_b \frac{d^2y}{dx^2} + K_o y = 0 \tag{2.1}$$

Under the boundary conditions

$$x = 0: \quad Q_v = P_b; \text{ horizontal loading} = -N_b; \; M = 0$$

$$x \to \infty: \quad y \to 0, \; M \to 0$$

the solution to (2.1) is given by

$$y = \frac{P_b}{\beta K_o} \frac{2\lambda^2}{3\alpha^2-\beta^2} e^{-\alpha x} [2\alpha\beta\cos\beta x+(\alpha^2-\beta^2)\sin\beta x]$$

We investigate a case of zero horizontal loading at the plate edge first and then we shall discuss the effects of horizontal loading later in this section. For $N_b = 0$, we have

$$y(x) = \frac{2\lambda P_b}{K_o} e^{-\lambda x} \cos\lambda x$$

TABLE 2.1

EXPLANATION OF THE SYMBOLS USED IN PART II, Chapter 2

P_b = vertical force/unit width, dyne cm^{-1}

N_b = horizontal force/unit width, dyne cm^{-1} (negative if compressional, positive if tensional).

y = plate deflection, cm

M = bending moment/unit width, dynes; $M = -D \frac{d^2y}{dx^2}$

Q_v = vertical shearing force/unit width, dynes cm^{-1};

$$Q_v = \frac{dM}{dx} + N_b \frac{dy}{dx}$$

ρ_m = densith of mantle underlying the elastic plate = 3.4 g cm^{-3}

ρ_a = density of air overlying the elastic plate

K_o = foundation modulus = $(\rho_m - \rho_a)g \approx \rho_m g$, dyne cm^{-3}

g = gravitational acceleration = 980 cm s^{-2}

D = flexural rigidity, dyne cm

$$D = \frac{Eh^3}{12(1-\nu^2)}$$

E = Young's modulus = 6.5×10^{11} dyne cm^{-2}

h = effective (elastic) thickness of plate = 25×10^5 cm

ν = Poisson's ratio = 0.25

$$\lambda = \sqrt[4]{\frac{Ko}{4D}}, \text{ cm}^{-1}$$

$$\alpha = \sqrt{\lambda^2 + \frac{Nb}{4D}}, \text{ cm}^{-1}$$

$$\beta = \sqrt{\lambda^2 - \frac{Nb}{4D}}, \text{ cm}^{-1}$$

x_{m_n} = distance from the plate edge to the n^{th} relative extremum of deflection.

$$y(0) = \frac{2\lambda P_b}{K_o} \tag{2.2}$$

The n^{th} extremum of plate deflection occurs at

$$x_{m_n} = (n - \frac{1}{4}) \frac{\pi}{\lambda} \qquad n = 1,2,3. \ . \ . \tag{2.3}$$

For the first one we have (Figure 2.4)

$$x_{m_1} = \frac{3\pi}{4\lambda} \tag{2.4}$$

and

$$y(x_{m_1}) = \frac{2\lambda P_b}{K_o} e^{-3\pi/4} \cos(\frac{3\pi}{4}) \tag{2.5}$$

We now calculate x_{m_1}, $y(0)$, and $y(x_{m_1})$ by employing some reasonable values for the parameters involved. Taking $E = 6.5 \times 10^{11}$ dyne-cm^{-2}, $v = 0.25$, $h = 25$ km (Caldwell *et al.*, 1976), we have $D = 9.03 \times 10^{29}$ dyne-cm, $\lambda = 1.743 \times 10^{-7}$ cm^{-1}, and $x_{m_1} \approx 135$ km (Figure 2.4). Figure 2.5 shows two topographic profiles, one across line AA and one across line BB of Figure 2.2. The overall topography is quite complicated with the northern part of the basin wider than the southern part (profiles AA′ and BB′ in Figure 2.5). We assume that the basin center is the first relative minimum corresponding to that in Figure 2.4 and treat the horizontal distance from the highest point in the Santo or Malekula island to the basin center as x_{m_1} (Figure 2.5). For profile AA′ we have $x_{m_1} = 118$ km which is consistent with the calculated value 135 km given above. For profile BB′, we obtain $x_{m_1} = 73$ km which is about half the calculated value. We next calculate P_b the total buoyant force, and $y(0)$, the maximum uplift. Since $P_b = V \cdot \Delta\rho \cdot g$, we need to know the volume of the ridge system,

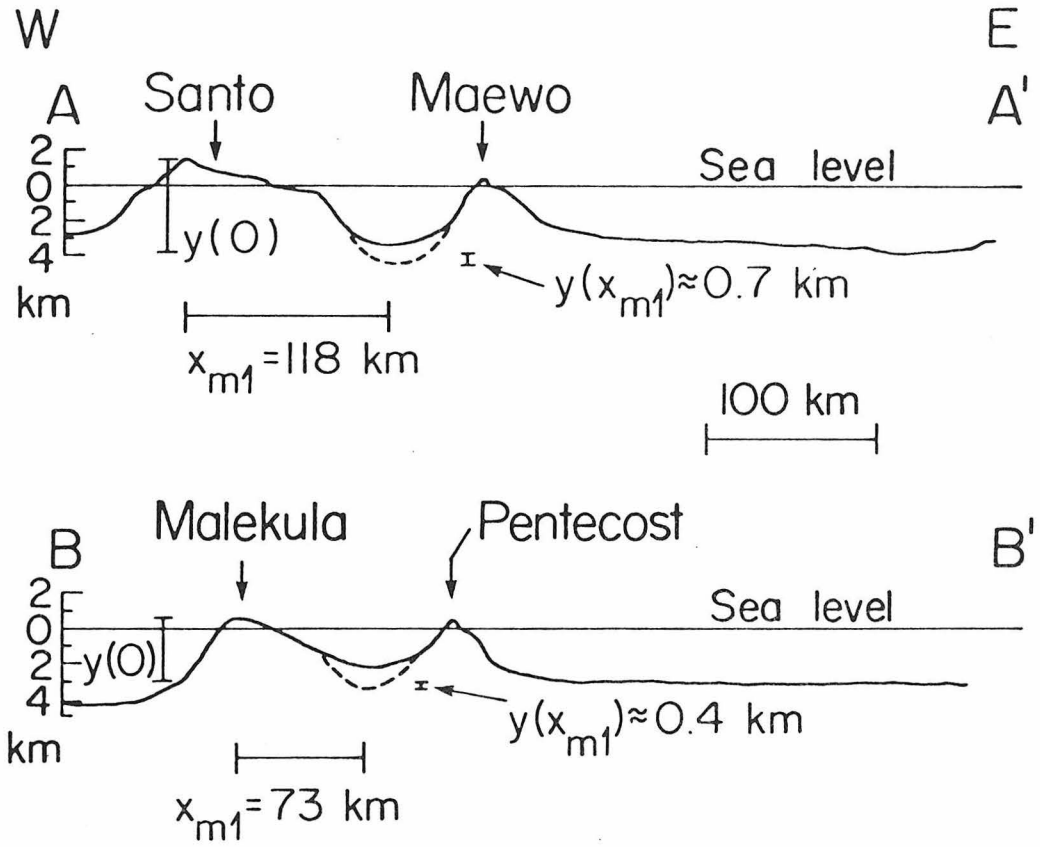

Figure 2.5. Topographic profiles of the New Hebrides island arc system across lines AA′ and BB′ , of Figure 2.2, perpendicular to the trend of the island arc. The dashed curves show the bottoms of the basin after sediment is removed while the solid curves above the dashed curves are the sediments. $y(0)$ is the maximum deflection at the plate edge ($x = 0$); x_{m_1} is the distance from the plate edge to the first relative minimum, and $y(x_{m_1})$ is the deflection at x_{m_1}.

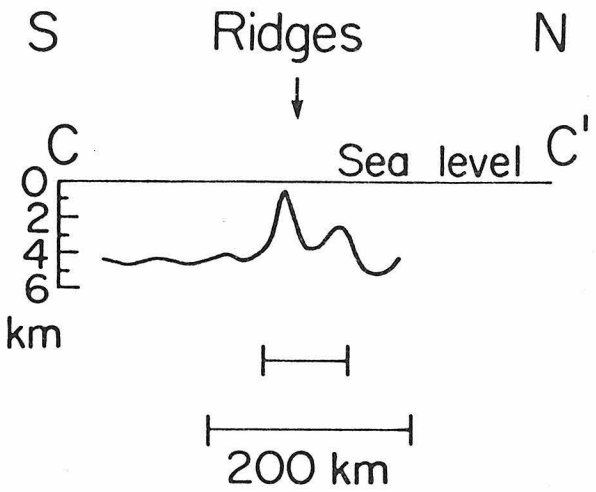

Figure 2.6. Topographic profile of the D'Entrecasteaux ridge-fracture zone system across line CC´ of Figure 2.2.

V, and the density contrast between ridge and oceanic plate in order to calculate P_b. Figure 2.6 shows the topographic profile across line CC′, of Figure 2.2, which is roughly perpendicular to the trend of the ridges. The horizontal scale, or the width, of the ridge system across this profile is about 80 km, but the thickness of the ridge is unknown. We assume that the thickness is one half the width of the ridge. The buoyant force is partially from the portion of ridge under the island arc and partially from the portion near the plate boundary but not beneath the island. If the ridge has gone down to 100 km in depth with a dip angle of 60°, the down-dip length of the subducted ridge is 120 km. We further assume that part of the buoyant force comes from a 40 km long unsubducted ridge. Then we can calculate the volume of the ridge. The density contrast between ridge and oceanic plate can be between 0.05 to 0.08 g/cm^3 (Kelleher and McCann, 1976); we take $\Delta\rho$ = 0.06 g/cm^3 in our calculation. From the above values we have upward force per unit width, $P_b \approx 4 \times 10^{15}$ dyne cm^{-1} and the maximum uplift at the plate edge, $y(0) \simeq 4$ km. On the profiles of AA′ and BB′ of Figure 2.2, the corresponding values of y(0), which is supposed to be measured from the undeflected position of the plate in Figure 2.5, should be measured from the averaged depth of the ocean floor to the east and far away from the island arc system to the highest point on the Santo or Malekula island. The measured value of y(0) from these two profiles is about 3.5 to 5 km which is consistent with the predicted value. The depth of the basin corresponding to $y(x_{m_1})$ given in equation (2.5) is calculated to be 0.28 km. In order to measure $y(x_{m_1})$ from Figure 2.5 we must

correct for the thickness of sediment in the basin, which is not well known. Luyendyk et al. (1974) report more than 1 km of undisturbed sediment in the basin. Here we use 1.3 km for the maximum thickness of the sediments. The dashed curves in Figure 2.5 represent the basin bottoms after the sediment is removed. The measured value of $y(x_{m_1})$ is about 0.4 to 0.7 km which agrees with the calculated value within a factor of three. Geological processes such as erosion, sedimentation, isostasy, and volcanic activity affect the topography as well, so we consider this agreement satisfactory. Our model, however, does not explain the topographic high associated with the Maewo and Pentecost islands (Figure 2.5). A more complicated plate model than used above is necessary to explain these features.

In principle, the above analysis provides an estimate of the stress level within the bending plate. However, as demonstrated by De Bremaecker (1977), the estimate of stress depends very much on the constitutive equation and the model used in the calculation and is not very meaningful.

In this analysis, the upward loading alone is enough to explain the observations. The effects of introducing a horizontal loading at the plate edge are (1) to shift the location of x_{m_1} or the basin center toward the plate edge, (2) to increase the amount of deflection, and (3) to increase the stress level within the plate. The first effect can bring the theoretical value of x_{m_1} closer to the observation.

In the islands of the western belt (Santo and Malekula [Figure 2.1]), stratified sediments dip eastward some with dip angles larger than 60°,

while those in the islands of the eastern belt (Maewo and Pentecost) dip westward with dip angles of about 20 to 30° (Mitchell and Warden, 1971; Luyendyk et al., 1974). This can fit our model very well.

In the present model the overriding plate is bent upward, so its upper part is subject to E-W compression. Chung and Kanamori (1978) studied the focal mechanisms of the larger earthquakes in the area. Shallow earthquakes occurring within the overriding plate are characterized by high angle thrust faulting with horizontal compressional stress axes trending about east-west. This is probably due to the upward bending as well as the horizontal compression from the Australian (or Indian) plate. The seismic activity near the center of the basin is low. The events which occurred there are small so that no well-constrained mechanisms could be determined. Nevertheless, available first-motion data show no indication of normal faultings near the basin center. This finding together with Luyendyk et al. (1974), suggests that no active and recent sea floor spreading is taking place in the basin between 14 and 16°S. Our model requires no extensional mechanism to form the interarc basin. In addition, our model explains why the well developed basin occurs only at the extension of the ridges and not elsewhere in the arc.

CONCLUSIONS

In this study we have investigated several tectonic features associated with the subduction of aseismic ridges in the New Hebrides island arc. Our conclusions are:

(1) The discontinuity of the New Hebrides trench can be interpreted as a consequence of subduction of the aseismic ridges of the D'Entrecasteaux zone and the subsequent uplift of the trench-floor and plate edge due to the buoyant force associated with the low density ridges.

(2) The islands of Santo and Malekula in the New Hebrides are probably formed by the uplifted outer arc or the mid-slope basement high, which is located between the trench and the frontal arc. Thus the two islands deviate from the general trend of the New Hebrides Island arc.

(3) The back-arc basin in the New Hebrides island arc system may have been formed as a result of subsidence of the overriding plate due to a vertical upward loading at the plate edge. This interpretation is consistent with geological observations.

(4) The uplift at the plate edge and the subsidence behind the uplifted area can be modeled by a deflection of a thin elastic half plate overlying a fluid quarter space with a vertical upward loading at the plate edge. With reasonable values of the magnitude of the upward loading, the computed values of the maximum uplift at the plate edge, the distance between the basin center and the plate edge, and the depth of the basin agree with the observed values reasonably well.

Although the details of the tectonic features produced in the process of aseismic ridge subduction may be a function of convergence

rate, mechanical properties of the overriding plate (continent or island arc), and the time duration from the beginning of the process (or the stage of plate interaction process), the phenomena investigated in this paper may be very general.

REFERENCES

Beniot, M. and J. Dubois (1971). The earthquake swarm in the New Hebrides Archipelago, August 1965, in Collins, B. W. and Fraser, R., (eds.), Recent Crustal Movements, The Royal Society of New Zealand, 141-148.

Caldwell, J. G., W. F. Haxby, D. E. Karig, and D. L. Turcotte (1976), On the applicability of a universal elastic trench profile, Earth Planet. Sci. Lett., 31, 239-246.

Chase, C. G. (1971). Tectonic history of the Fiji plateau, Bull. Geol. Soc. Am., 82, 3087-3110.

Chung, W.-Y. and H. Kanamori (1977). Seismicity and tectonic anomalies associated with aseismic ridge subduction in the New Hebrides Arc, EOS, Trans., Am. Geophys. Un., 58, No. 12, 1232.

Chung, W.-Y. and H. Kanamori (1978). Subduction process of a fracture-zone and aseismic ridges -- focal mechanism and source characteristics of the New Hebrides earthquake of January 19, 1969 and some related events, Geophys. J. R. astron. Soc., 54, 221-240.

Coleman, P. J. (1970). Geology of the Solomon and New Hebrides Islands as part of the Melanesian re-entrant, Pacific Sci., 24, 289-314.

Colley, H. and A. J. Warden (1974). Petrology of the New Hebrides Geol. Soc. Am. Bull., 85, 1635-1646.

De Bremaecker, J. C. (1977). Is the oceanic lithosphere elastic or viscous? J. G. R., 82, 2001-2004.

Dickinson, W. R. (1973). Widths of modern arc-trench gaps proportional to past duration of igneous activity in associated magmatic arcs, J. G. R., 78, 3376-3389.

Dugas, F., J. Dubois, A. Lapoulille, R. Louat and C. Ravenne (1977). Structural characteristics and tectonics of an active island arc -- The New Hebrides, (preprint).

Fitch, T. J. and C. H. Scholz (1971). Mechanism of underthrusting in southwest Japan: A model of convergent plate interactions, J. G. R., 76, 7260-7292.

Hanks, T. C. (1971). The Kurile Trench -- Hokkaido Rise system: Large shallow earthquakes and simple models of deformation, Geophys. J. Roy. astr. Soc., 23, 173-189.

Haskell, N. A. (1935). The motion of a viscous fluid under a surface load, Physics, 6, 265-269.

Hetenyi, M. (1946). Beams on Elastic Foundation, The University of Michigan Press, Ann Arbor, Michigan.

Karig, D. E. (1970). Ridges and basins on the Tonga-Kermadec island arc system, J. G. R., 75, 239-254.

Karig, D. E. (1971a). Structural history of the Mariana island arc system, Bull. Geol. Soc. Am., 82, 323-344.

Karig, D. E. (1971b). Origin and development of marginal basins in the western Pacific, J. G. R., 76, 2542-2561.

Karig, D. E. (1974). Evolution of arc systems in the western Pacific, Ann. Rev. of Earth and Planet. Sci., 2, 51-75.

Karig, D. E. and J. Mammerickx (1972). Tectonic framework of the New Hebrides island arc, Marine Geol., 12, 187-205.

Kelleher, J. and W. McCann (1976). Buoyant zones, great earthquakes, and unstable boundaries of subduction, J. G. R., 81, 4885-4896.

Luyendyk, B. P., W. B. Bryan and P. A. Jezek (1974). Shallow structure of the New Hebrides island arc, Bull. Geol. Soc. Am., 85, 1287-1300.

Mallick, D. I. J. (1973). Some petrological and structural variations in the New Hebrides, in Coleman, P. J. (ed.), The Western Pacific: Island Arcs, Marginal Seas, Geochemistry, Nedlands, Univ. Western Australia Press, 193-211.

Mitchell, A. H. G. (1968). Raised reef-capped terraces and sea-level changes, North Malekula, New Hebrides, J. Geol., 76, 56-67.

Mitchell, A. H. G. (1970). Facies of an early Miocene volcanic arc, Malekula Island, North Hebrides, Sedimentology, 14, 201-243.

Mitchell, A. H. G. and A. J. Warden (1971). Geological evolution of the New Hebrides island arc. Geol. Soc. London J., 127, 501-529.

Plafker, G. (1972). Alaskan earthquake of 1964 and Chilean earthquake of 1960; implications for arc tectonics, J. G. R., 77, 901-925.

Sweeney, J. F. (1977). Subsidence of the Sverdrup basin, Canadian Arctic islands, Bull. Geol. Soc. Am., 88, 41-48.

Vogt, P. R. (1973). Subduction and aseismic ridges, Nature, 241, 189-191.

Vogt, P. R., A. Lowrie, D. Bracey, and R. Hey (1976). Subduction of aseismic oceanic ridges: Effects on shape, seismicity, and other characteristics of consuming plate boundaries, Geol. Soc. Am. Spec. Paper #172, 59 pp.

Walcott, R. I. (1970). Isostatic response to loading of the crust in Canada, Can. J. Earth Sci., 7, 716-727.

Watts, A. B. and M. Talwani (1974). Gravity anomalies seaward of deep-sea trenches and their tectonic implications, Geophys. J. R. astron. Soc., 36, 57-90.

Chapter 3

SEISMICITY PATTERN ASSOCIATED WITH ASEISMIC RIDGE SUBDUCTION

INTRODUCTION

Recent studies (Vogt, 1973; Kelleher and McCann, 1976; Vogt et al., 1976; Chung and Kanamori, 1977, 1978a and b) have suggested that both seismicity patterns and tectonic features at consuming plate boundaries are significantly modified by the subduction of aseismic ridges. The aseismic ridges discussed here are topographic ridges on the ocean floor and are distinct from seismically active mid-ocean ridges. Kelleher and McCann (1976) found that where aseismic ridges and bathymetric highs interact with active trenches, large shallow earthquakes occur less frequently and have shorter rupture lengths than large events along adjacent segments of the plate boundary. They interpreted the observation in terms of buoyant forces associated with low density ridges which tend to resist and modify subduction. They also mentioned that the zones where aseismic ridges interact with active trenches are frequently characterized by gaps in intermediate-depth hypocenters. Vogt et al. (1976) found that a region of reduced seismicity seems to be associated with consumed ridges. Chung and Kanamori (1977 and 1978a) found a systematic change in the depths of intermediate-depth earthquakes near a location of ridge subduction in the New Hebrides arc. At the extension of the aseismic ridge the intermediate depth events have shallower focal depths than events occurring in the adjacent regions. There is also some suggestion that the dip angle of the Benioff zone where the ridge is subducting is smaller than that in the neighboring regions. They interpreted this as due to a combination of differential subduction and local uplift or deformation of the Benioff zone due to the buoyant force associated

with the aseismic ridge. Thus the buoyant force due to aseismic ridges not only affects the occurrence of great shallow earthquakes, as proposed by Kelleher and McCann (1976), but also seems to change the seismicity pattern and the shape of the seismic zone. Since Chung and Kanamori (1977, 1978a) studied only the New Hebrides Islands, it was not clear whether this seismicity pattern is a universal feature or a local effect.

Discontinuities in seismicity and bathymetry have also been reported by other investigators. Sykes (1966) found that the seismicity is relatively low in the region between the Tonga and Kermadec trenches. Katsumata and Sykes (1969) found that a region of low shallow seismicity and a discontinuity for deeper events in the Volcano Islands of the Bonin-Mariana island arc system adjacent to a prominent gap in the trench where the Marcus-Necker ridge intersects the arc. In this paper a more extensive and systematic study of seismicity associated with aseismic ridge subduction is carried out, to better define the nature of aseismic ridge subduction and its interaction with the overriding plate. We will investigate the seismicity of five regions of aseismic ridge subduction: New Hebrides, Tonga-Kermadec, Bonin-Mariana, Peru, and Chile. The seismicity patterns of these regions are compared and discussed in terms of buoyant force and mechanical properties of aseismic ridges.

SEISMICITY ASSOCIATED WITH ASEISMIC RIDGE SUBDUCTIONS IN FIVE SEISMIC ZONES

In this paper we will focus our attention on the geometry of the

seismic gap and the spatial variations in earthquake frequency and focal depth near locations of ridge subduction. The primary data source used is the hypocenter information reported in the U.S.G.S. and I.S.C. catalogues. These data are supplemented in specific regions by seismicity data by Santo (1970a and b) for the New Hebrides and Bonin-Mariana, and Sykes (1966) for Tonga-Kermadec.

New Hebrides

At about 15.5°S, 166.5°E, the New Hebrides Trench is interrupted by a ridge system, which is associated with and parallel to the D'Entrecasteaux zone. Seismicity of this arc has been studied by Santo (1970a), Karig and Mammerickx (1972), Chung and Kanamori (1977, 1978a), and Pascal et al. (1978). The spatial distribution of earthquakes which occurred from 1963 to 1967 is investigated in this study. Figure 3.1 presents the epicenter distribution of all the shallow intermediate, and deep events with $m_b \geq 4$ which occurred in 1963 and 1964. Different symbols are used to represent earthquakes of different depths in the figure. The region is divided into five parts, A, B, C, D, and F, of equal area. Areas A and B and areas D and E are to the north and south of the ridge-trench intersection respectively while area C includes the ridge and its extension. The distributions of intermediate and deep events for other years are similar although there are some variations in shallow seismicity. Figure 3.2 shows histograms of focal depth distributions for all the events which occurred in the period of 1963 to 1967 in the five areas. The intermediate-depth earthquakes under the ridge extension are systematically

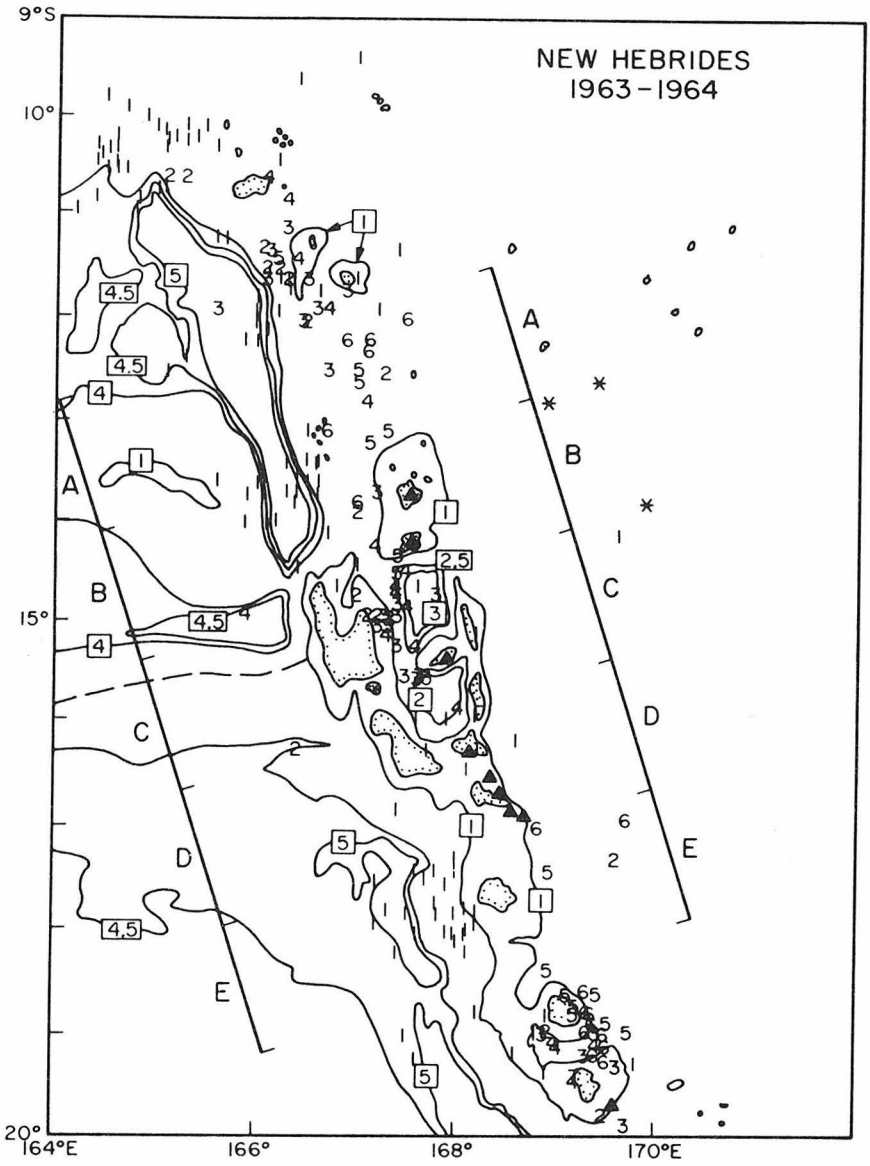

Figure 3.1. Distribution of earthquake epicenters for the period of 1963 and 1964 at and near the location of subduction of the D'Entrecasteaux ridge-fracture zone. Numbers is rectangles are depths of submarine contours (simplified from Chase, 1971) in kilometers. Different symbols represent epicenters at different depth (h: in km): 1 represents $0 \leq h \leq 70$; 2: $70 \leq h \leq 110$; 3: $110 < h \leq 150$; 4: $150 < h \leq 190$; 5: $190 < h \leq 230$; 6: $230 < h \leq 280$; 7: $280 < h \leq 340$; 8: $340 < h \leq 400$, 9: $400 < h < 500$, Δ: $500 < h \leq 600$, *: $600 < h$.

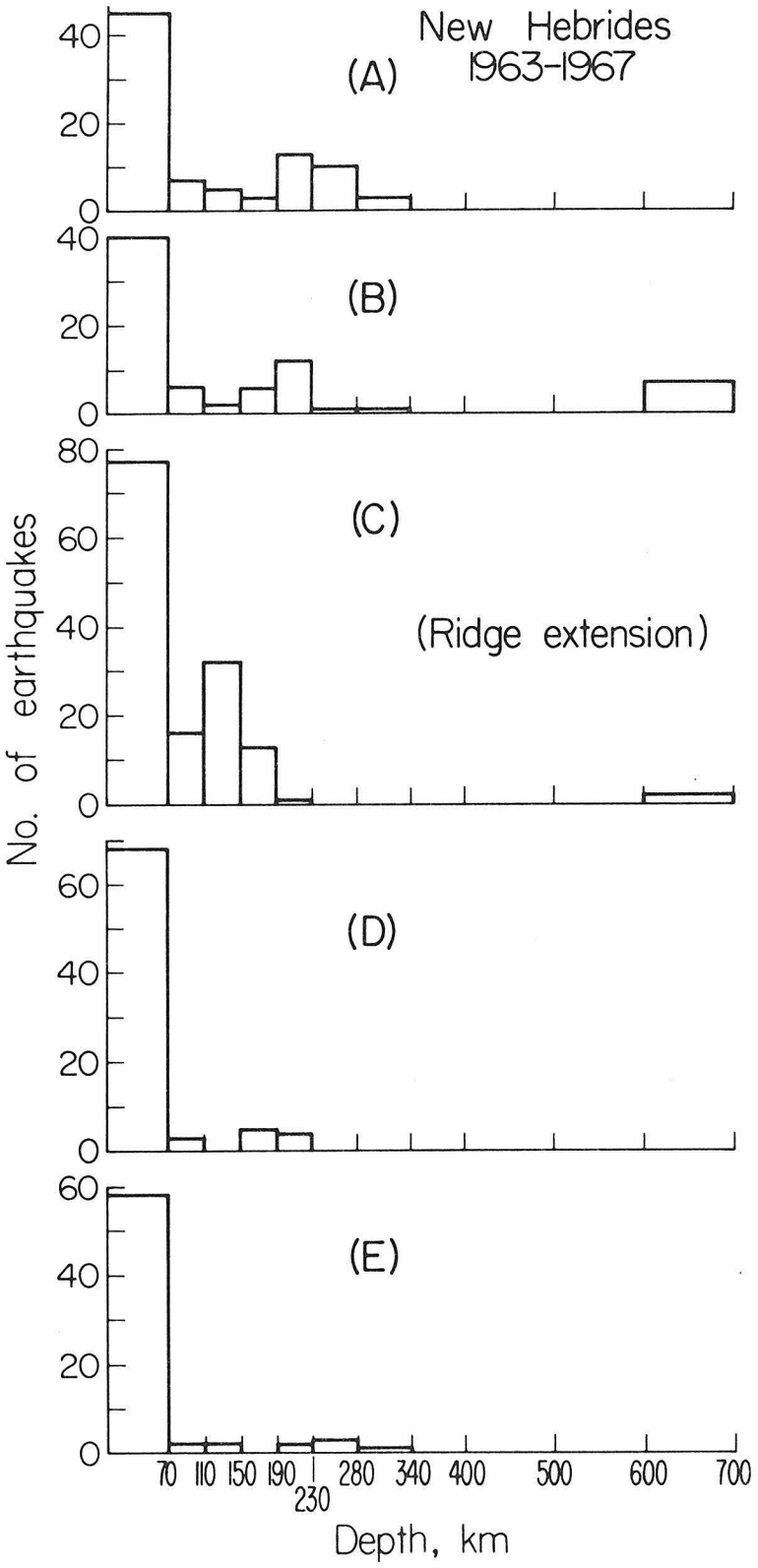

Figure 3.2. Distribution of focal depth of earthquakes at areas A, B, C, D, and E of Figure 3.1.

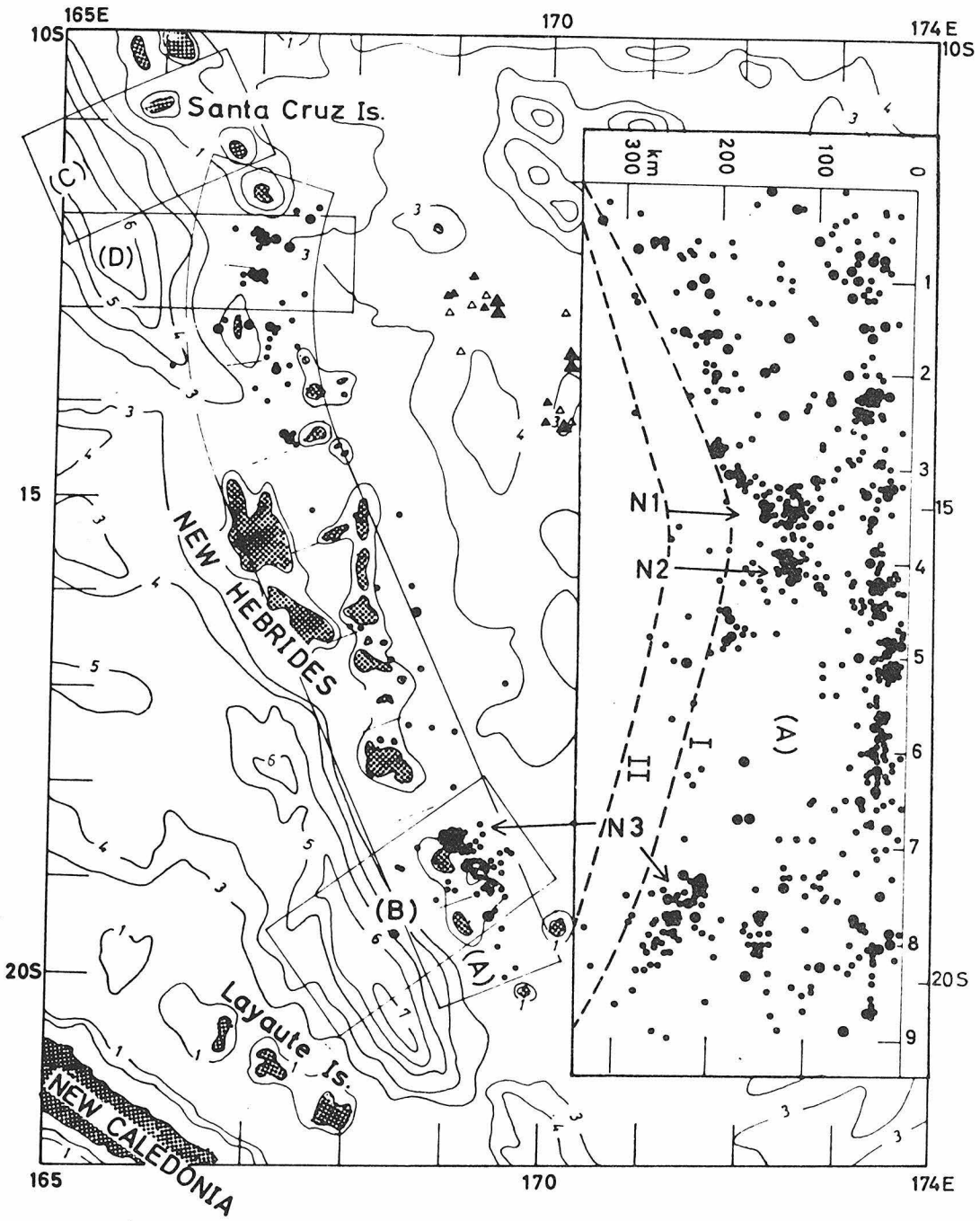

Figure 3.3. Distribution of epicenters of intermediate earthquakes (both ▲ and Δ). Attached figure -- foci distribution of all the events along the profile (A). N1, N2, and N3 are earthquake nests. Horizontal scales are in degrees (after Santo, 1970, with the addition of dashed curves I and II which roughly bound the maximum depth of the intermediate-depth events).

shallower than those occurring to the north and to the south. The intermediate-depth seismicity is particularly high under the ridge extension. Figure 3.3 is taken from Santo (1970a); the attached figure on the right is a projection of all the events within region A of the figure onto a vertical plane parallel to the arc. Santo studied this area without discussing the seismicity in terms of ridge subduction. Dashed curve I, added by the present author, approximately bounds the maximum depth of the most active region. Including the few events below the dashed line I, we get dashed curve II bounding the maximum depths of all events. We can see a very clear change of maximum focal depths in the area. The seismicity pattern of intermediate depth earthquakes is similar to that found by Chung and Kanamori (1977, 1978a) based on earthquake data covering different time periods. No area of reduced seismicity of shallow earthquakes is found near the ridge-trench intersection (Figure 3.2). This is consistent with the result obtained by Karig and Mammerickx (1972).

Bonin-Mariana

The Bonin-Mariana trench is interrupted by the Marcus-Necker ridge at about 143.5°E, 26°N. This situation is similar to that of the New Hebrides island arc. Seismicity of Bonin-Mariana has been studied by Katsumata and Sykes (1969) and Santo (1970b). Figure 3.4 shows the epicenter distribution of events during the period from 1968 to 1974. The symbols used for epicenters of different depths are identical to those employed in Figure 3.1. We define four areas, A, B, C and D, in Figure 3.4. Shallow seismicity, which includes all

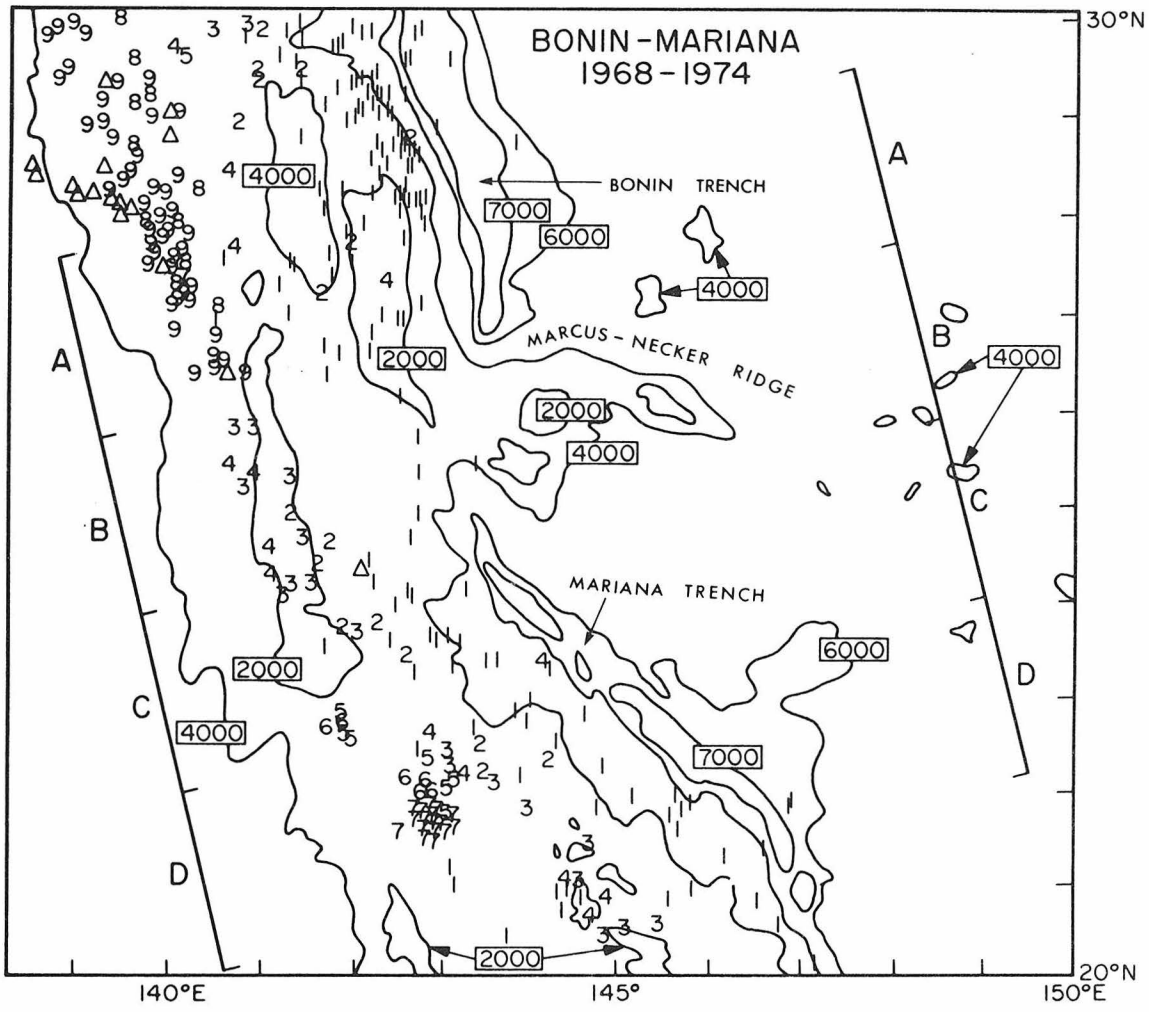

Figure 3.4. Distribution of earthquake epicenters for the period of 1968 to 1974 at and near the location of subduction of the Marcus-Necker ridge. Numbers in rectangles are depths of submarine contours (simplified from the base map published by Hydrographic Department of Maritime Safety Agency, Japan) in meters. Symbols for epicenters are identical to those used in Figure 1.

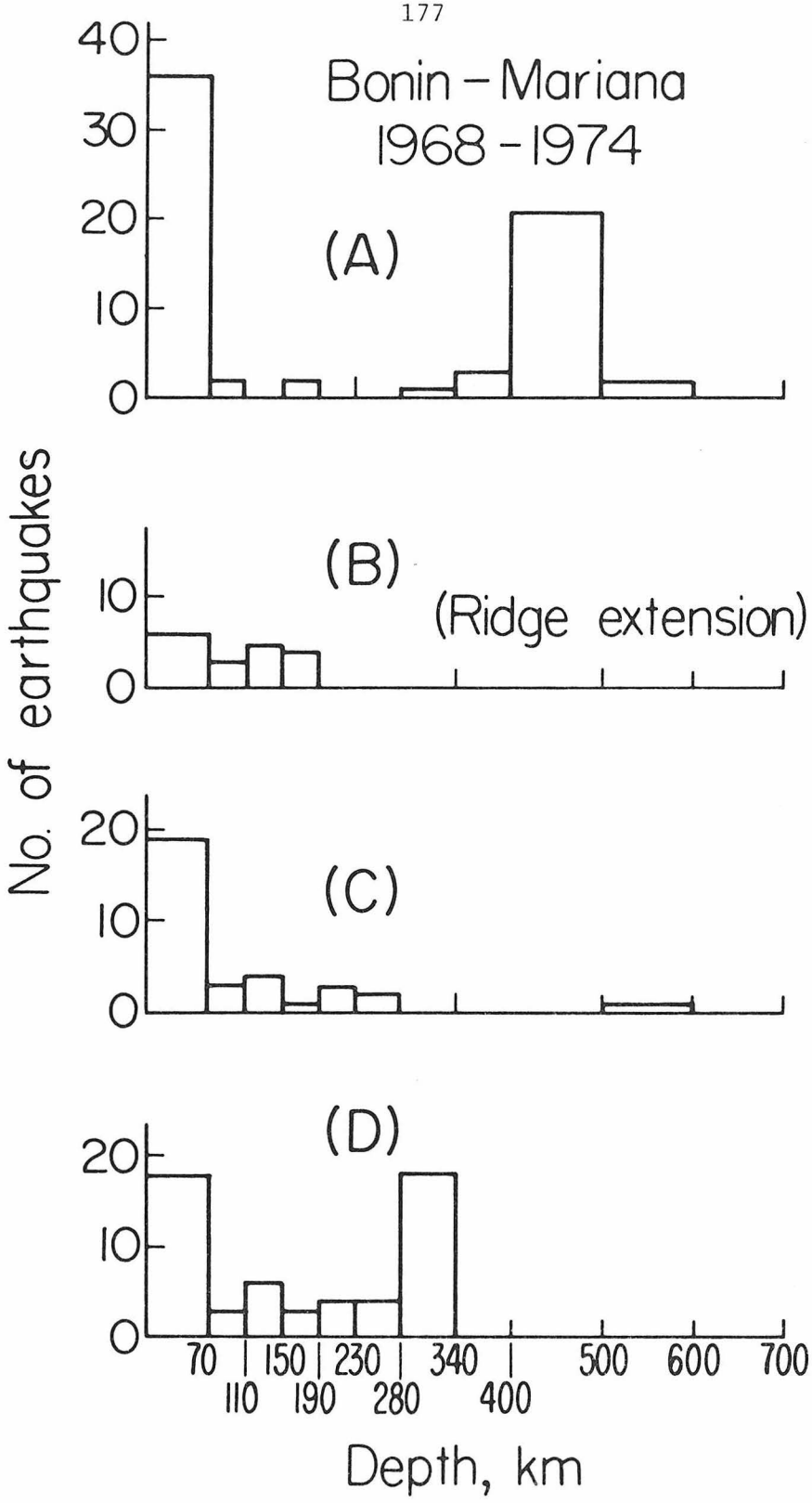

Figure 3.5. Distributions of focal depths of earthquakes at areas A, B, C and D, of Figure 3.4.

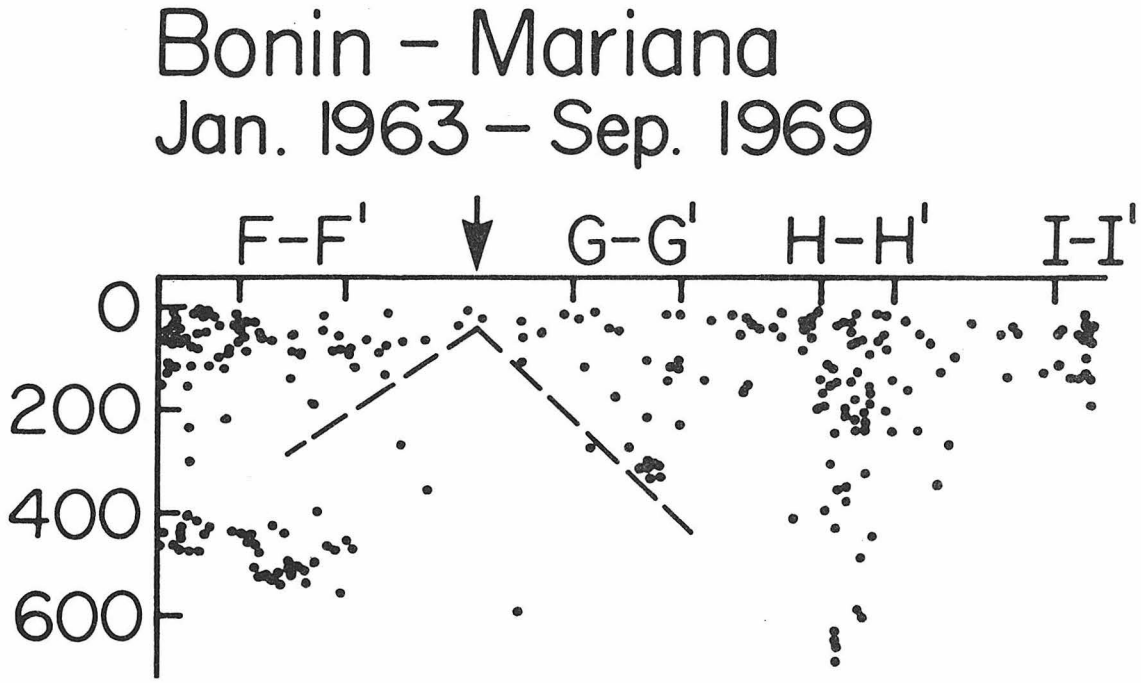

(a)

Figure 3.6. (a) Projection of hypocenters of events occurring between January 1963 and September 1969 onto a vertical plane running parallel to the arc (modified from Figure 6 of Santo, 1970b). The arrow marks the subduction location of the Marcus-Necker ridge. (b) Curves running parallel to the trend of the arc (taken from Figure 2C of Santo, 1970b).

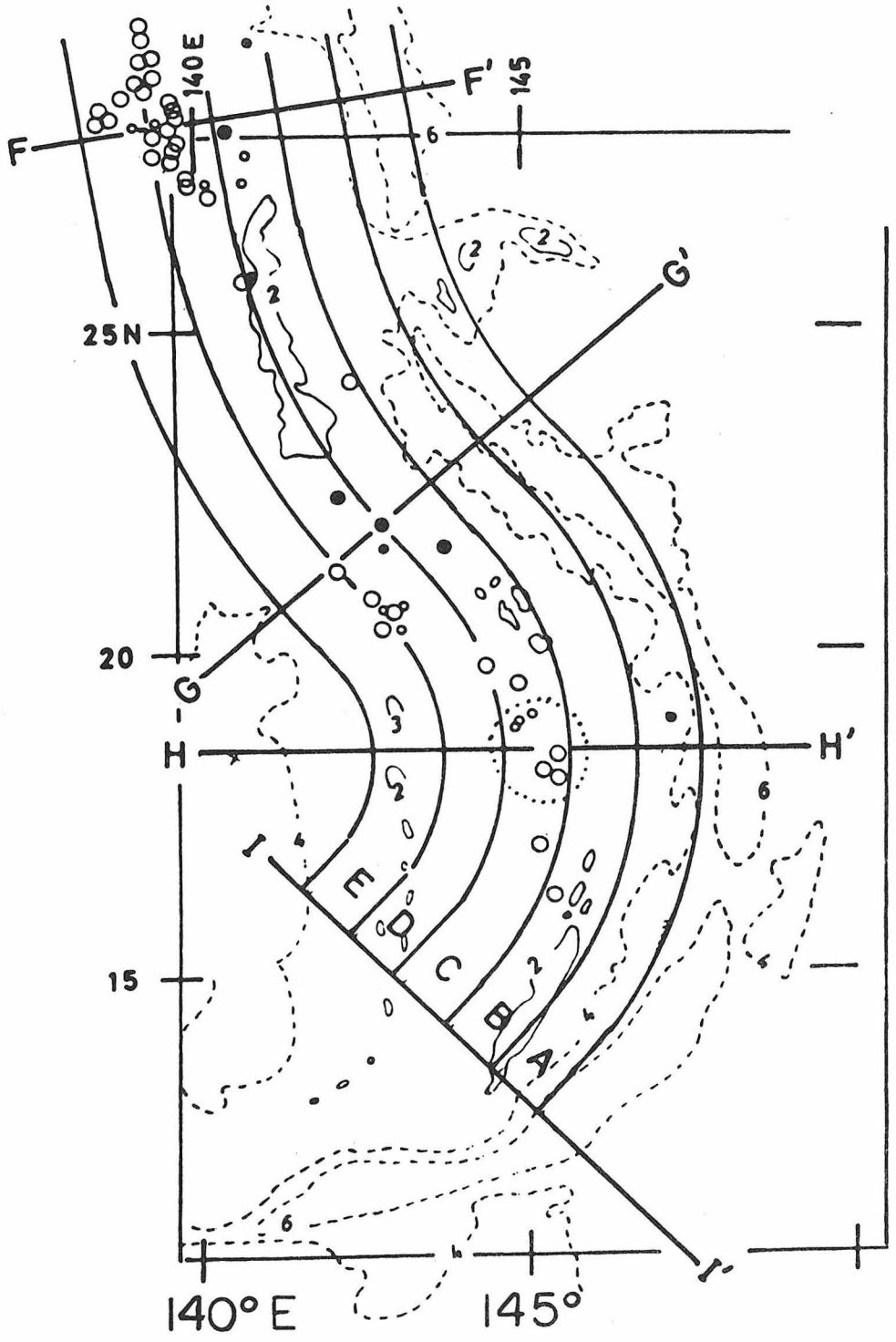

Figure 3.6. (b)

events of magnitude 4 and greater, is very much lower in area B compared with other areas. Area B probably corresponds to the area of reduced seismicity proposed by Vogt et al. (1976). The intermediate-depth earthquakes on the extension of the ridge are shallower than those occurring to the north and to the south. This pattern is similar to that in the New Hebrides Islands. Figure 3.5 shows the focal depth distribution in the four areas defined in Figure 3.4. Again we can see the systematic change of focal depth in the areas and the reduction of shallow seismicity at the locations of ridge subduction.

A similar pattern can be found in Santo (1970b) even though Santo did not point out any relationship between seismicity and ridge subduction in his work. Figure 3.6(a) shows the depth distribution of earthquakes along the island arc for the areas defined in Figure 3.6(b). With some scatter, the focal depth increases systematically with distance from the ridge. A gap or a quiet zone of intermediate-depth seismicity occurs under the ridge-arc intersection.

Tonga-Kermadec

The Louisville Ridge, an aseismic ridge associated with a transform fracture zone (Hayes and Ewing, 1971), intersects the island arc system of Tonga-Kermadec at about 26°S, 175.5°W. The 3800-fathom submarine contour is interrupted there. The seismicity of the Tonga-Kermadec region has been investigated by Sykes (1966) and Kelleher and McCann (1976). In this chapter, we study the data for the period from 1968 to 1974. Figure 7 shows the epicenter distribution for 1971 and 1972. Epicenter distributions for other years are similar and are

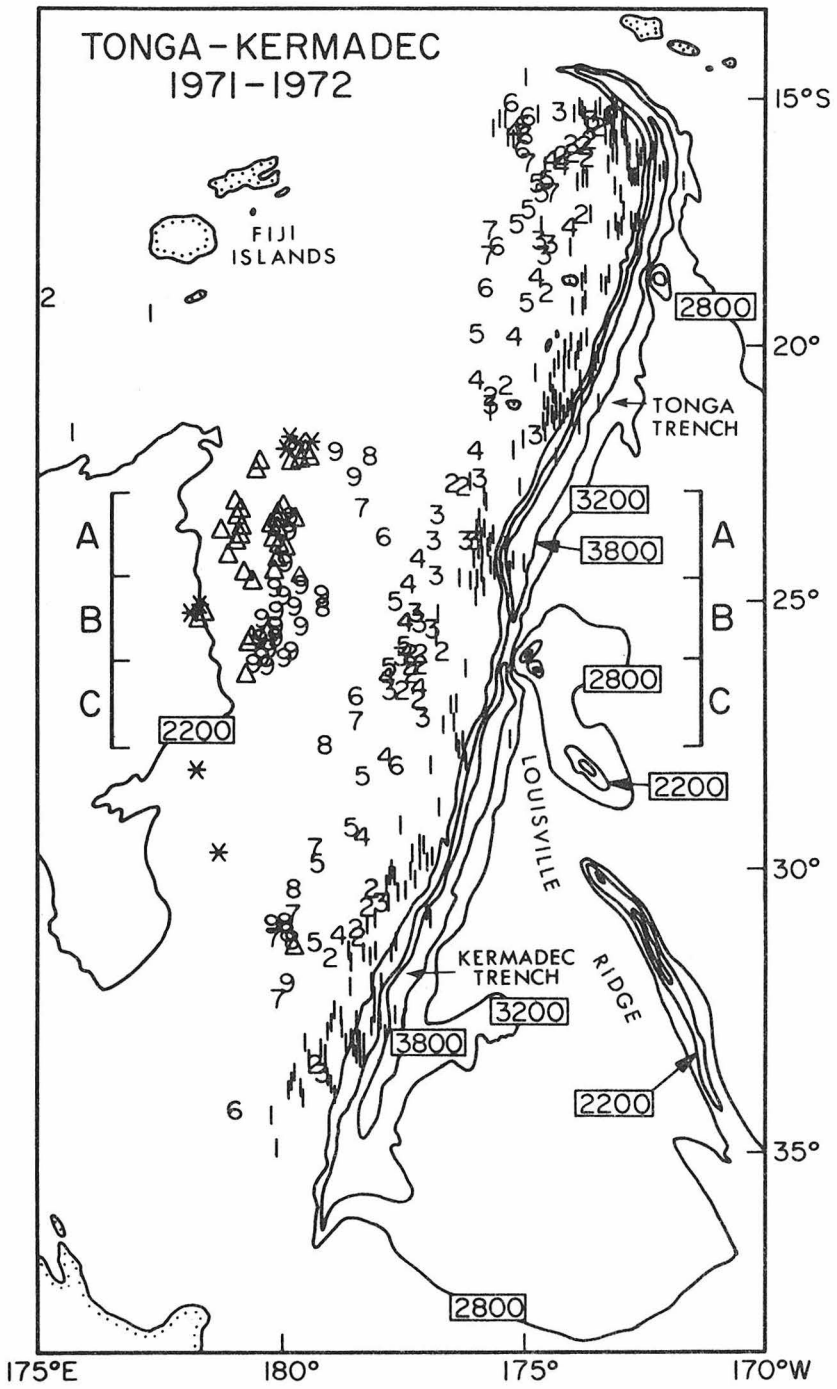

Figure 3.7. Distribution of earthquake epicenters for the period 1971 and 1972. Numbers is rectangles are depths of submarine contours simplified from Mammerickx et al. (1971) in fathoms. Symbols for epicenters are identical to those used in Figure 3.1.

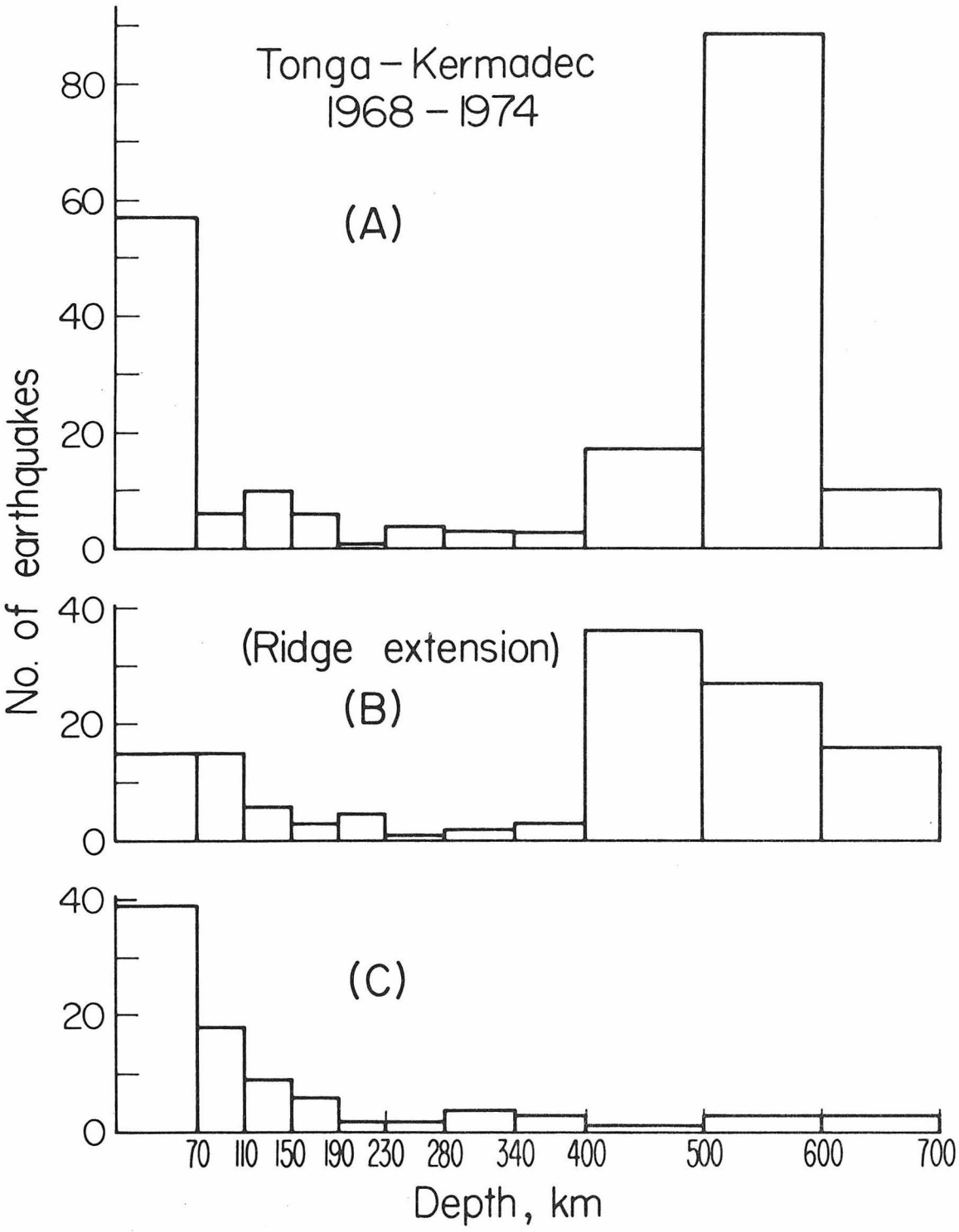

Figure 3.8. Distributions of focal depths of earthquakes at areas A, B, and C of Figure 3.7.

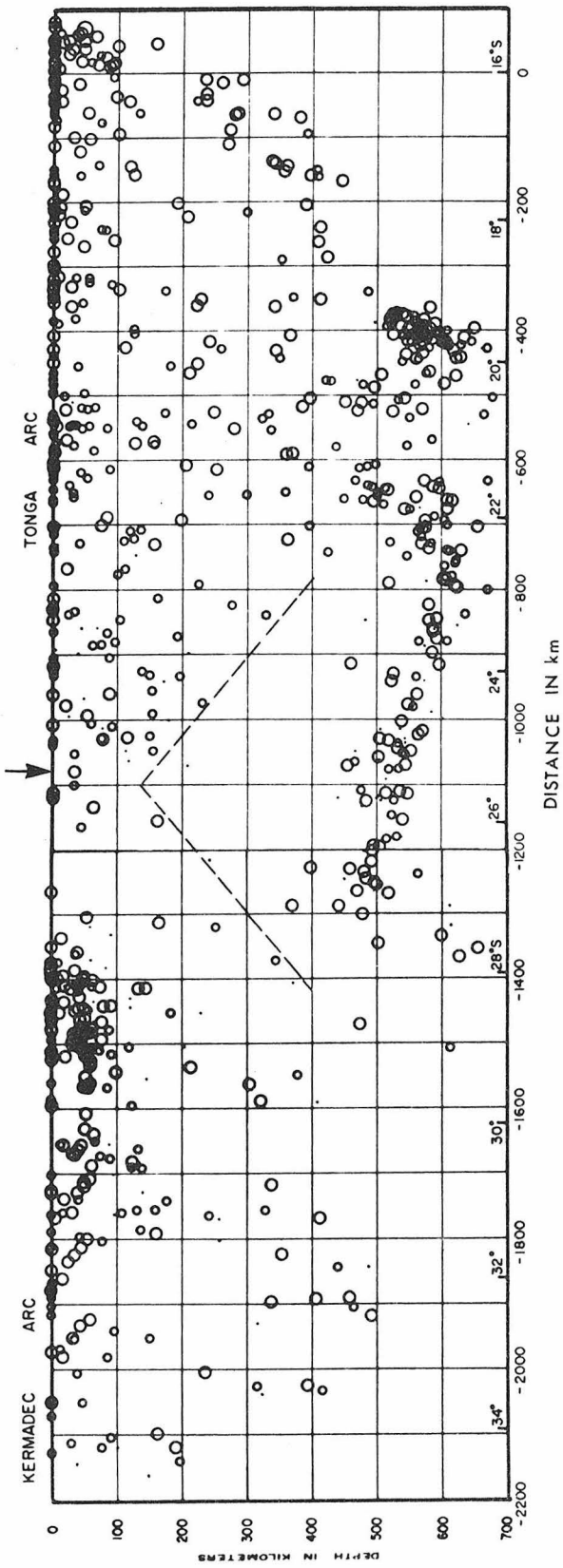

Figure 3.9. Projection of relocated hypocenters of earthquakes which occurred between January 1959 and February 1962 onto a vertical plane parallel to Tonga and Kermadec arcs (Figure 3.10). Zero distance on the abscissa corresponds to geographic position 16.0°S, 172.3°W shown in Figure 3.10. The intersection of the Louisville ridge and the Tonga-Kermadec arc system is marked by an arrow (modified from Sykes, 1966).

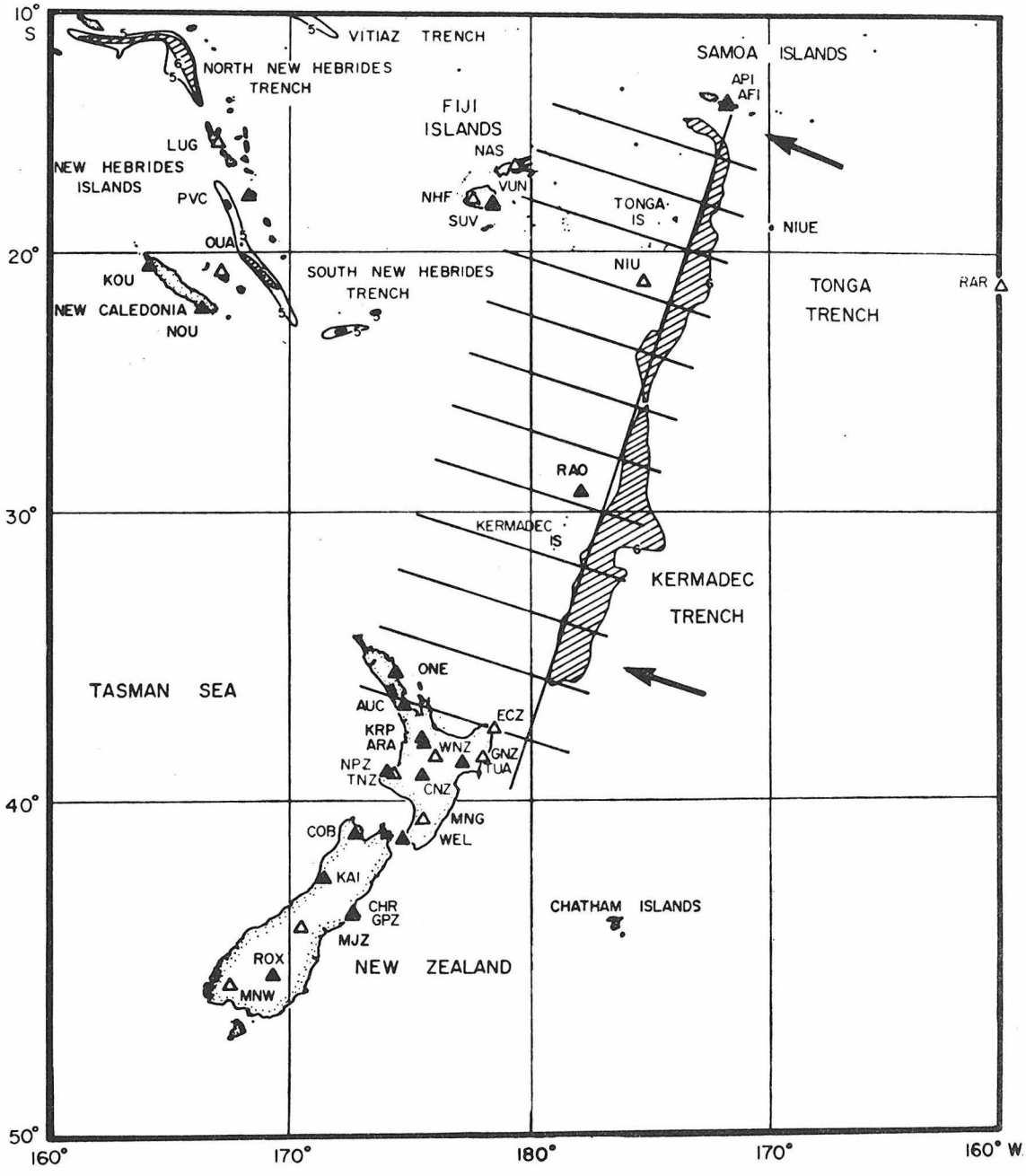

Figure 3.10. Location of the Tonga-Kermadec arc with the longest line segment indicating location of the vertical section used in Figure 3.9 (taken from Sykes, 1966).

not shown here. Three areas, A, B, and C, are defined in Figure 3.7. A small but prominent region of reduced shallow seismicity occurs at the ridge-arc intersection. This area approximately coincides with the region of reduced great earthquake activity found by Kelleher and McCann (1976). Focal-depth distributions for areas A, B, and C are displayed in Figure 3.8. Intermediate-depth events near the intersection are shallower than those to the north and south of the intersection. Figure 3.9 is a projection of earthquake foci (relocated by Sykes), which occurred between January 1959 and February 1962, onto a vertical plane parallel to the trend of the arc (Figure 3.10). The arrow in Figure 3.9 marks the location of ridge-arc insection under which intermediate-depth events are shallower than those on either sides of the intersection. A gap or a quiet region of intermediate-depth seismicity occurs under the intersection.

Peru

The Nazca Ridge subducts under Peru and divides the trench into two sections. The seismicity of Peru has been studied by Ocola (1966), Santo (1969), Teisseyre *et al.* (1974), Stauder (1975), and Barazangi and Isacks (1976). However, little attention has been paid to the effect of ridge subduction on seismicity pattern. The seismicity near the ridge-trench intersection is studied for the period from 1965 to 1971. The epicenter distribution for the period from 1969 to 1971 is shown in Figure 3.11. The focal depth distribution for events of 1965 to 1971 is presented in Figure 3.12. Figure 3.13 is a projection of hypocenters onto a vertical plane parallel to the trend

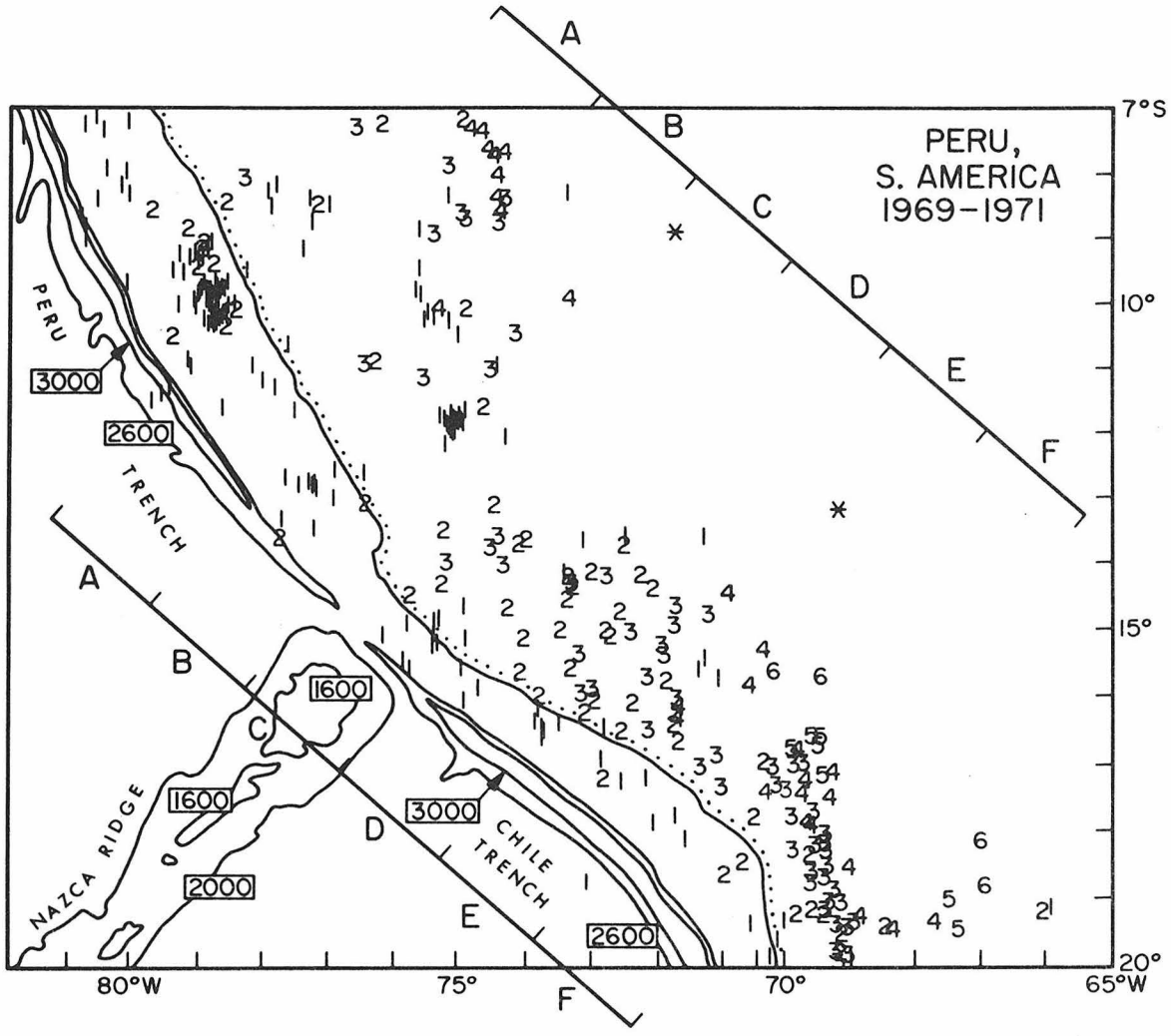

Figure 3.11. Distribution of earthquake epicenters for the period 1969 to 1971. Numbers in rectangles are depths of submarine contours (simplified from Mammerickx et al., 1975), in fathoms. Symbols for epicenters are identical to those used in Figure 3.1.

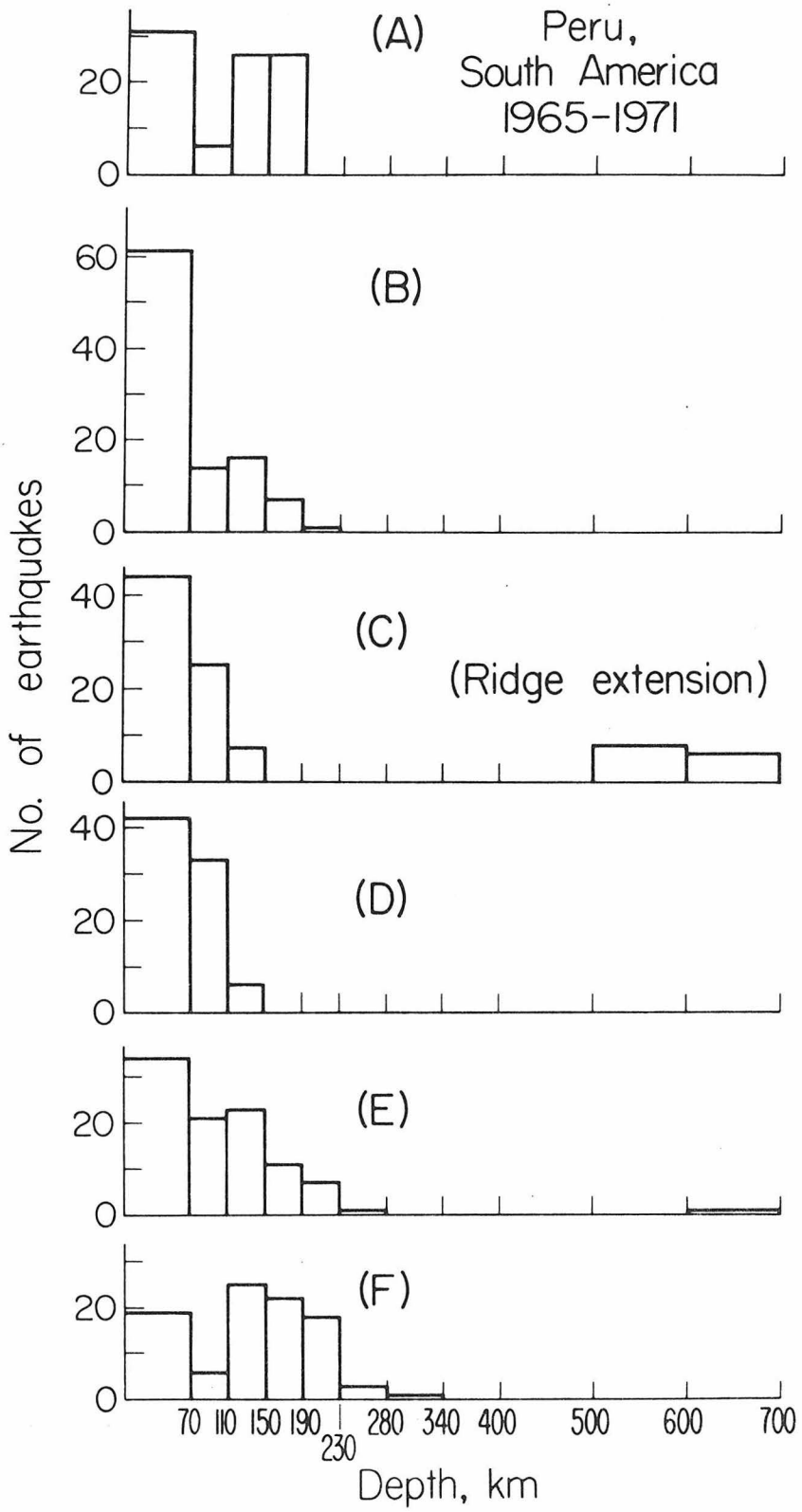

Figure 3.12. Distribution of focal depths of earthquakes at area A, B, C, D, E and F, of Figure 3.11.

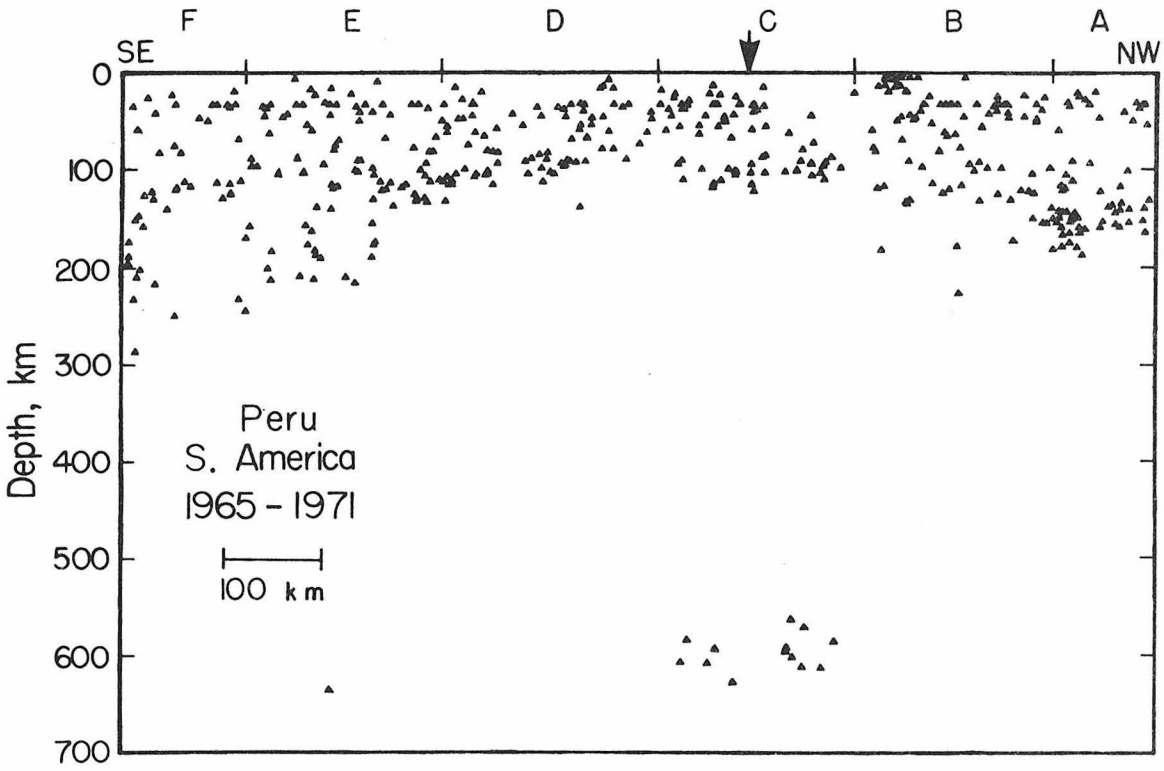

Figure 3.13. Projection of hypocenters of earthquakes occurring in the period 1965 to 1971 onto a vertical plane parallel to the Peru-Chile Trench.

of the Peru-Chile trench. The maximum depth of the intermediate earthquakes is significantly smaller in areas C and D than in other areas.

Northern Chile

At about 25.5°S, a ridge intersects the Chile Trench. Although the ridge is not particularly remarkable in terms of topography and the Chile trench is not interrupted, the seismicity near the location of ridge subduction has a very different spatial distribution than adjacent areas. The seismicity of Chile has been studied by Santo (1969), Stauder (1973), and Barazangi and Isacks (1976). In this paper, seismicity near the ridge-trench intersection for the period of 1965 to 1971 is investigated. Figure 3.14 shows the spatial distribution of epicenters of 1967 and 1968, and Figure 3.15 shows the focal-depth distributions in these areas over the period from 1965 to 1971. Figure 3.16 is a projection of all the foci of 1965 to 1971 onto a vertical plane parallel to the trend of the trench. The pattern is very similar to those discussed in the previous sections.

DISCUSSION

A region of reduced shallow seismicity occurs near the ridge-trench intersection in the Bonin-Mariana arc and the Tonga-Kermadec arc but not in the New Hebrides island arc, Peru, and northern Chile for the period investigated. As shown in Figure 3.2, the shallow seismicity in the New Hebrides is even slightly higher at the location of ridge-trench intersection. Thus the seismicity of small and

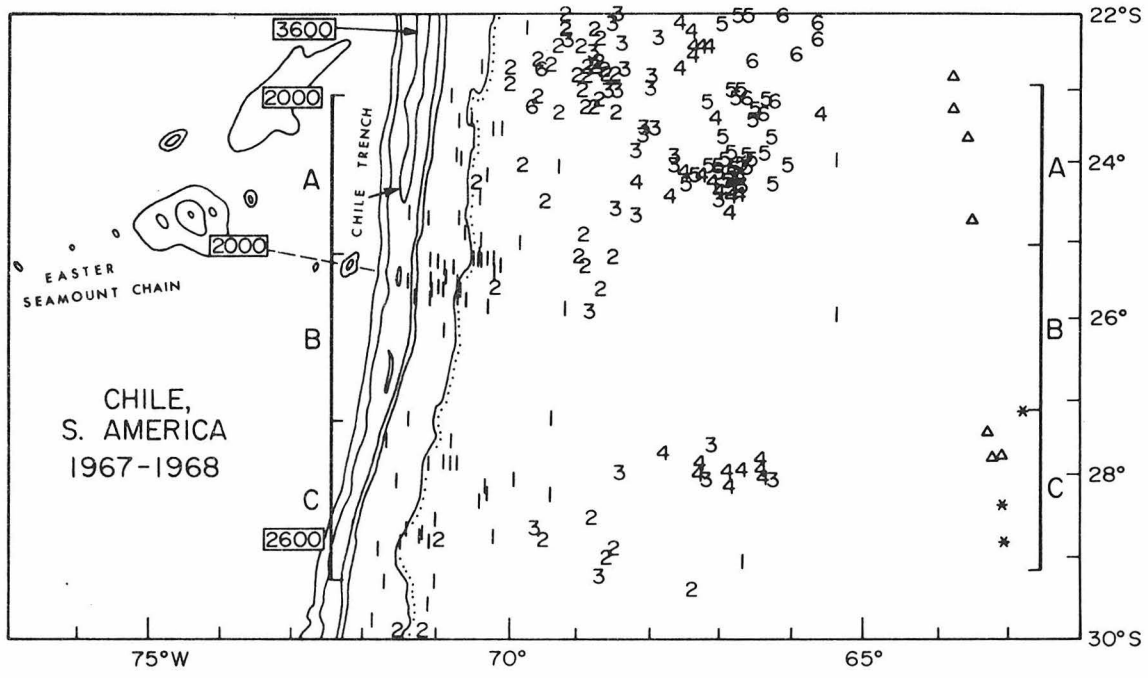

Figure 3.14. Distributuion of epicenters for earthquakes occurring in Chile in 1967 and 1968. Numbers in rectangles are depths of submarine contours (simplified from Mammerickx et al., 1975) in fathoms. Symbols for epicenters are identical to those used in Figure 3.1.

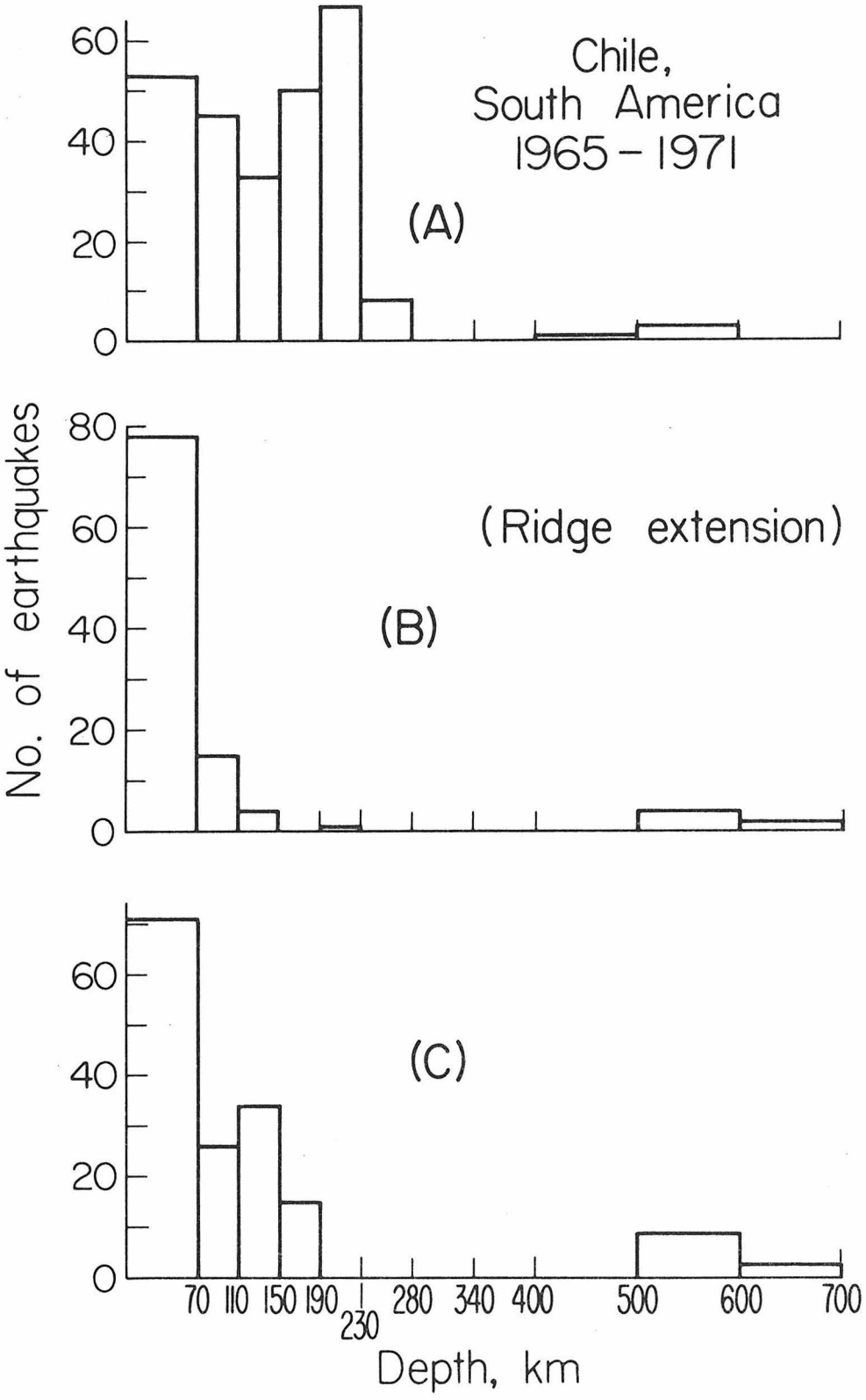

Figure 3.15. Distribution of focal depths of earthquakes at areas A, B, and C, of Figure 3.14.

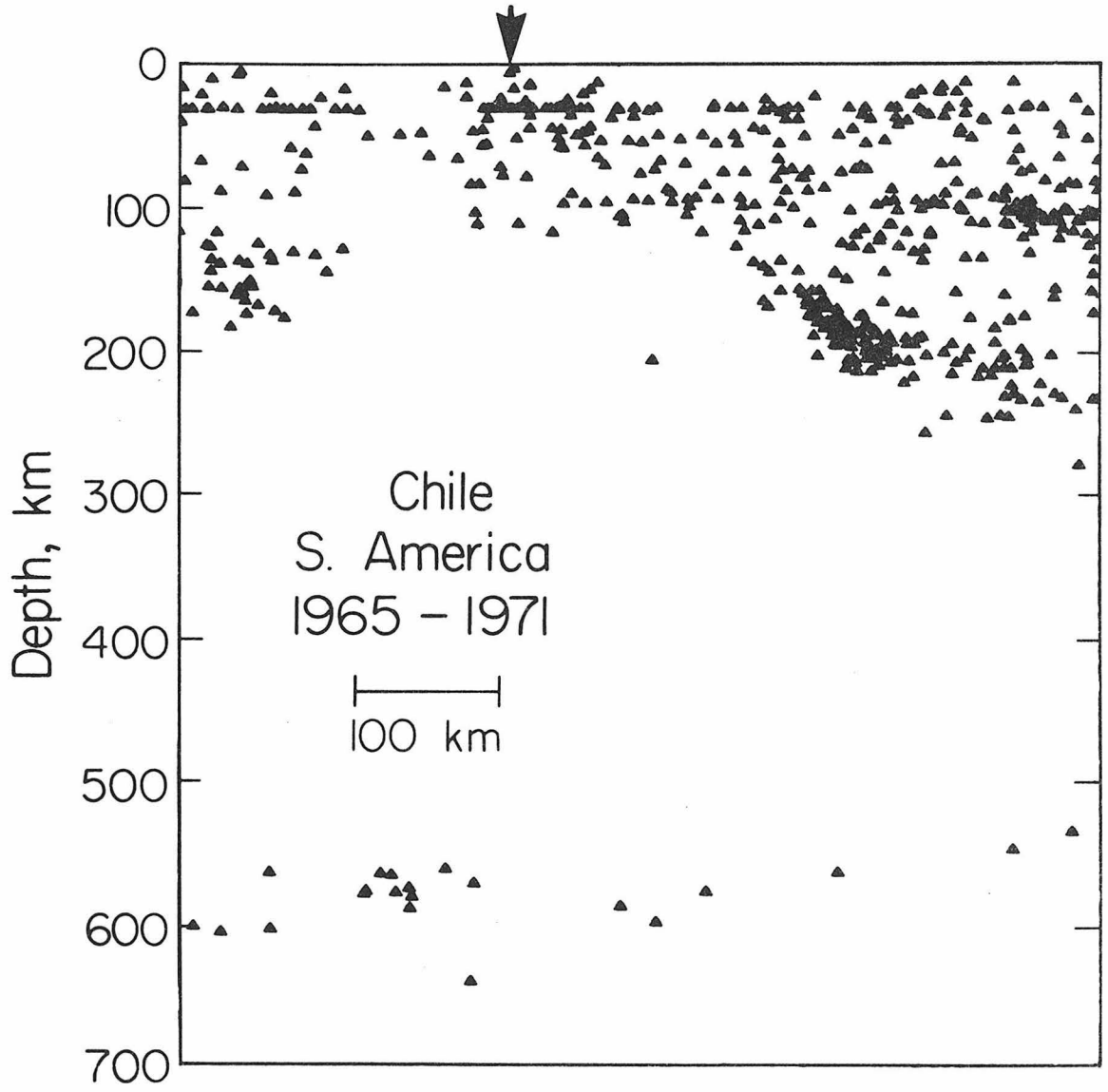

Figure 3.16. Projection of hypocenters of earthquakes occurring in northern Chile in the period of 1965 to 1971 onto a vertical plane parallel to the Chile trench.

intermediate size shallow events is not always lower at locations of aseismic ridge subduction even though great shallow earthquakes occur less frequently there, as suggested by Kelleher and McCann (1976).

For the regions we have investigated, the maximum depth of intermediate depth earthquakes is smaller under the location of ridge subduction than in the adjacent areas; this variation in focal depth sometimes forms a well-defined gap of intermediate depth seismicity. This appears to be a general pattern of seismicity associated with aseismic ridge subduction and probably can be explained by the following mechanisms. Uplifted regions in the ocean floor usually are characterized by structural roots and have crustal velocities, depth to the Moho, and average density intermediate between those for oceans and continents (Francis and Raitt, 1967; Den et al., 1971; Ludwig et al., 1973; Kelleher and McCann, 1976). Because of their lower density compared to other portions of the oceanic plate, aseismic ridges tend to resist subduction (Vogt, 1973; Vogt et al., 1976; Kelleher and McCann, 1976; Chung and Kanamori, 1977, 1978a, b). Thus, differential subduction takes place at plate boundaries with the lithospheres on the two sides of a ridge subducting with a faster rate. As a consequence the lithosphere on either side of the ridge sinks to a greater depth than the part with the buoyant ridge and causes deeper intermediate-depth seismicity. In addition, the lithosphere with a ridge is probably weaker than oceanic plates without a ridge. Because of this relative weakness, a ridge cannot accumulate a large amount of strain energy to cause strong earthquakes, and may have a greater tendency to deform aseismically or by creep

rather than brittle fracture. This may explain the observed seismic gap. Several explanations for the origin of aseismic ridges have been suggested; they may be hot-spot traces (Wilson, 1965; Morgan, 1971, 1972, 1973), fracture ridges (Menard and Chase, 1970), or remnant arcs (Karig, 1972). Unfortunately, the tectonic histories, age relationships, and heat flow data for the five ridges discussed above and their adjacent areas are either far from complete or not available. Thus their real thermal states are unknown. If an aseismic ridge was formed with hot material or by some thermal expansion process and its temperature at present is still higher than the adjacent oceanic plate, the ridge will lose its brittleness at a shallower depth in the hot mantle than other parts of the subducting plate. If the disappearance of earthquakes at the intermediate depth is due to an increased ductility of the lithosphere, the above difference in thermal state seems to provide an explanation for the observed seismic gap or systematic change in focal depth. Thus, the seismicity pattern associated with aseismic ridge subduction probably is due to differential subduction and differences in mechanical and thermal properties between aseismic ridges and pure oceanic plates.

REFERENCES

Barazangi, M. and B. L. Isacks (1976). Spatial distribution of earthquakes and subduction of the Nazca plate beneath South America, Geology, 4, 686-692.

Chase, C. G. (1971). Tectonic history of the Fiji plateau, Geol. Soc. Am. Bull., 82, 3087-3110.

Chung, W.-Y. and H. Kanamori (1977). Seismicity and tectonic anomalies associated with aseismic ridge subduction in the New Hebrides Arc (abstract), EOS, Trans. Amer. Geophys. Un., 58, 1232.

Chung, W.-Y., and H. Kanamori (1978a). Subduction process of a fracture-zone and aseismic ridges -- focal mechanism and source characteristics of the New Hebrides earthquake of January 19, 1969 and some related events, Geophys. J. R. astr. Soc., 54, 221-240.

Chung, W.-Y. and H. Kanamori (1978b). A mechanical model for plate deformation associated with aseismic ridge subduction in the New Hebrides Arc, Tectonophysics, 50, 29-40.

Den, N., W. J. Ludwig, S. Murauchi, H. Ewing, T. Asanuma, T. Yoshii, A. Kobotera and K. Hagiwara (1971). Sediments and structure of the Faruipik-New Guinea rise, J. G. R., 76, 4711-4723.

Francis, T. and R. Raitt (1967). Seismic refraction measurements in the Southern Indian Ocean, J. G. R., 72, 3015-3041.

Hayes, D. E. and M. Ewing (1971). The Louisville Ridge -- A possible extension of the Eltanin fracture zone, in Reid, J. L. (ed.), Antarctic Oceanology, V. 1, Washington D.C., Am. Geophys. Un., Antarctic Research Series, V. 15, 223-228.

Karig, D. E. (1972). Remnant arcs, Geol. Soc. Am. Bull., 83, 1057-1068.

Karig, D. E. and J. Mammerickx (1972). Tectonic framework of the New Hebrides island arc, Marine Geol., 12, 187-205.

Katsumata, M., and L. R. Sykes (1969). Seismicity and tectonics of the western Pacific: Izu-Mariana Caroline and Ryukyu-Taiwan region, J. G. R., 74, 5923-5948.

Kelleher, J. and W. McCann (1976). Buoyant zones, great earthquakes, and unstable boundaries of subduction, J. G. R., 81, 4885-4896.

Ludwig, W. J., S. Murauchi, N. Den, P. Buhl, H. Aotta, M. Ewing, T. Asamuma, T. Yoshii, and N. Sakajiri (1973). Structure of East China Sea-West Philippine Sea margin off southern Kyushu, Japan, J. G. R., 78, 2526-2636.

Mammerickx, J., R. N. Anderson, H. W. Menard and S. M. Smith (1975). Morphology and tectonic evolution of the East-Central Pacific, Geol. Soc. Am. Bull., 86, 111-118.

Mammerickx, J., T. E. Chase, S. M. Smith and I. L. Taylor (1971). Bathymetric chart of the South Pacific No. 12, Scripps Inst. of Oceanography.

Menard, H. W. and T. E. Chase (1970). Fracture zones, in Maxwell, A. E. (ed.), The Sea, V. 4, 421-443, Interscience Pubs., Inc., New York.

Morgan, W. J. (1971). Convection plumes in the lower mantle, Nature, 230, 43-43.

Morgan, W. J. (1972). Deep mantle convection plumes and plate motions, Am. Assn. Petrol. Geol. Bull., 56, 203-213.

Morgan, W. J. (1973). Plate motions and deep mantle convections, in Shagam, R. et al. (eds.), Studies in Earth and Space Sciences (Hess Volume), Geol. Soc. Am. Mem. 132, 7-22.

Ocola, L. (1966). Earthquake activity of Peru, in Steinhart, J. S. and Smith, T. J. (eds.), The Earth Beneath the Continents, 509-528, AGU, Washington, D.C.

Pascal, G., B. L. Isacks, M. Barazangi, and J. Dubois (1978). Precise relocations of earthquakes and seismotectonics of the New Hebrides island arc, J. G. R., submitted.

Santo, T. (1969). Characteristics of seismicity in South America, Bull. Earthquake Res. Inst., 47, 635-672.

Santo, T. (1970a). Regional study of the characteristic seismicity of the world, part III: New Hebrides Islands Region, Bull. Earthquake Res. Inst., 48, 1-18.

Santo, T. (1970b). Regional study on the characteristic seismicity of the world, part V: Bonin-Mariana Islands region -- comparative study on the reliability of U.S.C.G.S. seismic data since 1963, Bull. Earthquake Res. Inst., 48, 363-379.

Stauder, W. (1973). Mechanism and spatial distribution of Chilean earthquake with relation to subduction of the oceanic plate, J. G. R., 78, 5033-5061.

Stauder, W. (1975). Subduction of the Nazca plate under Peru as evidence by focal mechanisms and by seismicity, J. G. R., 80, 1053-1064.

Sykes, L. R. (1966). The seismicity and deep structure of island arcs, J. G. R., 71, 2981-3006.

Teisseyre, R., B. Wojtczak-Gadomska, E. Vesanen and M. L. Mäki (1974). Focus distribution in South American deep-earthquake regions and their relation to geodynamic development, Phys. Earth and Planet. Int., 9, 290-305.

Vogt, P. R. (1973). Subduction and aseismic ridges, Nature, 241, 189-191.

Vogt, P. R., A. Lowrie, D. Bracey and R. Hey (1976). Subduction of aseismic oceanic ridges: effects on shape, seismicity, and other characteristics of consuming plate boundaries, Geol. Soc. Am. Spec. Paper 172, 59 pp.

Wilson, J. T. (1965). Evidence from ocean islands suggesting movement in the earth, Roy. Soc. London Philos. Trans., Ser. A, 258, 145-165.